

Adaptive Trailing Edge Flaps for Active Load Alleviation in a Smart Rotor Configuration

Bergami, Leonardo; Gaunaa, Mac; Poulsen, Niels Kjølstad; Buhl, Thomas

Publication date:
2013

Document Version
Publisher's PDF, also known as Version of record

[Link to publication](#)

Citation (APA):

Bergami, L., Gaunaa, M., Poulsen, N. K., & Buhl, T. (2013). Adaptive Trailing Edge Flaps for Active Load Alleviation in a Smart Rotor Configuration. DTU Wind Energy. (DTU Wind Energy PhD; No. 0020(EN)).

General rights

Copyright and moral rights for the publications made accessible in the public portal are retained by the authors and/or other copyright owners and it is a condition of accessing publications that users recognise and abide by the legal requirements associated with these rights.

- Users may download and print one copy of any publication from the public portal for the purpose of private study or research.
- You may not further distribute the material or use it for any profit-making activity or commercial gain
- You may freely distribute the URL identifying the publication in the public portal ?

If you believe that this document breaches copyright please contact us providing details, and we will remove access to the work immediately and investigate your claim.

Adaptive Trailing Edge Flaps for Active Load Alleviation in a Smart Rotor Configuration



DTU Wind Energy - PhD

Leonardo Bergami
DTU Wind Energy PhD-0020(EN)
August 2013



Adaptive Trailing Edge Flaps for Active Load Alleviation in a Smart Rotor Configuration

Leonardo Bergami

DTU Wind Energy PhD-0020(EN)

August 2013

Author: Leonardo Bergami

Title: Adaptive Trailing Edge Flaps for Active Load Alleviation in a Smart Rotor Configuration

Department: DTU Wind Energy (Risø campus)

The dissertation is submitted to the Technical University of Denmark, in partial fulfillment of the requirements for the obtainment of the PhD degree from the PhD School DTU Wind Energy.

The PhD project was carried out in the years 2010-2012 at the Aeroelastic Design Section of DTU Wind Energy, Department of Wind Energy (formerly Risø DTU, Wind Energy Department). The dissertation was submitted in March 2013, and successfully defended on the 4th July 2013.

Main Supervisor: Senior Scientist, Mac Gaunaa, DTU Wind.

Co-supervisor: Associate Professor, Niels Kjølstad Poulsen, DTU Compute

Co-supervisor: Head of Section, Thomas Buhl, DTU Wind Energy.

DTU Wind Energy PhD-0020(EN)

August 2013

ISBN:

978-87-92896-52-0

Sponsorship:

Højteknologifonden, Advanced Technology Projects 2007, Development of ATEF system for wind turbines

Pages: 291

Tables: 5

References: 62

Technical University of Denmark

DTU Wind Energy

Risø campus

Frederiksborgvej 399

Building 125

DK-4000 Roskilde

Denmark

leob@dtu.dk

www.vindenergi.dtu.dk

Abstract

The work investigates the development of an active smart rotor concept from an aero-servo-elastic perspective. An active smart rotor is a wind turbine rotor that, through a combination of sensors, control units and actuators, is able to alleviate the fluctuating part of the aerodynamic loads it has to withstand. The investigation focuses on a specific actuator type: the Adaptive Trailing Edge Flap (ATEF), which introduces a continuous deformation of the aft part of the airfoil camber-line.

An aerodynamic model that accounts for the steady and unsteady effects of the flap deflection on a 2D airfoil section is developed, and, considering both attached and separated flow conditions, is validated by comparison against Computational Fluid Dynamic solutions and a panel code method. The aerodynamic model is integrated in the BEM-based aeroelastic simulation code HAWC2, thus providing a tool able to simulate the response of a wind turbine equipped with ATEF.

A load analysis of the NREL 5 MW reference turbine in its baseline configuration reveals that the highest contribution to the blade flapwise fatigue damage originates from normal operation above rated wind speed, and from loads characterized by frequencies below 1 Hz. The analysis also reports that periodic load variations on the turbine blade account for nearly 11 % of the blade flapwise lifetime fatigue damage, while the rest is ascribed to load variations from disturbances of stochastic nature.

The study proposes a smart rotor configuration with flaps laid out on the outer 20 % of the blade span, from 77 % to 97 % of the blade length. The configuration is first tested with a simplified cyclic control approach, which gives a preliminary indication of the load alleviation potential, and also reveals the possibility to enhance the rotor energy capture below rated conditions by using the flaps.

Two model based control algorithms are developed to actively alleviate the fatigue loads on the smart rotor with ATEF. The first algorithm features a linear quadratic regulator with periodic disturbance rejection, and controls the deflection of the flap on each blade based on measurements of the root

flapwise bending moment; each blade is considered as an independent Single Input-Single Output system. The second algorithm is a Multiple Input-Multiple Output Model Predictive Control (MIMO-MPC), which monitors the whole turbine response, and controls all the available actuators: ATEF, individual blade pitch, and generator. Both algorithms include frequency-dependent weighting of the control actions in order to limit high frequency control activity, and thus effectively reduce actuators use and wear.

The smart rotor performances are evaluated from HAWC2 simulations reproducing the response to standard turbulent wind fields. Both algorithms reduce the lifetime fatigue damage on the blade root flapwise bending moment by 15 % using the ATEF actuators. Whereas, by combining pitch and flap actions, the MIMO-MPC reports alleviation results close to 30 %. The MIMO-MPC requires lower flap activity, and also achieves higher reductions of the tower fatigue loads, thus indicating that a combined control approach that coordinates and integrates all available sensors and actuators has the potential for overall better results than achieved by a series of independent control systems.

Resumé

Denne afhandling omhandler udviklingen af et aktivt smart rotor koncept fra et aeroservoelastisk perspektiv. En aktiv smart rotor er en vindmøllerotor som igennem en kombination af sensorer, reguleringsenhed og aktuatorer, aktivt kan reducere den fluktuerende del af de aerodynamiske kræfter møllen skal modstå. Undersøgelsen omhandler en specifik aktuator type: Adaptive Trailing Edge Flap (ATEF), der består af en kontinuert deformation af den bagerste del af vingeprofilernes tværsnitsform.

Der er udviklet en aerodynamisk model som medtager både de stationære og instationære effekter af flapudbøjningen på en 2D vingesektion der opererer i både vedhæftet og separeret strømning. Modellen er valideret med resultater fra både Computational Fluid Dynamics simuleringer samt panelkodebaserede simuleringer. Denne aerodynamiske model er integreret i det BEM-baserede aero-elastiske simuleringværktøj HAWC2, som derved kan simulere responset af en vindmølle med ATEF's på.

Lastanalyser af NREL's 5MW referencevindmøllen i dennes basiskonfiguration viser at det største bidrag til vingernes flapvise udmattelsesskade stammer fra normaloperation ved vindhastigheder over nominel hastighed, og fra lastfrekvenser under 1Hz. Analysen viser ligeledes at de periodiske lastvariationer på vingerne står for cirka 11 % af vingernes flapvise levetids udmattelsesskade, hvorimod resten kommer fra laster af stokastisk oprindelse.

I denne afhandling foreslås en smart rotor konfiguration hvor 20 % af vingernes spanvidde er monteret med flapper, fra 77 % til 97 % af vingens længde. Denne konfiguration testes først med en simplificeret cyklisk regulering, som både giver en præliminær indikation af lastreduktionspotentialet og tillige indikerer muligheden for at forøge energiproduktionen for vindhastigheder under nominel hastighed ved brug af flapperne.

Der er udviklet to modelbaserede kontrolalgoritmer for aktivt at reducere udmattelseslasterne på en smart rotor med ATEF. Den første algoritme har en lineær kvadratisk regulator med afvisning af periodiske forstyrrelser, og baserer styringen af flappens udbøjning på hver vinge fra det flapvise moment ved vingeroden; hver vinge ses som et uafhængigt Single Input-Single Output

(SISO) system. Den anden algoritme er et Multiple Input-Multiple Output Model Predictive Control (MIMO-MPC) system, som monitorerer hele møllens respons og regulerer alle tilgængelige aktuatorer: ATEF, vingernes pitch samt generatoren. Begge algoritmer har frekvensafhængig vægtning af reguleringsaktiviteten for at kunne begrænse højfrekvent reguleringsaktivitet, og derigennem reducere brugen af og dermed også sliddet på aktuatorerne.

Ydeevnen af de forskellige smart rotor konfigurationer bliver evalueret ved hjælp af HAWC2 simuleringer for vindfelter med standard turbulens. Begge algoritmer reducerer den flapvise udmattelseskade for møllens levetid på 15 % ved hjælp af ATEF aktuatorerne. Denne reduktion forøges til tæt ved 30 % ved at kombinere pitch og ATEF aktuation ved hjælp af MIMO-MPC reguleringsmetoden. MIMO-MPC reguleringsmetoden kræver mindre flapaktivitet, og opnår desuden højere reduktioner af udmattelseslasterne på tårnet. Dette indikerer at en kombineret reguleringsmetode, som koordinerer og integrerer alle tilgængelige sensorer og aktuatorer har potentialet til at opnå bedre resultater end det der er opnåeligt ved brug af en serie uafhængige reguleringsystemer.

Foreword

This dissertation is submitted to the Technical University of Denmark, in partial fulfillment of the requirements for the obtainment of the PhD degree from the PhD School DTU Wind. The PhD project was carried out in the years 2010-2012 at the Aeroelastic Design Section of *DTU Wind, Department of Wind Energy* (formerly Risø DTU, Wind Energy Department), under the supervision of Senior Scientist Mac Gaunaa, DTU Wind, and co-supervision by Associate Professor Niels Kjølstad Poulsen, DTU IMM, and Head of Section Thomas Buhl, DTU Wind.

The dissertation is organized as a collection of papers, and is divided in two parts: the first part presents a concise synopsis of the study, and is integrated, in the second part, by a collection of six articles and two technical reports. The publications gathered in the second part are constituent elements of the dissertation and provide a more detailed description of the methods and of the results summarized by the synopsis.

During the last three years I have followed specialization courses for 32.5 ECTS. I took part in commercial projects and consultancy tasks, and I have been teaching in HAWC2 courses, in short seminars, and, as teaching assistant, in the course 46200 ‘Planning and development of Wind Farms’. Further ‘dissemination’ activities involved presentations at international conferences (EWEA, Torque, AIAA ASME, Sandia Workshop, PhD seminars), and the publication of articles and reports. A list of publications produced during the PhD study is reported; the publications included in the second part of the dissertation are marked by a bullet and by a boldface reference to the corresponding section. Please note that the bibliographic citations given in the synopsis chapters all refer to the bibliography reported at the end of the first part, whereas each of the publications has a reference list of its own.

List of publications

Peer-reviewed articles

- **[Article I]** Bergami, Leonardo, Mac Gaunaa, and Joachim Heinz. ‘Indicial Lift Response Function: An Empirical Relation for Finite-thickness Airfoils, and Effects on Aeroelastic Simulations’. *Wind Energy*, 16(5):681-693, July 2013 (published on-line in June 2012). Doi:10.1002/we.1516.
- Baek, Peter, Mac Gaunaa, Joachim Heinz, Leonardo Bergami, and John Korsgaard. ‘A Modified Dynamic Stall Model for Airfoils with Active Aerodynamic Devices’. *Submitted to Wind Energy* (December 2011).
- Castaignet, Damien, Leonardo Bergami, Thomas Buhl, Niels K. Poulsen, and J. J. Wedel-Heinen. ‘Robustness Assessment of a Flap Controller with Two Alternative Aeroelastic Simulation Tools’. *Submitted to Wind Energy* (January 2012).
- **[Article II]** Bergami, Leonardo, and Mac Gaunaa. ‘Analysis of Aeroelastic Loads and Their Contributions to Fatigue Damage’. Submitted to *Journal of Physics: Conference Series*. Torque conference, Oldenburg (October 2012).
- **[Article III]** Bergami, Leonardo, Vasilis A. Riziotis, and Mac Gaunaa. ‘Aerodynamic Response of an Airfoil Section Undergoing Pitch Motion and Trailing Edge Flap Deflection: a Comparison of Simulation Methods’. *Submitted to Wind Energy* (January 2013).
- **[Article V]** Bergami, Leonardo, and Niels K. Poulsen. ‘A Smart Rotor Configuration with Linear Quadratic Control of Adaptive Trailing Edge Flaps for Active Load Alleviation’. *Submitted to Wind Energy* (March 2013).

Conference articles

- Gaunaa, Mac, Leonardo Bergami, and Joachim Heinz. ‘Indicial Response Function for Finite-thickness Airfoils, a Semi-empirical Approach’. In *Conference Proceedings; 49th AIAA-ASME. 4-7 January 2011*. Orlando (FL), 2011.
- Bergami, Leonardo. ‘Adaptive Trailing Edge Flaps for Active Load Reduction’. In *Proceedings of 7th PhD Seminar on Wind Energy in Europe*. Delft, Netherlands: Delft University of Technology, 2011.
- Barlas, Thanasis, Frederik Zahle, Niels N. Sorensen, Mac Gaunaa, and Leonardo Bergami. ‘Simulations of a Rotor with Active Deformable Trailing Edge Flaps in Half-wake Inflow: Comparison of Ellipsys 3D with HAWC2’. In *European Wind Energy Conference & Exhibition*. Copenhagen, Denmark, 2012.
- **[Article IV]** Bergami, Leonardo, and Lars C. Henriksen. ‘Cyclic Control Optimization for a Smart Rotor’. In *Proceedings of 8th PhD Seminar on Wind Energy in Europe*. Zurich (CH), 2012.
- **[Article VI]** Henriksen, Lars, Leonardo Bergami, and Peter B. Andersen. ‘A Model Based Control Methodology Combining Blade Pitch and Adaptive Trailing Edge Flaps in a Common Framework’. In *Proceedings of European Wind Energy Association Conference*. Vienna, Austria, 2013.

Technical reports

- *ATEF Finalization report*. Edited by Wedel-Heinen, Jens Jakob, Tim Behrens, and Peter B. Andersen. Technical Report DTU Wind Energy E-0024: DTU Wind, Department of Wind Energy, Technical University of Denmark. Roskilde, Denmark. October 2011.

I was responsible for the report sections:

- Aeroelastic analysis tools for wind turbine systems
- Stability analysis of an airfoil with ATEF
- **[Report A]** Preliminary load analysis of the NREL 5 MW turbine

- **[Report B]** Bergami, Leonardo, and Mac Gaunaa. *ATEFlap Aerodynamic Model, a Dynamic Stall Model Including the Effects of Trailing Edge Flap Deflection*. Technical Report Risø-R-1792(EN). Roskilde, Denmark: Risø National Laboratory, Technical University of Denmark. February 2012.

Contents

Abstract	i
Resumé	iii
Foreword	v
I Synopsis	1
1 Introduction	3
1.1 Problem overview and state of the art	3
1.2 Scope of the work and project outline	7
2 Simulation Environment	11
2.1 HAWC2 aeroelastic code	11
2.2 NREL 5 MW Reference Wind Turbine	13
3 Load Analysis	15
3.1 Design Load Cases	17
3.2 Contributions to the fatigue damage	20
3.2.1 Periodic and stochastic components	20
3.2.2 Mean wind speed	22
3.2.3 Frequency contributions to fatigue damage	22
3.3 Aerodynamic model approximations, effects on load simulation	25

4	ATEFlap Aerodynamic Model	29
4.1	Attached flow dynamics	30
4.2	Dynamic stall model	31
4.3	Model validation	32
5	Adaptive Trailing Edge Flap rotor configuration	33
5.1	Flap steady aerodynamic properties	34
5.2	Flap placement along the blade span	35
5.3	Flap spanwise extension	39
5.4	Proposed ATEF rotor configuration	41
6	Preliminary investigations with feed-forward cyclic control	45
6.1	Cyclic control for blade load alleviation	46
6.2	Cyclic control for enhanced power capture	51
6.2.1	Preliminary BEM analysis	51
6.2.2	Cyclic optimization	54
7	Model Based control algorithms for a rotor with ATEF	59
7.1	Overview on control algorithms	60
7.1.1	Definition of the control models	60
7.1.2	Optimal controller algorithms	62
7.2	SISO Linear Quadratic control for active load alleviation	64
7.3	MIMO Model Predictive Control	70
8	Summary of findings and future work	75
8.1	Aerodynamic model	75
8.2	Load analysis	77
8.3	Smart rotor configuration and preliminary evaluation	78
8.4	Active Load Alleviation with Adaptive Trailing Edge Flaps	79
8.5	Cost of Energy estimation	82
8.6	Indications on flap actuator requirements	83
9	Conclusion	87
	Acknowledgments	91
	Bibliography	100

II	Articles and reports	101
Article I.	Indicial lift response for finite thickness airfoils	103
Article II.	Aeroelastic loads and contribution to fatigue damage	119
Article III.	Aerodynamics of an airfoil with flap: simulation comparison	131
Article IV.	Cyclic Control Optimization for a Smart Rotor	151
Article V.	Linear Quadratic control of ATEF for active load alleviation	161
Article VI.	A Model Based Control combining Blade Pitch and ATEF	181
Report A.	The ATEF project report: Preliminary load analysis	193
Report B.	ATEFlap Aerodynamic Model	213

Part I

Synopsis

Introduction

1.1 Problem overview and state of the art

During the past 25 years, the size of utility scale horizontal axis wind turbines grew uninterrupted, constantly seeking a reduction of the cost of energy, figure 1.1. As the rotor size increases, all wind turbine components, and the blades in particular, have to withstand higher loads; in the past, the higher structural requirements were mainly satisfied by increasing the weight of the structure, or by employing more expensive compounds with an higher specific strength. Sieros et al. [55] and Riziotis et al. [51] conclude that such growing trend is likely to hit a limit, above which further upscaling of the turbine size would not yield any benefit in terms of cost of energy reduction, unless technological breakthrough are introduced to allow for further upscaling in a cost-efficient way.

The upscaling problem could be solved by applying technologies capable of reducing the aerodynamic loads the rotor has to withstand, either with passive or active load control solutions. Passive load control could be achieved by bend-twist aeroelastic coupling of the blades deformations: the blades would

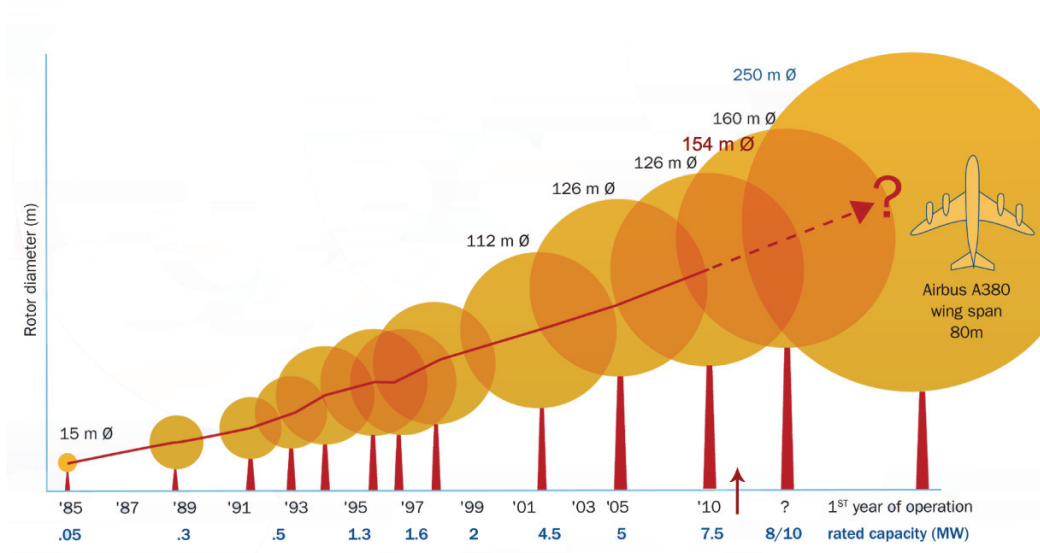


Figure 1.1: *The rated power and the rotor size of utility scaled horizontal axis wind turbines have been continuously growing for the past 25 years, the latest prototype put in operation has a diameter of 154 m, making modern wind turbines one of the largest man-built moving structures. Source: Upwind, design limits and solutions for very large wind turbines [61]*

respond to an increase of the aerodynamic forces with a torsion deformation that twists the blade toward lower angles of attack, and therefore reduces the aerodynamic loads [20, 46]. Active load control is instead achieved by a wind turbine rotor that, through a combination of sensors, control units, and actuators, compensates for the variations in the wind field swept by the blades, and thus actively reduces the aerodynamic loads it has to withstand. The concept is often referred to as *smart rotor*; detailed reviews of the literature on the subject are reported by Barlas and van Kuik [9], and Johnson et al. [33].

Smart rotors can employ different actuator types to modify the aerodynamic forces on the turbine blades. For instance, the traditional blade pitch system can be enhanced to control each blade individually, and thus partly compensate for the load variations the blade would encounter at different azimuthal positions, see for instance the investigations by Bossanyi [19], Larsen et al. [39], and Bossanyi et al. [18]. Other types of smart rotor actuator de-

vices compensate instead for variations in the incoming wind field by modifying the blade profile geometry at selected locations along the blade span; the profile geometry and hence the aerodynamic forces are modified by devices as microtabs [44, 57], rigid rotating plain flaps [57], or trailing edge flaps with a continuous deformation shape. The latter flap type differentiate from the traditional plain one as the flap causes a deformation of the airfoil profile geometry that is continuous, and thus avoids the air gaps and the surface discontinuities given by flaps rotating around their hinge point. Flaps with a continuous deformation shape have thus better aerodynamic qualities [56] and probably lower noise emissions than rotating flaps.

Several studies have focused on trailing edge flaps with a continuous deformation shape, an interest that is also reflected by the multitude of designations this particular type of actuator has so far received. As the naming coherence is sometimes lost even inside the same investigation group, it might be useful to recapitulate here some of the different names that designate this same device. The general category of active aerodynamic control devices distributed along the blade span, hence often the flaps by synecdoche, has been referred to as: Active Aerodynamic Devices (AAD) [5], Active Flow Control (AFC) [13], Active Aerodynamic Load Control (AALC) [15]. More specifically, a trailing edge flap with a continuous deformation shape has been referred to as: trailing edge flap [11], morphing trailing edge flap [62], Variable Trailing Edge Geometry (VTEG) [21], Deformable Trailing Edge Geometry (DTEG) [3], Deformable Trailing Edge Flap (DTEF) [2], and, according to the latest fashion, Adaptive Trailing Edge Flap (ATEF) [4, 23], which is the denomination that will be adopted throughout this work.

The presence of active flaps along the wind turbine blades requires aerodynamic models that account for both the steady and the dynamic effects that the flap deflection causes on the aerodynamic forces. Previous studies have addressed the problem of simulating unsteady aerodynamic forces on a 2D airfoil section with flaps by using, among others, Navier-Stokes solvers [30, 57], panel code methods [45], viscous-inviscid interaction models [49, 52], and simpler engineering methods, which considered either quasi-steady approximations [36], or attached flow models [8, 21], or dynamic-stall type of models [1, 5, 23]. On account of their lower computational requirements, engineering methods have often been integrated in Blade Element Momentum (BEM) based aeroelastic codes, allowing thus to simulate the

full response of a turbine with adaptive trailing edge flaps.

Another issue specific to smart rotors is how to design the rotor ‘brain’: a control algorithm that, based on the information received from the sensors, would determine the most appropriate control actions the actuators should put in place to steer the controlled wind turbine system in the desired fashion. The first studies on wind turbine rotors with adaptive trailing edge flaps mostly opted for control algorithms based on PID methods, applied either to each blade independently [2, 3, 5, 50, 53], or to the whole rotor through multi-blade coordinate transformation [8, 36]. Later studies have instead considered more advanced model based control algorithms, such as Linear Quadratic Regulators (LQR) [62], Model Predictive Control (MPC) [11, 23], or H_∞ control [60]. All the cited control algorithms aim at alleviating the variations of the loads over the rotor area, and thus require measurements that provide indications of the current load state over the blades. Most of the algorithms retrieve the information from the current blade deformation state; some studies assume the availability of sensors that provide measurements of the blade deflection and deflection rate [5, 13, 50, 62], whereas other controllers use instead measurements of the blade flapwise bending moment, either at selected locations along the span [2, 3], or, more simply, at the blade root [11, 12, 23, 36]. Some studies have also considered control algorithms where additional information on the in-flow condition along the blades are provided, for instance, by measurements performed with Pitot’s tubes mounted on the blade leading edge [3, 11, 23].

The primary focus of adaptive trailing edge flaps has been so far the alleviation of the fatigue loads caused by the fluctuation of the aerodynamic forces on the rotor blades. The flap potential for load alleviation was first assessed on 2D airfoil sections, with simulations [21, 33], and with wind tunnel experiments on non-rotating rigs [6, 59]; the variation of the aeroelastic stability limit (flutter limit) for the 2D airfoil section with adaptive trailing edge flaps was then investigated by Bergami and Gaunaa [16]. The performances of trailing edge flaps on full wind turbine rotors have been evaluated mainly by means of aeroelastic simulations, as in most of the works cited in the previous and the following paragraphs. Two rotating experiments have been also performed: the DUWIND group at Delft university tested a two bladed smart-rotor in an open jet wind tunnel [12, 60], and Castaignet et al. [24] carried out a full scale experiment on a 225 kW turbine with flaps on one of

the three blades.

All the investigations confirmed that smart rotors with adaptive trailing edge flaps have a potential for reducing the fatigue loads experienced by the turbine; furthermore, the studies from Lackner and van Kuik [37] and Castaignet et al. [22] reported that active flap controls designed for fatigue alleviation are likely to reduce also part of the extreme loads. In terms of fatigue load alleviation, the performance estimations found in literature are rather widespread, with figures ranging from 5 to 47 percent, see the summary compiled by Barlas et al. [11]. The differences are partly due to the variety of smart rotor configurations considered in the literature, in terms of turbine size and capacity, extension of the trailing edge flap actuators, control algorithm and sensors. Apart from that, the wind field simulation conditions also have a significant impact on the fatigue alleviation results, and simulations performed with low turbulence intensities are likely to return much higher load alleviation performances than results based on more realistic wind field conditions [5]. It is therefore important that evaluations and comparisons of smart rotor solutions are based on similar and realistic simulation conditions, following for instance, the prescriptions given by the IEC standard 61400 on wind turbine design requirements [26].

1.2 Scope of the work and project outline

The present work addresses the development of a smart rotor with an active load alleviation system featuring adaptive trailing edge flaps on the rotor blades; the smart rotor development is investigated from an *aero-servo-elastic* perspective. The scope of the project is thus to formulate an aero-servo-elastic simulation tool able to account for the presence of the adaptive trailing edge flaps, and thus to gain an insight on the effects the flaps have on the aerodynamic forces, henceforth on the response of the structure, and on the loads experienced by the turbine components. The insight is exploited to formulate two active load control algorithms, whose main focus is to alleviate the loads on the turbine rotor, and, in particular, to reduce the fatigue damage at the blade root from flapwise deflections, which is often considered a critical design parameter. The work continues the track opened by

the Ph.D. thesis by Andersen [4], and it partly developed in parallel with the Ph.D. studies of Barlas [10], Baek [5], and Castagnet [25], thus offering numerous chances of mutual inspiration, and of cheerful collaboration.

The starting point of this study is the aeroelastic analysis of a standard wind turbine in its baseline configuration, without any flap or other active load control device, chapter 3. The time series describing the turbine response are obtained from simulations performed with the state-of-the-art aeroelastic code HAWC2, which is briefly described in chapter 2; the same chapter presents the main characteristics of the NREL 5 MW wind turbine, which will be used as reference model throughout the study. The aeroelastic analysis of the baseline wind turbine is first used to quantify the bias caused by simplifications of the aerodynamic model in the simulations, thus providing an indication of the requirements for the development of the aerodynamic model that would account for the flap effects. Secondly, as the primary objective of the smart rotor control is to alleviate the loads on the turbine rotor, the preliminary analysis provides a useful insight on which load mechanisms are the dominant ones, chapter 3.

Chapter 4 introduces the *ATEFlap* aerodynamic model, an engineering type of model that accounts for the steady and dynamic effects of flap deflections on a 2D airfoil profile. The model is validated against numerical methods, and implemented in the HAWC2 code, thus providing a complete aeroelastic simulation tool for turbines with adaptive trailing edge flaps. A smart rotor configuration with flaps is proposed in chapter 5, and is used in the following investigations. A preliminary evaluation of the flap effects is performed with a simplified cyclic control approach, considering both load alleviation and power enhancement objectives, chapter 6. Finally, two model based control algorithms for active load alleviation with flaps are developed in chapter 7. The first algorithm follows a simple approach, where the flap control only focuses on alleviating the blade root flapwise bending moment variation, and each blade is treated independently from the rest of the structure. The second algorithm proposes instead an ‘holistic’ control framework, where the same controller is responsible for power tracking and load alleviation, and manages both blade pitch and flap deflection actions. The smart rotor performances are evaluated by means of aeroelastic simulations reproducing the wind field conditions prescribed by the IEC standard [26], and the effects of the flap active load alleviation are summarized in terms of fatigue damage

reductions. Chapter 8 recalls the structure of the synopsis and presents a concise summary of the main findings, a few considerations on the results, as well as possible future work topics; chapter 9 concludes the dissertation synopsis.

Far from being an exhaustive analysis on the smart rotor subject, the work omits to consider various other aspects of a smart rotor implementation; among others, considerations on economic feasibility and on the construction of reliable flap actuator devices are absent. By no means the omission implies that such aspects are considered of less importance than the aero-servo-elastic ones; on the contrary, it is only by considering all these aspects together that it will be possible to determine whether smart rotor solutions with adaptive trailing edge flaps have the potential to lead the way for the next generation of wind turbines.

CHAPTER 2

Simulation Environment

A substantial part of the investigations presented in the dissertation involves simulations of the aeroelastic response of a reference wind turbine model. All the simulations are performed with the in-house aeroelastic code HAWC2. The chapter briefly outlines the main characteristics of the aeroelastic code, and introduces the NREL 5 MW wind turbine, which will be used as reference model, first in its baseline configuration, and thereafter in a smart rotor configuration featuring adaptive trailing edge flaps.

2.1 HAWC2 aeroelastic code

The code HAWC2 (Horizontal Axis Wind turbine Code, 2nd generation) is a tool to perform time marching simulations of the aeroelastic response of an horizontal axis wind turbine. The code couples a multibody structural model with a Blade Element Momentum (BEM) aerodynamic model, and includes a wind field generator able to replicate the conditions prescribed by the International Electrotechnical Commission's (IEC) standard on wind

turbine design [26]; the wind field stochastic turbulence box is generated following Mann's method for three-dimensional wind simulations [43]. Extensive testing and validation of the aeroelastic code and its components was carried out in the past, partly under the IEA task 23 'Offshore Code Comparison Collaboration (OC3)' [35, 47], and is presently continued under the OC4 project [48].

The multibody structural model adopts a floating frame of reference formulation [54]: each body is defined in its own reference frame, which can translate and rotate with respect to another body or to the inertial reference frame. The wind turbine structure is modeled as an aggregate of bodies, and each body is modeled as a sequence of Timoshenko beam elements, thus intrinsically accounting for the torsional degree of freedom. The deformation state of each of the bodies is computed with respect to its own local coordinate system, and under the linear assumption of small deflections and rotations. Blades, or other turbine components subject to large deflections, are described by a series of bodies, where the (linear) deformation state of the last element in a body sets the translation and rotation of the following body reference frame. The non-linear effects caused by large deflection are thus accounted for.

The aerodynamic part of the model follows the Blade Element Momentum (BEM) formulation: the turbine rotor area is discretized into a polar grid, and each annular stripe of the grid is assumed independent from the others. Aerodynamic forces and moments are computed at radial stations along the blade span with 2D models that account for unsteady dynamics in attached and separated flow conditions. The dynamic stall model described by Hansen et al. [28] is used at first, and is then substituted by the ATE-Flap model to account for the aerodynamic effects of flap deflection, chapter 4; the two models return exactly the same results in case of null flap deflection. The induced velocities over the rotor area are resolved for each cell of the polar grid [42], and depend on both radial and azimuthal position. The method provides a better representation of the rotor aerodynamics in non-uniform inflow than given by the standard BEM approaches, which assume instead annular strips uniformity and azimuthal independence [42]. The model includes Glauert and Prandtl corrections, and accounts for the effects of dynamic inflow by applying Øye's second order low-pass filter on the induced velocities [29].

The BEM assumption of independent annular elements is only valid for small variations of the thrust coefficient along the blade radius. The condition is likely to be violated on a smart rotor with span-wise distributed aerodynamic control: a blade section with deflected flaps just adjacent to one without will often introduce strong discontinuities in the thrust distribution. Future work should consider investigating the response of a turbine with flaps using more advanced aerodynamic models, as for instance vortex wake methods or Computational Fluid Dynamic [7], and thus assess the importance of the limitations imposed by the BEM method, and their impact on the overall loads and alleviation predictions.

2.2 NREL 5 MW Reference Wind Turbine

The aeroelastic simulations presented in the following chapters are all based on the NREL 5 MW baseline wind turbine model in its on-shore configuration. The model describes a conceptual turbine design that is representative of modern utility-scale multi-megawatt machines. The turbine reaches a rated power of 5 MW and has an upwind three bladed rotor of 126 m diameter, table 2.1; the design characteristics are publicly available and they are presented in the technical report by Jonkman et al. [34]. The correct implementation of the wind turbine aeroelastic model is verified by comparing the turbine structural frequencies and steady operation curves returned by the HAWC2 code against the data provided in Jonkman et al. [34] [Report A].

The baseline turbine controller features a variable speed generator, and collective pitch-to-feather limitation of the power output above rated conditions. The control algorithm uses a PI feedback on low-pass filtered measurements of the high speed shaft rotational speed, and the control gain is rescheduled as a function of the collective pitch angle [34]. Most of the aeroelastic simulations presented in the work are obtained with the baseline turbine controller, which is maintained also when the flap load alleviation system is active. There are only two instances where the NREL baseline controller is substituted by other algorithms. First, during the full design load cases analysis (section 3.1) a similar PI-based algorithm [38], referred to as ‘Risø controller’, is instead used in order to include shut down events in the sim-

<i>NREL 5 MW Reference Wind Turbine</i>	
Rated Power	5 MW
Num.Blades	3
Rotor Orient.	upwind
Rotor Diam.	126 m
Blade length	61.5 m
Hub height	90 m
Rated Rotor Sp.	1.267 rad/s
Rated Wind Sp.	11.4 m/s
Cut-In, Cut-out Wind Sp.	3 m/s, 25 m/s
Baseline Ctrl.	PI, PRVS

Table 2.1: *Main characteristics of the NREL 5 MW baseline wind turbine [34], which is used as reference model for all the aeroelastic simulations presented in this work.*

ulations. The other exception is in the turbine smart rotor configuration presented in section 7.3, where the baseline controller is substituted by a model based controller, which pursues both power regulation and load alleviation objectives by combining pitch and flap actions.

Load Analysis

A first series of aeroelastic simulations is performed on the NREL 5 MW turbine in its baseline configuration [34]. The objective is to identify the operational conditions that give rise to loads that are critical for the turbine design; active load alleviation in such conditions would be in fact particularly beneficial, as it would allow for lower structural design requirements.

The operational conditions are characterized in terms of Design Load Cases (DLC): detailed specifications of simulation, wind field, and wind turbine conditions prescribed by the IEC standard on Wind Turbine design [26]. The analysis proposes a reduced set of design load cases, which collects the simulation conditions where critical loads arise; the reduced set thus provides a convenient test-bench to later evaluate the performance of the smart rotor.

The IEC standard makes a distinction between ultimate loads – the maximum loads expected on the structure – and fatigue loads – given by fatigue damage accumulation throughout the turbine lifetime. Different sets of DLC are prescribed for fatigue and ultimate loads analysis. The first part of the chapter deals both with fatigue and ultimate loads and indicates a reduced sets of DLC for each load type. The rest of the investigation will focus only

on fatigue loads, and the performance of the proposed smart rotor configurations will be evaluated in terms of fatigue load alleviation only. A more in depth investigation of the fatigue loads arising during normal operation is presented in the second part of the chapter: the aim is to determine the characteristics of the loads that bring the highest contribution to the turbine fatigue damage. A better knowledge of the loads the rotor has to face will be in fact helpful in determining the characteristics and requirements of the active load alleviation system and its control algorithm.

The emphasis given in all the investigation to fatigue loads during normal operation, and possibly their alleviation, derives from a simple consideration on the large amount of time a turbine is expected to operate in normal production. Nonetheless, it does not imply that ultimate loads are of scarce importance. On the contrary, an overall evaluation of the smart rotor potential should also include the positive or negative effects that active load alleviation strategies might have on the ultimate loads, as they might modify design-driving requirements.

In the third part of the chapter, load analysis is used to quantify the effects of modifications and simplifications of the aerodynamic model formulation [Article I, Report A]. In particular, the effects of different approximations in modeling the attached and separated flow dynamics are evaluated in terms of variations of the simulated fatigue loads, ultimate loads, and flutter stability limits. The results indicate that the aerodynamic model required to simulate the effects of active flap control should include both attached flow, and stall dynamics in order to avoid significant biases on the simulated loads.

The first part of the chapter resumes the findings of the design load cases analysis [**Report A**]; the second part presents a more detailed characterization of the fatigue damage loads, a subject covered mainly in [**Article II**]. The last section reports the effects of the aerodynamic model choices on the simulated loads, mainly discussed in [**Article I**]. Please refer to the publications enclosed in the second part of the dissertation for more details on the methods and the results.

3.1 Design Load Cases

The response of the NREL 5 MW turbine [34] is simulated with the aeroelastic code HAWC2, section 2.1, reproducing the conditions prescribed by the Design Load Cases (DLC) specified by the IEC standard [26]. Otherwise indicated, all simulations are carried out in the conditions specified for a class IIb turbine: the wind speed follows a Rayleigh distribution with average 8.5 m/s, and the reference turbulence intensity at 15 m/s is 16 %.

The ultimate loads are simply retrieved as the maximum loads reported in the simulated time-series, whereas the fatigue damage histories are summarized in terms of fatigue damage equivalent loads (DEL). The damage equivalent loads are computed using a rain-flow counting algorithm, and Palmgren-Miner rule for linear fatigue damage accumulation [Report A]; otherwise specified, Wöler curve exponents $m = 4$ for the blades, and $m = 10$ for the rest of the structure are used.

The design load case that corresponds to normal operation and power production (DLC 1.1) brings the highest contributions to the turbine lifetime fatigue damage, figure 3.1, mainly as a consequence of the considerable amount of time the turbine is expected to operate in normal conditions. DLC 1.1 dominates the fatigue loads for all monitored sensors; for the blade flapwise bending moment, the highest fatigue damages during normal operation are reported in case of positive yaw misalignment, while slightly lower loads than in the aligned case arise with a negative yaw error.¹ DLC 1.1 is the load case driving the turbine fatigue requirements, and active load alleviation systems aiming at reducing fatigue loads should primarily focus on alleviation during normal operation and production.

The ultimate load analysis returns a selection of three design load cases that return nearly the same maximum loads as observed with a complete load cases analysis, figure 3.2. The response to an extreme coherent gust with direction change (ECD wind field, DLC 1.4) set the ultimate loads at the blade root flapwise bending moment. DLC 1.3, extreme turbulence wind field, pro-

¹The definition of positive and negative yaw angle follows the HAWC2 reference system: a *positive* yaw angle implies that the right hand side of the rotor (looking downwind) is moved to leeward, and the left hand side is first hit by the wind.

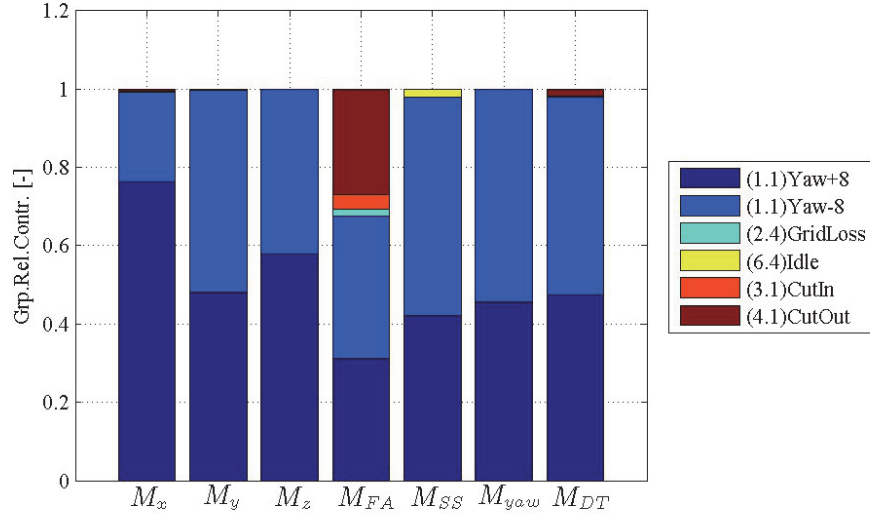


Figure 3.1: Relative contributions to the damage equivalent loads (DEL) from IEC standard [26] design load cases (DLC) [Report A]. The corresponding DLC number is reported in brackets in the legend; DLC 1.1 corresponds to normal operation and production. The DEL are evaluated for the blade root flapwise (M_x), edgewise (M_y), and torsion (M_z) bending moments; for the tower fore-aft (M_{FA}), side-to-side (M_{SS}), and yaw (M_{yaw}) moment; for the drive-train torsion (M_{DT}) on the low speed shaft. A material fatigue exponent $m = 4$ is used for tower and drive train, $m = 10$ for the blade.

duces the highest loads on the drive-train torsion, on the tower yaw moment, and also on the tower bottom side-to-side moment, if the parked turbine cases 6.1-6.3 were disregarded. The extreme coherent gust case (EOG wind field, DLC 2.3) returns the highest loads on the turbine edgewise bending moment, and on the tower fore-aft bending moment. As in the fatigue cases, the fore-aft loads at the tower bottom are strongly dependent on the turbine shut-down strategy, which is not univocally defined for the reference turbine, thus adding an element of uncertainty; the ultimate loads given by the same extreme wind conditions without a simultaneous turbine shut-down would be lower (tag *EOG, ngl* in fig.3.2).

The reduced set of design load cases highlighted by the ultimate load analysis is used to evaluate the effect of changes in the aerodynamic model, section 3.3. A part from that, no further studies on ultimate loads were carried out during

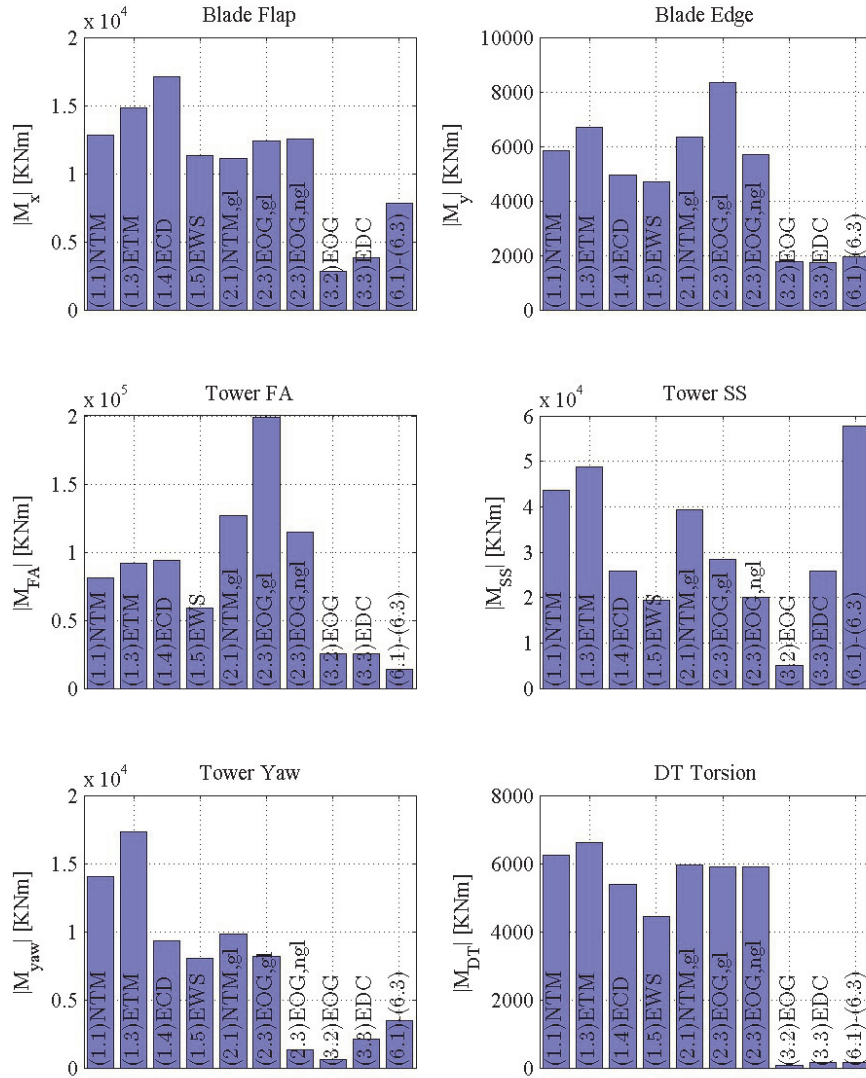


Figure 3.2: Ultimate load analysis, [Report A]. The columns indicate the maximum loads reported in each of the DLC prescribed by the IEC standard. DLC 2.3 is performed with two configurations: gl indicates a simultaneous grid loss event and hence turbine shut-down, ngl the turbines keeps producing during the gust.

this investigation. It is left to future work to evaluate whether the proposed smart rotor configurations would bring any benefit or disadvantage to turbine operations under extreme conditions, and to eventually broaden the analysis to include reasonable failure scenarios of the adaptive flap systems.

3.2 Contributions to the fatigue damage

Once established that most of the fatigue damage experienced by the turbine is produced during normal operation, an attempt is made to outline the characteristics of the aeroelastic load components that bring the largest fatigue contributions [Article II]. The load characteristics will provide useful indications for the development of the active load alleviation system and its control algorithm.

3.2.1 Periodic and stochastic components

A first characterization distinguishes the loads on the blade root into a *periodic* component and a *stochastic* one. The periodic (or deterministic) component of the loads can be interpreted as the result of constant or slow varying disturbances in the wind field (e.g. rotor tilt, yaw misalignment, tower passage effects, terrain shear), which produce periodic variations of the loads on the rotating blade. Periodic load variations are easy to predict, as they can be simply related to the blade azimuthal position. On the contrary, the *stochastic* component gathers variations that develops on top of the periodic ones, and do not follow a clear and predictable pattern; in the simulated cases, they originate from the wind field turbulence. In the investigated cases, the periodic load component is identified as the average load for each blade azimuthal position over one hour turbulent wind field simulations [Article II]; different results might hence be obtained with different time averaging windows.

Loads at the blade root in the flapwise direction are dominated by the stochastic component, figure 3.3, but load variations related to the peri-

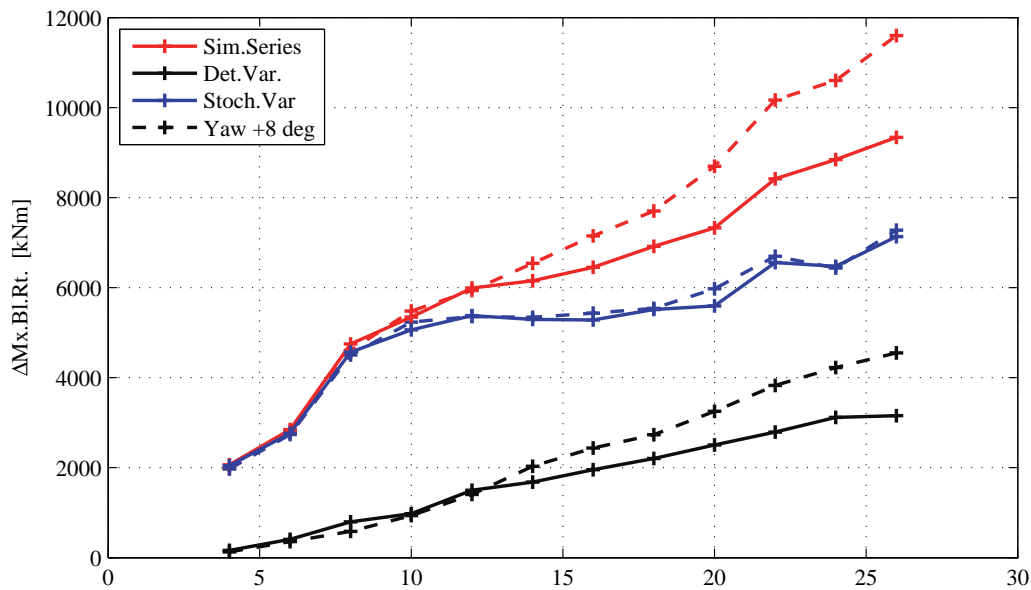


Figure 3.3: Blade root flapwise bending moment variations as function of mean wind speed, [Article II]. Total variation from simulations (red lines), variation with a periodic-deterministic nature (black), stochastic load variation (blue). A case with yaw misalignment is given for comparison, dashed lines.

odic component are also significant, especially at higher mean wind speeds. Ideally alleviating load variations from the whole periodic component would reduce the blade flapwise lifetime fatigue damage by approximately 11 %, figure 3.4.

To achieve fatigue damage reductions beyond the 11 % threshold, the alleviation system should also target stochastic load variations; as the stochastic components are not predictable, the smart rotor would require information on the actual load conditions, as given for instance by measurements of the blades bending moments. The 11 % fatigue damage contribution of the periodic load components also suggests that a smart rotor control algorithm might benefit from accounting for the predictable periodic load variations, either directly [12, 32, 60] or through multiblade coordinate transformation [8, 19, 36].

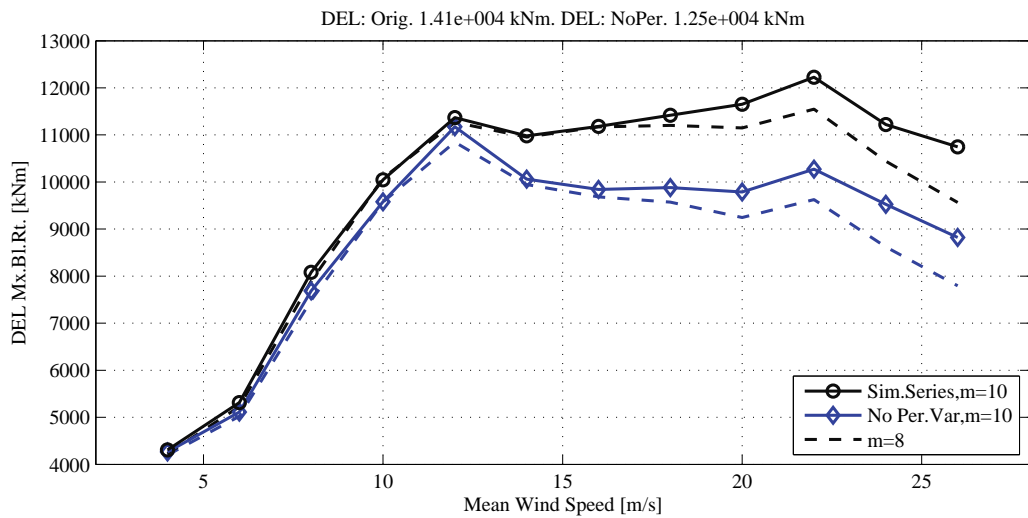


Figure 3.4: Blade root flapwise moment, fatigue damage equivalent loads for different mean wind speed operation (weighted by the wind distribution), [Article II]. Results for simulated loads (black line) and for series with an ideal complete alleviation of the periodic load component (blue lines).

3.2.2 Mean wind speed

The fatigue damage equivalent loads (DEL) evaluated at different mean wind speeds indicates that, even accounting for the less frequent occurrence, operation above rated wind speed account for most of the blade flapwise lifetime fatigue damage, figure 3.4. Active blade load alleviation below rated wind speed yields only a minor contribution to the overall fatigue damage; it might be thus beneficial to exploit the smart rotor capabilities for other scopes below rated conditions, for instance to increase the energy capture, a preliminary attempt in this direction is reported in section 6.2.

3.2.3 Frequency contributions to fatigue damage

The power spectral density (PSD) of the blade root flapwise bending moment displays a clear and dominant peak at the 1P frequency, corresponding to the blade revolution period, figure 3.5. The peak is reduced in the time series

with ideal alleviation of the periodic load components, but still dominates the spectrum, thus indicating that for a rotating blade also disturbances of stochastic nature return loads with dominant frequencies close to the rotational one.

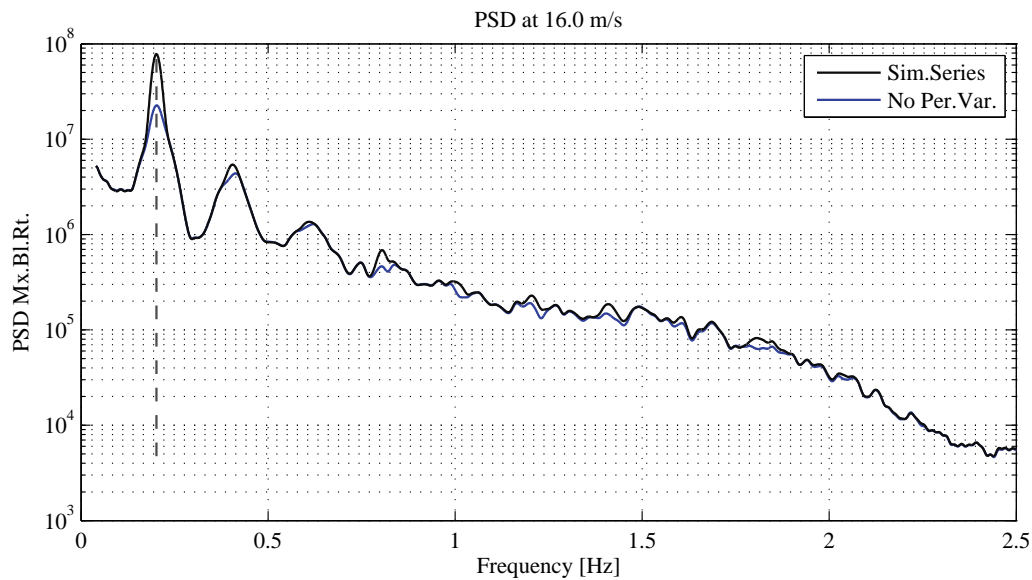


Figure 3.5: Blade root flapwise moment, Power Spectral Density (PSD) for the loads time series with mean wind speed of 16 m/s. Results for simulated loads (black line) and for series without deterministic load variations (blue lines).

A method to estimate the fatigue damage contributions from different frequency ranges is proposed in [Article II]. The damage contributions are then organized as functions of both the operating mean wind speed and the load frequency range, and are plotted as sort of ‘spectrograms’ with mean wind speed on the horizontal axis, load frequency on the vertical axis, and darker red colors to indicate higher fatigue contributions, figure 3.6. The loads responsible for the highest fatigue damage on the blade are characterized by frequencies close to the rotational one, and occur at wind speed above rated, figure 3.6. Similarly, non-rotating parts of the structure receive important fatigue damage contributions from loads with frequencies three times the rotational one (3P); the tower fore-aft spectrogram, figure 3.7, also presents marked contributions from the tower natural frequency (0.3 Hz), and a substantial increase of the fatigue damage is observed at low wind speed as the blade passage frequency approaches the tower natural frequency.

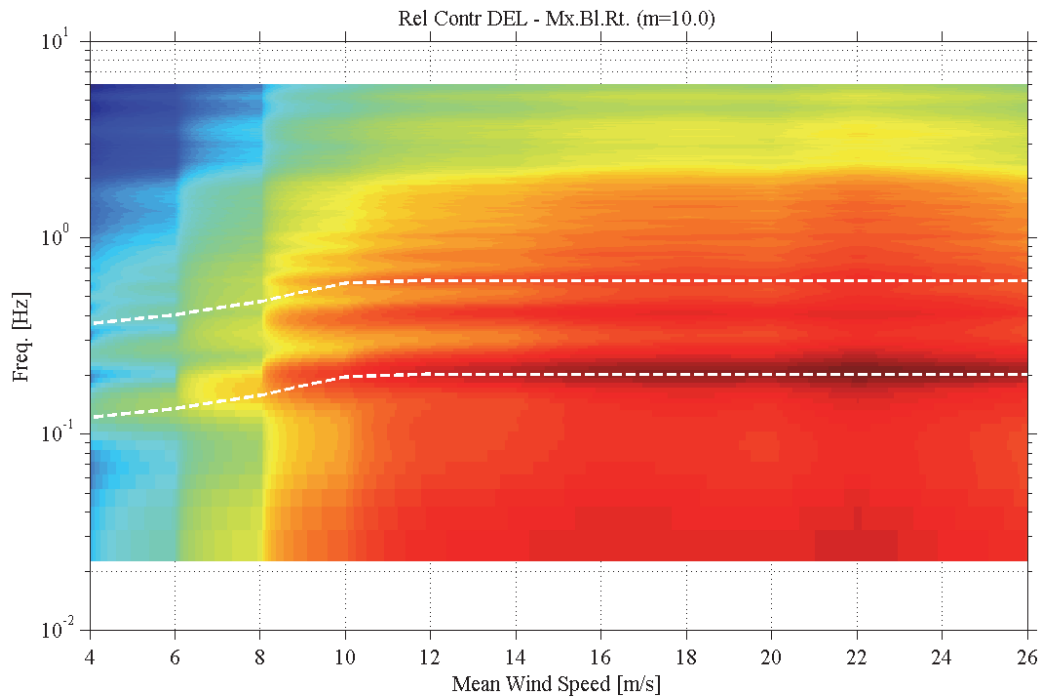


Figure 3.6: Spectrogram of the contribution per frequency and operating mean wind speed to the lifetime fatigue damage on the blade flapwise moment, [Article II]. Darker red colors indicates higher fatigue damage contributions; the dashed white lines mark the rotational frequency $1P$, and $3P$.

The fatigue damage is mainly driven by loads characterized by frequencies below 1 Hz, the contribution from loads above 2 Hz is scarcely significant; a result confirmed by rain flow counting fatigue analysis of the load time series processed with low pass filters [Article II]. The important role that rotational and low frequencies play on the blade fatigue damage provides an indication of the frequency range of interest for the active load alleviation system. Control actions focused on the low frequency range are thus expected to bring the largest contribution to active load alleviation, control activity in the high frequencies can be limited, thus reducing actuator wear and flap deflection rate requirements. A combination of flap activity with, for instance, cyclic pitch actions might also increase the alleviation potential.

3.3 Aerodynamic model approximations, effects on load simulation 25

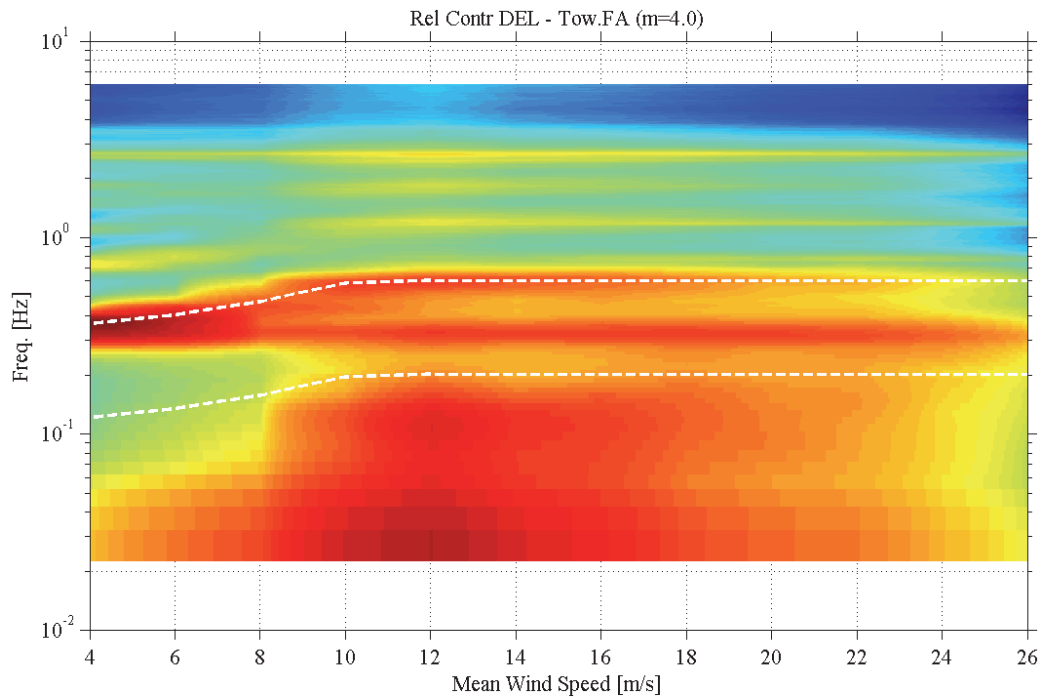


Figure 3.7: Spectrogram of the contribution per frequency and operating mean wind speed to the lifetime fatigue damage on the tower fore-aft bending moment, [Article II]. Darker red colors indicates higher fatigue damage contributions; the dashed white lines mark the rotational frequency $1P$, and the blade passage frequency $3P$.

3.3 Aerodynamic model approximations, effects on load simulation

The reduced set of design load cases, identified in section 3.1, is used to evaluate how the loads predicted by aeroelastic simulations would be affected by different approximations of the 2D aerodynamic modeling, both in terms of fatigue damage, table 3.1, and ultimate loads, table 3.2. The effects of dynamic modeling in attached flow are assessed in case of quasi-steady flow assumption (Δ *Quasi-St.*), and in case of indicial lift response functions tuned to reproduce the indicial response of a finite thickness airfoil (Δ *DU 250*) [Article I]. The effects of excluding the stall dynamics are then evaluated by setting the corresponding time constants (Δ *No Dyn.St.*) to zero [Report I].

S_{eq}	Blade Flapw.	Blade Edgew.	Blade Tors.	Tower FA	Tower SS	Tower Tors.	Shaft Tors.
Ref. Fl.Pl. [MNm]	13.73	10.69	0.25	77.12	39.55	20.60	3.86
Δ Quasi-St	5.49 %	1.10 %	20.54 %	6.44 %	3.89 %	9.15 %	15.05 %
Δ DU 250	-1.06 %	0.00 %	-2.48 %	-1.02 %	-0.39 %	-1.83 %	-2.21 %
Δ No Dyn.St.	-0.54 %	-0.06 %	-2.15 %	-0.53 %	-0.10 %	-1.17 %	-1.03 %

Table 3.1: Fatigue Damage Equivalent Loads (DEL), variations due to changes of the indicial lift response coefficients [Article I] and stall dynamics [Report I]. Simulations for: Jones’s flat plate indicial response coefficients (reference case, first row), Quasi-Steady indicial response, DU 91-W2-250 indicial response coefficients, stall dynamics ignored (flat plate response in attached flow). The variations Δ are normalized by the equivalent loads of the flat plate reference case. The results refer to an equivalent number of load cycles $n_{eq} = 10^6$, 25 years lifetime, Wöler material fatigue exponent $m = 10$ for blade loads, $m = 4$ for tower and drive-train.

$\max(M)$	Blade Flapw.	Blade Edgew.	Blade Tors.	Tower FA	Tower SS	Tower Tors.	Shaft Tors.
Ref. Fl.Pl. [MNm]	14.94	6.92	0.22	112.46	45.08	17.44	6.62
Δ Quasi-St.	6.93 %	2.29 %	25.26 %	-1.98 %	3.44 %	6.07 %	5.45 %
Δ DU 250	-0.73 %	-0.39 %	-2.21 %	0.41 %	-0.55 %	-1.14 %	-1.33 %
Δ No Dyn.St.	10.52 %	-1.89 %	11.73 %	-1.99 %	1.72 %	-2.19 %	-1.02 %

Table 3.2: Ultimate loads from reduced set of cases, variations due to changes of the indicial lift response coefficients [Article I] and stall dynamics [Report I]. Simulations for: Jones’s flat plate indicial response coefficients (reference case, first row), Quasi-Steady indicial response, DU 91-W2-250 indicial response coefficients, stall dynamics ignored (flat plate response in attached flow). Variations Δ normalized by the ultimate loads of the flat plate reference case.

Neglecting attached flow dynamics with a quasi-steady approximation causes significant biases on the simulated loads, both in terms of fatigue damage, table 3.1, and ultimate loads, table 3.2; the flutter stability limit would be also underestimated by nearly 25 %, figure 3.8. Neglecting flow separation dynamics has only small effects on the fatigue loads, as in normal operation attached flow conditions prevail; on the contrary, the ultimate loads, often recorded during design load cases where sections of the turbine blades operates in separated flow conditions, are instead overestimated by neglecting the stall dynamics.

Changing the indicial response function to a finite thickness airfoil one causes only minor variations to the overall turbine loads and stability results. On

3.3 Aerodynamic model approximations, effects on load simulation 27

the other hand, an indicial function that accounts for the airfoil thickness improves the estimation of the unsteady aerodynamics on a 2D airfoil [Article I]; a characteristic that will come handy in the future validation of the ATEFlap aerodynamic model, section 4.3.

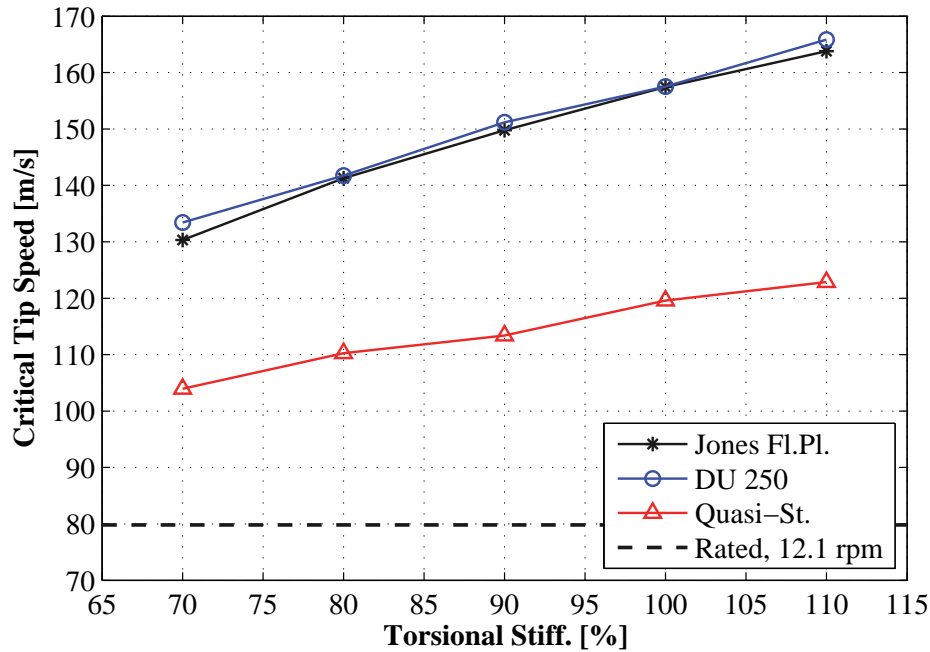


Figure 3.8: Critical tip speed at which instability (flutter) due to rotor over-speeding arises: variations due to changes of the indicial lift response coefficients, [Article I]. Simulations for: Jones’s flat plate indicial response coefficients (black with stars), Quasi-Steady indicial response (red with triangles), DU 91-W2-250 indicial response coefficients (blue with circles). The values are plotted versus the scaling factor applied to the blade torsional stiffness.

To conclude, the aerodynamic model for an airfoil equipped with trailing edge flaps should include unsteady aerodynamics, both for attached and separated flow conditions; otherwise, the aeroelastic simulations might return strongly biased loads and stability limits.

CHAPTER 4

ATEFlap Aerodynamic Model

The load analysis has highlighted the importance of an aerodynamic model able to describe not only the steady (or quasi-steady) effects of airfoil motion and flap deflection, but also the unsteady dynamics of the forces and moments, both in attached and stalled flow conditions. The model should also have low computational requirements to allow for an efficient integration with the BEM-based simulation environment of the aeroelastic code HAWC2, section 2.1.

The proposed *ATEFlap* aerodynamic model is an ‘engineering’ model for 2D airfoil sections. It takes as input the steady lift, drag and moment coefficients as functions of both angle of attack and flap deflection, figure 4.1, and returns the unsteady integral aerodynamic forces and pitching moments for the airfoil section undergoing arbitrary motion and flap deflection. The computational requirements are kept low by adopting Gaunaa’s [27] potential flow solution, coupled with the Beddoes-Leishmann dynamic stall model by Hansen et al. [28], an approach first suggested by Andersen et al. [1].

The details of the aerodynamic model, its implementation in the aeroelastic code, and the differences from previous implementations are described

in [Report B], enclosed in the second part of the dissertation. The technical report contains a first validation of the model; more comprehensive validation tests are presented in [Article III], where the results from *ATE-Flap* are compared against the solutions obtained with Computational Fluid Dynamics and with NTUA's viscous-inviscid interaction code.

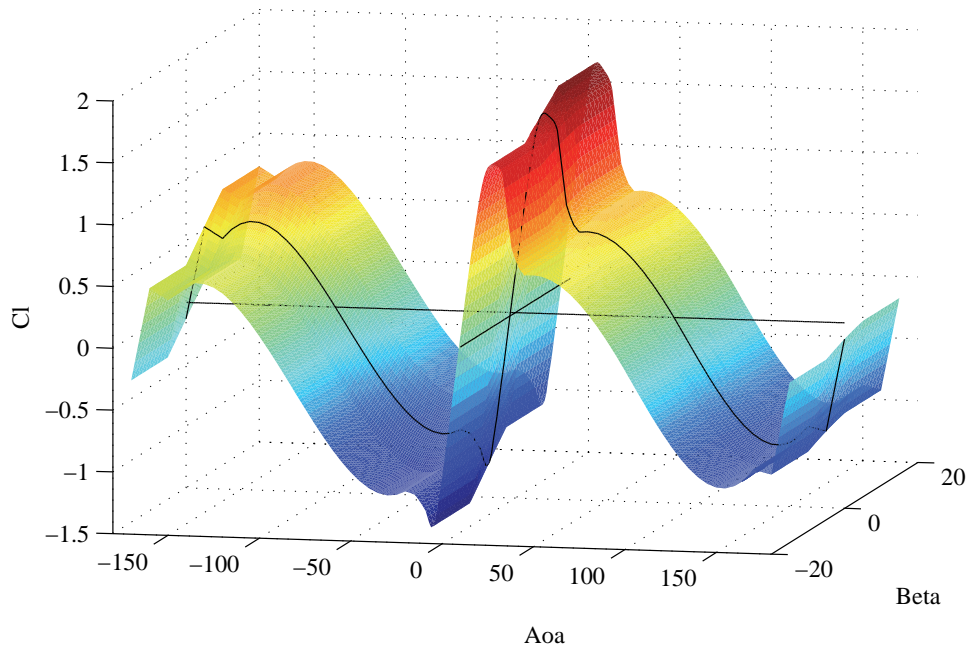


Figure 4.1: Steady lift coefficient C_l^{st} in the case of an airfoil with trailing edge flap. The steady lift, drag, and moment coefficients are function of both angle of attack α and flap deflection β , and can be represented by surfaces in the space.

4.1 Attached flow dynamics

The attached flow part of the model follows the formulation derived by Gawnaa [27] for a thin airfoil in potential flow. The dynamic effects are separated into a *non-circulatory* contribution, and a *circulatory* one: the non-circulatory (or added mass) contribution only depends on the instantaneous motion of the airfoil or the flap deflection; the circulatory contribution, which

accounts for the effects given by the vorticity shed into the wake as the airfoil circulation changes, also depends on the angle of attack and flap deflection histories.

The circulatory effects are described by the model as a superposition of indicial lift responses. Circulatory lift variations caused by either changes of angle of attack or flap deflection are all described by the same Wagner-like indicial response function, which is formulated in exponential terms to allow for efficient time integration [Report B].

Airfoil sections with finite thickness have indicial response functions that differ from the flat plate one [Article I]. Although the difference has only minor effects on the overall turbine aeroelastic loads, section 3.3, it does have a visible impact on the unsteady aerodynamic force histories of a 2D airfoil section. Applying an indicial response function that accounts for the airfoil thickness improves the agreement between the forces predicted by the ATE-Flap model and the results of more complex computational methods [Article I], thus bringing a valuable contribution to the validation and comparison process [Article III].

4.2 Dynamic stall model

The part of the model that describes the dynamics of flow separation follows the formulation of the Beddoes-Leishmann model presented by Hansen et al. [28]. The lift is expressed as a weighted sum of a fully attached lift contribution, and a fully separated one; the separation dynamics are modeled through the weight factor of the sum, which introduces a low pass filter behavior.

The fully attached, fully separated lift components, and the steady weight factors are retrieved from the steady lift input, and are thus functions of both angle of attack and flap deflection, figure 4.1. The retrieval process might give rise to singularity points that could bias the model output. As the attempt to formulate a reliable method that would automatically sort out the singularity points was unsatisfactory, the retrieval process is performed

in an external pre-processor unit, and the possibility -and responsibility- to verify and eventually correct the resulting data is left to the user [Report B].

4.3 Model validation

A first verification of the correct model implementation is carried out by simulating the aerodynamic forces and pitching moment on an airfoil section undergoing harmonic pitching motion while the flap is maintained undeflected. The results from *ATEFlap* are compared against the ones from the model by Hansen et al. [28] implemented in HAWC2: the forces and moments time histories predicted by the two models are overlapping, section 4.1 in [Report B].

Further validation of the model performances are presented in [Article III], where the results of the ATEFlap model are compared against aerodynamic forces and moments simulated with Computational Fluid Dynamics (CFD), and with the viscous-inviscid interaction code developed at NTUA. The simulations are performed for an airfoil undergoing harmonic pitching motion and harmonic trailing edge flap deflection; they cover both attached, and separated flow conditions, with different combinations of oscillation amplitudes and reduced frequencies.

In attached flow conditions, the comparison shows a very good agreement, both in response to angle of attack and flap deflection variations. As flow conditions complicate due to stall separation, discrepancies arise between the ATEFlap results and the ones from the more complex models. Although with poorer performances in stalled conditions than in attached flow -a limitation probably shared by most engineering type of aerodynamic models- the ATEFlap model is judged adequate to simulate the dynamics of the unsteady forces and moment of an airfoil equipped with a trailing edge flap. The model is implemented in the HAWC2 code, thus providing an aero-servo-elastic simulation tool for a turbine with ATEF.

Adaptive Trailing Edge Flap rotor configuration

The chapter proposes a smart rotor configuration for the NREL 5 MW turbine with Adaptive Trailing Edge Flaps (ATEF) on each of the blades. First, the ATEF aerodynamic properties are presented, thereafter, aeroelastic simulations are performed to determine the blade root flapwise bending moment response to step deflections of flaps located at different positions along the blade span. The response characteristics are used to decide the placement and extension of the flap actuators, thus defining the smart rotor configuration that will be used in all the following active load alleviation analysis. A brief comparison of the blade root load variation achieved by the proposed actuator configuration, and the bending moment variations observed on the turbine rotor during normal operation concludes the chapter.

5.1 Flap steady aerodynamic properties

Trailing edge flaps characterized by a smooth and continuous deflection shape, figure 5.1, are expected to have lower noise emissions and produce higher lift variations than rigid plain flaps of the same extension that rotate around an hinge point [56]. The trailing edge flap considered in this investigation extends 10 % of the airfoil chord length, the flap deflection angle is then defined as the angle between the lines that connect the airfoil trailing edge to the flap starting point (at 90 % chord length) in the deflected and undeflected positions; when deflected by one degree, the flap introduces a deformation to the airfoil camber which outlines a circular arc, figure 5.1; the analytical equation describing the flap deflection shape is reported in [Article III].

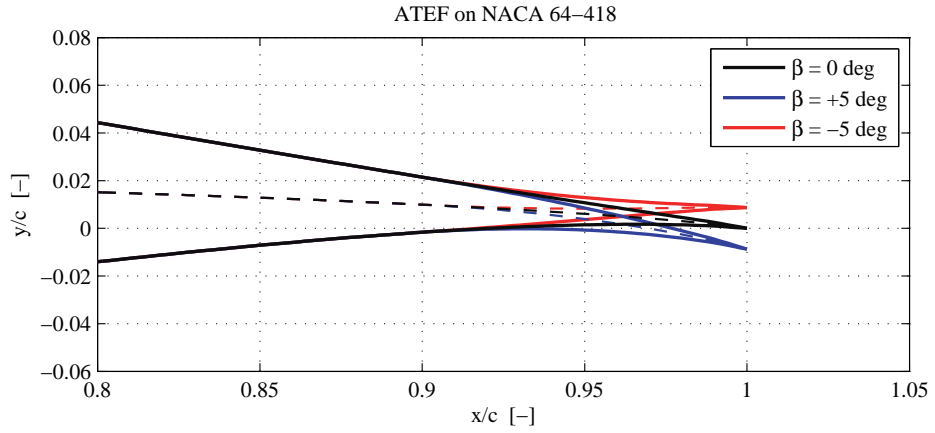


Figure 5.1: *Camber-line deformation introduced by the considered ATEF for deflections of $\pm 5^\circ$, the flap deflection angle is given by the line joining the airfoil trailing edge to the flap starting point (at 90 % chord length). In the figure, the flap is applied to a NACA 64-418 airfoil profile, the configuration is used to determine the steady aerodynamic characteristics of the flap with Computational Fluid Dynamics [Article III].*

The steady aerodynamic properties are derived by performing CFD simulations of a NACA 64-418 airfoil where the aft portion of the camber-line is deformed following the flap deflection shape for different angles [Article III]; steady CFD simulations are repeated for different flap deflection angles and at different airfoil angles of attack. The flap effects are quantified in

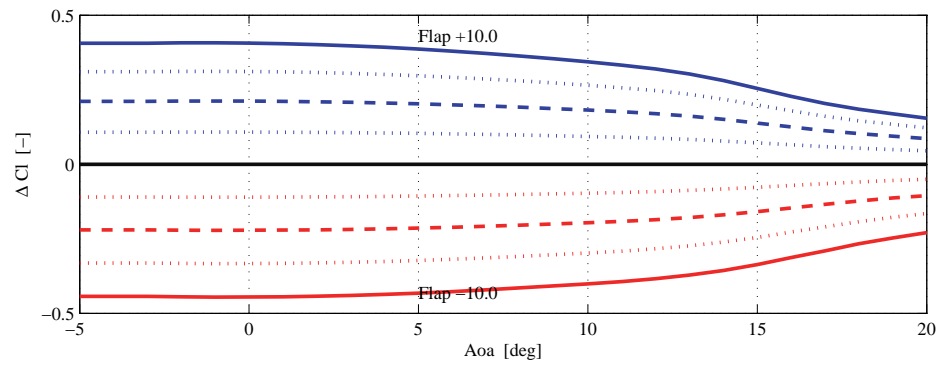
terms of steady lift, drag, and moment coefficient variations from the steady coefficients obtained for the airfoil with undeflected flap, figure 5.2, and the same coefficient variations are then superimposed to the steady coefficient curves of the airfoil profiles encountered on the NREL 5 MW blades. The flap deflection is limited to $\pm 10^\circ$, and returns maximum lift coefficient variations ranging from -0.45 to +0.41, figure 5.2(a), which roughly correspond to angles of attack changes from -3.9° to $+3.6^\circ$; the flap deflection introduces only a minor drag penalty at small angle of attack, fig. 5.2(b), but a considerable variation of the aerodynamic pitching moment, fig. 5.2(c).

5.2 Flap placement along the blade span

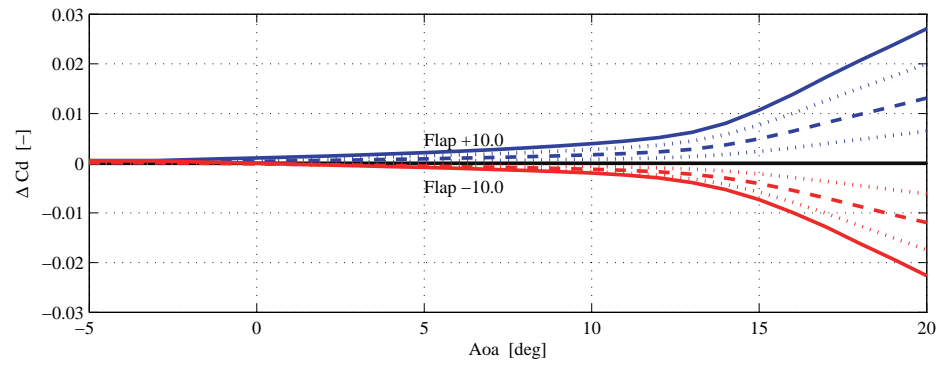
In this work, adaptive trailing edge flaps are added to the turbine blades with the main scope of alleviating the fluctuation of flapwise loads at the blade root. Their positioning along the blade span is hence evaluated by considering the effects that their deflection produces on the blade root flapwise bending moment. The blade is divided into sections 2.5 m long, each mounting a trailing edge flap with the aerodynamic characteristics presented in the previous section. The response of the blade root flapwise bending moment to the step deflection of each of the flap sections is simulated in HAWC2, and it is characterized in terms of: bending moment steady variation ($M_{t=\infty} - M_{t=0}$), minimum bending moment variation, and response time lag, given as the time required for the bending moment to reach 50 % and 80 % of the total steady bending moment variation, figure 5.3.

As the location of the deflected flap is moved outboard, the steady variation achieved in the blade root flapwise bending moment increases, but so does the delay in the response, compare the responses plotted in figure 5.3 for increasingly outboard flap placements. Furthermore, flaps located in the outboard part of the blade generate a response with a marked non-minimum phase transient: the bending moment variation is first negative, and, only after reaching a minimum, increases toward the positive value reached in steady conditions.

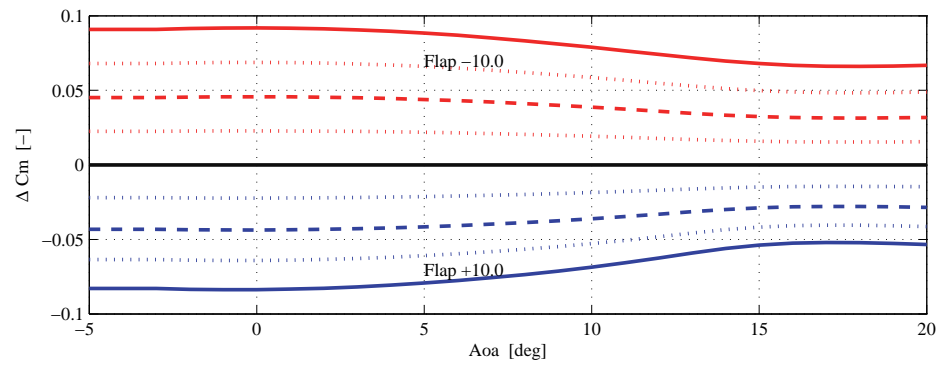
In his Ph.D. thesis, Baek [5] addresses the problem of flap placement along



(a) Lift Coefficient



(b) Drag Coefficient



(c) Moment Coefficient

Figure 5.2: Airfoil section steady aerodynamic coefficient variations achieved by the investigated Adaptive Trailing Edge Flaps. Blue lines indicate positive (downward) flap deflections, red lines negative (upwards) deflections; full lines corresponds to the maximum deflections of $\pm 10^\circ$, dashed lines to $\pm 5^\circ$, and the dotted lines to $\pm 2.5^\circ$ and $\pm 7.5^\circ$.

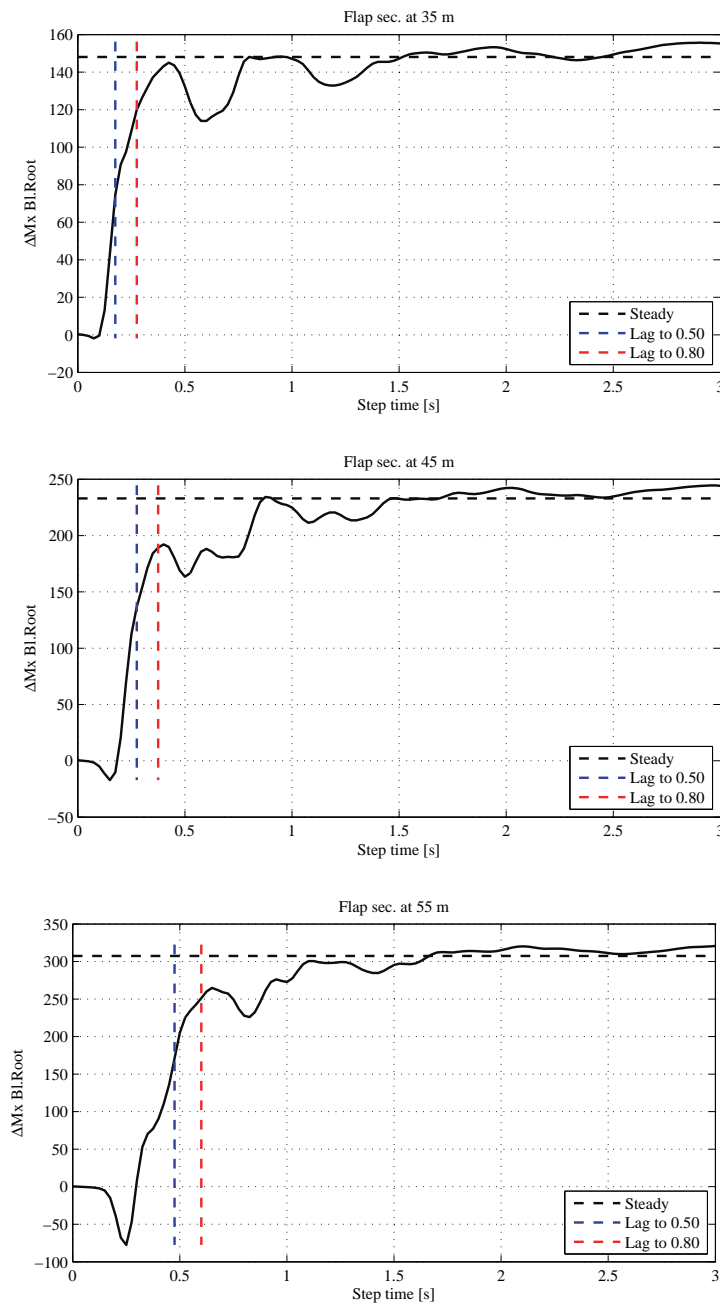


Figure 5.3: Blade root flapwise bending moment response to deflection steps of flap actuators located at three positions along the blade span, from inboard (top) to outboard (bottom plot). Aeroelastic simulations of the step responses are performed in ideal conditions: uniform inflow, null tilt and gravity, stiff tower and shaft.

the blade span, and implements a more elegant approach to the problem: the flexible blade is described by a linear state-space model, where the lift variations from the flap deflection act as external forces on the system; he then computes the blade eigen-modes, and evaluates the effects of the flap deflection on the blade flapwise bending moment in terms of controllability gramians for the linear system. Baek also reports non-minimum phase responses on the blade root bending moment, and explains them as a consequence of the fact that the second blade flapwise bending mode dominates the initial transient of the response to the step deflection of a flap located outboard. In fact, the curvature of the second eigen-mode near the blade root is opposite to the first mode curvature, thus causing bending moment variations of opposite sign. It is comforting to observe that the non-linear step response simulations presented in this chapter return similar results to Baek's systematic linear model analysis.

The characteristics of the simulated bending moment responses are gathered as function of the span-wise location of the flap section, figure 5.4. A first estimation of the steady moment variation as function of the flap location can be obtained from the analytical expression of the contribution to the blade root moment variation given by a ΔL^{dr} lift variation on the $\text{d}r$ long blade portion, located r meters from the blade root:

$$\Delta M_x^{\text{dr}} = r \cdot \Delta L^{\text{dr}} = r \frac{1}{2} \rho U_r^2 c(r) \Delta C_l. \quad (5.1)$$

By assuming that the ΔC_l variation from the flap deflection is not depending on the radial position and approximating the squared flow speed at the section U_r as the section rotational speed $\Omega^2 (r + r_{\text{hub}})^2$, equation (5.1) simplifies to a term proportional to the section chord length, the span-wise location r , and the hub radius r_{hub} . For small hub radii, the equation further simplifies to a function of the chord length and the cube of the span-wise position:

$$\Delta M_x^{\text{dr}} \propto (r + r_{\text{hub}})^2 r \cdot c(r) \approx r^3 \cdot c(r), \quad (5.2)$$

the curve corresponding to the bending moment contribution expected from the analytical equation is plotted for comparison in figure 5.4 (dashed gray line).

The results of the aeroelastic step analysis (line with black circles) are in good agreement with the analytical curve trend, and indicate that the maximum

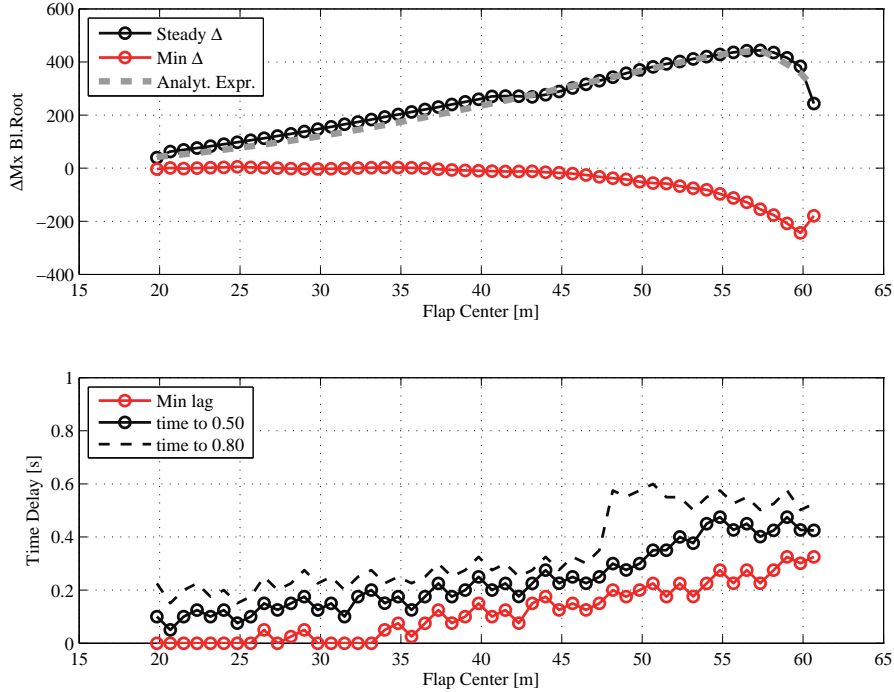


Figure 5.4: Characteristics of the blade root flapwise bending moment response as function of the spanwise location of the flap actuator. The curve obtained from the simplified analytical equation (5.2) is reported as comparison (dashed gray line); the analytical curve is scaled to have its maximum at $\Delta M_x = 400$ kNm.

steady variation of the blade root flapwise bending moment is achieved with flaps located around 90 % of the blade span. On the other hand, outboard placement of the flaps also implies longer delays in the response, and deeper non-minimum phase transients.

5.3 Flap spanwise extension

A brief analysis on the effects of the spanwise extension of the flap actuators is carried out following a similar procedure: the characteristics of the bending

moment response are now plotted as function of the flap span-wise extension for flap actuators starting at 60 m span, and progressively extending inboard, figure 5.5. Unsurprisingly, the more extended the blade span covered by flap actuators, the larger the variation achieved in the blade root bending moment, and the shorter the time delay in the response. The increase is nearly linear for the first 15-20 % of blade span, and is progressively reduced thereafter. This work, as many of the previous ones [5,11,36], will consider a smart rotor configuration with adaptive trailing edge flaps extending for 20 % of the blade span.

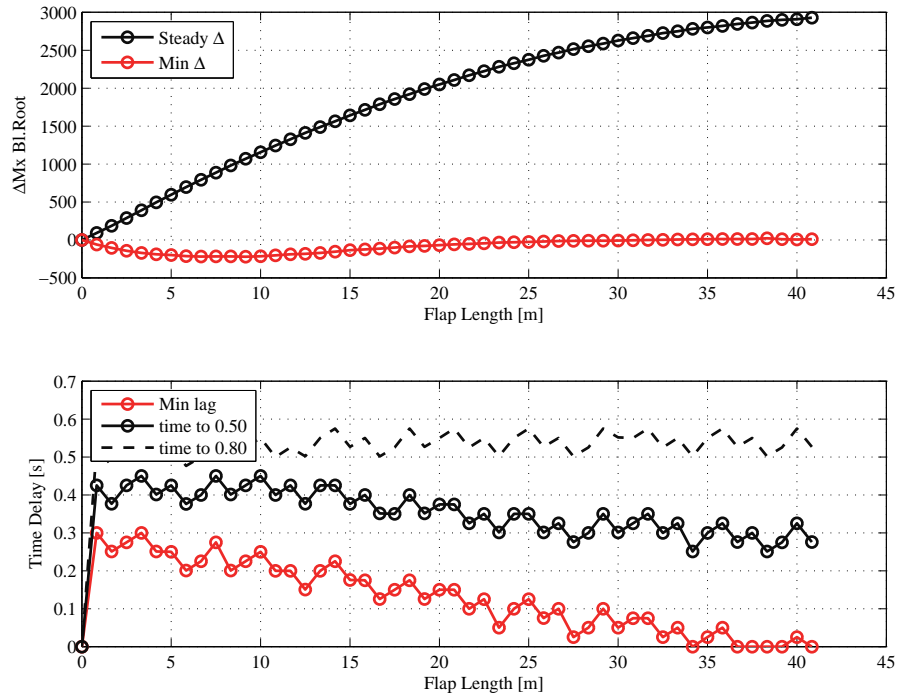


Figure 5.5: Characteristics of the blade root flapwise bending moment response as function of the spanwise extension of the flap actuator. The flap actuators start at 60 m blade span and extends inboard by the length on the x axis.

5.4 Proposed ATEF rotor configuration

The definition of an optimal flap actuator placement along the blade span is very far from being univocal. Even by restricting the design envelope to a specific blade structure, and to the specific aim of alleviating blade root flapwise bending moment variations during normal operation, more than one ‘optimal’ flap placement can still be defined. For instance, assuming we will control the flap based on measurements of the bending moment at the blade root, control algorithms sensitive to system delays and non-minimum phase responses will perform better with inboard placements of the flaps; on the contrary, a control algorithm better coping with the response characteristics will correspond to an ‘optimal’ flap placement further outboard, so to achieve higher moment variations. The definition of an optimal flap placement thus represents an example of integrated design problem, where a truly optimal solution is only achieved if all the elements (aerodynamics, structural response, control algorithm) are considered simultaneously, thus pursuing an integrated aero-servo-elastic design optimization.

As for now, a much simpler approach is followed instead: the model based control algorithms that will be implemented are assumed to be able to cope with the delayed non-minimum phase response; therefore, the flap actuators are placed to achieve the maximum steady flapwise bending moment variation at the blade root. In the proposed smart rotor configuration, the flaps extend for 20 % of the blade length, from 47.7 m to 60.0 m span; table 5.1 summarizes the main characteristics of the smart rotor setup that will be considered in the following investigations.

In this configuration, the flaps lead to a maximum variation of the blade root flapwise bending moment of about ± 1100 kNm, above rated wind speed conditions. The maximum bending moment variation quantifies the total ‘muscle power’ available to the smart rotor for active load alleviation. A comparison of the bending moment variation observed on the blade root during normal operation, section 3.2, with the variation from maximum flap deflection gives an indication of the limits of the flap load alleviation potential, figure 5.6. The comparison suggests that for achieving higher load alleviations a more powerful actuator setup would be required. Larger or longer flap actuators could be used, also, a stronger configuration could be

<i>ATEF smart rotor configuration</i>	
Flap chordwise ext.	10%
Deflect.limits	$\pm 10^\circ$
Max. ΔCl	$-0.45 \sim +0.41$
Spanwise length	12.3 m (20% blade length)
Spanwise loc.	from 47.7 m to 60.0 m span
Max. ΔM_x .Bl.Rt	approx. ± 1100 kNm

Table 5.1: *Main characteristics of the proposed smart rotor configuration with Adaptive Trailing Edge Flaps. The configuration is used in all the following active load alleviation simulations.*

obtained by combining the flap actuators to blade pitch activity, which, although slower and requiring more actuator power, allows to reach larger load variations, figure 5.6. In the following investigations, the flap actuator size will not be changed, whereas a combination of flap and pitch actions will be considered in the simplified cyclic control setup, section 6.1, and in the combined model predictive control framework presented in section 7.3.

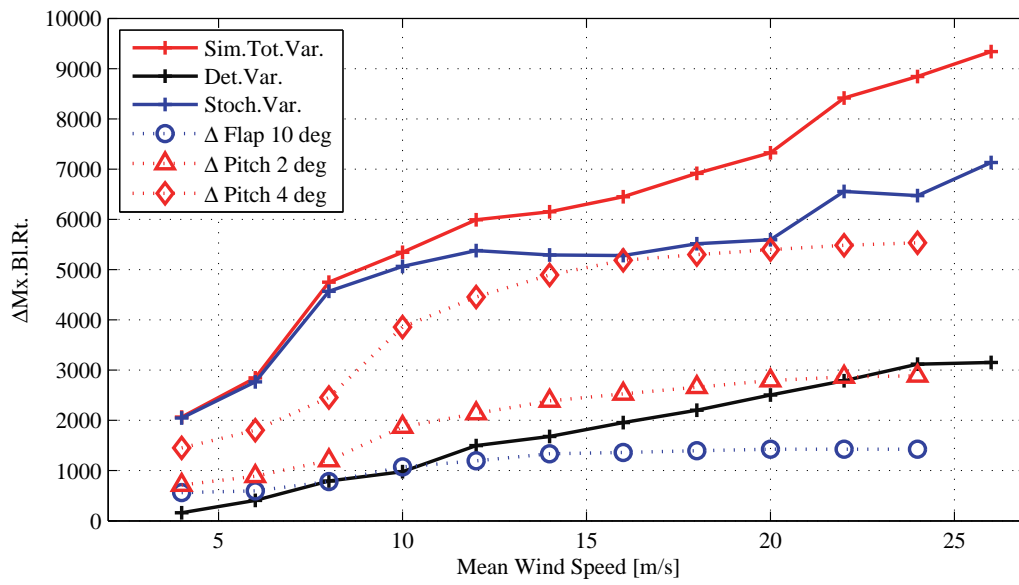


Figure 5.6: Blade root flapwise bending moment variation at different mean wind speed operation. Comparison of the maximum variation achieved by the flaps, of the variation observed during normal production, and of the variation obtained by pitching the whole blade by 2° and 4° .

CHAPTER 6

Preliminary investigations with feed-forward cyclic control

Preliminary investigations on the smart rotor potential are carried out with a simplified feed-forward control approach: flap deflections and blade pitch angles follow pre-determined cyclic trajectories; the control signals are thus only function of the blade azimuthal position, and are repeated identically at each rotor revolution. The cyclic trajectories are determined offline by solving a constraint optimization problem that directly targets the control objectives: blade root flapwise bending moment variation, and aerodynamic power output.

The feed-forward cyclic control approach does not require any additional information nor measurements of the system to control, and it does not depend on particular choices of feedback control algorithms. Thanks to its simplicity, the cyclic approach allows for a preliminary evaluation of the smart rotor actuators performance, and could provide a standard framework to compare different smart rotor configurations and actuator types in similar conditions.

The control performance is limited by the fact that the feed-forward approach

can only address periodic disturbances; although the periodic component has a significant impact on the turbine response (see the load analysis in section 3.2), the overall performance of a smart rotor strongly depend on its ability to compensate for stochastic disturbances as well. The response to stochastic variations can not be evaluated with the proposed feed-forward method; in fact, in order to address the stochastic component of the load variation, the smart rotor would require additional information on the current turbine state, and more complex control algorithms, as presented in the next chapter. Another limitation of the method arises from the optimization procedure: as each optimization iteration requires time marching aeroelastic simulations, in order to maintain reasonable computational time requirements, the simulations are performed excluding the effects of atmospheric turbulence, and the simulation time is further reduced by assuming a stiff turbine. The results presented in this chapter thus serve merely as a preliminary indication of the smart rotor potential.

The optimized cyclic control is first applied with the objective to evaluate the load alleviation potential of the smart rotor configuration presented in the previous chapter; both pitch and flap cyclic control actions are considered and compared. The cyclic load alleviation results are reported in **[Article IV]**, and briefly summarized in the first part of the chapter. In the second part of the chapter, the simplified smart rotor cyclic control approach is instead exploited to evaluate the possibility of increasing the energy produced below rated conditions.

6.1 Cyclic control for blade load alleviation

The feed-forward cyclic control is first employed to reduce the blade root flapwise bending moment variation caused by periodic disturbances above rated wind speed. Cyclic control trajectories result from solving a constraint optimization problem, where, to limit the problem dimension, the continuous control signal trajectory is discretized by a set of values at determined azimuthal locations, and piecewise cubic Hermite interpolation is applied between the fixed points [Article IV].

The investigation considers one reference case and three smart rotor configurations:

- Reference (*Ref.*), the NREL baseline control limits the power output by collective pitching to feather, load alleviation is not addressed.
- Cyclic pitch (*CPC*), the blade pitch follows the cyclic control trajectory; the mean pitch angle is regulated by the NREL baseline controller for power limitation.
- Cyclic flap (*CFC*), the flap deflection follows the optimized cyclic control trajectory; the collective blade pitch angle is determined by the NREL baseline controller.
- Cyclic pitch and flap (*CPCF*), the optimization returns a control trajectory for the blade pitch angles, and another for the flap deflection values.

The load alleviation performance is assessed in terms of lifetime fatigue damage equivalent loads for the blade root flapwise bending moment. A first assessment is performed for the same ideal conditions considered during the cyclic trajectory optimization: the wind field has no turbulence, and the turbine is stiff, thus the blade root bending moment is only the result of the integrated aerodynamic forces, figure 6.1. As they refer to ideal conditions, the resulting fatigue damage equivalent loads (DEL) give only an approximate indication of the maximum alleviation potential that can be achieved by the smart rotor actuator configurations.

The optimized cyclic control actions effectively reduce the moment variations (circle marks in fig. 6.1), and the cyclic pitch action display higher alleviation potential than the cyclic flap: in ideal conditions, the lifetime DEL of the aerodynamic moment caused by periodic disturbances is reduced by 72 % with cyclic pitch, and by 60 % with cyclic flap. Even higher alleviation potential (77 %) is achieved by combining cyclic pitch and cyclic flap actions (blue line with diamond marks in fig. 6.1). At higher wind speeds, where the deterministic load variation is higher, the alleviation potential is lower than at lower wind speeds, especially so for the cyclic flap case, as the actuators deflection limits are reached.

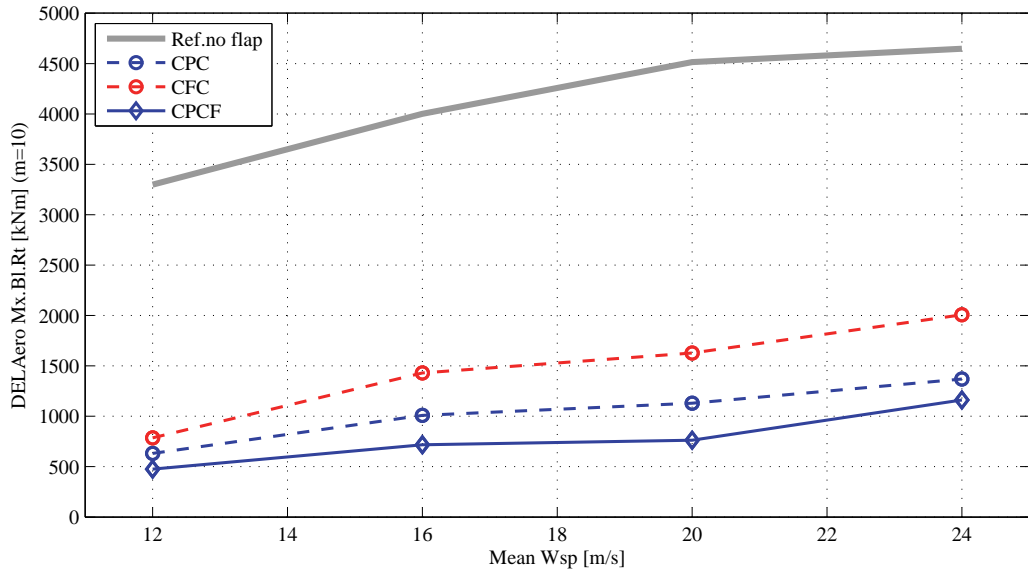


Figure 6.1: *Stiff turbine, deterministic wind conditions. Alleviation of the Damage Equivalent Load of the aerodynamic flapwise bending moment at the blade root with optimized feed-forward cyclic control trajectories for: blade pitch (CPC), flap deflection (CFC), and both (CPCF). The DEL refer to the turbine lifetime and account for the mean wind speed occurrence.*

An attempt is made to estimate the energy requirements for flap and pitch control actions from the distribution of aerodynamic forces on the airfoil profiles and along the blade [Article IV]. Although rather approximate, the analysis confirm the intuition that the energy required to deflect the adaptive trailing edge flaps is much less than to pitch the whole blade: the energy for one degree deflection of the 20% span flap is estimated 20 to 90 times lower than for one degree pitch variation. Although the energy consumption might not be much of a concern compared to the turbine power output, the figures give a rough indication on the actuators requirements, sizing, and wear. The total energy demand by pitch and flap cyclic control actions under the different control configurations is reported in figure 6.2. Although achieving lower load alleviation, the cyclic flap configuration (*CFC*, red line with circles) requires approximately ten times less energy than the cyclic pitch control. By combining the flap low-energy activity with the pitch load variation potential, the combined control configuration (*CPCF*) achieves the highest load alleviation with a pitch actuators work load nearly half the one

from cyclic pitch alone. The combination of pitch and flap control action has thus an interesting potential for smart rotor application, and will be further investigated in section 7.3 in a combined model based control configuration.

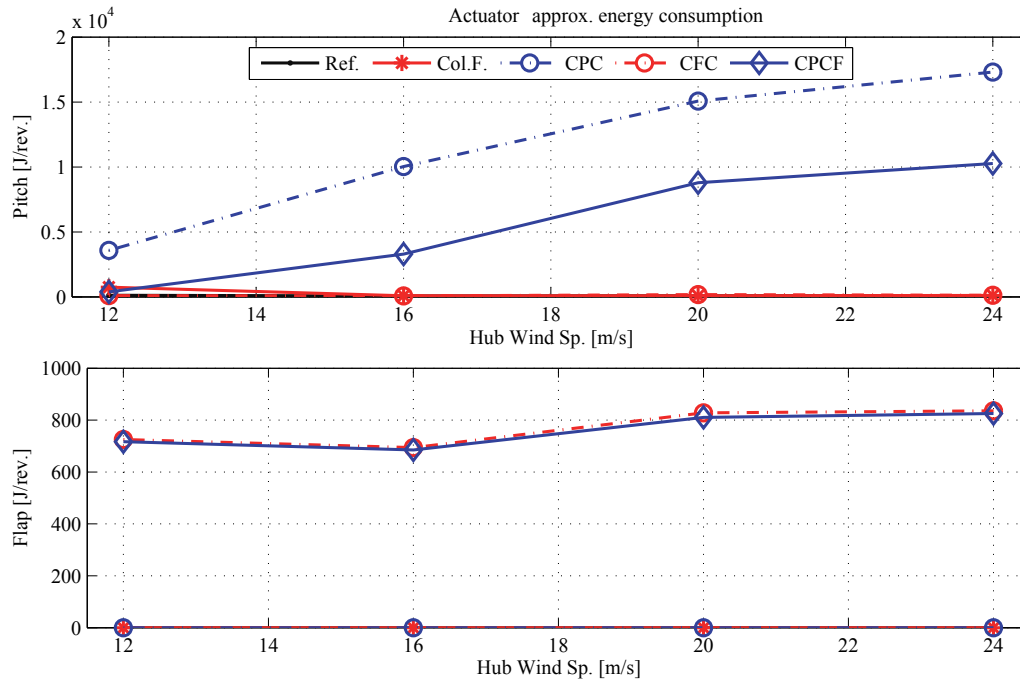


Figure 6.2: Estimation of the energy requirements for cyclic control actions aimed at reducing the flapwise bending moment variation. Energy requirements for one blade pitch actuator (top plot), and one blade ATEF actuator (bottom plot); feed-forward cyclic control configurations with: flap actuators only (CFC), pitch actuators only (CPC), and a combination of the two (CPCF). Combining flap and pitch actuators nearly half the work load on the pitch.

The same cyclic control trajectories optimized for the stiff turbine model are tested in realistic simulation conditions, figure 6.3: the structural degrees of freedom are included, and the wind field accounts for atmospheric turbulence as prescribed by the IEC standard [26] for a class B turbine; a total of one hour turbulent wind field is considered for each mean wind speed (6 times 10 minutes turbulence series). The stochastic variations introduced by the wind turbulence increases the fatigue loads, and, as the cyclic control can not compensate for the stochastic load variations, the total alleviation is significantly reduced. The control trajectories are not optimized for the flexible

turbine; nevertheless, the results give an indication of the minimum performance a control algorithm based on the same actuators setup is expected to deliver: the alleviation obtained with cyclic pitch (9.4 %) is still higher than obtained with the flap (7.1 %). The results are in good agreement with the analysis on the fatigue load contributions, section 3.2, which indicated a maximum fatigue alleviation of 11 % from the periodic component of the loads. Furthermore, opposite to the deterministic wind simulations, higher load alleviations are now reported at high wind speed, as the contribution to the total fatigue damage from periodic load variations is more marked for operation at high mean wind speeds.

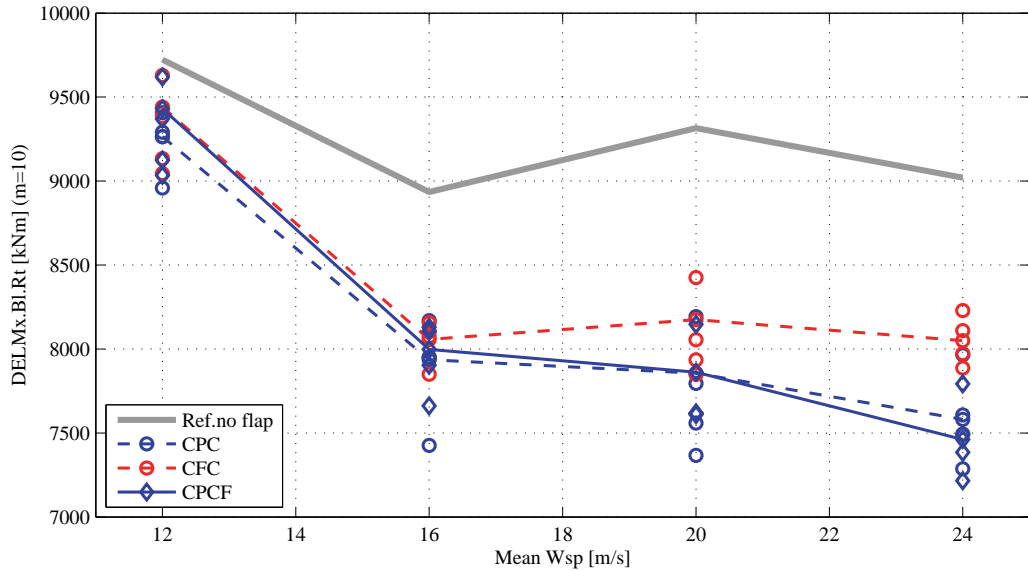


Figure 6.3: Complete turbine model, turbulent wind field as prescribed by IEC standard. Alleviation of the fatigue Damage Equivalent Load of the flapwise bending moment at the blade root with optimized feed-forward cyclic control trajectories for: blade pitch (CPC), flap deflection (CFC), and both (CPCF). The DEL refer to the turbine lifetime and account for the mean wind speed occurrence. The marks without any line indicate the DEL alleviation reported in each of the 10 minutes time series, whereas the lines indicate the average DEL over one hour simulation.

6.2 Cyclic control for enhanced power capture

Active load alleviation below rated conditions gives only a small contribution to the reduction of the overall lifetime fatigue damage of the turbine blade (see figure 3.4), and, at the same time, might reduce the turbine power output, see the results by Castaignet [25]. It is thus worth to consider whether a smart rotor configuration could be exploited for scopes other than load alleviation below rated conditions, for instance to enhance the turbine energy capture.

6.2.1 Preliminary BEM analysis

A first investigation is carried out with a steady blade element momentum (BEM) model of the NREL 5 MW rotor; the model follows a standard formulation that includes Glauert's and Prandtl's corrections [29]. Flap deflections modify the steady lift and drag forces of the blade sections; therefore, the rotor power and thrust coefficients, as well as the induced velocities, depend not only on the rotor tip-speed ratio¹ and the collective pitch, but also on the collective flap deflection angle. The rotor power coefficient is evaluated over a range of tip speed ratios λ , and the ratios corresponding to the rotor speed prescribed by the baseline NREL 5 MW controller are marked by squares in figure 6.4: note that at low wind speeds the turbine operates at relatively higher λ , as the rotor speed is not further reduced in order to avoid exciting the tower natural frequency. The analysis is performed in steady conditions, for a stiff rotor, and uniform inflow over all the rotor area.

The baseline NREL 5 MW controller operates at constant zero pitch below rated conditions: the corresponding power coefficient C_p curve is marked by the black line in figure 6.4; the maximum power coefficients obtained when the collective blade pitch is allowed to vary are instead marked by the blue line with stars, whereas the red line with crosses indicates the maximum C_p obtained when both collective pitch and collective flap can vary. Figure 6.6 reports the collective pitch and flap settings that return the maximum

¹The rotor tip-speed ratio is defined as the rotational speed of the blade tip normalized by the undisturbed wind speed: $\lambda = \omega R / U_0$.

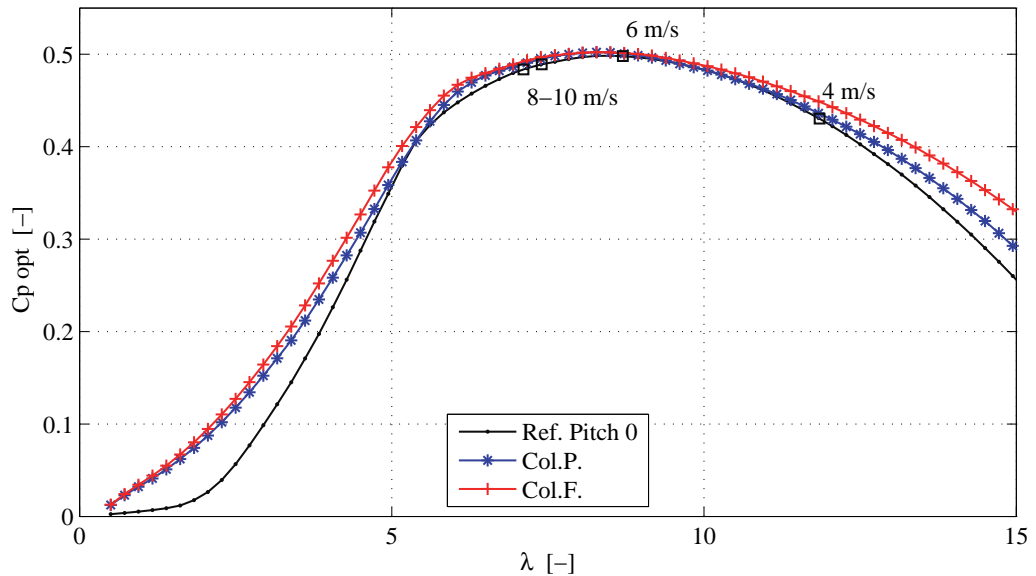


Figure 6.4: Steady BEM analysis of the NREL 5 MW rotor, power coefficient C_p as function of the rotor tip-speed ratio λ ; blade pitch fixed to zero (Ref.), collective pitch for maximum power coefficient (Col.P.), collective pitch and collective flap (Col.F.) for maximum C_p . The square marks indicate the tip-speed ratios at which the baseline NREL 5 MW turbine operates at the given wind speeds (all below rated conditions).

C_p , and figure 6.5 plots the corresponding rotor thrust coefficients C_t . The maximum power coefficient at optimal tip speed ratio is not increased by adjusting the collective blade pitch nor by deflecting the flaps, figure 6.4; on the other hand, optimal collective pitch and flap settings return milder C_p curves, and thus give higher power coefficients at sub-optimal tip-speed ratios. As the turbine often operates at tip-speed ratios far from the optimal one, especially at low wind speed for the tower frequency constraints, pitch and flap control below rated wind speed can, at least in theory, increase the power capture. An estimation of the power increase in terms of Annual Energy Production is given in the next section.

At tip-speed ratios slightly below the optimal one ($\lambda = 5 \sim 6$), the pitch and flap settings for maximum C_p indicate that the maximum power output is obtained by increasing the loading on the rotor: by deflecting the flap to positive angles and pitching the blade to negative angles (increased angles of attack), figure 6.6. The corresponding thrust curve is thus higher than the

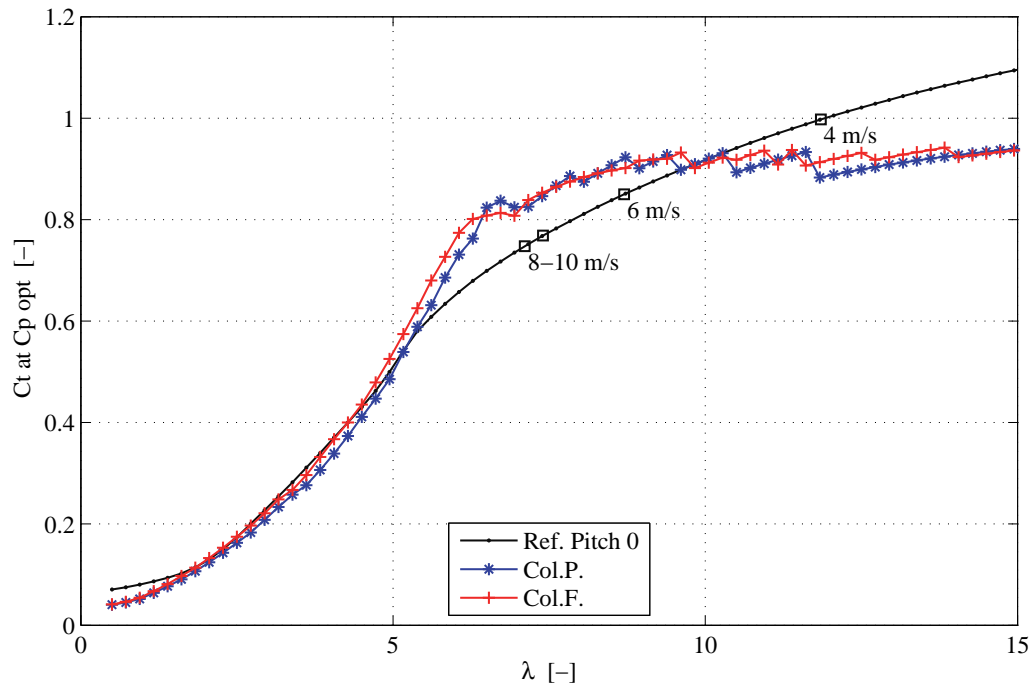


Figure 6.5: Steady BEM analysis of the NREL 5 MW, rotor thrust coefficient C_t corresponding to the maximum power coefficient settings at different tip-speed ratios λ . Square marks indicate the operating points reported for the NREL 5 MW in its baseline configuration for the given wind speed conditions.

reference one, figure 6.5. On the contrary, as the tip-speed ratio is further increased, optimal power output requires a decrease of the rotor loading for increasing λ , by pitching toward feather and deflecting the flap upwards (negative flap deflection); the corresponding thrust curves in the turbine operating regime have thus a milder slope than in the fixed-pitch reference case.

The BEM formulation presented in this section will be later used to define a linear approximation of the steady aerodynamics of a rotor with adaptive trailing edge flaps. The approximation will be included in the linear model used by the predictive control algorithm presented in section 7.1.

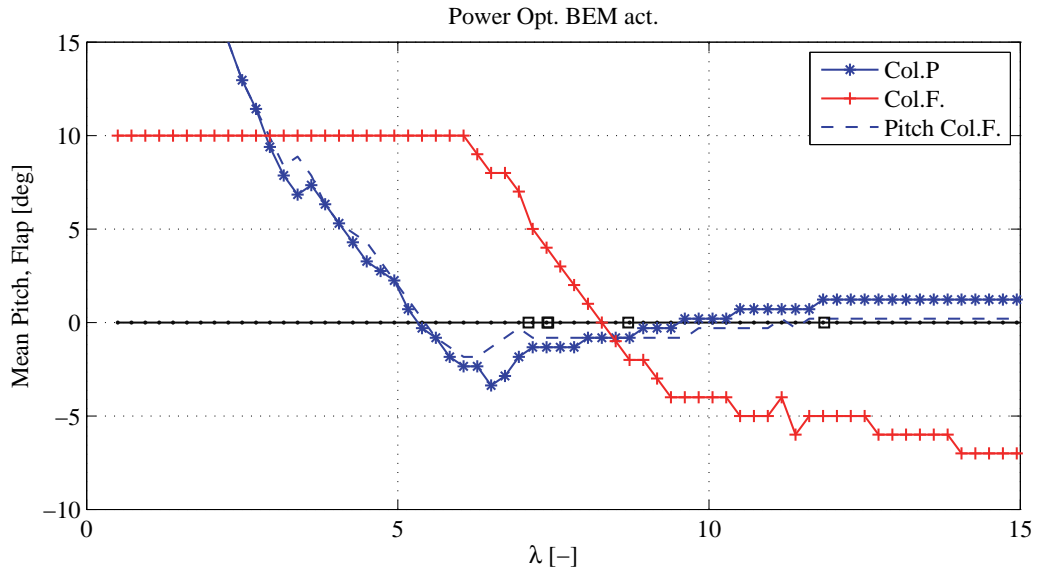


Figure 6.6: Steady BEM analysis of the NREL 5 MW, collective pitch (*Col.P*), and collective flap (*Col.F.*) settings that return the maximum power coefficient at each tip-speed ratio λ ; the dashed blue line *Pitch Col.F.* indicates the optimal collective pitch settings when the flaps are deflected.

6.2.2 Cyclic optimization

The possibility of controlling the smart rotor to increase the turbine energy output below rated wind speed is explored in ideal conditions by applying the feed-forward cyclic control procedure presented in the previous section; the optimization cost function is now simply given by the square of the rotor aerodynamic power.

First, the optimization focuses on the collective pitch angle (*Col.P.* tag in fig. 6.7), and on collective pitch and flap deflection (*Col.F.* tag). Thereafter, the possibility to further increase the energy capture by compensating for the periodic wind speed variations from terrain shear and tower shadow is investigated by including cyclic control trajectories for the pitch (*CPC*), and the flap (*CFC*), figure 6.7; the cyclic control trajectories are both superimposed to the optimized collective pitch angle. The results are in good agreement with the BEM analysis: the largest contribution to the power increase comes from the optimized collective pitch angle (approximately 2 %), and the opti-

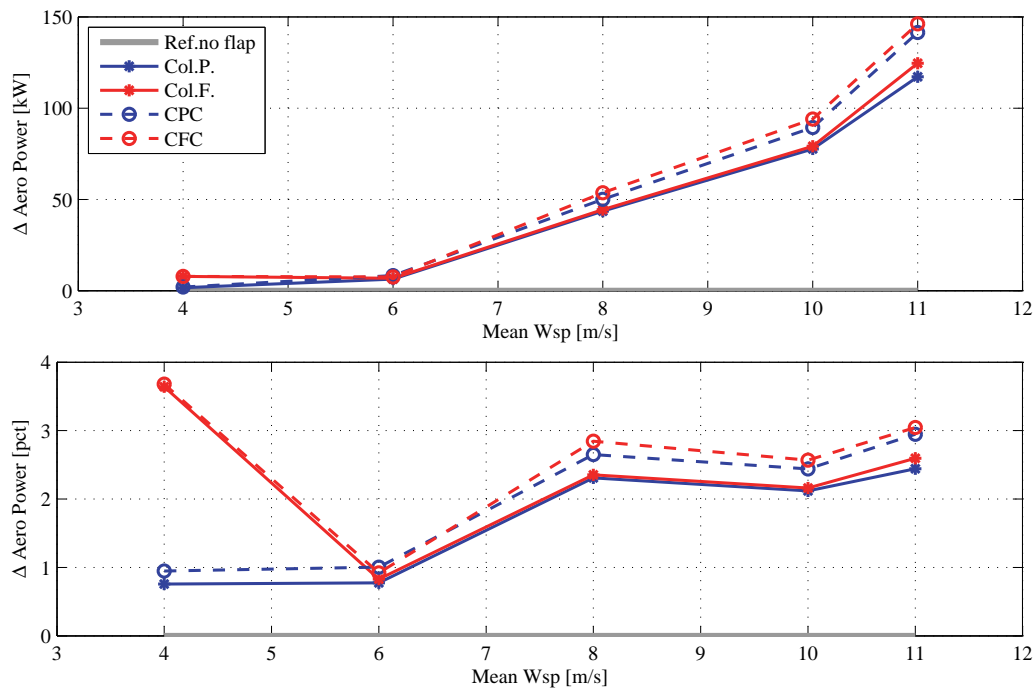


Figure 6.7: Increase of rotor aerodynamic power output below rated conditions with optimized collective pitch (*Col.P.*), collective flap and pitch (*Col.F.*), and feed-forward cyclic control of blade pitch (*CPC*), and flap deflection (*CFC*). Stiff NREL 5 MW turbine, wind field with terrain shear, tower shadow and no turbulence.

mized collective flap deflection leads to a further increase, which is significant at low wind speed (3 % more, fig. 6.7), but rather small otherwise.

The increase in power capture below rated condition is summarized in terms of Annual Energy Production (AEP) for a Rayleigh wind distribution with 8.5 m/s mean, which corresponds to a class II turbine in the IEC standard [26], table 6.1. The collective pitch optimization reports an AEP increase by nearly 1 %, the collective flap optimization increases the AEP by an additional 0.07 %, and the cyclic flap control adds a further AEP increase of 0.2 %. An attempt is made to test the same optimized control trajectories in simulations with a flexible turbine model and IEC standard wind turbulence. The simulations with turbulence have confirmed the increase of AEP by adjusting the collective pitch angle (2 % increase for the tested model), and an additional 0.14 % increase by adjusting the collective flap deflection;

the cyclic control actions did not bring any improvement, and they would probably need to be re-tuned to account for the dynamics of the flexible turbine.

	<i>Ref.</i>	<i>Col.P.</i>	<i>Col.F.</i>	<i>CPC</i>	<i>CFC</i>
<i>AEP</i> [GWh]	19.87	20.08	20.09	20.11	20.13
Δ <i>AEP</i> [%]	-	+0.99	+1.06	+1.16	+1.24

Table 6.1: *Feed-forward control for increased power capture below rated conditions, increase in the turbine Annual Energy Production (class II wind distribution). Ideal simulation conditions with a stiff wind turbine and wind field with terrain shear, tower shadow, but no atmospheric turbulence.*

Cyclic control actions to enhance the energy output leads to an inevitable increase of the aerodynamic load variation over the rotor area. In fact, as the wind speed decreases (blade moving downwards, toward azimuth 0°), the cyclic control trajectories optimized for power capture further decrease the loading on the blade by either deflecting the flap upwards or by pitching to feather, figure 6.8; the other way around as the wind speed increases, thus amplifying the variations of the loads on the blade. The behavior is implicit in the rotor steady aerodynamics highlighted by the BEM analysis: in the operating tip-speed range, the thrust curves for optimal power extraction have a smaller slope than the reference curve, figure 6.5, thus indicating a much lower increase in thrust coefficient as the tip-speed ratio is augmented. The decrease in the free wind speed seen by the blade moving downwards can be interpreted as an increase in the ‘local’ blade tip-speed ratio; while in the reference not-controlled case the ‘local’ thrust coefficient would increase with the local lambda, the control actions aimed at tracking the maximum power coefficient tends to maintain a constant local blade thrust coefficient. Therefore, the decrease of the thrust force on the blade caused by the wind speed reduction is not compensated by the increase in the thrust coefficient as much as in the reference case, thus causing higher variations of the loads on the blade.

Below rated conditions, the control actions aiming at alleviating the flapwise load variation on the blade will inevitably cause a decrease of the energy output, and vice versa. The smart rotor can thus increase the energy output of the turbine below rated wind speed (if an adequate controller is formulated for realistic applications); nonetheless, the benefits from the increased annual

energy output should be weighted against the increase of fatigue loads on the turbine structure that the same control actions will generate. In the cyclic control cases, the blade root flapwise fatigue damage equivalent load is in fact increased by nearly 18 % for the 8 and 10 m/s mean wind speed time series; the impact on the overall lifetime DEL is however expected to be lower.

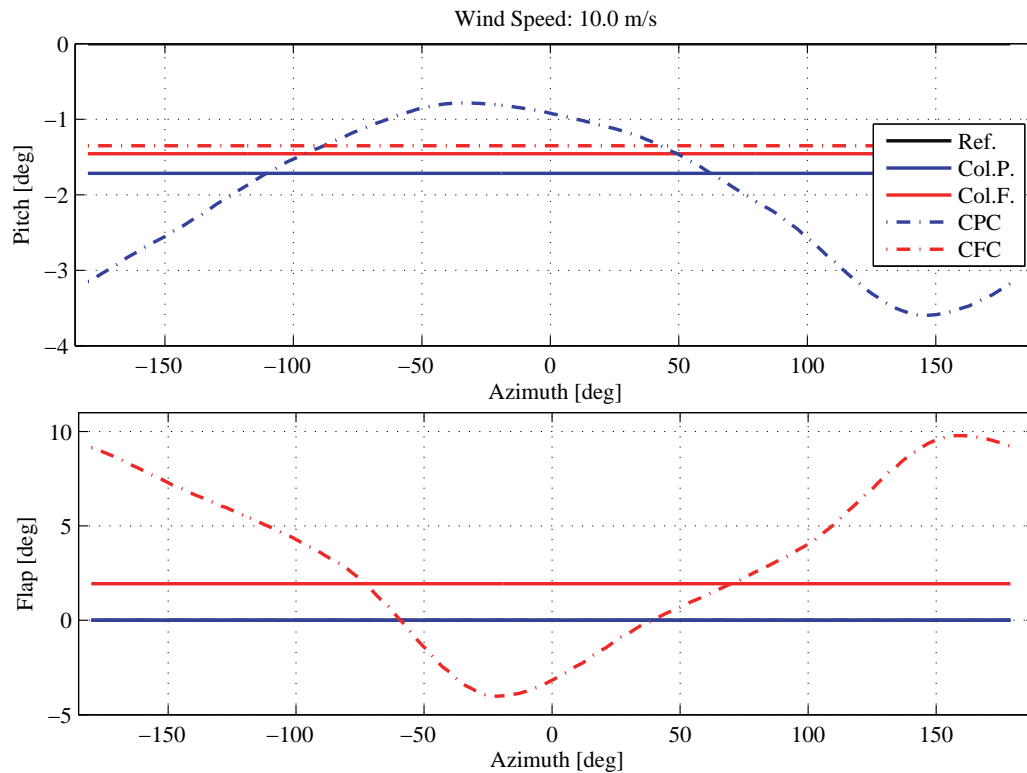


Figure 6.8: Optimized cyclic control trajectory for increased power extraction below rated condition, pitch (top) and flap (bottom) signals. Optimization based on stiff NREL 5 MW turbine model. Azimuth 0° corresponds to the blade pointing downward.

CHAPTER 7

Model Based control algorithms for a rotor with ATEF

The chapter presents two control algorithms that aim at actively alleviating the load variations on the turbine structure using the ATEF smart rotor configuration presented earlier. The control algorithms include feedback from measurements of the actual turbine structural deformations, and are thus able to address load variations of both periodic and stochastic nature, overcoming the limitations of the feed-forward cyclic control presented in the previous chapter.

The first control algorithm adopts a simple approach where each of the rotor blades is treated independently: the deflection of the flap on one blade only depends on measurements of the flapwise bending moment at the root of the same blade. The control problem thus simplifies to a series of independent Single Input-Single Output (SISO) systems, and it is solved using a linear quadratic (LQ) formulation. The second control algorithm presents a more complex and comprehensive approach: the whole turbine is monitored by one controller, which regulates not only the flap deflection angles, but also the blades pitch and the generator torque; the resulting Multiple Input-Multiple Output (MIMO) control problem is solved with a Model Predictive method

(MPC). The MIMO-MPC control algorithm was first developed by Henriksen et al. [31], and is here expanded to account for the presence of the ATEF actuators on the rotor blades [Article VI].

The load alleviation performances of the two control algorithms are assessed by means of aeroelastic simulations of the turbine response during normal operation, and finally quantified in terms of fatigue damage reduction. The first control algorithm is described in [Article V], enclosed in the second part of the dissertation, and section 7.2 briefly presents the achieved load alleviation results. The second control algorithm and its performances are instead documented in [Article VI], and section 7.3 reports the main results. The following section gives an overview of the two control algorithms, and highlights their similarities and differences; please refer to the enclosed articles for a more detailed descriptions of the algorithms.

7.1 Overview on control algorithms

7.1.1 Definition of the control models

This study proposes and investigates two control algorithms for active load alleviation on a smart rotor: a Single Input-Single Output Linear Quadratic (SISO-LQ) control, and a Multiple Input-Multiple Output Model Predictive Control (MIMO-MPC). The two algorithms explore rather different approaches to the control problem, but also have some points in common. Both controls use as *input signals* measurements of the blades azimuthal position, and of the flapwise bending moment at the root of the blades; in addition, the MIMO-MPC algorithm also employs measurements of the tower top acceleration, and of the drive train torque and rotation speed.

Both algorithms have a *model based* control approach, where a linear time invariant model of the system to control is made available to the controllers, so they can predict the system response to the control actions. The model based approach was chosen to better cope with the control challenges given by the response of the blade root bending moment to flap deflection, which

is characterized by large delays and a non-minimum phase transient (section 5.2). The linear model used in the SISO-LQ algorithm simply represents the dynamics of an isolated rotating blade, and describes the response from flap deflection to blade root flapwise bending moment; each of the three blades is treated as an independent Single Input-Single Output system.

The model in the MIMO-MPC formulation describes instead the response of the whole turbine; it features a simplified structural model where the deformations of the turbine components are described by a superposition of predetermined mode-shapes. The structural model is then coupled with a quasi-steady BEM-based aerodynamic model, where aerodynamic forces and induction factors are computed a-priori, and then retrieved through table look-up; the dynamic inflow effects are accounted for by a first order low-pass filter on the axial induction factor [31]. The effects of flap deflection are included assuming a linear dependency on the lift and drag forces, and on the induction factors [Article VI]; the linear approximation, although rather crude, proved valid for small angles of attack in the considered flap deflection range.

The models utilized by the control algorithms are formulated in both cases in a *state-space form*. As the system states can not be measured directly, both the SISO-LQ and the MIMO-MPC algorithms estimates the states for the respective systems by using *Kalman filter* estimators, which are based on the same linear models the MPC and LQ controller use.

Two different approaches to obtain the linear models required by the controllers and the Kalman estimators are explored: the model in the MIMO-MPC algorithm is retrieved directly from *first principles* modeling [31], whereas the one in the SISO-LQ method results from *system identification* [Article V]. The system identification approach follows the subspace method described by Ljung [41], thus directly returning a model in state-space form and an estimation of the Kalman filter gain matrix; the identification also includes fictitious periodic input signals to avoid identification biases from the periodic load variations observed on the rotating blade [58]. The two linear models are verified by comparing the frequency response they predict against the response obtained with HAWC2 simulations: both modeling approaches proved adequate to their scope.

As a general consideration, between the two modeling approaches tried in the study, system identification seemed to have the advantage of not requiring an extensive and accurate knowledge of the system to control as instead demanded to formulate a model from first principles; the identification could be performed, at least in theory, directly on data series retrieved from experiments [59,60]. On the other hand, a comprehensive Multiple Input-Multiple Output model of the whole turbine response might be difficult to obtain exclusively from system identification; in fact, reaching a signal-to-noise ratio adequate to identify the response in all the turbine structural components might require excitations that are in practice unfeasible, unsafe, or simply too expensive to obtain. In future work, it might be thus worth to consider a combination of the two approaches: an approximate model would be first obtained from physical first principles, and thereafter refined and tuned using system identification methods.

The *rotation* of the turbine blades poses some challenges in defining linear and time invariant models of the system. As mentioned, in the SISO-LQ case, the problem of periodic -and therefore time dependent- load variations on the rotating turbine blades is solved by including additional periodic inputs in the system identification phase. The same periodic signals are then treated as measured disturbances by the Linear Quadratic controller, thus allowing anticipation of the periodic load variations [Article V]. The MIMO-MPC control algorithm tackles the problem using instead a *multi-blade coordinate transformation* [17], thus mapping loads and control actions on the rotating blades into a non-rotating reference frame with collective, tilt, and yaw components [31].

7.1.2 Optimal controller algorithms

Once a sufficiently accurate linear model of the system to control is available, the control solution should find the most appropriate actions to steer the modeled system in the desired direction. The control problems considered in the present study are solved with two approaches: a Linear Quadratic control (LQ), and a Model Predictive Control (MPC). Both algorithms support SISO and MIMO models, and could be applied to either of the linear control models introduced in the previous paragraphs. In this investigation, the LQ solution

is applied to the SISO problem description [Article V], whereas the MPC solution is used to address the MIMO problem formulation [Article VI].

Both LQ and MPC are *optimal controllers*: namely, the control actions result from the solution to an optimization problem that minimizes a control cost function. Since the objective of the smart rotor is to alleviate the blade root flapwise fatigue damage, the *cost functions* for the SISO-LQ and the MIMO-MPC algorithms both include terms to address the variations of the flapwise loads at the root of the blades. The cost functions also include terms to limit the control actions of the flaps, and, in the MIMO case, of the pitch actuators and of the generator torque; the control action terms are *frequency weighted* so to discourage control activity in the high frequency range. Avoiding high frequency control activity reduces actuator use and wear, and only has a minor impact on the load alleviation potential, as the contribution to the overall fatigue damage from high frequency loads was found to be small (section 3.2.3). Furthermore, in the high frequency range the system to control is less accurately described by the linear control models, frequency weighting thus prevents control activities that might be counter-productive.

The optimization control problem is cast in a *quadratic formulation*. The LQ algorithm solves the quadratic optimization problem over an infinite time horizon, and, by solving off-line a Discrete time *Algebraic Riccati Equation* (DARE), returns an optimal gain matrix, which, multiplied by the state vector estimated by a Kalman filter, gives at each time step the optimal control action; the standard LQ formulation is here modified to handle anticipation of the load variation from periodic disturbances [40]. The MPC algorithm instead solves the optimization problem at each time step iteration, and it considers a receding and finite time horizon optimization; the optimization problem is subject to constraints and is solved by iterative *Quadratic Programming* methods: the optimization returns directly a sequence of control actions, and not a gain matrix as in the LQ case.

Leaving aside the formal differences and the esoteric theories behind the LQ and MPC control formulations, from a practical point of view, LQ provides a much faster solution to the control problem, as the optimal gain matrix is computed once, and can be applied as long as the system model does not vary. The MPC solves instead the constrained optimization problem at every

time step iteration, and thus presents higher computational requirements, which might be more challenging to meet in real time operations at high sampling frequencies, especially for system models with a large number of states. Another benefit of the LQ approach, besides having a formulation less hostile to non-control disciplines, is to express the control action as a feedback on the states, thus allowing for a closed loop representation of the system. Although the topic was not addressed in this study, a closed loop aero-servo-elastic description of the system might be useful to immediately identify stability issues, which might be relevant for rotors equipped with trailing edge flaps [16]; furthermore, a closed loop description could be eventually included in an integrated aero-servo-elastic concurrent design process [20]. On the other hand, with hindsight, some of the MPC properties would have been beneficial also in the SISO case where LQ was used instead, most notably the ability of the control algorithm to directly handle the constraints on the flap total deflection angle. In fact, as the load variations caused by the disturbances on the blade are larger than the variation achieved by the flaps (section 5.4), the limit deflection are often reached; in the LQ case, the deflection constraint is simply enforced by truncating the control signal coming from the controller. In future work, it might be interesting to apply an MPC algorithm to the same SISO flap control problem, and assess the differences in performances from the LQ controller.

7.2 SISO Linear Quadratic control for active load alleviation

The SISO problem of controlling the flap on each blade based on measurements of the blade root flapwise bending moment on the same blade is solved with the Linear Quadratic controller. The load alleviation LQ control is simply superimposed to the baseline NREL control, which takes care of the power regulation by adjusting generator torque and collective pitch angle; mutual interaction between the load alleviation and the power controller is found to be negligible.

The controller includes a periodic disturbance term that depends on the

blade azimuthal position and is used to handle anticipation of the periodic load variations [Article V]. Three configurations with different periodic disturbance terms are explored:

- *d 00*. The LQ control receives no information about the periodic disturbances, it acts only on feedback from the bending moment measurement.
- *d Sin-Cos*. The periodic disturbance signal is given by a classic harmonic signal with sine and cosine functions of the blade azimuthal angle.
- *d Wsp*. The periodic disturbance signal is a simple function of the blade azimuthal position retrieved from a basic model of the free wind speed variation caused by terrain shear and tower shadow [Article V].

The control configurations performances are evaluated for normal operation at different mean wind speed above rated, and compared to the reference case given by the baseline NREL controller with no active load alleviation. The simulations are performed with a turbulent wind field, as prescribed by the IEC standard for a class B turbine [26]. Some of the results are summarized in the following paragraphs, please refer to [Article V] for further comments on the simulation results.

The smart rotor with LQ flap control is able to alleviate both the periodic and the stochastic component of the blade root flapwise loads, figure 7.1, thus reducing the load standard deviation, as well as the maximum load range. The three control configurations have similar performances concerning the alleviation of the stochastic components of the loads (mainly addressed by the feedback part of the LQ control), whereas the *d Sin-Cos* and *d Wsp* configurations, as expected, perform better in alleviating the periodic load component, and thus reduce the flapwise bending moment standard deviation at the blade root by approximately 22 %. The alleviation of the blade loads, as well as the flap activity, are mainly concentrated at frequencies close to the 1P rotor revolution frequency (0.2 Hz, above rated conditions) for all three control configurations [Article V].

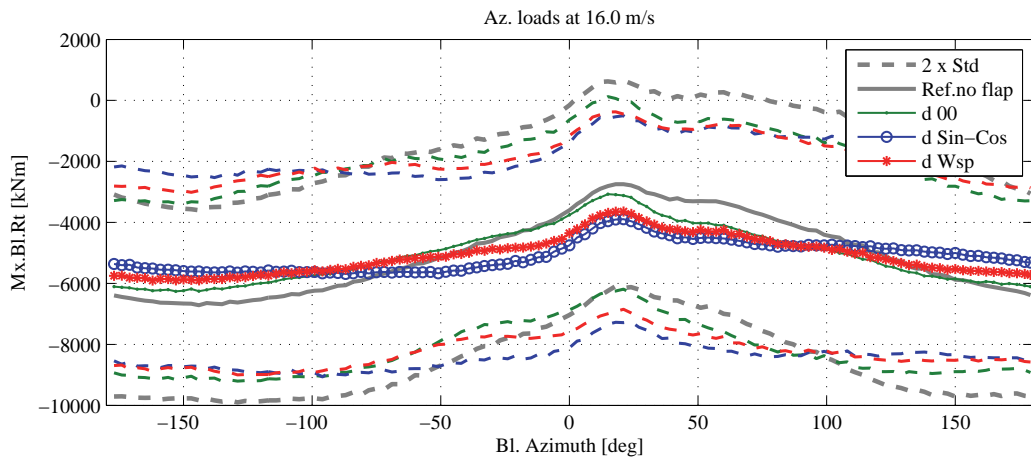


Figure 7.1: Blade root flapwise bending moment versus blade azimuthal position. Results for 1 hr simulation at mean wind speed of 16 m/s. For each azimuthal position the means of the simulated loads (lines with markers) indicate the periodic component of the load variation, the standard deviations (dashed lines) are instead proportional to the stochastic load variation. Active flap control reduces both components of the flapwise load variation [Article V].

The load alleviation performance of the smart rotor with LQ flap control is evaluated in terms of fatigue damage equivalent load (DEL) reduction; simulations at different mean wind speeds are performed, figure 7.2, and the total lifetime fatigue damage alleviation is estimated for a Rayleigh wind speed distribution for a class II turbine [26]. The $d\ 00$ control configuration lowers the lifetime DEL on the blade root flapwise bending moment by 10 %, whereas the configurations with periodic loads anticipations reach higher alleviations: 13.8 % with the $d\ Sin-Cos$ configuration, and 14.5 % with $d\ Wsp$. The increase in load alleviation potential by nearly 4 % achieved by including periodic load anticipation is comparable to the increase previous investigations have attained using additional in-flow sensors [3, 11], with the advantage that the periodic load anticipation approach does not require a sensor setup as complicate and delicate as demanded instead by in-flow measurements. Similar alleviations of the fatigue damage equivalent loads on the blade flapwise bending moment are also confirmed in yawed inflow conditions.

The differences in load alleviation performances observed among the 10 minutes turbulent wind series, highlighted by the markers in figure 7.2, are reported in detail in figure 7.3 for a single mean wind speed case. Drawing a

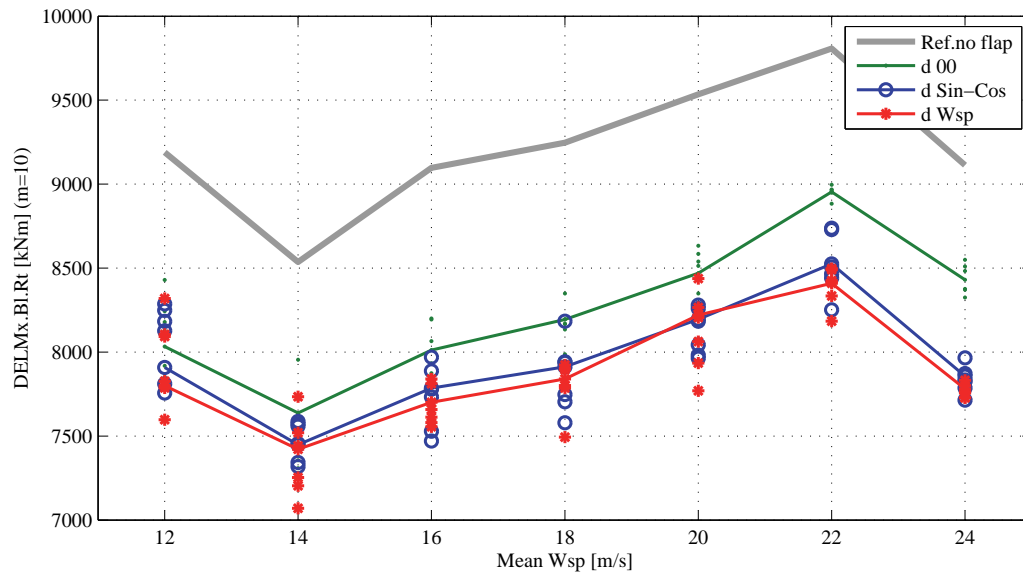


Figure 7.2: *Fatigue Damage Equivalent Loads (DEL) at the blade root flapwise bending moment. The DEL refer to a 25 yr lifetime and 10 millions equivalent cycles, the figures at each mean wind speed are weighted by the occurrence of the mean wind speed according to a Rayleigh distribution for a class IIb turbine. The dots report the spreading of fatigue damage reduction recorded in each of the 10 minutes simulation series [Article V].*

conclusion on the load alleviation potential based on only 10 minutes simulations might yield to variations of the DEL reduction estimations up to $\pm 3\%$; it is thus important that future simulations or experiments in stochastic turbulent conditions will consider at least 40 minutes of data for each wind speed case, so to reach alleviation estimations within $\pm 1\%$ of what returned by 60 minutes turbulent wind simulation, which is the minimum requirement prescribed by the standard for turbine load analysis [26].

The control action required to the flap actuators is measured as the total angular distance traveled by the flap either with upward or downward deflections; the angular distance is then normalized by the total operation time, thus returning an average deflection speed, figure 7.4. The *d Wsp* control configuration, which achieves higher reductions of the flapwise loads standard deviation, also demands higher flap activity; the *d 00* configuration instead, in spite of lower alleviation performances, requires higher flap activity than the *d Sin-Cos* configuration. The maximum deflection rate of the flap actu-

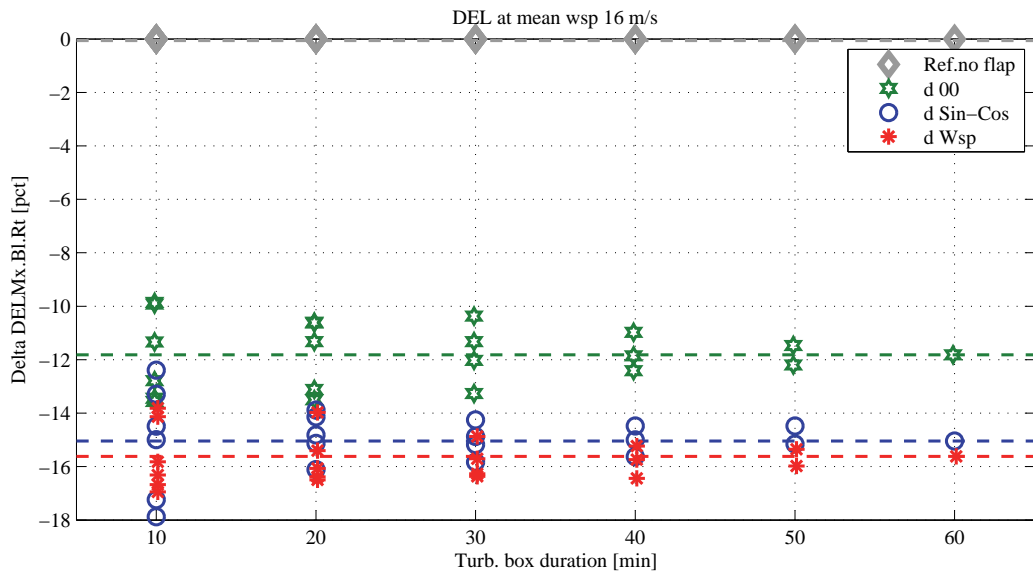


Figure 7.3: Spread of fatigue DEL alleviation depending on the simulation time. LQ-SISO control algorithm for turbulent wind with 16 m/s mean; results given as percentage variations from the reference baseline case without active load alleviation. The dash lines indicate the results obtained with 60 minutes turbulent simulations.

ator is not constrained in the simulations. Nevertheless, with the frequency weighting penalizing high frequency flap activity, 99 % of the flap actions observed in the simulations occur with deflection rates below 90 deg/s.

The LQ control cost function only includes load variations at the blade root; nevertheless, in spite of not being directly addressed by the active control, positive alleviations of the lifetime fatigue DEL are reported also at the tower bottom flange in the fore-aft direction, figure 7.5: 6.5 % with the d_{00} configuration, 5.6 % with d_{Wsp} and 3 % with $d_{Sin-Cos}$. On the other hand, the DEL of other parts of the structure are increased by the active control actions, most notably, the lifetime fatigue DEL of the blade root torsion moment is increased by nearly 10 % as a result of the additional aerodynamic pitching moment variations introduced by the flap deflection.

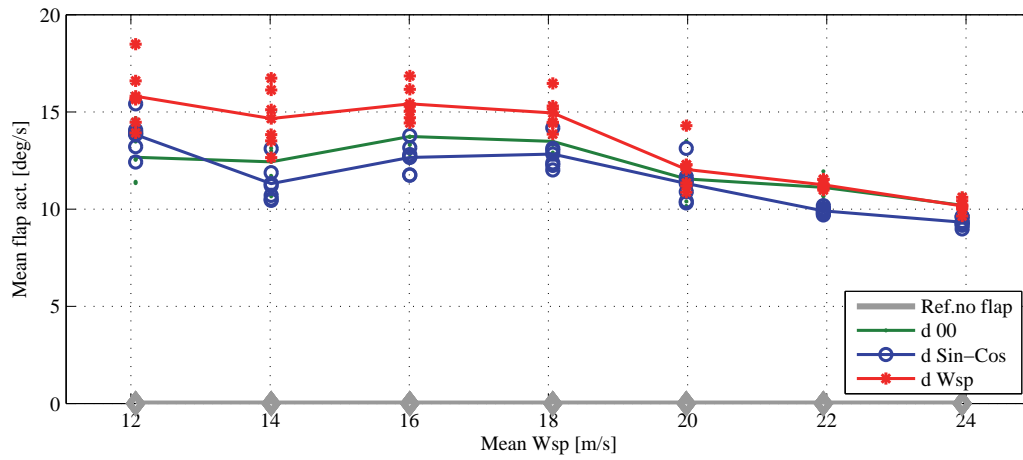


Figure 7.4: Flap activity for the three LQ control configurations. Total flap traveled distance normalized by the simulation time, for each of the investigated mean wind speeds [Article V].

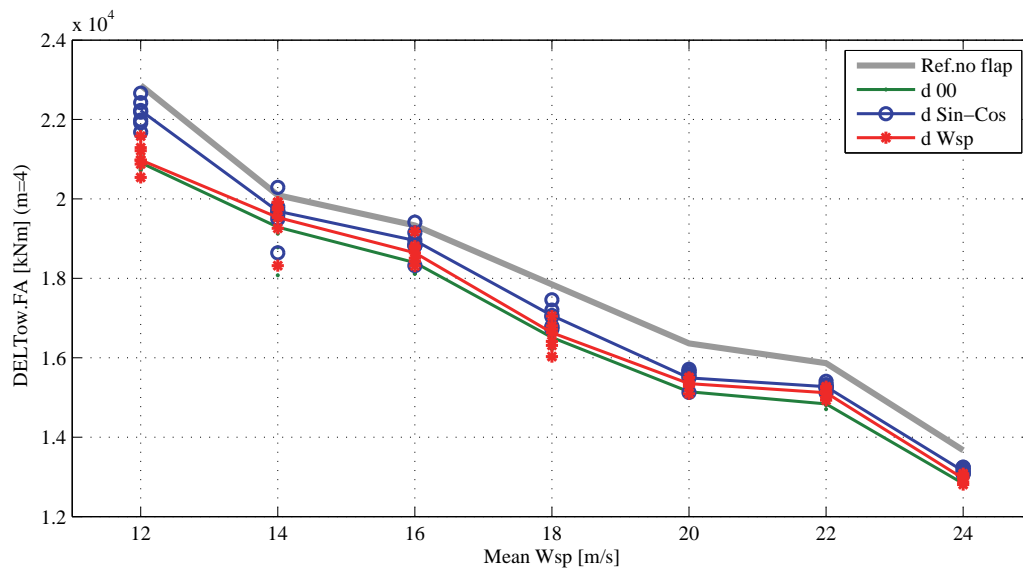


Figure 7.5: Fatigue Damage Equivalent Loads (DEL) at the tower bottom flange in fore-aft direction. The DEL at each mean wind speed account for the time each mean speed is expected to occur (higher wind speeds are less likely, hence they yield lower fatigue damage) [Article V].

7.3 MIMO Model Predictive Control

The MIMO-MPC control is based on a simplified and linearized model of the whole wind turbine, and simultaneously controls the generator torque, the blades pitch angle, and the deflection of the adaptive trailing edge flaps; the same controller thus combines both power tracking and load alleviation objectives [Article VI]. Different control configurations are obtained by varying the weights in the cost function that determine how much the control should focus on blade load alleviation, and whether the control should favor individual blade pitch or flap deflection actions. Aeroelastic simulations are performed with a mean wind speed of 18 m/s, and, once again, the results are summarized in terms of fatigue damage equivalent load (DEL) variations from the baseline reference case with the NREL standard control and no active load alleviation.

It is illustrative to plot the DEL alleviation results as function of the control activity that is required to achieve them, figure 7.6, both in terms of blade pitch variation (horizontal axis) and flap deflection (vertical axis). Pitch and flap activities, as in the LQ case, are quantified by the total angular distance traveled by the actuators, normalized by the operation time; as a term of comparison, the NREL baseline controller requires an average pitch activity of 0.3 deg/s for power tracking. The distribution of the load alleviation results, figure 7.6, confirms that to achieve higher load alleviation, higher control activity is required, either from individual blade pitch or from flaps actuators.

By using exclusively flap actions to target the load variations, the DEL are reduced by approximately 15 % (upper left corner in fig. 7.6). Higher alleviations are reported for the control configuration with only individual blade pitch actions: nearly 19 %, albeit with six times as much pitch activity as in the reference case (lower right corner in fig. 7.6). By combining instead blade pitch and flap deflection actions, the fatigue DEL can be reduced by up to 30 %. Another advantage of the combined control approach is the possibility to shift the alleviation workload between the pitch and the flap actuators, and thus have the option to control and limit the actuators wear. For instance, an average pitch activity of 1.5 deg/s would be required to reduce the DEL by 16 %; the same alleviation can be achieved with one third of the pitch

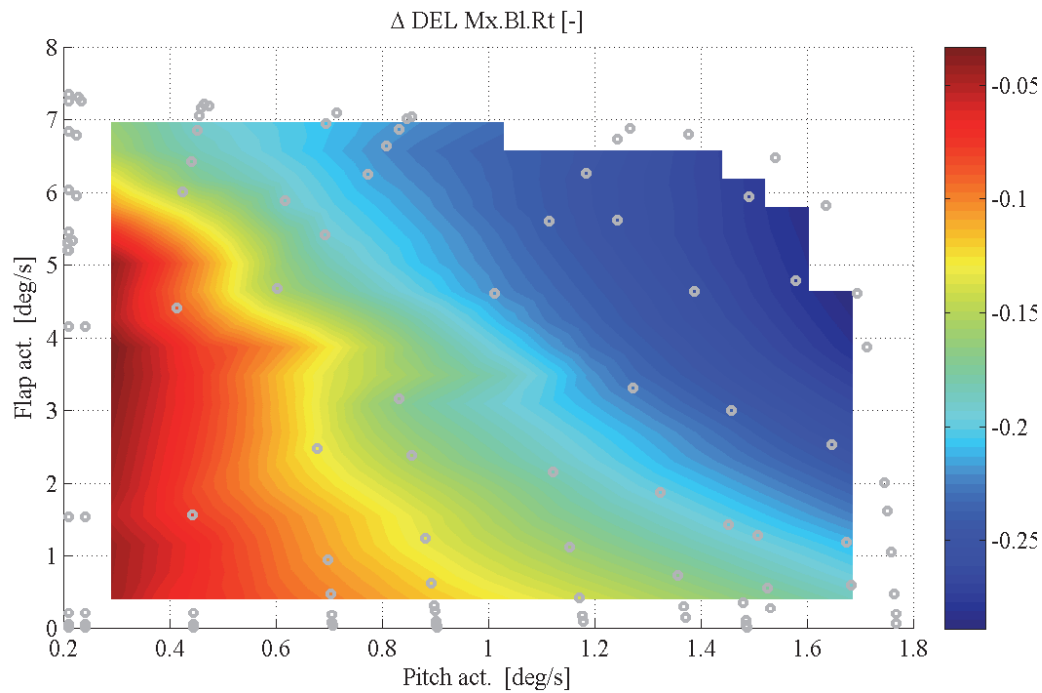


Figure 7.6: *Fatigue Damage Equivalent Loads (DEL) alleviation of the blade root flap-wise bending moment, Wöhler curve exponent of 10. The colors indicate DEL variations from the baseline NREL 5 MW turbine, and the color scale displays reductions ranging from 4 % to nearly 30 %. The load alleviation is plotted as a function of both the blade pitch actuator traveled distance (horizontal axis), and the flap actuator traveled distance (vertical axis), the baseline NREL control requires a collective pitch activity of 0.3 deg/s. Simulation data are only available for the points indicated by the gray circles.*

activity when the flap actuators take part in the task.

A direct comparison between the MIMO-MPC results and the SISO-LQ ones is made difficult by the marked differences both in the control modeling approach, and in the control algorithm formulations and objectives. Nevertheless, in the case of active load alleviation with exclusively flap deflection actions, both model based controller achieve similar DEL reductions: approximately 15 % at 18 m/s mean wind speed. The MIMO-MPC requires nearly 30 % less flap activity than in the SISO-LQ case; it would be interesting in the future to determine whether the difference is due to a more complete model of the system dynamics in the MIMO approach, or to a better man-

agement of the maximum flap deflection constraint by the MPC formulation, or a combination thereof. Another major difference between the two algorithms concerns the alleviation of loads at the tower bottom flange, figure 7.7. Tower loads were not included in the SISO-LQ model nor in its control objectives, nevertheless alleviations in the order of 5 % were reported in the fore-aft direction. On the contrary, the MIMO-MPC algorithm includes the tower dynamics in the model, considers tower top acceleration measurements, and directly targets the tower loads in the control cost function; the result is a much higher alleviation of the tower fatigue DEL: nearly 14 % with flap actuators and collective pitch, and up to 30 % with a combination of flap and individual pitch actions.

To conclude, assuming an adequate model of the system to control and sufficient computational power for real time applications are available, an ‘holistic’ control approach that considers the response of the whole turbine, collects measurements from all the available sensors, and coordinates all the available control actuators (generator, blade pitch, flap deflection) appears to give better performances than the traditional approach, where fractionated parts of the problem are dealt with by a series of independent control algorithms, each exclusively focused on its own specific task.

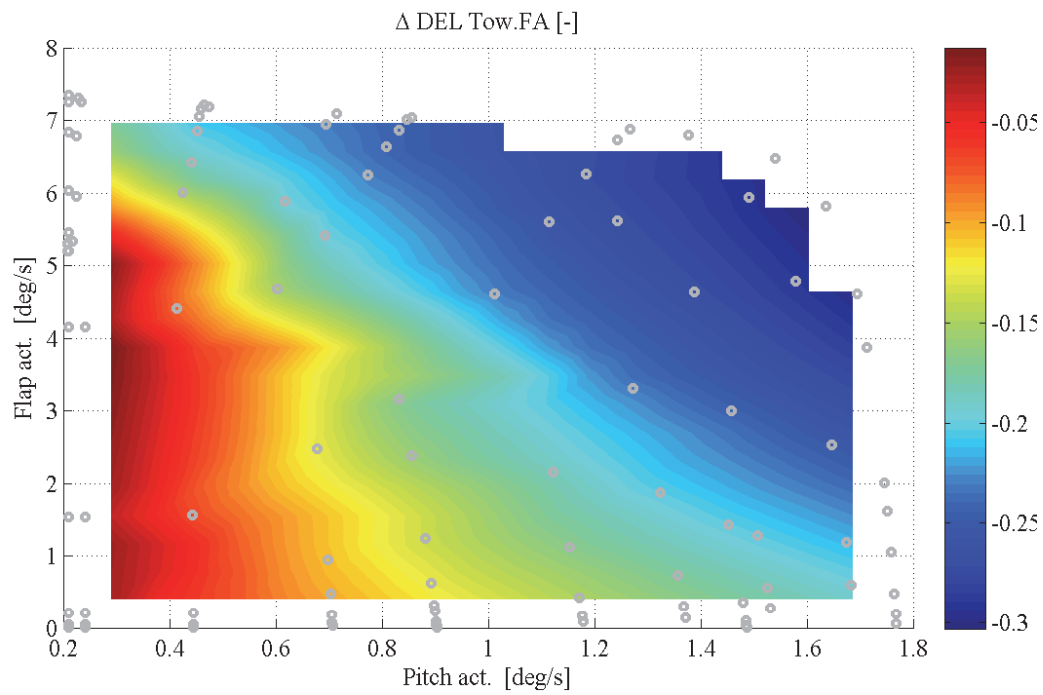


Figure 7.7: *Fatigue Damage Equivalent Loads (DEL) alleviation for the tower bottom flange fore-aft bending moment, Wöhler curve exponent of 4. The colors indicate DEL variations from the baseline NREL 5 MW turbine, and the color scale displays reductions ranging from 3 % to 30 %. Simulation data are only available for the points indicated by the gray circles.*

CHAPTER 8

Summary of findings and future work

The chapter briefly recalls the steps undertaken in the development and the analysis of the smart rotor configuration. First, the main findings from the previous chapters are summarized, accompanied by suggestions for future research work. Then, a brief discussion on the estimation of the cost of energy with a smart rotor configuration follows, and the chapter is concluded by few indications on desirable characteristics for an Adaptive Trailing Edge Flap actuator.

8.1 Aerodynamic model

A reliable aerodynamic model that accounts for the flap effects is a prerequisite for simulating and assessing the aero-servo-elastic response of a smart rotor with Adaptive Trailing Edge Flaps. A correct representation of the attached flow dynamics is necessary to avoid biased estimations of the stability limits, and of the turbine loads during normal operation. In fact, a

quasi-steady approximation of the section aerodynamics would return 5 to 20 % higher lifetime fatigue damage estimations, and nearly 25 % lower rotor flutter stability limits; a model that neglects stall separation dynamics would mainly affect the ultimate loads estimations, with biases up to 10 %.

The ATEFlap model developed in this study describes the steady and dynamic effects of angle of attack change and flap deflection on a 2D airfoil, both in attached and separated flow conditions. The attached flow part of the model uses a superposition of indicial responses to represent the dynamics of the circulatory lift component. The indicial response function for finite thickness airfoils differs from the default flat plate one, and varies depending on the airfoil geometrical characteristics. An approximate method to retrieve an indicial function that better fits the response of a finite thickness airfoil is proposed; although the indicial function variation is scarcely noticeable on the wind turbine load simulations, it does improve the aerodynamic force prediction on the 2D airfoil.

The ATEFlap model is validated against the results from computational fluid dynamics, and a viscous-inviscid interaction code. In attached flow conditions, the model reproduces very well the dynamics of the unsteady lift force, both for pitch and flap deflection variations; at higher angles of attack, the results are less accurate, but still capture the main characteristics of the dynamic lift response. The model returns correct drag and moment dynamics, with a slight over-prediction of the dynamic effects from changes in the angle of attack, and a closer match on the dynamics from flap deflection. The aerodynamic model is finally implemented in the aeroelastic code HAWC2, thus providing a tool that is able to perform time marching simulations of the aero-servo-elastic response of a wind turbine with adaptive trailing edge flaps.

The HAWC2 aerodynamic model inherits most of the limitations imposed by a BEM formulation. In particular, the model assumes independent radial sections over the blade span, thus neglecting that sharp changes of aerodynamic loads caused by the flap deflection will also affect contiguous blade sections. In future work, the importance of such effects should be assessed by comparing the BEM results against, for instance, near wake models or 3D CFD computations. Future work might also consider comparing the aerodynamic forces returned by the numerical models against measurements from

wind tunnel experiments, both in steady and dynamic conditions.

8.2 Load analysis

The load analysis on the multi-MW turbine in its baseline configuration showed that normal operational conditions are responsible for most of the lifetime fatigue damage on the rotor blades, and, in spite of occurring less frequently, operations at high wind speed cause the largest contributions to the flapwise fatigue damage. The adaptive trailing edge flaps should hence focus on alleviating the loads for the turbine in normal operation, and especially at mean wind speed above rated, as active load alleviation below rated conditions would bring only a small contribution to the blade lifetime fatigue damage reduction.

The largest contribution to the fatigue damage originates from load variations of stochastic nature, i.e. mainly related to the wind atmospheric turbulence; nevertheless, the periodic load component also yields a significant contribution, which is estimated to account for 11 % of the lifetime fatigue damage on the blade root flapwise bending moment. Henceforth, the knowledge and prediction of the periodic load variation can be exploited by the active load alleviation system to enhance the fatigue damage reduction; whereas, achieving load alleviations above the 11% threshold requires addressing also loads of stochastic nature. The analysis highlighted that load variations characterized by frequencies below 1 Hz, and, in particular, by frequencies close to the rotational one (0.2 Hz) are responsible for the largest contribution to the blade fatigue loads. It is therefore convenient to limit the activity of the load alleviation devices at higher frequencies, as the frequency limitation would reduce the use and wear of the actuators without a significant reduction of the load alleviation performance.

8.3 Smart rotor configuration and preliminary evaluation

A smart rotor configuration with Adaptive Trailing Edge Flaps covering 20 % of the blade span was proposed; the ATEF extends for 10 % of the chordwise length of the blade sections, and covers a blade surface of 2.82 m^2 , which corresponds to approximately 1.3 % of the total blade surface. The flaps are placed on the outer part of the blade, from 77 % to 97 % blade span, so to maximize the steady flapwise bending moment variation achieved by deflecting the flaps; on the other hand, the outboard placement of the flaps causes a non-minimum phase transient and a significant delay in the bending moment response observed at the root. Future work might consider solving the problem of optimizing the flap placement along the blade in a concurrent design optimization framework, as the definition of an ‘optimal’ placement of the flaps inevitably depends also on the control algorithm and on the sensors that will be used.

The response and the performance of the turbine with ATEF were analyzed with HAWC2 simulations reproducing the turbulent wind field specified by the IEC standard for a class B turbine. The HAWC2 model includes the blade torsion degree of freedom, which is of particular importance given the large aerodynamic pitching moment introduced by the flap deflection; omitting to consider the blade torsion compliance would in fact cause an overestimation of the flap effects on the blade root moment variation.

A preliminary evaluation of the smart rotor potential was performed using a cyclic control approach, which, albeit limited to ideal simulation conditions, greatly simplifies the problem of formulating a suitable control algorithm. The analysis showed that by targeting the periodic load variations the turbine fatigue damage can be reduced by nearly 9 %, and that a combination of flap and individual pitch actions gives higher alleviation potential than using either flap or pitch actuators alone. The simplified control approach was also used to investigate the possibility of enhancing the turbine power output below rated conditions. The results showed that the highest contribution to the energy increase would come from the optimization of the collective pitch angle (approximately 2 % increase of the AEP), and an ad-

ditional increase by 0.14 % could be obtained by adjusting the collective flap deflection; cyclic control actions, if correctly specified, might also lead to a further increase, which is estimated around 0.1-0.2 % of the AEP, and should be better evaluated in future work. Both the cyclic control simulations, and the steady BEM analysis highlighted that cyclic actions aiming at increasing the energy capture will inevitably augment the aerodynamic load variation on the rotor blades; vice versa, active alleviation of the blade loads below rated power would reduce the energy output of the turbine, while bringing only a marginal benefit in terms of lifetime fatigue damage reduction.

8.4 Active Load Alleviation with Adaptive Trailing Edge Flaps

The problem of defining a suitable control algorithm for active load alleviation was investigated by exploring two model based control formulations. First a simple SISO-LQ controller was considered, where the flap on each blade is controlled independently from the other blades; later, a more complex MIMO-MPC approach that accounts for the whole turbine response was tested. The linear time invariant models required by the control algorithms were formulated using system identification in one case, and first principle modeling in the other. Both modeling approaches provided good descriptions of the relevant dynamics of the systems of interest, and proved adequate to their control scopes. It should be mentioned though that system identification was applied to a relatively simple SISO problem, and the MIMO first principles modeling benefited from the availability of accurate data to describe the controlled turbine. In less favorable conditions it might be convenient to try a combined ‘grey box’ approach, where system identification techniques are applied to refine and tune a model first sketched from physical principles. Furthermore, future work should also consider a model formulation suitable for operation at variable mean wind speeds or with variable wind shear, for instance by using linear parameter variation formulations, or adaptive control approaches.

By performing aero-servo-elastic simulations of the smart rotor configuration

with flaps controlled by the two algorithms it is observed that:

- Using Adaptive Trailing Edge Flap actuators and blade root bending moment sensors, both control algorithms reduce the lifetime fatigue damage equivalent load at the blade root flapwise bending moment by nearly 15 %, a result in line with previous studies that considered a similar setup [5].
- It is beneficial to account for the periodic load variations occurring on the rotating blades, either by means of periodic disturbance terms (SISO-LQ formulation), or with multi-blade coordinate transformation (MIMO-MPC formulation). The analysis performed in the SISO-LQ case showed that including periodic disturbance anticipation in the control algorithm accounts for nearly 4 % of the lifetime DEL alleviation. The figure is close to the increase of the load alleviation potential that previous investigations have attained by using additional in-flow sensors [11]; periodic load anticipation has furthermore the advantage of requiring only measurements of the blade azimuthal position, which can be achieved with a much simpler and robust sensor setup than required for in-flow measurements.
- Frequency weighting of the control action further penalizes the flap activity in the high frequency range, thus providing an efficient method to limit the overall flap usage and actuator wear, with only a minor reduction of the load alleviation potential.
- The load alleviation potential achieved by the Adaptive Trailing Edge Flap rotor configuration appears to be mainly constrained by the limited strength of the flap setup, rather than by the ‘brainpower’ of the control algorithm. In fact, the variation of the blade root flapwise bending moment achieved by deflecting completely the flaps is simply too small to compensate to an higher degree for the bending moment variations encountered during normal operation. A solution to obtain more actuation power is proposed by the MIMO-MPC combined control approach, which pursues the load alleviation objective using both the flaps and the blade pitch actuators; the load alleviation potential is thus increased to 30 % of the blade flapwise lifetime DEL.

- The reduction of the loads on the blade root flapwise bending moment and on the tower is accompanied by an increase of other loads on the structure, most notably, the blade torsion fatigue damage rises by nearly 10 % at the blade root. To determine the impact of active load alleviation on the overall structural requirements, future work should also include an exhaustive analysis of the turbine structure, so to better identify which loads drive the design requirements. In this sense, it is important to evaluate the response of a smart rotor also during ultimate load events, and to include plausible scenarios of flap actuator failures, as design-driving loads might result from such events.

A comparison of the active load alleviation obtained with the two control algorithms appears in favor of the MIMO-MPC combined control approach, which presented some advantages over the simpler SISO-LQ formulation:

- By combining both adaptive trailing edge flaps and individual blade pitch actuators, the MIMO-MPC algorithm can achieve higher blade fatigue load reductions (up to 30 %).
- The flap activity required by the MIMO-MPC algorithm is approximately 35 % lower than demanded by the SISO-LQ controller. In the future, it would be interesting to investigate whether the difference is due to a better model formulation, or to a better management of the flap deflection constraints in the MIMO-MPC case.
- The MIMO-MPC combined approach allows to control the distribution of the workload between flaps and individual blade pitch, thus potentially increasing the lifetime of the actuators. Eventually, in combination with an actuator wear monitoring system, the workload distribution could be employed to regulate each actuator usage in order to limit the need for non-scheduled maintenance interventions.
- The MIMO model provides a description of the entire wind turbine, thus allowing the control algorithm cost function to encompass different objectives, and to manage load reduction at different locations on the structure. An example is given by the loads at the tower fore-aft bending moment: the SISO-LQ control does not target tower loads,

but still reports load reductions close to 5 % of the lifetime fatigue DEL. Instead, the MIMO-MPC algorithm, which explicitly includes the tower load in the control formulation, reduces the tower fore-aft lifetime DEL by 15 % (a reduction of 30 % is reached using both flap and pitch actions).

8.5 Cost of Energy estimation

The ultimate goal of developing smart rotors with active load alleviation solutions is to reduce the cost of energy produced by the wind turbine; however, whether the reduction of loads and of structural requirements achieved with the ATEF is sufficient to guarantee a lower cost of energy still remains an open question. Berg et al. [14, 15] attempted an answer by estimating the increase of rotor size that active load alleviation would allow; the approach, known as *Grow-The-Rotor (GTR)*, implies that rotor blades where the loads are reduced by active alleviation are elongated until the blade flapwise damage equivalent load matches the damage reported on the original blade without active load control. The increase in rotor size yields an increase of the turbine Annual Energy Production (AEP), hence, together with an estimate of the cost of the adaptive flap system, the approach allows for an evaluation of the cost of energy produced with the smart rotor configuration. For a 1.5 MW turbine, Berg et al. [15] report a blade flapwise fatigue damage load reduction of 26 %, which they evaluate would permit a 10 % increase of the rotor size, hence an AEP increase from 10 % to 14 %; they thus estimate a reduction of the cost of energy ranging between 5 % and 8 %, depending on the mean wind speed at the site.

Baek [5] applies a similar approach to a model of the NREL 5 MW turbine equipped with adaptive trailing edge flaps. He estimates that a 15 % reduction of the blade flapwise fatigue damage allows to increase the rotor size by 8 % until the flapwise fatigue damage of the baseline turbine is matched, but he also warns that other loads would exceed the original design envelope already with a 2 % increase of the blade size. The increase in AEP estimated by Baek is more modest: 5 % with 8 % increase of the rotor size, and 1.5 % if only a 2 % size increase is allowed.

In this work, the load alleviation achieved with exclusively ATEF actions is close to Baek's one, therefore similar AEP figures should be expected. Higher blade fatigue load alleviations (up to 30 %) are reported in the case of combined ATEF and individual blade pitch control actions, thus justifying higher expectations for the AEP increase; however, the expectations will need to be verified and quantified in future investigations monitoring the complete load design envelope. In addition, in order to estimate the impact of the ATEF on the cost of energy, future investigations will also require rather accurate estimations of the increase of installation and operational costs necessary for multi-MW smart rotor configurations.

8.6 Indications on flap actuator requirements

The practical realization of reliable Adaptive Trailing Edge Flap actuators represents a major challenge to the implementation of ATEF systems on actual turbine rotors. The problem is not addressed in the present work, nevertheless, the results from the aero-servo-elastic analysis and from previous stability investigations [16] can provide some indications of desirable aerodynamic and structural characteristics of the actuators:

- By comparing the blade root flapwise bending moment variation achieved by deflecting the flaps to the moment variation caused by the disturbances in the wind field, it is concluded that a flap actuator setup returning higher lift variations would be desirable. If the blade structure and the cost-gain balance allow, flap actuators extending more than 10 % of the profile chord might help to achieve larger lift variations.
- The wind turbine sections with ATEF operate at small angles of attack. The primary objective for the aerodynamic design of the flap actuators should hence be to achieve large lift variations in attached flow conditions. Lift variations from flap deflection at higher angles of attack are not as important.
- As the airfoil sections with flap operate at small angles of attack, and flap control for active load alleviation is mainly implemented above

rated conditions, obtaining a low drag penalty from flap deflection appears less important than achieving high lift variations.

- Due to the torsion compliance of the outboard part of the turbine blades, the aerodynamic moment variation introduced by the flap modifies the airfoil angle of attack in a way that counteracts the flap lift variation. If possible, the installation of ATEF actuators should not reduce the blade torsional stiffness.
- The flap actuators should be as light as possible to limit the weight increase in the outer span of the blade and thus the gravity loading. Furthermore, the weight added at the trailing edge should be low in order to keep the location of the center of gravity as fore as possible, and thus limit blade flutter stability problems [16]. It might be worth to consider actuator solutions where the flap is moved by means of rods and the heavy part of the machinery is kept close to the blade elastic axis.
- The ATEF should be sufficiently stiff not to deflect excessively under the actions of the inertial forces or the aerodynamic pressure difference. The flap should be able to maintain sufficient stiffness also in case of failures in the actuator system, otherwise the rotor flutter limit might be critically reduced [16]. The danger of failures resulting in stiffness loss is probably higher for flaps relying on pneumatic actuation systems.
- As the flap is located at the profile trailing edge, the work required to deflect against the aerodynamic pressure difference is estimated to be rather low, approximately $2.48 J/(\text{deg } m^2)$ for a flap placed at the aft 10 % portion of the airfoil chord length.
- The flap deflection speed requirements also appear rather modest. Due to the frequency weighted control algorithms limiting the high frequency flap activity, a maximum deflection rate of $90 \text{ deg}/s$ is adequate to cope with the activity demanded by the LQ control; even lower maximum deflection rates are reported with the MPC algorithm ($50 \text{ deg}/s$).
- The biggest challenge to the flap actuators probably comes from the large amount of duty cycles they should endure. In the simulated cases,

the traveled distance each flap has to cover amounts to nearly 43 thousand degrees for each hour of operation with the LQ controller, and approximately 35 % less with the MPC algorithm (28 kdeg /hr).

The guidelines are derived for the specific flap and turbine rotor configuration considered in this study; further investigations would be hence required prior to confirm the findings and eventually generalize them to other smart rotor configurations.

Conclusion

The study presented the development of a smart rotor configuration with Adaptive Trailing Edge Flaps (ATEF) for active load alleviation. The smart rotor performance is evaluated by means of simulations with the aero-servo-elastic code HAWC2, reproducing the wind field conditions specified by the IEC standard. The ATEFlap aerodynamic model is implemented in the simulation code to account for the steady and dynamic effects of the flap deflection on the aerodynamic forces and pitching moment of 2D airfoil sections; a good agreement between the model and computational fluid dynamic simulations is reported both in attached and separated flow conditions.

The smart rotor considered in the present work features ATEF on the outer 20 % of the blade span, and is controlled by load alleviation algorithms that mainly aim at reducing the blade root flapwise fatigue damage. Two model based control algorithms are proposed: a simple Single Input-Single Output Linear Quadratic (SISO-LQ) controller, and a combined Multiple Input-Multiple Output Model Predictive Control (MIMO-MPC). The SISO-LQ algorithm treats each blade as an independent system, and controls the ATEF based on measurements of the blade azimuthal position and of the blade root flapwise bending moment. The MIMO-MPC pursues both power control and

load alleviation objectives, it controls all the flaps, the blade pitch actuators, and the generator torque; in addition to the blades azimuthal positions and the root bending moments, the controller also employs measurements of the tower top acceleration and of the drive-train rotational speed.

The aero-servo-elastic analysis of the smart rotor, performed considering different control configurations, leads to the following conclusions:

- Active alleviation of the blade loads should focus on operational conditions above rated wind speed. In fact, the largest contributions to the lifetime fatigue loads arise during operation above rated conditions, moreover, active alleviation below rated wind speed would decrease the turbine energy output. Below rated conditions, the smart rotor configuration could be instead exploited to increase the energy production.
- The load alleviation algorithms should primarily target blade loads in the low frequency range (below 1 Hz), which are responsible for the highest contribution to the blade root fatigue damage. Control actions in the high frequency range can be hence avoided by proper frequency weighting, thus effectively limiting actuator wear and usage.
- The load alleviation algorithms benefit from the knowledge of the periodic variations of the aerodynamic loads on the rotating blade. Such knowledge is used to formulate control actions that anticipate part of the load variation, and thus achieve higher fatigue damage reduction.
- By using the ATEF the blade root flapwise lifetime fatigue damage equivalent load is reduced by 15 %. The alleviation potential seems to be mainly limited by the small aerodynamic force variation that is achieved by the investigated ATEF setup. In fact, by increasing the available actuation power with a combination of ATEF and individual pitch control actions the blade flapwise damage equivalent load is reduced by up to 30 %.
- The combined MIMO-MPC control approach presents several advantages over the simple SISO-LQ controller: higher overall blade load alleviation potential by combining ATEF and individual blade pitch, higher alleviation of tower loads (15 % with ATEF, 30 % with ATEF

and individual pitch), possibility to distribute the alleviation workload between pitch and flap actuators, and lower flap activity compared to the SISO-LQ control.

- The investigation highlights that a comprehensive control algorithm that receives information from all the available sensors and centrally coordinates all the available actuators is likely to achieve better overall performances than a traditional control approach, where multiple control systems work independently, each pursuing its own individual objectives. Nevertheless, some prerequisites are necessary for an effective centralized control approach: a sufficiently detailed and accurate model of the system to control, enough computational power for on-line applications, and properly formulated controller objectives and cost function.
- The load alleviation potential can be converted to an increase of Annual Energy Production (AEP) by using the Grow-The-Rotor approach indicated by Berg et al. [15]. However, the estimation of the AEP increase is still uncertain, and, based on the results from Berg et al. [15] and Baek [5], it might range from 1.5 % to 14 %. The estimation depends not only on the fatigue damage reduction achieved, but also on assumptions on which loads drive the rotor design requirements. In fact, while reducing the lifetime fatigue damage at the blade root in the flapwise direction and at the tower bottom, the active load control has no effect or even increases the loads on other parts of the structure, most notably, on the blade torsional moment. An accurate estimation of the rotor growth allowed by active load alleviation would hence require a detailed structural analysis, so to identify and monitor the loads that drive the design requirements.

To conclude, it is indeed not an easy task to determine whether smart rotor solutions with adaptive trailing edge flaps will allow for larger, more powerful, and more profitable wind turbines. The task involves bringing together expertise from different disciplines and combining them with an ‘holistic’ design approach. Retrofitting a pre-existing wind turbine model by adding sensors and actuators, as in this work, is a useful exercise to develop analysis tools, and to grasp a first indication of the smart rotor potential. However, a fair and comprehensive evaluation of the overall performance of smart rotor

solutions should be based on a different approach, where the turbine design process accounts for the availability of active control devices since its earliest stages. A new concurrent design approach would be hence required in order to integrate and simultaneously optimize all the structural, aerodynamic, and control variables of the problem. Such a design task might be not feasible, certainly not trivial, but undeniably very fascinating.

Acknowledgments

The PhD study was partly funded by the project *Development of Adaptive Trailing Edge Flap (ATEF) System for Wind Turbines* by the Danish Advanced Technology Foundation, Advanced Technology Projects 2007.

Throughout the study I was followed by a superlative team of supervisors: Mac, Niels, and Thomas; thank you for your patience and for being always available for the uncountable questions, doubts, and problems I have been coming up with. Especially, thank you Mac for your continuous support and guidance throughout the project, for your unconditional positive attitude, and for sharing your passion for research.

Special thanks also to the whole AED group, for their help, and for a splendid working environment. In particular, thanks to Lars for helping me in the esoteric control world, and to Torben for the HAWC2 support. I would also like to acknowledge all the flap-boys: Peter B.A., Thanasis, Peter B., and Damien; thank you for clearing the path I have been taking from not a few thorns, and for many pleasant and interesting discussions, not only limited to flaps.

Talking about unlimited discussions, I should acknowledge some persons I am very glad I have been spending in the last years most of the time with, my great office-mates (in clock-wise order): Joachim, Carlo, Sri, David, Witold, Ivan, Tilman, and Knud. Thank you for many cheerful moments, for the

questions answered, and for the ones left open, thank you for the numerous discussions on technical subjects, and on the meanings of life; the latter topic often investigated thoroughly in connection with the national brewed amber-colored beverage.

I would also like to acknowledge all those who are maybe not so much into the thesis topic, and nonetheless had a very important role in rendering these PhD years a memorable time. It would be rather lengthy to list every name, luckily, there is a word that comprises them all: friends. Some of them have been near for some years now, others for less time, others are geographically more distant but never far away; sometimes we share the same passion for travels, for white slopes, for towering peaks, or for boundless seas, but also for dinners, for animated discussions, or for eternal we-just-go-for-a-quick-beer/coffee. Thank you all for many great moments and smiles! Particular thanks to the Poppelgade and Ahornsgade people for, eh well, you know, for being the way you are!

To conclude, many thanks to two very important ladies: my mamma Stefania, and my sister Giulia. Thank you for sharing your happiness whenever I am around, and for trying to hide away your sadness whenever I leave again. Thank you for all the things you have been teaching me, and for the ones you are still trying to teach.

A big hug to everybody,
Leonardo
Roskilde, March 2013.

Bibliography

- [1] P. B. Andersen, M. Gaunaa, C. Bak, and M. H. Hansen. A dynamic stall model for airfoils with deformable trailing edges. *Wind Energy*, 12(8):734–751, 2009.
- [2] P. B. Andersen, L. Henriksen, M. Gaunaa, C. Bak, and T. Buhl. Deformable trailing edge flaps for modern megawatt wind turbine controllers using strain gauge sensors. *Wind Energy*, 13(2-3):193–206, March 2010.
- [3] P. B. Andersen, L. C. Henriksen, M. Gaunaa, C. Bak, and T. Buhl. Integrating deformable trailing edge geometry in modern mega-watt wind turbine controllers. In *Scientific proceedings. 2008 European Wind Energy Conference and Exhibition, Brussels (BE)*, pages 15–21, 2008.
- [4] Peter B. Andersen. *Advanced load alleviation for wind turbines using adaptive trailing edge flaps: sensing and control*. Ph.D. thesis, Risoe National Laboratory for Sustainable Energy, Technical University of Denmark, Roskilde, Denmark, 2009.
- [5] Peter Baek. *Unsteady Flow Modeling and Experimental Verification of Active Flow Control Concepts for Wind Turbine Blades*. Ph.D. thesis, Technical University of Denmark, Department of Wind Energy, Roskilde, Denmark, December 2011.

-
- [6] C. Bak, M. Gaunaa, P. B. Andersen, T. Buhl, P. Hansen, and K. Clemmensen. Wind tunnel test on airfoil risø-b1-18 with an active trailing edge flap. *Wind Energy*, 13(2-3):207–219, 2010.
- [7] T. Barlas, F. Zahle, N. N. Sorensen, M. Gaunaa, and L. Bergami. Simulations of a rotor with active deformable trailing edge flaps in half-wake inflow: comparison of ellipsys 3D with HAWC2. In *European Wind Energy Conference & Exhibition, Copenhagen, Denmark*, Copenhagen, Denmark, April 2012.
- [8] T. K. Barlas and G. A. M. Van Kuik. Aeroelastic modelling and comparison of advanced active flap control concepts for load reduction on the upwind 5MW wind turbine. In *European Wind Energy Conference, Marseille, France*, pages 16–19, 2009.
- [9] T. K. Barlas and G. A.M. van Kuik. State of the art and prospectives of smart rotor control for wind turbines. *Journal of Physics: Conference Series*, 75(1):012080 (20 pp.), 2007.
- [10] Thanasis Barlas. *Active aerodynamic load control on wind turbines: Aeroservoelastic modeling and wind tunnel*. Ph.D. thesis, TU Delft: Aerospace Engineering: Wind Energy, Delft, Netherlands, October 2011.
- [11] T.K. Barlas, G.J. van der Veen, and G.A.M. van Kuik. Model predictive control for wind turbines with distributed active flaps: incorporating inflow signals and actuator constraints. *Wind Energy*, Early view(published on-line), 2011.
- [12] T.K. Barlas, W. van Wingerden, A.W. Hulskamp, G.A. M. van Kuik, and H.E.N. Bersee. Smart dynamic rotor control using active flaps on a small-scale wind turbine: aeroelastic modeling and comparison with wind tunnel measurements. *Wind Energy*, Early View(published on-line), 2012.
- [13] D. Berg, D. Wilson, B. Resor, J. Berg, T. Barlas, A. Crowther, C. Halse, and R. House. System ID modern control algorithms for active aerodynamic load control and impact on gearbox loading. In *Proceedings of the Conference on the Science of Making Torque from Wind*, 2010.

-
- [14] D.E. Berg, D.G. Wilson, M.F. Barone, JC Berg, BR Resor, J.A. Paquette, and J.R. Zayas. The impact of active aerodynamic load control on fatigue and energy capture at low wind speed sites. In *European Wind Energy Association, Marseille, France*, page 16–19, 2009.
- [15] D.E. Berg, D.G. Wilson, B.R. Resor, M.F. Barone, J.C. Berg, S. Kota, and G. Ervin. Active aerodynamic blade load control impacts on utility-scale wind turbines. In *Proceedings of WindPower Conference & Exhibition*, 2009.
- [16] L. Bergami and M. Gaunaa. Stability investigation of an airfoil section with active flap control. *Wind Energy*, 13(2-3):151–166, 2010.
- [17] G. Bir. Multiblade coordinate transformation and its application to wind turbine analysis. In *Proc. AIAA/ASME Wind Energy Symp*, Reno, Nevada, January 2008.
- [18] E. Bossanyi, B. Savini, M. Iribas, M. Hau, B. Fischer, D. Schlipf, T. Engelen, M. Rossetti, and C. E Carcangiu. Advanced controller research for multi-MW wind turbines in the UPWIND project. *Wind Energy*, 15(1):119–145, January 2012.
- [19] E. A. Bossanyi. Individual blade pitch control for load reduction. *Wind Energy*, 6(2):119–128, 2003.
- [20] C. Bottasso, F. Campagnolo, A. Croce, and C. Tibaldi. Optimization-based study of bend-twist coupled rotor blades for passive and integrated passive/active load alleviation. *Wind Energy*, Early View(published online), 2012.
- [21] T. Buhl, M. Gaunaa, and C. Bak. Potential load reduction using airfoils with variable trailing edge geometry. *Transactions of the ASME. Journal of Solar Energy Engineering*, 127(4):503–516, 2005.
- [22] D. Castaignet, T. Buhl, N. K. Poulsen, and J. J. Wedel-Heinen. Trailing edge flaps impact on fatigue and extreme loads in power production. In *Proceedings of the European Wind Energy Conference & Exhibition*, Brussel (BE), March 2011.
- [23] D. Castaignet, N. K. Poulsen, T. Buhl, and J. J. Wedel-Heinen. Model predictive control of trailing edge flaps on a wind turbine blade. In

- Proceedings of the American Control Conference 2011*, San Francisco, CA, USA, June 2011.
- [24] D. Castaignet, J. J. Wedel-Heinen, T. Kim, T. Buhl, and N. K. Poulsen. Results from the first full scale wind turbine equipped with trailing edge flaps. In *Proceedings of 28th AIAA Applied Aerodynamics Conference*, Chicago, IL (US), June 2010. American Institute of Aeronautics and Astronautics.
- [25] Damien Castaignet. *Model predictive control of trailing edge flaps on a wind turbine blade*. Ph.D. thesis, Technical University of Denmark, Department of Wind Energy, Roskilde, Denmark, November 2011.
- [26] International Electrotechnical Commission. IEC 61400-1: Wind turbines part 1: Design requirements. Technical report, International Electrotechnical Commission, 2005.
- [27] M. Gaunaa. Unsteady two-dimensional potential-flow model for thin variable geometry airfoils. *Wind Energy*, 13(2-3):167–192, 2010.
- [28] M. H. Hansen, M. Gaunaa, and H. A. Madsen. A beddoes-leishman type dynamic stall model in state-space and indicial formulations. Technical Report R-1354(EN), Risoe National Laboratory, Roskilde (DK), 2004.
- [29] Martin Hansen. *Aerodynamics of wind turbines : rotors, loads and structure*. James & James Ltd, London, 2000.
- [30] J. Heinz, N. N. Sørensen, and F. Zahle. Investigation of the load reduction potential of two trailing edge flap controls using CFD. *Wind Energy*, 14(3):449–462, 2011.
- [31] L. C. Henriksen, M. H. Hansen, and N. K. Poulsen. Beyond the CP-curve in model-based control of wind turbines. In *Conference proceedings, European Wind Energy Conference 2012, Copenhagen, Denmark*, Copenhagen, Den, April 2012.
- [32] I. Houtzager, J. W. van Wingerden, and M. Verhaegen. Wind turbine load reduction by rejecting the periodic load disturbances. *Wind Energy*, Early View(published on-line), May 2012.

-
- [33] S. J. Johnson, J. P. Baker, C. P. van Dam, and D. Berg. An overview of active load control techniques for wind turbines with an emphasis on microtabs. *Wind Energy*, 13(2-3):239–253, March 2010.
- [34] J. Jonkman, S. Butterfield, W. Musial, and G. Scott. Definition of a 5-MW reference wind turbine for offshore system development. Technical Report NREL/TP-500-38060, National Renewable Energy Laboratory (NREL), February 2009.
- [35] J. Jonkman and W. Musial. Offshore code comparison collaboration (OC3) for IEA task 23 offshore wind technology and deployment. Technical Report NREL/TP-5000-48191, National Renewable Energy Laboratory (NREL), Golden, CO (US), December 2010.
- [36] M. A. Lackner and G. van Kuik. A comparison of smart rotor control approaches using trailing edge flaps and individual pitch control. *Wind Energy*, 13(2-3):117–134, March 2010.
- [37] M. A. Lackner and G. A. M. van Kuik. The performance of wind turbine smart rotor control approaches during extreme loads. *Journal of Solar Energy Engineering*, 132(1):011008, 2010.
- [38] T. J Larsen and T. D Hanson. A method to avoid negative damped low frequent tower vibrations for a floating, pitch controlled wind turbine. In *Journal of Physics: Conference Series*, volume 75, page 012073, 2007.
- [39] T. J. Larsen, H. A. Madsen, and K. Thomsen. Active load reduction using individual pitch, based on local blade flow measurements. *Wind Energy*, 8(1):67–80, 2005.
- [40] F. L. Lewis, D. Vrabie, and V. L. Syrmos. *Optimal control*. Wiley, 2012.
- [41] Lennart Ljung. *System identification: theory for the user*. PTR Prentice-Hall, Upper Saddle River (NJ), 1999.
- [42] H. A. Madsen, V. Riziotis, F. Zahle, M. O.L Hansen, H. Snel, F. Grasso, T. J Larsen, E. Politis, and F. Rasmussen. Blade element momentum modeling of inflow with shear in comparison with advanced model results. *Wind Energy*, Early View(published on-line), May 2011.

-
- [43] J. Mann. Wind field simulation. *Probabilistic Engineering Mechanics*, 13(4):269–282, October 1998.
- [44] D. T. Y. Nakafuji, C. P. van Dam, R. L. Smith, and S. D. Collins. Active load control for airfoils using microtabs. *Transactions of the ASME. Journal of Solar Energy Engineering*, 123(4):282–289, 2001.
- [45] B. F. Ng, R. Palacios, J. M. R. Graham, and E. C. Kerrigan. Robust control synthesis for gust load alleviation from large aeroelastic models with relaxation of spatial discretization. In *Conference proceedings, European Wind Energy Conference 2012*, Copenhagen, Denmark, April 2012.
- [46] J. Paquette and P. S. Veers. Increased rotor size through passive load control and weight reduction concepts. In *Proceedings of European Wind Energy Conference & Exhibition*, Marseille, France, March 2009. Sandia National Laboratories.
- [47] P. Passon, M. Kühn, S. Butterfield, J. Jonkman, T. Camp, and T. J. Larsen. OC3-Benchmark exercise of aero-elastic offshore wind turbine codes. *Journal of Physics: Conference Series*, 75:012071, July 2007.
- [48] W. Popko, F. Vorpahl, A. Zuga, M. Kohlmeier, J. Jonkman, A. Robertson, T. J. Larsen, A. Yde, K. Saetertro, and K. M. Okstad. Offshore code comparison collaboration continuation (OC4), phase i-results of coupled simulations of an offshore wind turbine with jacket support structure. Technical Report NREL/CP-5000-54124, National Renewable Energy Laboratory (NREL), Golden, CO., Golden, CO (US), March 2012.
- [49] Nestor Ramos Garcia. *Quasi-3d aerodynamic code for analyzing dynamic flap response*. Ph.D. thesis, Technical University of Denmark, Department of Mechanical Engineering, Lyngby, Denmark, April 2011.
- [50] B. Resor, D. Wilson, D. Berg, J. Berg, T. Barlas, J. W. van Wingerden, and G. A. M. van Kuik. Impact of higher fidelity models on simulation of active aerodynamic load control for fatigue damage reduction. In *Proceedings of the 48th AIAA/ASME*, Orlando, FL, 2010.
- [51] V. A. Riziotis, H. A. Madsen, F. Rasmussen, E. Politis, and Spyros G. Voutsinas. Implications on loads by up-scaling towards 20 MW size. In

- Proceedings of European Wind Energy Conference*, Copenhagen, Denmark, April 2012.
- [52] V. A. Riziotis and S. G. Voutsinas. Aero-elastic modelling of the active flap concept for load control. In *Conference proceedings, European Wind Energy Conference 2008, Marseille, France, 2008*.
- [53] V. A. Riziotis and S. G. Voutsinas. Aeroelastic modeling of the active flap concept for load control. In *Scientific proceedings. 2008 European Wind Energy Conference and Exhibition, Brussels (BE)*, pages 22–26, 2008.
- [54] A.A. Shabana. Flexible multibody dynamics: review of past and recent developments. *Multibody system dynamics*, 1(2):189–222, 1997.
- [55] G. Sieros, P. Chaviaropoulos, J. D. Sørensen, B. H. Bulder, and P. Jamieson. Upscaling wind turbines: theoretical and practical aspects and their impact on the cost of energy. *Wind Energy*, 15(1):3–17, 2012.
- [56] N. Troldborg. Computational study of the Riso-B1-18 airfoil with a hinged flap providing variable trailing edge geometry. *Wind Engineering*, 29(2):89–113, 2005.
- [57] C. P. van Dam, R. Chow, J. R. Zayas, and D. E. Berg. Computational investigations of small deploying tabs and flaps for aerodynamic load control. *Journal of Physics: Conference Series*, 75(1):012027–1–10, 2007.
- [58] G.J. van der Veen, J.W. van Wingerden, and M. Verhaegen. Closed-loop system identification of wind turbines in the presence of periodic effects. In *Proc. of the 3rd conference, The Science of Making Torque from Wind*, Eraklion, Crete, Greece, June 2010.
- [59] J. W. van Wingerden, A. W. Hulskamp, T. Barlas, B. Marrant, G. A. M. van Kuik, D. P. Molenaar, and M. Verhaegen. On the proof of concept of a 'Smart' wind turbine rotor blade for load alleviation. *Wind Energy*, 11(3):265–280, 2008.
- [60] J.W. van Wingerden, A. Hulskamp, T. Barlas, I. Houtzager, H. Bersee, G.A.M. van Kuik, and M. Verhaegen. Smart dynamic rotor control:

- Part 3, advanced controller design. In *Proc. of the 3rd conference, The Science of Making Torque from Wind*, pages 702–708, Iraklion, Crete, Greece, June 2010.
- [61] VV. AA. UpWind, design limits and solutions for very large wind turbines. Technical report, European Wind Energy Association, March 2011.
- [62] D.G. Wilson, B.R. Resor, D.E. Berg, T.K. Barlas, and G.A.M. van Kuik. Active aerodynamic blade distributed flap control design procedure for load reduction on the UpWind 5MW wind turbine. In *Proceedings of the 48th AIAA Aerospace Sciences Meeting*, pages 4–7, 2010.

Part II

Articles and reports

Article I

Indicial lift response function: an empirical relation for finite-thickness airfoils, and effects on aeroelastic simulations

The article was published in *Wind Energy*, 16(5): 681-693, July 2013 (first published on-line in June 2012). The Ph.D. dissertation that is made publicly available contains the article version prior to the minor revisions indicated during the peer-review process, so to conform with the journal copyright requirements.

The content of the article is recalled in the synopsis sections related to:

- *Load Analysis*, section 3.3: sensitivity of the simulated loads to changes in the aerodynamic model.
- *ATEFlap Aerodynamic Model*, section 4.1: attached flow dynamics, indicial response function accounting for the airfoil thickness.

RESEARCH ARTICLE

Indicial lift response function: an empirical relation for finite-thickness airfoils, and effects on aeroelastic simulations

Leonardo Bergami¹, Mac Gaunaa¹ and Joachim Heinz¹

¹Risø National Laboratory for Sustainable Energies - Technical University of Denmark, Roskilde, 4000 Denmark

ABSTRACT

The aeroelastic response of wind turbines is often simulated in the time domain using indicial response techniques. Unsteady aerodynamics in attached flow are usually based on Jones's approximation of the flat plate indicial response, although the response for finite-thickness airfoils differs from the flat plate one.

The indicial lift response of finite-thickness airfoils is simulated with a panel code, and an empirical relation is outlined connecting the airfoil indicial response to its geometric characteristics. The effects of different indicial approximations are evaluated on a 2D profile undergoing harmonic pitching motion in the attached flow region; the resulting lift forces are compared to CFD simulations. The relevance for aeroelastic simulations of a full wind turbine is also evaluated, and the effects are quantified in terms of variations of equivalent fatigue loads, ultimate loads, and stability limits.

The agreement with CFD computations of a 2D profile in harmonic motion is improved by the indicial function accounting for the finite-thickness of the airfoil. Concerning the full wind turbine aeroelastic behavior, the differences between simulations based on Jones's and finite-thickness indicial response functions are rather small; Jones's flat-plate approximation results in only slightly larger fatigue and ultimate loads, and lower stability limits.

Copyright © 2012 John Wiley & Sons, Ltd.

KEYWORDS

Indicial Lift Response Function; Jones's Flat Plate Approximation; Unsteady Lift in Attached flow

Correspondence

Wind Energy Division - VEA 118, Risø DTU, Roskilde, 4000 Denmark. E-mail: leob@risoe.dtu.dk

Received . . .

1. INTRODUCTION

Aeroelastic simulation tools require aerodynamic models accounting for unsteady aerodynamic effects. The aerodynamic model should be computationally light, as to limit the resources required in time marching simulations, but, at the same time, complex enough to predict with sufficient accuracy the aerodynamic loads arising on the blade, both in attached and separated (stalled) flow conditions.

A large contribution to the total aerodynamic loading is generated on the outer sections of the blades, which, in modern wind turbines, operate most of the time in attached flow conditions. Unsteady aerodynamic forces in attached flow are frequently described in the time domain using indicial formulations, as described by Beddoes [1] and Leishman [2]. Wind turbine simulation tools based on this approach include, among others, the aeroelastic code HAWC2[3, 4], Bladed [5], and FAST[6, 7].

The unsteady lift force in attached flow is described, following Theodorsen's theory [8], as the sum of two contributions: a non-circulatory and a circulatory one. The non-circulatory lift, or added mass term, represents the lift force that would arise on the airfoil in a non-circulatory flow due to the reaction of the fluid accelerated with the airfoil motion; the non-circulatory term has no dependency on time, and only depends on the instantaneous acceleration of the fluid around the airfoil. The circulatory lift, on the contrary, carries a memory effect, which originates from the vorticity shed into the

wake to compensate the change of circulation around the airfoil, as governed by Kelvin's theorem on the constancy of 2D vorticity [9].

The circulatory lift for an airfoil undergoing arbitrary motion is computed in the time domain applying Duhamel's superposition integral of indicial step responses [9]:

$$L_c = 2\pi\rho Ub \left[w_{3/4}(0) \cdot \Phi(\tau) + \int_0^\tau \frac{dw_{3/4}}{d\sigma} \Phi(\tau - \sigma) d\sigma \right]. \quad (1)$$

Where, b is the half-chord length, $w_{3/4}$ is the downwash at the three-quarters chord, and the dimensionless variable τ expresses the time dependency, as the distance in half-chords traveled by the airfoil:

$$\tau = \frac{Ut}{b}. \quad (2)$$

The indicial response function $\Phi(\tau)$ represents the ratio between the actual unsteady circulatory lift, and the corresponding steady value, following a unit step change in the quasi-steady loading. Wagner[9] determines the indicial response for a flat plate in incompressible flow as a function that tends asymptotically to unit, and starts from a value of 0.5 at $\tau = 0$, indicating that half the change in circulatory lift is obtained at the initial instant. Wagner's function is not formulated in simple analytical terms, rendering Duhamel integration rather complex; to obviate the problem, the response function is approximated as a linear combination of exponential terms [9]:

$$\Phi \approx 1 - \sum_{i=1}^{N_{\text{terms}}} A_i \exp^{b_i \tau}; \quad (3)$$

The exponential form of the response function allows for a very efficient numerical integration of Duhamel's expression. In fact, Duhamel's integral, eq. (1), at time $t + \Delta t$ can be then evaluated as the sum of a decay, and an increment term; the decay term depends on the integral value at the previous time step t , while the increment term only includes an integration from time t to $t + \Delta t$, thus avoiding to perform integration from the time origin $t = 0$ at every new time step [9].

Using the exponential form of the indicial lift response function, Jones[10] proposes a two terms approximation for the flat plate indicial response (figure 3):

$$\Phi = 1 - 0.165 \exp^{-0.045\tau} - 0.335 \exp^{-0.3\tau}. \quad (4)$$

Several references report indicial lift responses for airfoils with finite thickness that differ from the flat plate response. Giesing[11] shows indicial curves below the flat plate one for the response of Von Mises and Jukowsky airfoils; similar results are obtained by Basu and Hancock[12], who simulate the step response of a Von Mises airfoil with a panel code. Chow[13] concludes that finite thickness airfoils have a slower step response, and the response speed decreases as the airfoil thickness and trailing edge angle are augmented.

More recently, Gaunaa [14] applies a panel code method to compute the response of NACA symmetric airfoils with different thicknesses, and shows that the response curve tends to the flat plate one as the thickness is reduced. In Hansen et al. [4], the same panel code method is used to simulate the step response of a 24% thick airfoil; the resulting indicial response is approximated by a two term exponential function which is then supplied to the Beddoes-Leishman model described in the report. Hansen et al. show that, for an airfoil undergoing harmonic pitch variations, the unsteady lift force based on the finite-thickness response is in better agreement with CFD simulations.

Nevertheless, Jones's approximation for the flat plate response remains a widespread standard in incompressible attached flow models, and, to the authors knowledge, no investigations evaluating the effects that different indicial response approximations would cause on wind turbine aeroelastic simulations are reported in literature.

The present work proposes an empirical function relating the geometric characteristics of an airfoil to its indicial lift response. Gaunaa's[14] panel code is used to compute the indicial response for a set of airfoils with different geometries; the indicial response curves are approximated with Jones-like two-term exponential functions, in the form of eq. (3). The different airfoils and corresponding indicial responses provides the dataset on which regression methods are applied to outline the empirical function, which is then tested on airfoils outside the dataset.

The effects of modified lift response functions are investigated for an airfoil undergoing harmonic pitching motion, and the resulting unsteady lift histories are compared to CFD simulations. The consequences on aeroelastic computations for a full wind turbine are evaluated by running time marching simulations of the NREL 5-MW baseline turbine [15] with the aeroelastic tool HAWC2 [3].

The method described in this article builds on the work presented by Gaunaa et al. [16] at the 49th AIAA-ASME conference. Compared to the preliminary results reported in the conference paper [16], the present article broadens the analysis on how changes in the indicial lift function affects aeroelastic loads simulations, and also includes an investigation on the effects on stability limits prediction.

2. MODEL AND METHOD

In order to estimate the effects that different airfoil geometries have on the indicial lift response function, several airfoil profile shapes have been considered. Each airfoil profile is discretized into panels, and the circulatory indicial lift response is simulated using a panel code. The simulated indicial lift response is fitted with a two term exponential function, and an empirical relation is sought in order to link the coefficients defining the exponential indicial response function (A_1, A_2, b_1, b_2 , eq. (3)) to the airfoil geometric characteristics.

2.1. Airfoil profiles

A preliminary investigation considered airfoil shapes taken from the modified NACA 4-digits family[17]. The profiles have a simple geometry, which is obtained as a superposition of thickness distribution to the airfoil mean line, and it is fully described by a set of five parameters.

The investigation needs then to be widened to include additional airfoil shapes, as the profiles in the 4-digits family have wider trailing edge angles than airfoils with the same thickness from other families (fig. 1); as well as that, throughout the NACA 4-digits family, the ratio of airfoil thickness over trailing edge angle shows very small variations.

To overcome such limitations, the investigated database is widened by modifying the thickness distribution, which is scaled with an half-cosine function aft the point of maximum thickness x_{thm} . The scaling function depends on an additional parameter k_{cos} :

$$\frac{t_{mod}}{t_{NACA}} = \begin{cases} 1 & \text{for } x \leq x_{thm} \\ 0.5 + 0.5 \cos\left(\pi \frac{x-x_{thm}}{1-x_{thm}} k_{cos}\right) & \text{for } x > x_{thm} \end{cases} \quad (5)$$

The thickness modification allows for profiles with sharper trailing edges (figure 1), and introduces further variation in the dataset of investigated airfoil shapes.

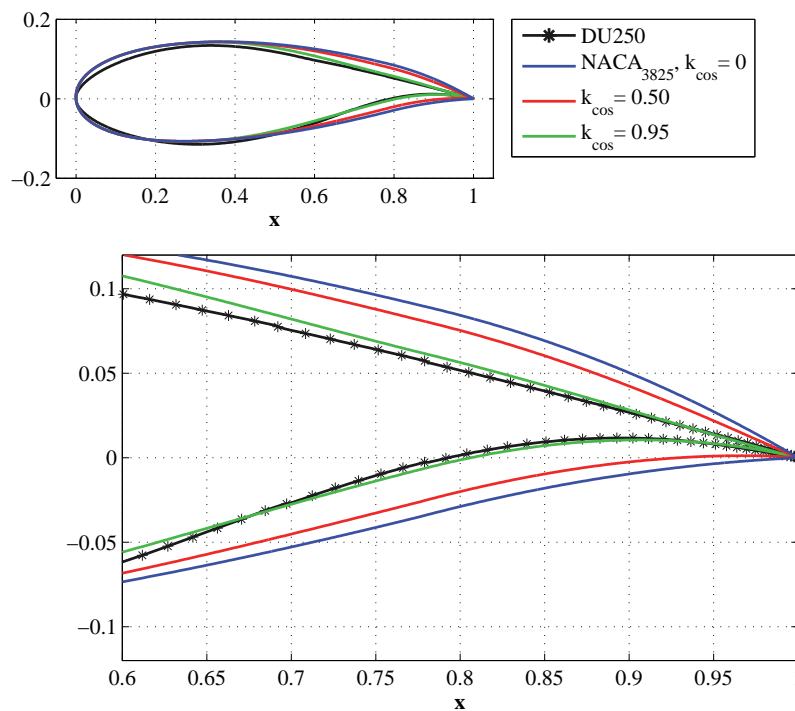


Figure 1. Airfoil shapes and Trailing Edge angle. The NACA-3825 airfoil (blue line) has the same thickness and maximum camber as the DU91-W2-250 (black line), but a wider TE angle. The cosine thickness modification (red and green lines) yields to a sharper trailing edge.

2.2. Panel code simulation

The indicial response of each airfoil in the dataset is first obtained from panel code simulations. The code has been developed by Gaunaa[14], following Hess's formulation[18], where the singularity elements are given by: constant strength source distribution, constant strength vortex distributions, and two dimensional point vortices in the wake. A detailed description of the model, and its validation are presented in Gaunaa[14].

As previously mentioned, the unsteady aerodynamic forces in attached flow can be described as the sum of a non-circulatory (added mass), and a circulatory contribution. Von Karman and Sears [19] adopt a similar description in their study on unsteady aerodynamic forces of a thin airfoil undergoing motion, under the plane wake approximation. Von Karman and Sears further split the circulatory contribution in a quasi-steady and a wake memory part; the wake memory part represents the deficiency, with respect to the quasi-steady force, following a change in the airfoil quasi-steady loading, and, thereof, a change in the airfoil circulation. They show that the wake memory effects do not depend on how the change in quasi-steady loading is generated.

The same behavior is reported in the work by Gaunaa [20], where the aerodynamic forces due to arbitrary motion and deformation of an airfoil are derived under thin airfoil assumptions. Gaunaa shows that the quasi-steady loading of the airfoil can be represented by an equivalent three-quarters chord downwash $w_{3/4}$; the equivalent downwash $w_{3/4}$ encompasses, in a single term, all the sources of quasi-steady loading, as, for instance, the airfoil linear motion, the angle of attack and its angular rate, the camberline deformation and its time derivatives. The wake memory effect depends directly on the change in the equivalent three-quarter chord downwash $w_{3/4}$, and not on which source has caused the change.

It can be thus concluded from thin airfoil analysis that the indicial response function accounting for the wake memory effects will be the same, independently of the cause of the step change in the quasi-steady loading (impulsively started flow, step in angle of attack, step in a trailing edge flap deflection, step in heave velocity, etc.); consequently, under the usual assumptions of thin airfoil theory, the circulatory indicial lift response function derived from an impulsively started flow is identical to the response function derived from a step change in angle of attack.

Furthermore, it is worth mentioning that the indicial lift response function for a step change in the airfoil quasi-steady loading differs from response functions for disturbances traveling along the airfoil, as for instance the gust response function. Nevertheless, most aeroelastic simulation codes do not distinguish between step-change (Wagner-type response), and traveling disturbances (Küssner-type response), and a step change indicial response function is usually adopted in all the cases; an evaluation of the error introduced by this approximation is reported in Buhl et al.[21].

Based on the previous considerations and for practical purposes, it is chosen to perform panel code simulations of the indicial lift response by reproducing an impulsively started flow, where the free stream flow velocity is switched from zero to a finite value simultaneously in the whole computation domain. The indicial lift response function is then determined by letting the simulation advance in time, without further changes to the free stream speed. Preliminary computations have verified the validity of the assumption that, also for finite thickness airfoils, the circulatory lift response for an impulsively started flow matches the response following a step change in angle of attack.

By applying small time steps to the initial instants of the simulation, the panel code returns an unusual behavior of the indicial lift, which starts decreasing from a value above the steady one. Such results are similar to the transient behavior described by Graham [22] for an airfoil in impulsively started flow where the roll up of wake vorticity dominates the unsteady aerodynamics. In these conditions, the indicial lift presents an initial singularity: it first decreases with time, and only subsequently monotonically increases, as in Wagner's indicial response function.

As observed by Graham, an airfoil does not encounter a truly impulsive start under realistic conditions. The wake dynamic is thus generally dominated by downstream convection of the vorticity, rather than roll up, and the indicial lift increases monotonically to the steady value. The present investigation focuses on the response of airfoils under realistic conditions, therefore, time steps are selected as large as sufficient to avoid the singularity induced by the dynamics associated with the rolling up of the initial part of the shed wake vortex sheet. The response at time zero is then obtained from a quadratic extrapolation of the first computed points.

2.3. Exponential curve fitting

The simulated indicial response can be approximated by a n -term exponential function, eq. (3); the more terms, the better the approximation. It is chosen to use a two-term function, which returns a sufficiently accurate approximation (figure 3) and keeps similarity with Jones's expression:

$$\Phi = 1 - A_1 \exp^{b_1 \cdot \tau} - A_2 \exp^{b_2 \cdot \tau}, \quad (6)$$

with: $b_1 < b_2 < 0$.

The two-term function is defined by 4 *indicial response coefficients*: b_1 giving the decay of the fast term, b_2 for the slow decaying term, and A_1 and A_2 giving the weights of the two components. The coefficients are found through minimization of the weighted sum of the squared differences between the simulated response and the fitted curve.

The weight function is set to be equal to the difference between the simulated indicial response, and the unit steady value. In this way, the minimization algorithm values more the fitting for points in the initial part of the transient, reducing the influence from the almost stationary tail of the indicial curve; for the same purpose, the curve tail is truncated where the response reaches 99.9% of the final value.

2.4. Profile Surface Angle

A preliminary investigation indicates that the lift response coefficients are related to the angle between upper and lower surface of the profile, especially close to the trailing edge, as it was also observed in Chow[13].

It is therefore chosen to represent the geometric characteristics of an airfoil in terms of a *profile surface angle* $\beta(x)$. For a given chord-wise coordinate \tilde{x} , $\beta(\tilde{x})$ is defined as the angle between two lines that originate at the trailing edge and intersect the profile upper and lower surface at the points of chord-wise coordinate \tilde{x} , figure 2.

Each airfoil is thus characterized by a specific curve $\beta(x)$ of profile angles along the chord; the same airfoil is also associated to a set of indicial response coefficients (A_1, A_2, b_1, b_2) . Therefore, a relation between the indicial response coefficients and the angles β would allow to estimate the indicial lift response function of an airfoil from simple measurement of its geometric characteristics.

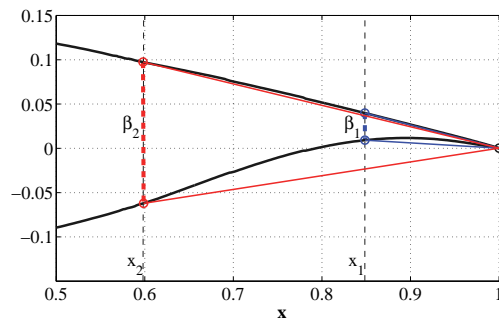


Figure 2. Profile angle β at chord-wise position x_1 and x_2

3. RESULTS

A preliminary investigation is carried out on simple airfoils shapes from the NACA 4-digits family. It is observed that the indicial lift response function is scarcely influenced from variations of airfoil camber and leading edge radius; on the contrary, the airfoil thickness and the location of the point of maximum thickness affect the shape of the indicial response function. As also observed in Gaunaa[14] and Chow [13], thicker airfoils have a slower response and the indicial lift response functions have a starting value below $\Phi_{(\tau=0)} = 0.5$ of a flat plate; as the airfoil thickness is reduced, the response tends to the flat plate one, figure 3.

The investigation is then enlarged to a wider dataset of airfoil profiles, including several combinations of airfoil thickness and cosine scaling parameter. For each profile in the dataset, the panel code simulates the indicial lift response, which is then fitted with the two term approximation; every airfoil profile i is thus associated with a set of four indicial response coefficients $(A_1^i, A_2^i, b_1^i, b_2^i)$, as in eq. (6), and a set of profile angles measured at different chord-wise locations: $\beta(x)_i$. A relation is sought between the indicial response coefficients and the profile angle at few selected locations.

At first, it is assumed that the each of the four indicial response coefficients can be expressed as a quadratic function of the profile angle measured at one single chordwise location x_1 :

$$\hat{y} = a_0 + a_1\beta_{x_1} + a_2\beta_{x_1}^2, \quad \text{where} \quad \hat{y} = \hat{A}_1, \hat{A}_2, \hat{b}_1, \text{ or } \hat{b}_2. \quad (7)$$

The problem is formulated as a linear model regression, where, for each profile i , the actual value of the indicial response coefficient $\zeta_{i,1}$ ($\zeta_{i,1} = A_1^i, A_2^i, b_1^i, \text{ or } b_2^i$) is the dependent variable (regressand), and the profile angle at a selected location $\beta(\tilde{x})_i$ is the independent variable (regressor). The regression parameters a_0, a_1, a_2 are constant throughout the dataset, and a different set of regression parameters is associated to each indicial response coefficient.

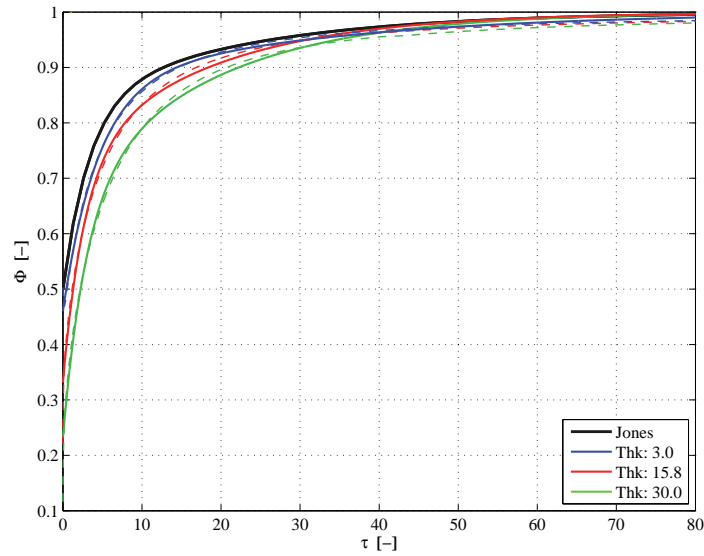


Figure 3. Indicial lift response function for NACA 44xx airfoils with different thicknesses and for a flat plate (Jones’s coefficients). Dashed lines: response simulated by the panel code; full lines: two terms exponential approximation.

The problem is solved with an ordinary least square method, minimizing the squared sum of residuals $(\hat{y}_i - \zeta_{i,1})^2$; the regression is repeated considering different locations \tilde{x} of the profile angle measurement point.

For each chordwise location \tilde{x} , the quality of the regression is evaluated by the coefficient of determination $r^2(\tilde{x})$; the minimum points of the curves $(1 - r^2)$ (figure 4, top) thus indicate the optimal locations x^* : the corresponding profile angles $\beta(x^*)$ give the regression with the best explanation of the variation observed in the indicial response coefficients.

Although optimally placed, measurements of the profile angle at only one point are not sufficient to account for all the variation observed in the indicial response coefficients. A profile angle measured in a second point x_2 is thus introduced in the empirical function: $\hat{y} = f(\beta_{x1}, \beta_{x2})$.

The optimal location of the second point is determined from the coefficient of determination r^2 in a second regression, where the regressand variables $\zeta_{i,2}$ are the residuals from the first regression: $\zeta_{i,2} = \hat{y}_{i,1} - \zeta_{i,1}$. The minima of the $(1 - r^2)$ curves (figure 4, bottom) give the optimal placement for the second profile angle measurement β_{x2} . Note that, since the second regression (figure 4, bottom) fits the residuals of the first, whenever the second measurement point x_2 coincides with the first x_1 , the coefficient $(1 - r^2)$ is one, which indicates that the second point, being identical to the first, does not contribute to further data explanation.

The regression analysis indicates for each indicial response coefficient the optimal locations of the two measurements points for the profile angle. The optimal locations are slightly moved from the curves minima so to reduce the total number of points to 3; the resulting pair of measurement points are reported in the first columns of table I. For each indicial response coefficient, one point is located close to the airfoil trailing edge, the other to mid-chord; thus indicating that the geometric parameters that more affects the indicial lift response function are the airfoil thickness (roughly proportional to the profile angle at mid-chord), and the profile ‘opening’ near the trailing edge.

Each indicial response coefficient is then estimated as a quadratic function of the profile angle β at the two selected locations (x_1 and x_2) along the profile:

$$\hat{y}_i = a_0 + a_{11}\beta_{x1} + a_{12}\beta_{x1}^2 + a_{21}\beta_{x2} + a_{22}\beta_{x2}^2. \tag{8}$$

Both the profile angle location pair (x_1 and x_2), and the set of regression parameters a_i depend on which of the four indicial response coefficient is being considered: $\hat{y}_i = \hat{A}_1, \hat{A}_2, \hat{b}_1,$ or \hat{b}_2 (table I); the regression parameters are again determined by solving a least square regression problem.

Table I reports the profile angle location and the regression parameters for each indicial response coefficient. The parameters for the quadratic terms (a_{12}, a_{22}) are rather close to zero, highlighting a dominant linear behavior; nevertheless, no regression parameter admits the zero value inside its 95% confidence interval, thus also the quadratic terms are significant in the fitting. Substituting the sets of regression parameters in equation (8) yields to a set of four empirical

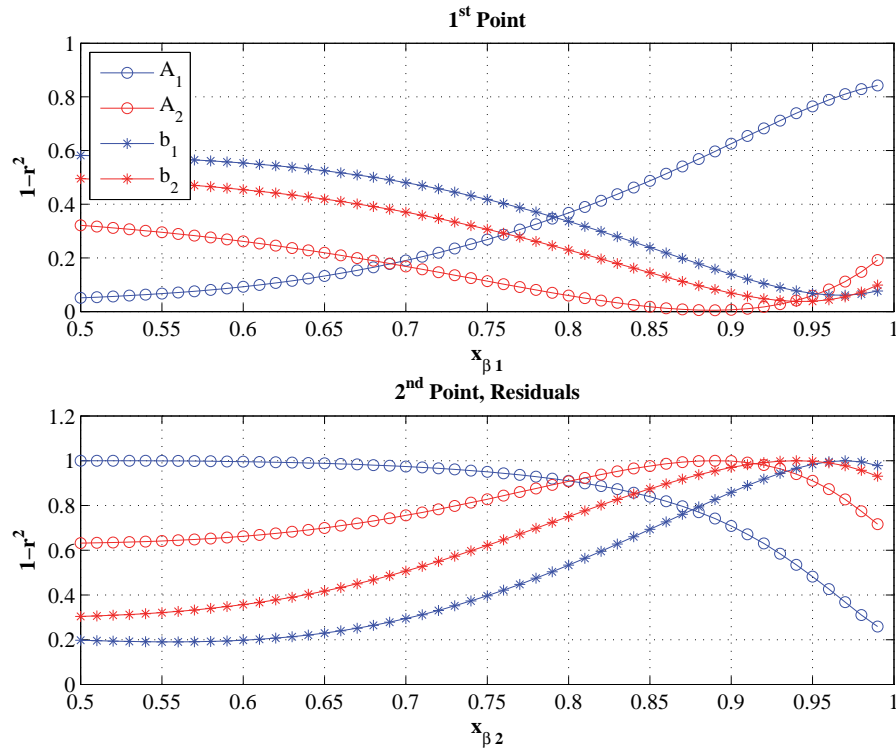


Figure 4. One minus coefficient of determination versus the location of the profile angle measurement point; the curve minima correspond to the best regression. Top: location of the first profile-angle point x_1 , regression on the dataset. Bottom: location of the second profile-angle point x_2 , regression on the residuals.

equations, one for each indicial response coefficient; the equations allow to estimate the indicial lift response function of an arbitrary profile by simply measuring its profile angle in three different locations.

Lift Coef.	x_1	x_2	a_0	a_{11}	a_{12}	a_{21}	a_{22}
A_1	0.95	0.5	3.93E-01	-1.32E-03	3.41E-05	2.06E-05	5.33E-05
A_2	0.88	0.5	1.01E-01	9.41E-03	-7.80E-05	2.35E-03	-9.24E-05
b_1	0.95	0.5	-1.90E-01	-8.35E-03	1.04E-04	-7.16E-03	2.65E-04
b_2	0.95	0.5	-2.83E-02	-1.29E-03	1.85E-05	-1.04E-03	3.44E-05

Table I. Empirical estimation of the indicial lift response coefficients. Location of the two profile angle measurement points: x_1, x_2 . Regression parameters to be applied in equation (8) for coefficient estimation; the parameters refer to profile angles measured in degrees.

3.1. Validation

The set of empirical equations derived in the previous section is tested for three airfoil profiles used on the reference rotor of the MEXICO project[23]: DU 91-W2-250, RISOE A1-21, and NACA 64-418. The airfoils have profile shapes commonly employed on wind turbine blades, they differ in thickness and camber characteristics, and none of them was part of the dataset used in the regression.

For each airfoil, the indicial lift response coefficients are estimated with the empirical relation in eq. [3], and the coefficients in table I (circles, in figure 5); the indicial response coefficients are then compared with the coefficients resulting from the direct fitting of the indicial lift response function simulated by the panel code (stars). The estimated values are found very close to the panel codes ones, and they give a better approximation of the indicial lift response than Jones’s coefficients.

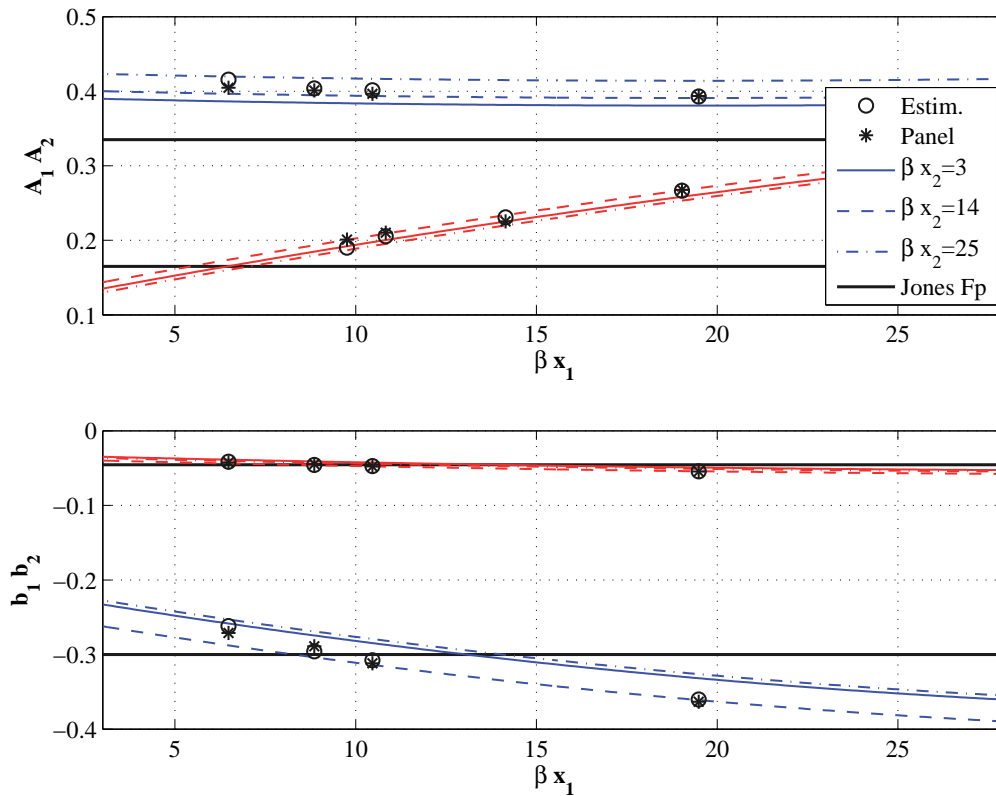


Figure 5. Lift response coefficients as function of the airfoil profile angle at location x_1 . Estimated (circles) and panel code (stars) coefficients for the airfoils: DU 91-W2-250, RISØE A1-21, NACA 64-418 (from the left). The plot reports curves from the empirical estimation function for three arbitrary β_{x_2} profile angles, and the flat plate coefficients from Jones’s approximation.

The empirical equations are further tested to verify that plausible lift response functions are obtained for profile angles ranges:

$$\forall \text{ profile } \begin{cases} 2^\circ \leq \beta_{x_1} \leq 50^\circ \\ 3^\circ \leq \beta_{x_2} \leq 40^\circ \end{cases} \quad (9)$$

The empirical equation might result in an unreasonable indicial lift response when applied to airfoils falling outside this range.

4. RELEVANCE TO AEROELASTIC SIMULATIONS

4.1. CFD comparison

Changing the indicial lift response function conditions the dynamics of the aerodynamic forces. The effects are first evaluated in the simple case of a 2D airfoil undergoing harmonic pitching motion. The effects are first evaluated in the simple case of a 2D airfoil undergoing harmonic pitching motion. The effects are first evaluated in the simple case of a 2D airfoil undergoing harmonic pitching motion. The same three airfoil profiles as in the previous validation are considered; the profiles are hinged at the quarter chord point, and the angle of attack is changed from 1° to 3° with two reduced frequencies: $k = \omega b/U = 0.1$, and a faster one $k = 0.5$.

The unsteady lift force is computed with the analytical model described in Hansen et al.[4]; the model, here simplified for attached flow conditions, is based on superposition of indicial lift response functions approximated by exponential terms. For each airfoil, three sets of indicial response coefficients are considered: the ones from Jones’s flat plate expression, the estimations from the empirical equation, eq.8, and the ones obtained by exponential fitting of the panel code response.

The resulting lift loops (figure 6) are compared against CFD simulations. The CFD results were obtained using EllipSys, Risø’s in-house CFD code, developed as a cooperation between the Department of Mechanical Engineering at the Technical University of Denmark and the Department of Wind Energy at RisøNational Laboratory [24, 25, 26]. Simulations are

run with a standard set-up for 2D airfoils: fully turbulent flow, $k-\omega$ SST (Shear Stress Transport) turbulence model, and Reynolds number of 6 millions.

The estimated indicial response coefficients are very close to the panel code ones (see figure 5): the corresponding loops (respectively, blue line and red circles in figure 6) are thus practically overlapping. The loops based on the estimated indicial response coefficients are closer to the CFD results (black lines) than the loops with flat plate coefficients, indicating thus a better approximation of the airfoil indicial lift response function. The differences among the loops are increased as the reduced frequency is augmented.

4.2. Full Wind Turbine Simulations

In most aeroelastic codes for wind turbine loads simulation, the indicial response coefficients are given by Jones's approximation of the flat plate response. As observed in the previous sections, the response of an airfoil with finite thickness differs from the flat plate one, and the higher is the reduced frequency of the unsteady motion, the larger the difference in the resulting aerodynamic forces.

To assess the impact of differences in the indicial lift response function on the simulated response of a full wind turbine, the NREL offshore 5-MW baseline wind turbine [15] is modeled with the aeroelastic tool HAWC2[3]. Three different set-ups of the aerodynamic model are considered in the simulations, where the indicial response coefficients are given by:

- Jones's flat plate response. The default value in most aeroelastic simulation tools.
- Estimated coefficients for the DU 91-W2-250 airfoil. The airfoil has a thickness ratio of 25%, suitable for mid-span sections. The current version of the aeroelastic tool does not allow to vary the indicial lift response coefficients along the blade span, therefore, the DU 91-W2-250 indicial response approximation is applied to the whole blade.
- Quasi-Steady approximation ($A_1 = A_2 = 0$) for the circulatory lift contribution in attached flow; also a rather common assumption.

The effects of the different indicial response approximations on aeroelastic simulations are quantified in terms of variations of equivalent fatigue loads, ultimate loads, and stability limits.

4.2.1. Fatigue and Ultimate Loads

The equivalent fatigue loads are determined using a standard procedure [27] based on rain flow counting method, and Palmgren-Miner linear damage assumption. The simulations reproduce power production load cases as described in the IEC standard 61400-1 [28] (DLC 1.1); wind conditions for turbine class *IIB* are adopted, and a yaw misalignment of $\pm 8^\circ$ is included. The stochastic wind field is reproduced through Mann's turbulence model [3], and the same turbulence seeds are repeated for the three indicial response set-ups.

The ultimate load are computed as the maximum load among a reduced set of simulation cases from the same standard [28]: production with extreme turbulence model (DLC 1.3), extreme coherent gust (DLC 1.4), and extreme operating gust (DLC 2.3) without grid-loss.

Table II and III report the variation in simulated equivalent fatigue loads and ultimate loads for bending moments measured at the blade root, and at the tower bottom flange, and torsion moments at the tower top, and on the low speed shaft; the loads variations are normalized by the loads obtained with the default flat plate indicial response coefficients.

Although the figures might vary depending on the specific wind turbine and control model, it can be concluded that the assumption of quasi-steady circulatory lift in attached flow leads to significantly higher estimations of both fatigue and ultimate loads. Using the finite-thickness indicial lift response function leads to a reduction in the predicted loads, in comparison with simulation based on a flat-plate indicial response, but the variations are on a much smaller scale than in the quasi-steady case.

S_{eq}	<i>Blade Flapw.</i>	<i>Blade Edgew.</i>	<i>Blade Tors.</i>	<i>Tower FA</i>	<i>Tower SS</i>	<i>Tower Tors.</i>	<i>Shaft Tors.</i>
<i>Ref. Fl.Pl. [MNm]</i>	13.73	10.69	0.25	77.12	39.55	20.60	3.86
Δ <i>Quasi-St</i>	5.49 %	1.10 %	20.54 %	6.44 %	3.89 %	9.15 %	15.05 %
Δ <i>DU 250</i>	-1.06 %	0.00 %	-2.48 %	-1.02 %	-0.39 %	-1.83 %	-2.21 %

Table II. Equivalent fatigue loads, variations due to changes of the indicial lift response coefficients. Simulations for: Jones's flat plate indicial response coefficients (reference case, first row), Quasi-Steady indicial response, DU 91-W2-250 indicial response coefficients; variations Δ normalized by the equivalent loads of the flat plate reference case. Results refer to an equivalent number of load cycles $n_{eq} = 10^6$, material fatigue exponent $m = 10$ for blade loads, $m = 4$ for tower and drive-train.

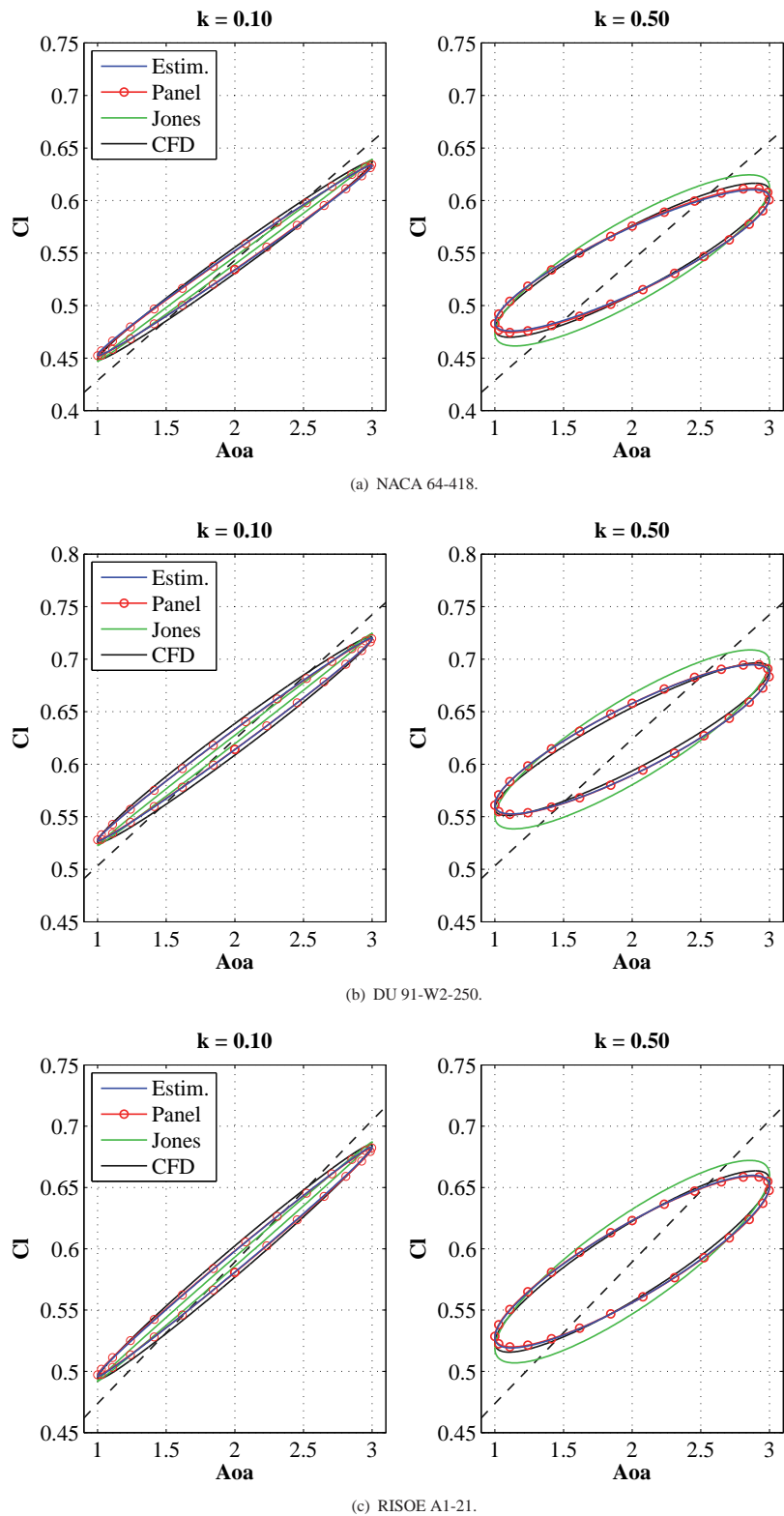


Figure 6. Lift coefficient loops for airfoils undergoing harmonic pitching motion. Comparison between CFD results (black) and analytical model based on indicial response coefficients from: empirical estimation function (blue), panel code response (red line with circles), Jones's flat plate coefficients (green).

$\max(M)$	<i>Blade Flapw.</i>	<i>Blade Edgew.</i>	<i>Blade Tors.</i>	<i>Tower FA</i>	<i>Tower SS</i>	<i>Tower Tors.</i>	<i>Shaft Tors.</i>
<i>Ref. Fl.Pl. [MNm]</i>	14.94	6.92	0.22	112.46	45.08	17.44	6.62
Δ <i>Quasi-St.</i>	6.93 %	2.29 %	25.26 %	-1.98 %	3.44 %	6.07 %	5.45 %
Δ <i>DU 250</i>	-0.73 %	-0.39 %	-2.21 %	0.41 %	-0.55 %	-1.14 %	-1.33 %

Table III. Ultimate loads from reduced set of cases, variations due to changes of the indicial lift response coefficients. Simulations for: Jones's flat plate indicial response coefficients (reference case, first row), Quasi-Steady indicial response, DU 91-W2-250 indicial response coefficients; variations Δ normalized by the ultimate loads of the flat plate reference case.

4.2.2. Stability limits

The wind turbine stability limits in the three indicial response cases are estimated by running simulations with a constant wind inflow, and attached flow conditions on the blades; the rotor speed is progressively increased until unstable oscillations are observed. The results are presented in figure 7 as the tip speed corresponding to the critical rotor speed at which instability occurred; the torsional stiffness of the blade has been scaled (values on the abscissa) to verify the consistency of the results for different stiffness values.

As discussed for fatigue and ultimate loads, neglecting the circulatory lift dynamics in attached flow causes the largest variations in the simulated response. The stability limit encountered with the quasi-steady assumption is in fact much lower than in the other two cases; Lobitz [29] reported a similar result for the flutter limit of an isolated blade. The finite-thickness indicial lift response function results in slightly higher stability limits, but the difference from the flat plate case is rather small; variations of similar magnitude were reported in the flutter analysis of a 2D profile [30].

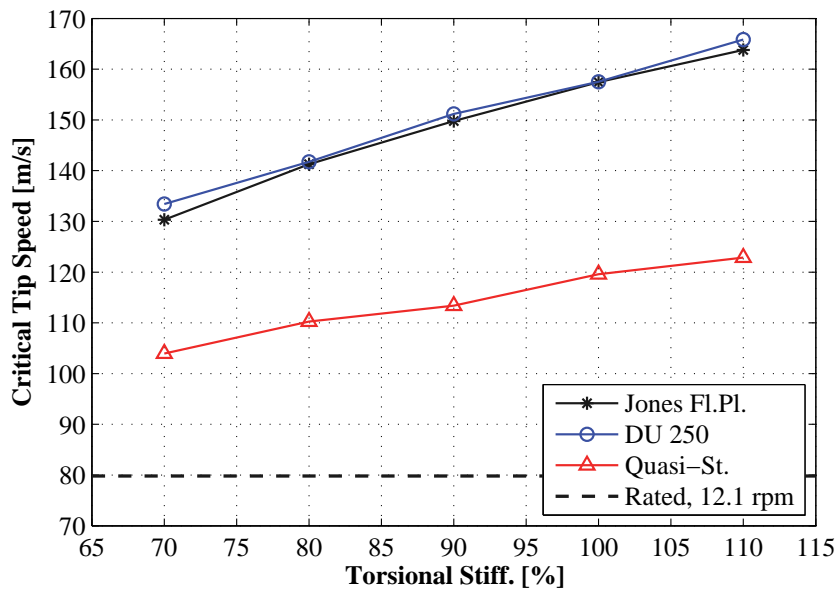


Figure 7. Critical tip speed at which instability (flutter) due to rotor over-speeding arises; variations due to changes of the indicial lift response coefficients. Simulations for: Jones's flat plate indicial response coefficients (black with stars), Quasi-Steady indicial response (red with triangles), DU 91-W2-250 indicial response coefficients (blue with circles). The values are plotted versus the scaling factor applied to the blade torsional stiffness.

5. CONCLUSION

Airfoils with finite-thickness have an indicial lift response function that is different from the flat plate one, which is usually adopted in aeroelastic simulations through Jones's approximation.

The indicial response of several airfoil shapes is determined using a panel code, and then approximated by a two-term exponential function; the exponential function is similar to Jones's expression for the flat plate, and is defined by four indicial response coefficients, eq. (6).

An empirical relation is proposed, where the four indicial response coefficients are estimated by quadratic functions of the airfoil profile angles, measured at three locations along the chord. The relation allows to estimate the indicial lift response function of a finite-thickness airfoil from simple geometric characteristics.

The indicial response function conditions the dynamics of the simulated unsteady aerodynamic forces. The effects are evident in the case of a 2D airfoil undergoing harmonic pitching motion, where the indicial response accounting for the thickness of the airfoil leads to a better agreement with results from CFD simulations.

The effects of different indicial response approximations on the overall estimation of the wind turbine aeroelastic behavior are quantified for the NREL 5-MW baseline turbine [15]. The quasi-steady response function has a significant impact on the simulated turbine response: fatigue and ultimate loads are larger, and the stability limits lower, than the corresponding values obtained with a flat-plate indicial response. The indicial response function that accounts for the airfoil thickness, in comparison to Jones's flat-plate indicial response, leads to a slight reduction of the aeroelastic loads, and a small increase of flutter stability limits; although the variations from the default flat-plate case are small.

To conclude, is important for an aeroelastic model to account for the dynamics of the circulatory lift also in the attached flow region. The indicial response function accounting for the airfoil thickness yields to more accurate predictions of the aerodynamic forces than Jones's flat-plate indicial response; nevertheless, the difference induced by the finite-thickness indicial response function with respect to the flat plate one becomes scarcely significant as the aeroelastic behavior of the whole wind turbine is considered.

6. ACKNOWLEDGMENTS

It is gratefully acknowledged that this work is partly funded by the Danish project *Development of Adaptive Trailing Edge Flap (ATEF) System for Wind Turbines* by the Advanced Technology Foundation, Advanced Technology Projects 2007.

REFERENCES

1. Beddoes TS. Practical computations of unsteady lift. *Vertica* 1984; **8**(1):55–71.
2. Leishman JG, Nguyen KQ. State-space representation of unsteady airfoil behavior. *AIAA Journal* 1990; **28**(5):836–844.
3. Larsen TJ. How 2 HAWC2 the user's manual. *Technical Report R-1597(EN)*, Risø National Laboratory. Technical University of Denmark 2009.
4. Hansen MH, Gaunaa M, Madsen HA. A Beddoes-Leishman type dynamic stall model in state-space and indicial formulations. *Technical Report R-1354(EN)*, Risø National Laboratory, Roskilde (DK) 2004.
5. Bossanyi E. GH Bladed theory manual. *Technical Report*, Garrad Hassan and Partners Ltd 2003.
6. Jonkman JM, Buhl MLJ. Fast user's guide - updated august 2005. *Technical Report NREL/TP-500-38230*, National Renewable Energy Laboratory (NREL) 2005.
7. Moriarty PJ, Hansen AC. Aerodyn theory manual. *Technical Report NREL/TP-500-36881*, National Renewable Energy Laboratory (NREL) 2005.
8. Theodorsen T. General theory of aerodynamic instability and mechanism of flutter. *Technical Report 496*, National Advisory Committee for Aeronautics (United States Advisory Committee for Aeronautics) 1935.
9. Bisplinghoff RL, Ashley H, Halfman RL. *Aeroelasticity*. Dover Publications, Inc, 1996.
10. Jones RT. The unsteady lift of a wing of finite aspect ratio. *Technical Report 681*, National Advisory Committee for Aeronautics (United States Advisory Committee for Aeronautics) 1940.
11. Giesing JP. Nonlinear two-dimensional unsteady potential flow with lift. *Journal of Aircraft* 1968; **5**:135–143.
12. Basu BC, Hancock GJ. Unsteady motion of a two-dimensional aerofoil in incompressible inviscid flow. *Journal of Fluid Mechanics* 1978; **87**(JUL):159–178.
13. Chow CY, Huang MK. The initial lift and drag of an impulsively started airfoil of finite thickness. *Journal of Fluid Mechanics* 1982; **118**(MAY):393–409.
14. Gaunaa M. Unsteady aerodynamic forces on NACA 0015 airfoil in harmonic translatory motion. PhD Thesis, Department of Mechanical Engineering, Technical University of Denmark 2002.
15. Jonkman J, Butterfield S, Musial W, Scott G. Definition of a 5-MW reference wind turbine for offshore system development. *Technical Report NREL/TP-500-38060*, National Renewable Energy Laboratory (NREL) Feb 2009.
16. Gaunaa M, Bergami L, Heinz J. Indicial response function for finite-thickness airfoils, a semi-empirical approach. *Conference proceedings, 49th AIAA Aerospace Sciences Meeting*, Orlando (FL), 2011.
17. Stack J, Doenhoff AEV. Tests of 16 related airfoils at high speed. *Technical Report NACA-TR-492*, National Advisory Committee for Aeronautics (United States Advisory Committee for Aeronautics) 1935.

18. Hess J. Higher order numerical solution of the integral equation for the two-dimensional Neumann problem. *Computer Methods in Applied Mechanics and Engineering* 1973; **2**(1):1–15.
19. Karman T, Sears WR. Airfoil theory for non-uniform motion. *Journal of the Aeronautical Sciences* 1938; **5**(10):379–390.
20. Gaunaa M. Unsteady two-dimensional potential-flow model for thin variable geometry airfoils. *Wind Energy* 2010; **13**(2-3):167–192.
21. Buhl T, Gaunaa M, Bak C. Potential load reduction using airfoils with variable trailing edge geometry. *Transactions of the ASME. Journal of Solar Energy Engineering* 2005; **127**(4):503–516.
22. Graham JMR. The lift on an aerofoil in starting flow. *Journal of Fluid Mechanics* 1983; **133**(AUG):413–425.
23. Snel H, Schepers JG, Montgomerie B. The MEXICO project (Model experiments in controlled conditions): The database and first results of data processing and interpretation. *Journal of Physics: Conference Series*, vol. 75, 2007; 012 014.
24. Michelsen JA. Block structured multigrid solution of 2D and 3D elliptic PDE's. *Technical Report AFM 94-06*, Technical University of Denmark 1994.
25. Michelsen JA. Basis3D - a platform for development of multiblock PDE solvers. *Technical Report AFM 92-05*, Technical University of Denmark 1992.
26. rensen NNS. General purpose flow solver applied to flow over hills. *Technical Report Risø-R-827(EN)*, Risø National Laboratory 1995.
27. Hansen M. *Aerodynamics of wind turbines : rotors, loads and structure*. James & James: London, 2000.
28. IEC. IEC 61400-1: Wind turbines part 1: Design requirements. *Technical Report*, International Electrotechnical Commission 2005.
29. Lobitz DW. Aeroelastic stability predictions for a MW-sized blade. *Wind Energy* 2004; **7**(3):211–224.
30. Bergami L, Gaunaa M. Stability investigation of an airfoil section with active flap control. *Wind Energy* 2010; **13**(2-3):151–166.

Article II

Analysis of aeroelastic loads and their contribution to fatigue damage

The article was presented at the 4th EAWC conference *The Science of Making Torque from Wind*, Oldenburg (Germany), 9-11 October 2012; the article, as part of the proceedings, is submitted for publication to *Journal of physics: conference series*.

The content of the article is recalled in the synopsis sections related to:

- *Load Analysis*, section 3.2: characteristics of the loads responsible for the highest fatigue contributions.

Analysis of aeroelastic loads and their contributions to fatigue damage

L Bergami and M Gaunaa

Technical University of Denmark, Department of Wind Energy
Risø Campus, Roskilde - Denmark

E-mail: leob@dtu.dk

Abstract. The paper presents an analysis of the aeroelastic loads on a wind turbine in normal operation. The characteristic of the loads causing the highest fatigue damage are identified, so to provide indications to the development of active load alleviation systems for smart-rotor applications. Fatigue analysis is performed using rain-flow counting and Palmgren-Miner linear damage assumption; the contribution to life-time fatigue damage from deterministic load variations is quantified, as well as the contributions from operation at different mean wind speeds. A method is proposed to retrieve an estimation of the load frequencies yielding the highest fatigue contributions from the bending moment spectra. The results are in good agreement with rain-flow counting analysis on filtered time series, and, for the blade loads, show dominant contributions from frequencies close to the rotational one; negligible fatigue contributions are reported for loads with frequency above 2 Hz.

1. Introduction

The size of modern utility-scaled horizontal-axis wind turbines (HAWT) shows a continuously increasing trend. As the rotor size increases, so do the loads that act on the turbine. Recent studies have proposed *smart-rotor* concepts, where the wind turbine actively alleviates the loads it would have to withstand; several solutions have been investigated, using either conventional pitch actuators [1, 2], or active aerodynamic devices distributed along the blade span, such as micro-tabs [3], or trailing-edge flaps [4, 5].

In most cases, the primary objective of the smart-rotor is to reduce the fatigue loads that the turbine experiences during normal production. The aim of this paper is to contribute to smart-rotor research by identifying the characteristics of the aeroelastic loads that are responsible for the largest fatigue contributions. The loads yielding to the higher fatigue contributions are the one the active alleviation system should focus on; therefore, their characteristics will provide useful indications for the design of a smart-rotor system.

The loads are here characterized in terms of: stochastic and deterministic components, equivalent fatigue damage contribution from rain-flow counting analysis, spectral content, and, a particular focus is given to the estimation of the frequency characteristics of the loads causing the highest contribution to the fatigue damage. The four points determine the structure of the paper, as each of them is dealt with in a separate section; general conclusions follow in the last section.

The whole analysis starts from simulations of loads time series for the NREL 5-MW reference wind turbine [6] in its on-shore configuration. The response of the turbine is simulated using the

aeroelastic code HAWC2 [7], which includes a multi-body structural model, and a BEM-based aerodynamic model; modeling the unsteady effects of the airfoils aerodynamic forces has proved necessary to avoid biased estimations of the fatigue loads [8], hence the aerodynamic model by Hansen et al. [9] is adopted. The turbine has variable speed regulation below rated power, and collective pitch-to-feather control above rated; the standard controller by Jonkman et al. [6] is applied.

As most of the fatigue loads originate during normal operation, simulation conditions are set according to the design load case (DLC) 1.1 in the IEC standard [10]. A turbulent wind field is generated according to class IIb specifications, including the effects of tower shadow, and the terrain shear, as prescribed in the standard [10]; six turbulent series of ten minutes each are simulated for every mean wind speed.

2. Deterministic and stochastic characterization

The fatigue damage on the wind turbine structure originates from the load variations and, in a first approximation, it does not depend on the mean load level. In this study, the load variations at the blade root are classified as *deterministic*, or *stochastic*. It is chosen to define as *deterministic* the load variations that present them self in regular cycles, where the cycle period corresponds to the natural period of one rotor revolution; the remaining load variations are defined as non-deterministic, or *stochastic*.

The blade root bending moment from the simulated time series are plotted as function of the blade azimuthal position, green dots in figure 1. The variation of the loads around the mean level directly relates to the fatigue damage, and is here described as three-times the loads standard deviation, red lines in figure 1. The *deterministic* contribution is assumed to be responsible for the underlying trend in the load variation, and is thus estimated as the mean load value for each azimuthal position (black line in fig. 1). The remaining load variation, once the deterministic one is filtered out, is considered as the *stochastic* contribution (blue lines in fig. 1).

The deterministic loads are related to variations in the wind field which are constant throughout the simulated one hour series; in this case, they represent the effects of terrain shear and rotor tilt as sampled by the rotating blade, as well as the tower shadow effect, which gives the clearly marked notch after the tower passage at 0 deg azimuth. Different estimations of the deterministic contribution would results from different choices in the definition: for instance, adopting a shorter averaging time window to identify the deterministic variation would classify as deterministic contribution also the effects of large scale turbulence, thus returning an higher contribution.

Deterministic and stochastic contribution to the load variation are estimated at different mean wind speeds for the blade root flapwise and edgewise bending moments. From the original load time series, ‘stochastic-only’ time series are obtained by subtracting for each blade azimuthal position the corresponding deterministic load variation. The stochastic-only load time series would correspond to an ideal smart-rotor, with a cyclic control able to compensate for the whole deterministic load variation. The processed time series will be considered in the following sections in order to evaluate the fatigue contribution from the stochastic components of the loads.

The load variation in the blade root flapwise bending moment increases with the mean wind speed (red lines in fig. 2). The main contribution originate from stochastic load variations (blue lines); nevertheless, deterministic variations are also relevant (black lines), and increase at higher wind speed, which is partly due to gravity contributions, as the blade is pitched out of the rotor plane. In case of yaw misalignment, the increase in the overall load variation is mainly due to the deterministic component; a similar effect would be also expected in case of partial wake operation.

The variations of loads at different mean wind speed provides a convenient term of comparison

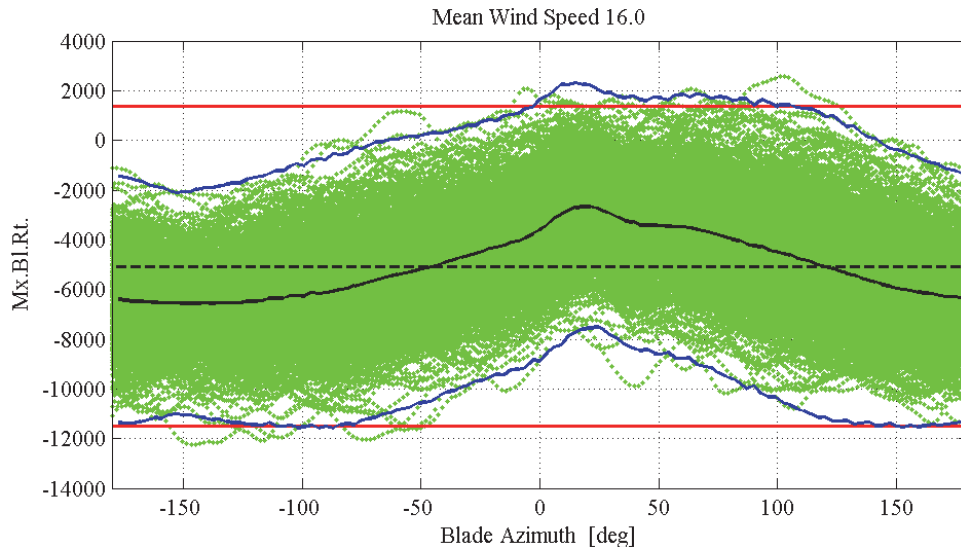


Figure 1. Blade root flapwise bending moment variations versus blade azimuthal position. Simulated time series (green dots), total variation of the simulated loads (red lines), deterministic contribution (black), stochastic contribution (blue).

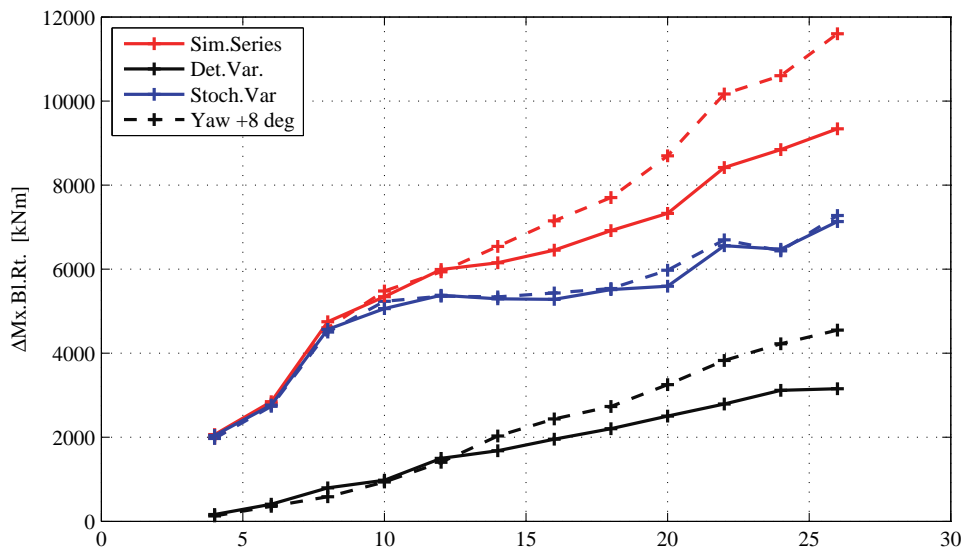


Figure 2. Blade root flapwise bending moment variations as function of mean wind speed. Simulated loads (red lines), deterministic load variation (black), stochastic load variation (blue). A case with yaw misalignment is given for comparison, dashed lines.

to estimate the load-variation capability required to smart-rotor actuators. Furthermore, the load variation due to deterministic component gives an estimate of the gain in load alleviation performances that could be achieved by including measured periodic disturbances in the smart-rotor controller, see for instance van Wingerden et al. [11].

3. Rain-flow counting fatigue analysis

Equivalent fatigue loads are computed from the loads time series by applying a rain-flow counting (RFC) algorithm, and Palmgren-Miner rule for linear fatigue damage accumulation [12]. The life

time equivalent fatigue loads account for the amount of time the turbine is expected to operate in each wind speed condition; the wind distribution follows a Rayleigh distribution with average speed of 8.5 m/s, as prescribed by the IEC standard for a class II turbine [10].

Figure 3 shows the equivalent fatigue loads for the blade root flapwise bending moment at different operating wind speed, and accounts for the amount of hours each wind speed is encountered during the turbine life-time. High wind speeds are less frequent than low ones, nevertheless, operation at high wind still causes the largest contribution to the life-time fatigue damage. The equivalent fatigue loads computed with a lower material exponent ($m = 8$ instead of 10) show nearly no change below rated speed, while for high winds, the fatigue loads are lower than with exponent 10, thus indicating larger fatigue contribution from wide range load cycles.

The same RFC analysis is performed on the time series obtained by subtracting the deterministic load variations (blue line with diamonds in fig. 3). The equivalent fatigue loads are lowered, especially at wind speeds above rated; the overall lifetime equivalent fatigue load is 11% lower than the lifetime fatigue load returned by the original time series. The measured fatigue reduction gives an estimate of the upper-limit to the fatigue-load alleviation that could be obtained by a smart-rotor control that only addresses cyclic load variations [13], and, at the same time, quantifies the importance of including periodic disturbances rejection in a smart-rotor control system.

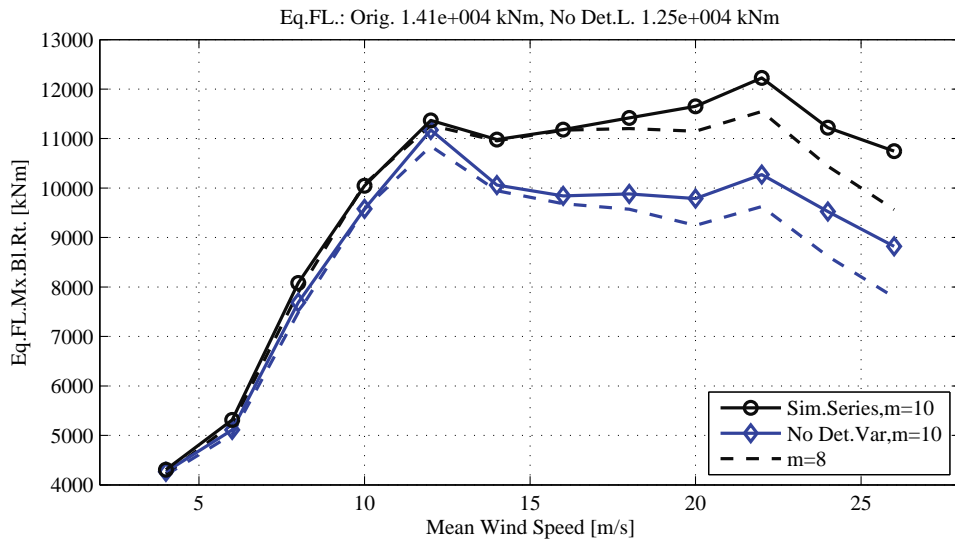


Figure 3. Blade root flapwise moment, equivalent fatigue loads for different mean wind speed operation (weighted by the wind distribution). Results for simulated loads (black line) and for series without deterministic load variations (blue lines).

A similar analysis is performed for the blade edgewise bending moment (fig. 5). As the fatigue damage is mainly gravity driven, it shows higher contributions for the wind speed bins that occur more frequently; furthermore, since the gravity load variation is periodic, the edgewise equivalent fatigue load for the time series without deterministic variation is less than half the original one.

Equivalent fatigue loads for the shaft tilting and yawing moments show higher contributions for wind speeds at, and above rated (fig. 6). The tower bottom flange fore-aft lifetime fatigue damage is mainly affected by operation at, and below rated wind speed (fig. 7); on the contrary, the side-to-side moment receives most of the fatigue contribution from wind speed above rated.

4. Spectral load characterization: Power Spectral Density

The Power Spectral Density (PSD) of the load time series is computed using Welch’s method as implemented in Matlab; the PSD obtained with different turbulence series for the same mean wind speed are then averaged together. A similar procedure is applied to the blade root moments time series where the deterministic variations of the load had been removed.

The blade root flapwise bending moment PSD (fig. 4) is characterized by high energy content around the rotational frequency ($1P = 0.2 \text{ Hz}$), and, less, at its first harmonic. The PSD rapidly decreases above 1-1.5 Hz, and its energy content is nearly insignificant above 2.5 Hz. The PSD of the series without deterministic loads variation shows, as expected, a marked reduction of the peak at the rotational frequency $1P$ (blue lines in fig. 4); nevertheless, the peak at $1P$ still dominates the spectrum, thus implying that the stochastic component of the loads accumulates spectral energy contributions that, for a rotating blade, are mainly located around the rotational frequency.

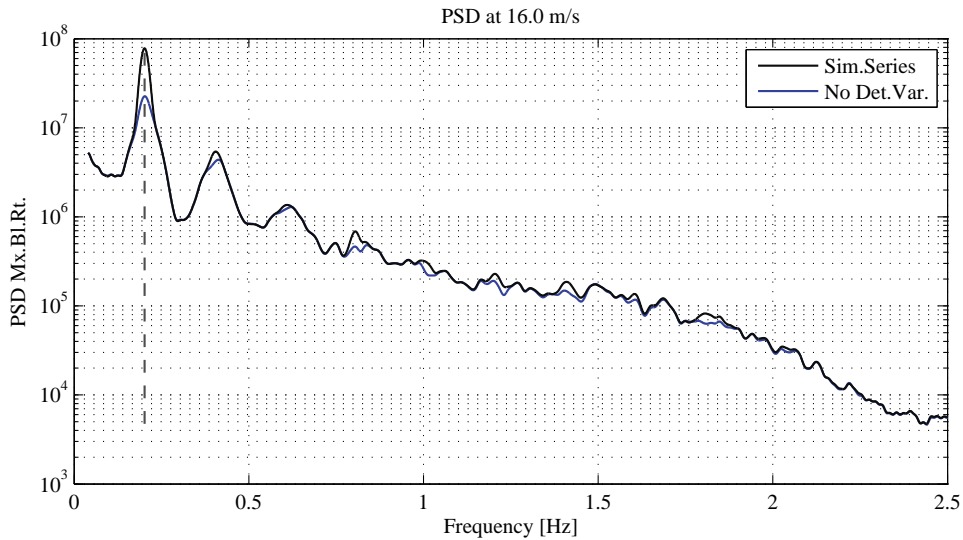


Figure 4. Blade root flapwise moment, Power Spectral Density (PSD) for the loads time series with mean wind speed of 16 m/s. Results for simulated loads (black line) and for series without deterministic load variations (blue lines).

5. Estimation of frequency contributions to fatigue damage

5.1. From PSD to fatigue damage ratio

Benasciutti and Tovo [14] propose a method to estimate the rain-flow fatigue damage from the stress power spectral density (PSD). The method is based on the assumption of Gaussian stationary process, and linear Palmgren-Miner rule for fatigue damage. The rain-flow fatigue damage ratio (D_{RFC}) is estimated as a weighted sum of the damage rate for a narrow-banded process (D_{NB}), and the range-mean counting damage (D_{RC}) [14]:

$$D_{RFC} = b_{wgt}D_{NB} + (1 - b_{wgt})D_{RC}. \quad (1)$$

The range-mean counting damage is approximated as a function of the narrow-band damage rate (D_{NB}), the second bandwidth parameter α_2 , and the fatigue strength exponent m :

$$D_{RFC} \approx b_{wgt}D_{NB} + (1 - b_{wgt})D_{NB}\alpha_2^{m-1} = (b_{wgt} + (1 - b_{wgt})\alpha_2^{m-1}) D_{NB}. \quad (2)$$

The expression for the narrow-band damage reads

$$D_{NB} = \frac{1}{S_0^m} \nu_0 \left(\sqrt{2\lambda_0} \right)^m \Gamma(1 + 0.5 m), \quad (3)$$

where S_0^m is the critical stress level, ν_0 is the rate of mean upcrossings, λ_i is the i -th spectral moment of the one-sided spectrum $W(\omega)$, and α_1 and α_2 are bandwidth parameters, as given in [14]. The factor b_{wgt} in eq. (1) determines the weight between the narrow-banded fatigue damage and the range-mean counting damage; Benasciutti and Tovo [14] suggest an expression derived from empirical data fitting for the weight value as a function of the first and second bandwidth parameters α :

$$b_{wgt} = \frac{(\alpha_1 - \alpha_2) [1.112 (1 + \alpha_1 \alpha_2 - \alpha_1 - \alpha_2) e^{2.11 \alpha_2} + \alpha_1 - \alpha_2]}{(\alpha_2 - 1)^2}. \quad (4)$$

The method proposed by Benasciutti and Tovo is applied to the spectra of the bending moments computed in the previous section. The equivalent fatigue damage rates obtained at each mean wind speed are weighted by the wind distribution function, so to obtain an indication of the relative contribution that operations at different mean speeds yield to the total life-time fatigue damage. The relative contributions obtained from the PSD method are compared to results from the rain-flow counting analysis (fig. 5 – 7); relative contribution returned under the narrow-banded process assumption (i.e. $b_{wgt} = 1$) are also plotted (red lines with squares).

In spite of fundamental differences between the two methods, the relative contributions computed by the frequency-domain PSD method are in good agreement with the figures from the time-domain RFC method. The strongest contributions to fatigue on the blade flapwise moment originate at high winds (fig. 5, left), whereas the blade edgewise (fig. 5, right), and the shaft bending moments (fig. 6), show higher contributions from wind speeds around rated, which are more frequent. The narrow-banded (NB) approximation returns estimations very close to the full model ones for the blade and shaft bending moments, while larger differences are observed on the tower relative contributions (fig. 7).

5.2. From PSD fatigue damage to frequency band contributions

The contribution to the total fatigue damage from a single frequency band df_j is estimated by comparing the equivalent fatigue damage computed on the full PSD, with the damage

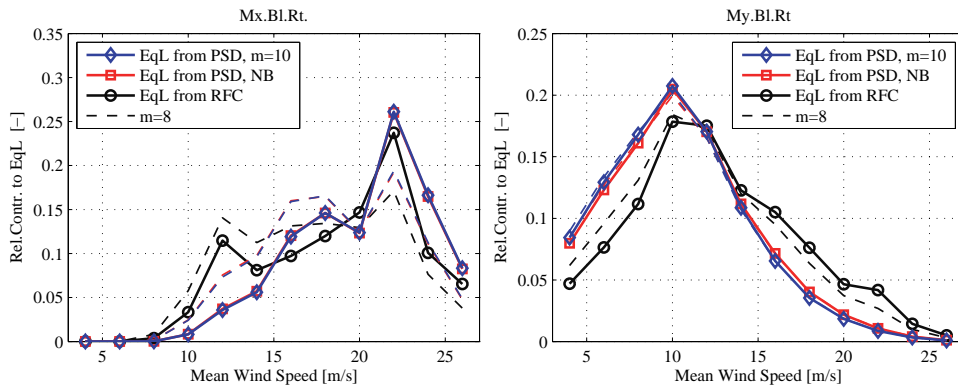


Figure 5. Blade root bending moments: flapwise (left), and edgewise (right). Relative contributions to the total lifetime fatigue damage from operation at different mean wind speed, from rain-flow analysis (RFC) and spectral methods.

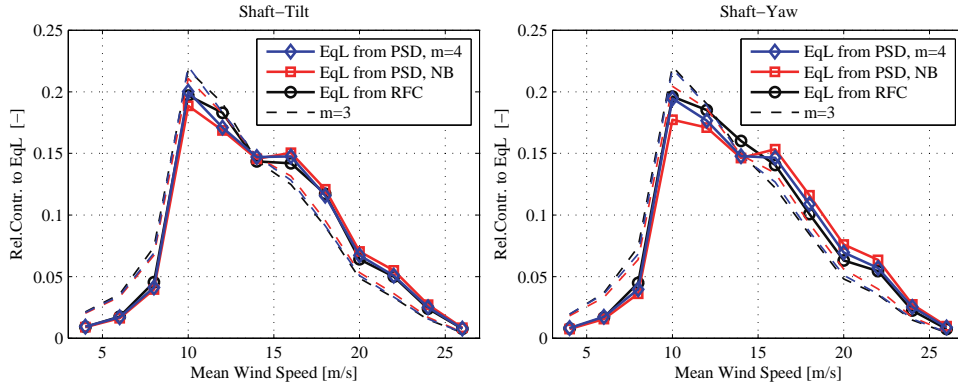


Figure 6. Shaft tilt (left) and yaw (right) moments, fatigue damage contributions from operation at different wind speed. Estimations from spectral and rain-flow counting methods.

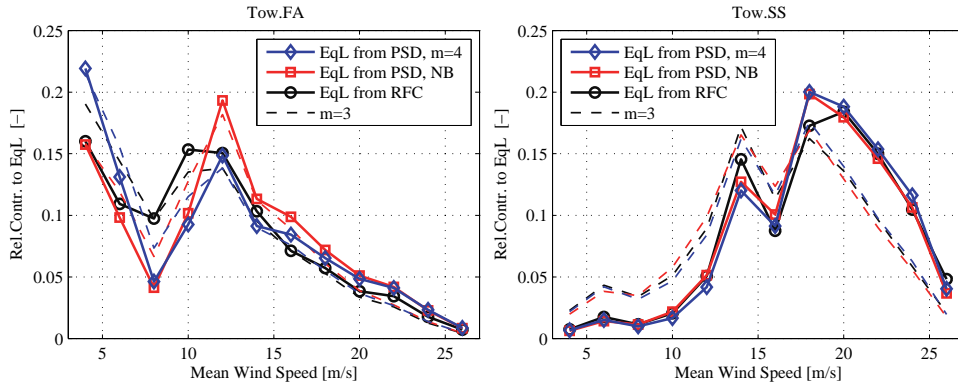


Figure 7. Tower bottom flange fore-aft (left) and side-to-side (right) bending moments, fatigue damage contributions from operation at different wind speed. Estimations from spectral and rain-flow counting methods.

resulting from a spectrum where the energy content at the frequency band df_j is set to zero. By repeating the same procedure for different frequency bins throughout the spectrum, is possible to characterize the frequency range of the loads that are responsible for the largest fatigue contributions.

To assess the validity of the spectral fatigue method, the results are compared with frequency contribution estimations based on RFC analysis of filtered time series. The series are filtered with a Butterworth low pass filter, and the RFC equivalent fatigue loads are computed for increasing cutoff frequency $f_{c,LPF}$ (fig. 8(a), top); as the cutoff frequency is raised, the fatigue loads converge to the ones of the original unfiltered time series.

The gradient of the curve gives an indication of the contribution brought to the total fatigue damage by loads in the specific frequency range (fig. 8(a), bottom), and provides a term of comparison for the frequency fatigue contribution computed with the spectral method, figure 8(b) top. The agreement between the two methods is rather good; in both cases the highest fatigue contributions are characterized by loads with frequency close to 1P, whereas very low fatigue contribution are reported for frequencies above 2 Hz. In the series where the deterministic variations of the loads have been removed (lighter colored lines) the contribution from frequencies around 1P is lower, but still remains the dominant one in the spectrum. A good agreement between the RFC results and the ones based on spectral analysis is also reported for the edgewise,

the shaft, and the tower bottom bending moments.

5.3. Fatigue damage spectrograms

The frequency contributions to the life-time fatigue damage are organized in ‘spectrogram-like’ plots, where the load frequency is on the abscissa, and the mean wind speed on the ordinate. The surface color gives a qualitative indication of the contribution to the overall fatigue damage: dark red colors indicate ‘harmful’ loads, heavily contributing to the fatigue damage; blue colors indicate ‘harmless’ loads. The dashed white lines highlight the 1P and 3P rotational frequencies.

Fatigue on the blade root flapwise bending moment (fig. 8(b)) is characterized by strong damage contributions from operation at high wind speed, and from loads with frequencies close to 1P; loads with frequencies above 2 Hz are found to be nearly ‘harmless’.

The shaft fatigue damage (fig. 9(a)) shows marked contributions close to 3P, and at the lower frequency range; the highest contributions to the life-time fatigue damage are reported from wind speed close to the rated one.

The spectrogram for the tower bottom fore-aft bending moment (fig. 9(b)) also displays clear fatigue contributions from loads with frequency of 3P; in addition, the contribution of frequencies close to the first tower mode (0.3 Hz) are also well marked. It is worth noticing the considerable fatigue damage contribution uprising at low wind speeds, where the 3P rotational frequency approaches the tower natural frequency.

6. Conclusion

The paper presents an analysis of the aeroelastic loads acting on a wind turbine during normal operation, and highlights the characteristics of the loads that are responsible for the strongest contributions to the fatigue damage.

The fatigue damage caused by deterministic load variations is estimated to be 11% of the total life-time damage, for the specific turbine model. The figure indicates the potential benefit of including deterministic (periodic) disturbance rejection in a smart-rotor control system. At the same time, it fixes an upper limit to the load alleviation achieved by purely cyclic control actions; information on the stochastic variations of the loads have to be included in the control algorithm to overcome this threshold.

The contribution to the blade root flapwise life-time fatigue damage from wind speeds above rated was found significantly higher than below rated conditions. It should be thus consider to exploit the control potentiality of a smart-rotor for different objectives below rated power, as, for instance, to increase the energy capture.

A method to characterize the load frequencies that cause the highest fatigue contributions is proposed, and proved reliable by comparison with rain-flow counting fatigue analysis. Results show that the loads inflicting the strongest fatigue damage on the blades are characterized by frequencies close to the rotational one, both in the case of deterministic, and stochastic load components. Accordingly, fatigue loads on fixed frames, as the shaft bearings or the tower bottom flange, show marked contributions from the 3P frequency; in addition, the fatigue damage on the tower receives important contributions also from loads with frequencies close to the structural ones. In all cases, only minor contributions are received from loads with frequency above 2 Hz, thus giving an indication on the bandwidth requirements for the active load alleviation system.

The paper identifies the loads that most heavily contribute to the structure fatigue damage. Active alleviation of these loads would return a direct benefit on the overall design requirements; the loads characteristics highlighted by the study can therefore provide useful indications for the future design of a smart-rotor with active load alleviation.

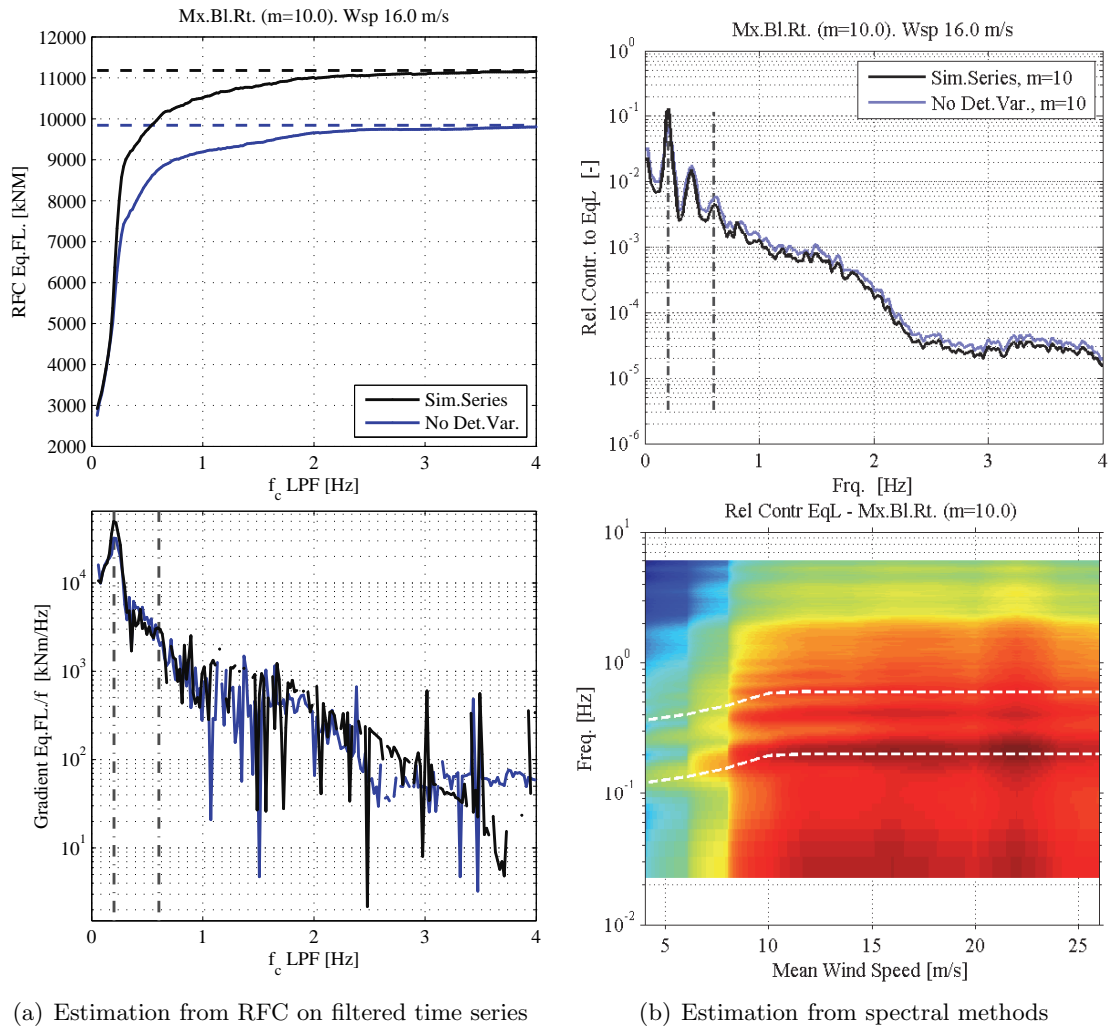


Figure 8. Blade root flapwise moment, frequency contribution to the total fatigue damage.

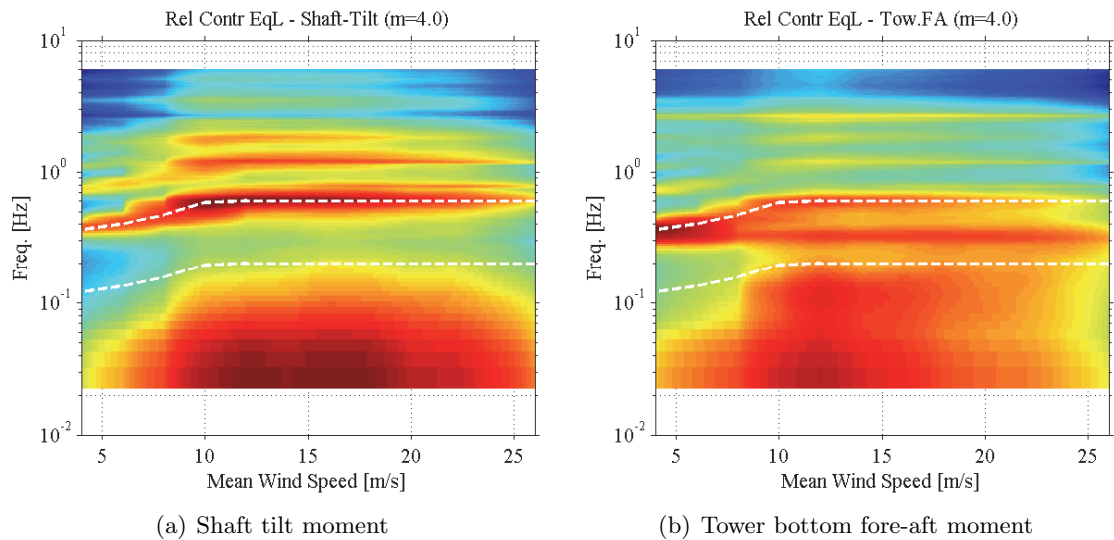


Figure 9. Spectrograms of the estimation of the frequency fatigue contribution.

References

- [1] Bossanyi E A 2003 *Wind Energy* **6** 119–128 ISSN 10954244
- [2] Larsen T J, Madsen H A and Thomsen K 2005 *Wind Energy* **8** 67–80 ISSN 10954244
- [3] Johnson S J, Baker J P, van Dam C P and Berg D 2010 *Wind Energy* **13** 239–253 ISSN 10954244
- [4] Andersen P B, Henriksen L, Gaunaa M, Bak C and Buhl T 2010 *Wind Energy* **13** 193–206 ISSN 10954244
- [5] Barlas T 2011 *Active aerodynamic load control on wind turbines: Aeroservoelastic modeling and wind tunnel* Ph.D. thesis TU Delft: Aerospace Engineering: Wind Energy Delft, Netherlands
- [6] Jonkman J, Butterfield S, Musial W and Scott G 2009 Definition of a 5-MW reference wind turbine for offshore system development Tech. Rep. NREL/TP-500-38060 National Renewable Energy Laboratory (NREL)
- [7] Larsen T J 2009 How 2 HAWC2 the user's manual Tech. Rep. R-1597(EN) Risoe National Laboratory. Technical University of Denmark
- [8] Bergami L, Gaunaa M and Heinz J 2012 *Wind Energy* Pre-print ISSN 1099-1824
- [9] Hansen M H, Gaunaa M and Madsen H A 2004 A Beddoes-Leishman type dynamic stall model in state-space and indicial formulations Tech. Rep. R-1354(EN) Risoe National Laboratory, Roskilde (DK)
- [10] International Electrotechnical Commission 2005 IEC 61400-1: Wind turbines part 1: Design requirements Tech. rep. International Electrotechnical Commission
- [11] van Wingerden J W, Hulskamp A, Barlas T, Houtzager I, Bersee H, van Kuik G and Verhaegen M 2011 *IEEE Transactions on Control Systems Technology* **19** 284–296 ISSN 1063-6536
- [12] Hansen M 2000 *Aerodynamics of wind turbines : rotors, loads and structure* (London: James & James) ISBN 9781902916064
- [13] Houtzager I, van Wingerden J W and Verhaegen M 2012 *Wind Energy* ISSN 1099-1824
- [14] Benasciutti D and Tovo R 2006 *Probabilistic Engineering Mechanics* **21** 287–299 ISSN 02668920

Article III

Aerodynamic response of an airfoil section undergoing pitch motion and trailing edge flap deflection: a comparison of simulation methods

The article was submitted for publication as research article to the *Wind Energy* journal in January 2013.

The content of the article is recalled in the synopsis sections related to:

- *ATEFlap Aerodynamic Model*, section 4.3: model validation by comparison with results from CFD and NTUA's viscous-inviscid interaction method
- *Adaptive Trailing Edge Flap rotor configuration*, section 5.1: characteristics and analytical expression for the flap deflection shape

RESEARCH ARTICLE

Aerodynamic response of an airfoil section undergoing pitch motion and trailing edge flap deflection: a comparison of simulation methods

Leonardo Bergami*, Vasilis A. Riziotis[‡], Mac Gaunaa*

* DTU Wind - Department of Wind Energy, Technical University of Denmark, Denmark.

[‡] Fluids Department, School of Mechanical Engineering, National Technical University of Athens, Greece.

ABSTRACT

The study presents and compares aerodynamic simulations for an airfoil section with an adaptive trailing edge flap, which deflects following a smooth deformation shape. The simulations are carried out with three substantially different methods: a Reynolds Averaged Navier-Stokes solver, a viscous-inviscid interaction method with single and double wake implementations, and an engineering dynamic-stall model suitable for implementation in aeroelastic codes based on Blade Element Momentum theory. The aerodynamic integral forces and pitching moment coefficients are first determined in steady conditions, at angles of attack spanning from attached flow to separated conditions, and accounting for the effects of flap deflection. The paper characterizes then the dynamics of the unsteady forces and moments generated by the airfoil undergoing harmonic pitching motions, and harmonic flap deflections. The dynamic responses produce important variations of the aerodynamic coefficients over their corresponding steady values. The dynamics characteristics of the unsteady response are predicted with an excellent agreement among the investigated methods in attached flow conditions, both for airfoil pitching and flap deflection. For higher degrees of flow separation, the methods still depict similar overall dynamics, but larger discrepancies are reported, especially for the simpler engineering method.

Copyright © 2012 John Wiley & Sons, Ltd.

KEYWORDS

Adaptive Trailing Edge Flap; Unsteady aerodynamic modeling; Numerical methods for Smart Rotors

Correspondence

Leonardo Bergami, DTU Wind, Risø Campus, Frederiksborgvej 399, 4000 Roskilde, Denmark. Email: leob@dtu.dk

Received . . .

1. INTRODUCTION

Several research projects have highlighted the potential benefits of a new generation of wind turbine rotors, which would allow for enhanced active load alleviation by including active aerodynamic devices distributed along the blades [1, 2]. Active aerodynamic devices are able to alter the aerodynamic forces locally along the blade span by modifying the geometry of the airfoil section; they thus allow to vary the aerodynamic loading on the whole blade, without acting on its pitch angle. Particularly promising results in terms of fatigue load alleviation have been reported by simulations considering adaptive trailing edge flap (ATEF) devices [3, 4, 5, 6]. The adaptive trailing edge flap modifies the geometry

of the airfoil by deflecting the aft portion of its camber-line; Trolborg et al. [7] have shown that deflections following a smooth continuous deformation shape return better aerodynamic performances compared to a classic rigid flap rotating around its hinge point.

The presence of the active flaps poses new challenges to the aerodynamic models used in the design and aeroelastic simulation of the turbine response; the steady aerodynamic forces and moment on the blade sections as well as their unsteady dynamics will in fact depend not only on the section angle of attack, but also on the flap deflection. Previous studies have addressed the problem of simulating unsteady aerodynamic forces on an airfoil section with flaps by using, among others, Navier-Stokes solvers [8, 9], panel code methods [10], viscous-inviscid interaction models [11, 12], and simpler engineering methods, which considered either quasi-steady approximations [13], or attached flow models [3, 14], or dynamic-stall type of models [15, 5]. On account of their lower computational requirements, engineering methods have often been integrated in Blade Element Momentum (BEM) based aeroelastic codes, allowing thus to simulate the full response of a turbine with active flaps.

The paper considers three state-of-the-art methods to simulate the integral aerodynamic forces and moment coefficients of a 2D airfoil section undergoing pitching motion, and trailing edge flap deflections. The methods are, in decreasing order of computational requirements: *EllipSys 2D*, a Reynolds Averaged Navier-Stokes (RANS) solver [9]; *NTUA* viscous-inviscid interaction method [16] with a double wake, and a single wake implementation; *ATEFlap*, a dynamic-stall engineering model [17].

The aim is to characterize the unsteady aerodynamic response of the airfoil to changes in the angle of attack or the flap deflection, and to compare the responses simulated by the three methods. Similarities and differences among the simulated responses provide an indication of the codes modeling performances; in particular, the comparison of the simpler *ATEFlap* dynamic-stall model against more complex methods will serve to validate the model capabilities, and to highlight its limitations. The *ATEFlap* model, thanks to its low computational requirements, can be conveniently integrated in a BEM-based aeroelastic simulation tool, and thus employed to design and assess the response of a wind turbine with active flaps. The paper further develops the code comparison task carried out initiated within the frame of the UpWind European project, work package 2 “Aerodynamics and aero elastics” [18].

The following section briefly describes the investigated methods, and their prominent characteristics, thorough descriptions are provided in the bibliographic references. Section 3 lists the specification of the test case considered in the simulations, and describes the airfoil and trailing edge flap set-up. Aerodynamic forces for different angles of attack and flap deflections are first computed with *EllipSys* and the *NTUA* codes in steady conditions; the results, presented in section 4, serve as input to the *ATEFlap* model. Simulations are then performed for the airfoil undergoing prescribed harmonic pitching motion, and harmonic flap deflection; the aerodynamic response is simulated at different mean angles of attack, covering attached flow conditions, separation onset, and stalled flow, section 5.

2. COMPUTATIONAL METHODS

2.1. *EllipSys*

EllipSys 2D is a CFD (Computational Fluid Dynamic) code originally developed by Michelsen [19, 20], and Sørensen [21]. The code solves the incompressible Reynolds Averaged Navier-Stokes (RANS) equations in general curvilinear coordinates, using a multiblock finite volume discretization. The computations shown in this work are all carried out under the assumption of fully turbulent flow, and applying the $k-\omega$ Shear Stress Transport (SST) eddy-viscosity turbulence model from Menter [22].

The motion of the airfoil is simulated by moving the computational grid, and accounting for the additional fluxes that are generated as the grid cells vertices are displaced. The flap deflection is modeled through a grid morphing routine [9], where the position of the grid points for an arbitrary flap deflection are determined by linear interpolation of the two meshes

generated with the flap at maximum upwards and downwards deflection ($\pm 5^\circ$ in this study); the additional fluxes caused by the displacement of the cell vertices are also accounted for.

Among the investigated methods, the EllipSys RANS solver is the one with the highest computational requirements: simulations of a 10 seconds time series of the aerodynamic forces on a typical 2D airfoil section, as the one presented here, require approximately 3 minutes when parallelized on 4 CPUs.

2.2. NTUA 1W and NTUA 2W

NTUA 1W and NTUA 2W are viscous-inviscid interaction codes that have been developed at NTUA [23, 12, 16]. In both codes the potential flow part is simulated by singularity distributions along the airfoil geometry and along the wake (sources and vortices). The wake is represented by vortex particles (point vortices), which are allowed to freely move with the local flow velocity (free wake approach). The viscous flow solution is obtained by solving the unsteady integral boundary layer equations. The coupling of the two sets of equations is achieved through a transpiration velocity distribution along the airfoil surface that represents the mass flow difference over the boundary layer height between the real viscous flow and the equivalent inviscid flow. The boundary layer equations are discretized using finite differences, and the final set of non-linear equations (potential and boundary layer) is solved simultaneously using Newton-Raphson algorithm. The boundary layer solution is supplemented by a transition prediction model based on the e^N spatial amplification theory, and by a dissipation closure equation for the maximum shear stress coefficient C_t over the turbulent part.

The main difference between the NTUA 1W and NTUA 2W codes is that in NTUA 1W the boundary layer equations are integrated over the whole airfoil surface and the trailing edge wake, while in NTUA 2W they are only solved up to the position where flow separation takes place. Thereafter, a second vortex sheet is shed from the separation location and interacts with the trailing edge vortex sheet; together they form the separation bubble. By introducing this second vortex sheet, convergence of the solution can be achieved even in deep stall conditions. This is the main advantage of the double wake approach against conventional boundary layer methodologies.

Among the different methods tested in the paper, NTUA 1W and NTUA 2W models are intermediate in terms of computational cost. A 10 seconds simulation of a 2D airfoil is resolved in about two minutes on a single CPU. Although the simulation gets slower, as the number of particles in the wake increases, hybrid wake acceleration techniques have been developed with the aim to keep computational effort constant [24].

2.3. ATEFlap

The ATEFlap is an engineering model, which couples a potential flow solution with a Beddoes-Leishmann-type dynamic stall model. The model develops, and partially amends the shortcomings of the dynamic-stall model presented in Andersen et al. [15]; a more detailed description is reported in Bergami and Gaunaa [17].

The potential flow part of the model is based on Gaunaa's [25] model for a thin airfoil undergoing arbitrary motion and camber-line deformation; the dynamics effects on the circulatory forces are described through a superposition of indicial response functions of the Wagner type. The indicial response function is formulated in exponential terms to allow for an efficient time integration scheme, and the function coefficients are tuned to fit the indicial response of the investigated airfoil, table I, as it differs from Jones's standard flat-plate response [26].

Flow separation dynamics are represented by a Beddoes-Leishmann type dynamic stall model, as described in Hansen et al. [27], where the total circulatory lift force is computed as a weighted sum of a fully attached contribution, and a fully separated one. The separation dynamics are enclosed in the weight factor of the sum, which result from a sequence of two first-order low-pass filters, whose time constants depend on two non-dimensional parameters τ_P and τ_B [27, 17]. The values used in the computations are reported in table I.

The model requires as input the airfoil steady integral forces and moment coefficients at various angles of attack, as well as the coefficient variations caused by steady flap deflections. In the study, three set of steady input referring to the same airfoil and flap configuration are considered: one generated from steady computations with EllipSys 2D, and two sets retrieved from steady simulations with the NTUA code, using either the single or the double wake configuration.

A_i	0.1784	0.07549	0.3933	τ_P	1.5
b_i	0.8000	0.01815	0.1390	τ_B	6.0

Table I. Computation set-up for the ATEFlap dynamic-stall model. Indicial lift response function coefficients for NACA 64-418 airfoil, and dynamic stall non-dimensional time parameters.

Simulations with the ATEFlap model have very low computational requirements, rendering the model particularly attractive for implementation in time marching aeroelastic simulation codes [17]; as an indication, a 10 seconds simulation of unsteady forces on a 2D airfoil section is resolved in less than one second on a single CPU.

3. TEST CASE

The airfoil considered in the study has a NACA 64-418 profile, and is fitted with an adaptive trailing edge flap, which extends for the last 10% of the chord. At null flap deflections, the airfoil has the standard NACA 64-418 profile, while positive flap angles corresponds to a downwards deflection of the trailing edge (increased lift), and vice-versa for negative flap angles, figure 1.

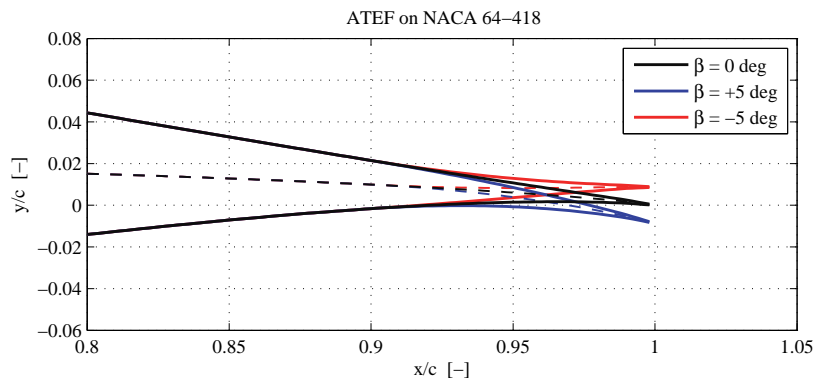


Figure 1. Camber-line deformation corresponding to flap deflections of $\pm 5^\circ$ on the investigated NACA 64-418 airfoil profile.

The deflection of the flap is modeled as a deformation of the camber-line, leaving the airfoil thickness unchanged. The camber-line points are displaced normally to the chord-line by a distance $\Delta y_{\text{amb}} = \beta \cdot y_{fl}$, where β is the flap deflection (in degrees), and the function y_{fl} describes the flap deflection shape, i.e. the camber-line variation for a unitary flap deflection. The deflection shape for a unit chord length airfoil is defined as a circular arc starting at 90 % of the chord length; the radius of the circle is set so that the line connecting the point on the arc at the trailing edge with the flap starting point forms an angle of 1 degree with the undeformed chord-line, figure 1:

$$y_{fl}/c \begin{cases} y_{fl}/c = 0.0 & \text{for } x/c < 0.9 \\ y_{fl}/c = \sqrt{R_c^2 - (x/c - 0.9)^2} - R_c & \text{for } x/c \geq 0.9 \end{cases} \quad (1)$$

where the radius of the circular arc is given by

$$R_c = \frac{0.1^2 + \delta_y^2}{2\delta_y}, \quad (2)$$

$$\delta_y = 0.1 \tan(1 \cdot \pi/180). \quad (3)$$

Simulations are carried out for the airfoil undergoing harmonic variations of the angle of attack (aoa), obtained by prescribed pitch motion with respect to a rotation axis located at the quarter-chord of the airfoil. A combination of different amplitudes and mean angles of attack is considered, table II, spacing from fully attached to stalled flow conditions. Additional simulations evaluate the response to prescribed harmonic flap deflections of various amplitudes, table II, and with the airfoil fixed at the same mean angles of attack as specified before; note that, in this study, the airfoil angle of attack is always defined with respect to the chord-line corresponding to the undeflected flap.

The simulations are replicated for harmonic variations with three reduced-frequencies k , also listed in table II. The reduced-frequency is a dimensionless quantity, which gives an indication of the degree of ‘unsteadiness’ of the aerodynamic problem; it is defined as

$$k = \frac{\omega b_{hc}}{U_\infty}, \quad (4)$$

where ω is the frequency of the harmonic variations, b_{hc} is the half-chord length, and U_∞ the free-stream flow speed. The investigation comprises reduced frequencies that fall within the intervals of what are typically defined as quasi-steady ($k = 0.02$), unsteady ($k = 0.1$), and highly-unsteady ($k = 0.5$) conditions; the first two values corresponds to the reduced frequencies typically encountered on wind turbine blades in relation to the rotational frequency. All the simulations are carried out with a Reynolds number of six millions based on the airfoil chord.

Mean Aoa	[deg]	0, 8, 12, 16, 18
Aoa ampl.	[deg]	0.5, 1.0, 2.5
Flap ampl.	[deg]	1.0, 2.0, 5.0
Red.frq. k	[-]	0.02, 0.1, 0.5

Table II. Test matrix for the code comparison unsteady simulations. Each combination of mean angle of attack and oscillation amplitude (for either the angle of attack or the flap) is replicated for each of the three reduced frequencies.

4. STEADY AERODYNAMIC RESPONSE COMPARISON

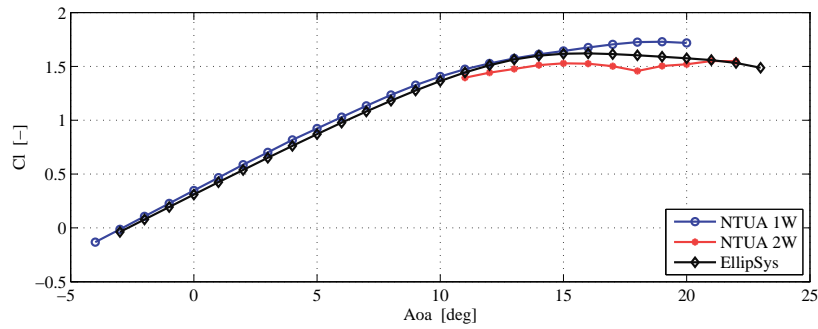
The steady aerodynamic responses of the airfoil and flap are simulated with EllipSys, and the NTUA codes, with single (1W), and double wake (2W) configurations; the double wake implementation is considered exclusively in separated flow conditions, for angles of attack from 11 to 22 degrees. The steady data provide a baseline indication of the unsteady loops mean values; as the three methods return different steady responses, each method will provide a separate set of steady input data for the ATEFlap model.

The steady responses are presented first for the airfoil with the flap fixed in neutral position, thus corresponding to a standard NACA 64-418 profile; the steady effects of flap deflection are then reported as variations around the baseline values for the integral aerodynamic forces and moment at different angles of attack.

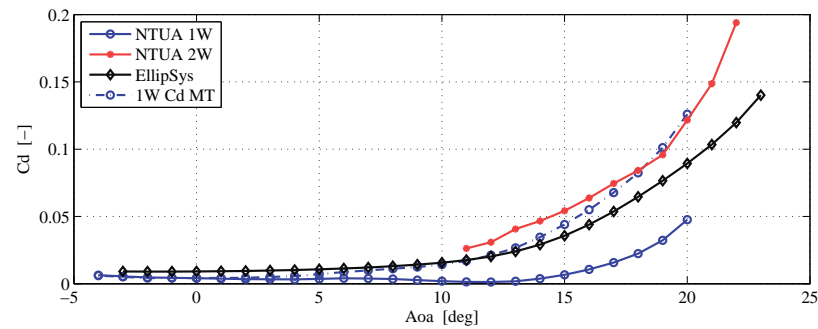
4.1. Baseline airfoil

The steady lift coefficients returned by EllipSys and NTUA 1W are in very good agreement in the attached flow linear region, figure 2(a); the curves have nearly the same slope, and only a small offset on the angle of attack corresponding to zero lift. The agreement deteriorates at higher angles of attack, where, due to more pronounced flow separation, the thin wake assumption made in the single wake method is no longer valid, and the NTUA 1W code returns higher lift values. The double wake method returns slightly lower lift coefficients, with a marked dip around 18° not seen in the EllipSys results.

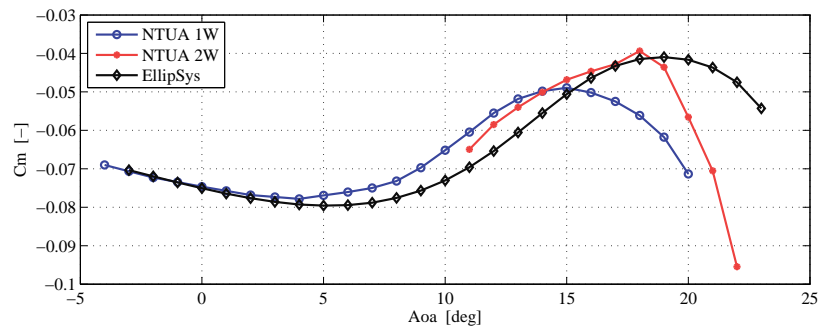
The prediction of drag forces, figure 2(b), is more problematic for the boundary layer methods, as the drag force returned by direct pressure integration is biased by the suppression of the streamline curvature effects [12]. The bias is particularly marked in the NTUA 1W response, which predicts very low drag coefficients, initially decreasing with the



(a) Lift Coefficient



(b) Drag Coefficient. The steady drag computations based on momentum theory for the NTUA 1W result are included for comparison (1W Cd MT).



(c) Moment Coefficient

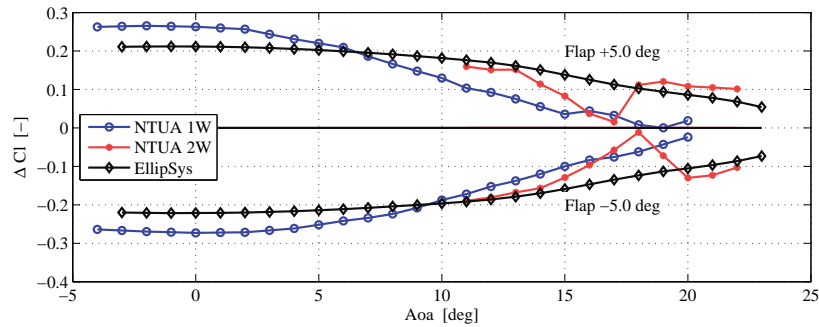
Figure 2. Steady aerodynamic response for the NACA 64-418 and flap in neutral position.

angle of attack. The drag coefficients returned by the momentum equation applied to a control volume around the airfoil are in better agreement with the CFD results, although the drag increase at higher angles of attack is more marked, as shown by the dashed blue line in figure 2(b); a steep drag increase at high angles of attack is also reported in the NTUA 2W results, red line in figure 2(b).

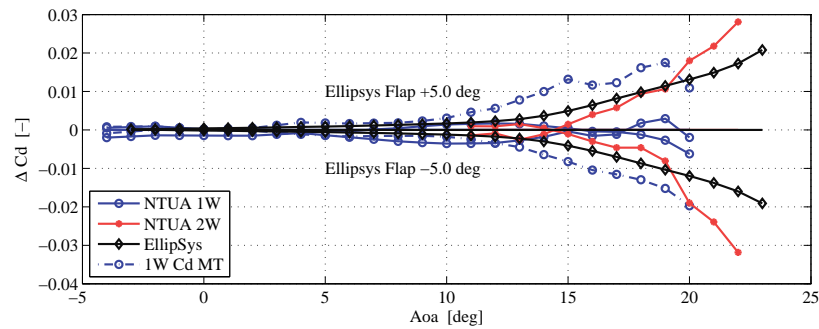
The three codes agree in predicting negative (‘nose-down’) aerodynamic moments, figure 2(c) and display similar trends of the moment coefficient versus angle of attack, although, especially at higher angles, the coefficient values predicted by the codes are rather different.

4.2. Trailing edge flap variations

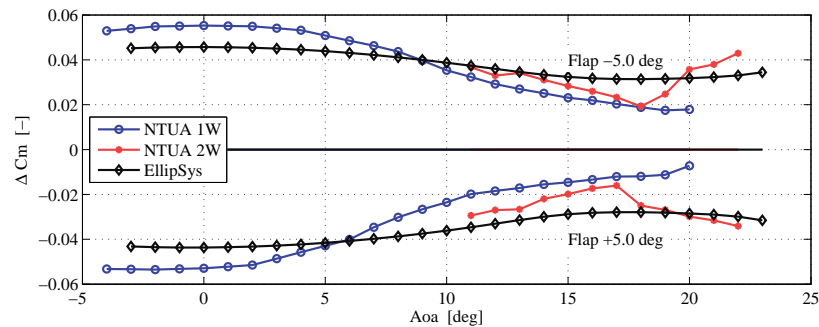
The steady aerodynamic responses to trailing edge flap deflection are presented as variations of the steady coefficients from the baseline airfoil with undeflected flap.



(a) Lift Coefficient



(b) Drag Coefficient. The steady drag computations based on momentum theory for the NTUA 1W result are included for comparison (1W Cd MT).



(c) Moment Coefficient

Figure 3. Steady aerodynamic response for flap deflection. The steady effects are expressed in terms of variations from the aerodynamic coefficients of the airfoil with undeflected flap.

The maximum lift increase predicted by EllipSys for $+5^\circ$ flap deflection is approximately equivalent to an increase of angle of attack of 1.8° , figure 3(a). NTUA 1W predicts higher maximum lift variations (equivalent to a 2.3° increase in angle of attack), and a marked decline of the flap effects with increasing angle of attack, especially for positive flap deflections: at 10° angle of attack the lift variation is already half the maximum one. The decline predicted by EllipSys is smoother, the flap effects are halved above 17° aoa, and nearly symmetric for positive and negative flap deflections. For higher angles of attack, NTUA 2W returns steady lift variations that are on average closer to EllipSys results, but displays a marked dip around 18° aoa, which has no correspondence in EllipSys, figure 3(a).

The drag predictions from direct pressure integrations of the boundary layer methods are affected by the same bias discussed in the previous section, and the single wake code returns a decrease in drag for positive flap deflections, figure 3(b). The results based on the momentum theory are closer to EllipSys, and both methods indicate that for lower angles of attack the flap deflection does not involve significant drag variations. As the angle of attack is increased and the flow

starts to separate, the steady drag variation produced by the flap is increased, rather mildly according to EllipSys, whereas a steeper increase of the drag penalty is predicted by the NTUA 1W momentum theory and NTUA 2W results, dashed blue and red lines in figure 3(b).

The variation in the aerodynamic moment, figure 3(c), resemble the variations in the lift coefficient, with NTUA 1W predicting larger variations at low angles of attack, but also a steeper decrease. Note that a positive flap deflection, which would displace the trailing edge downwards, results in an increase in lift and drag, and in a negative (i.e. 'nose-down') aerodynamic moment.

5. UNSTEADY RESPONSE COMPARISON

5.1. Harmonic pitching motions

The simulation capabilities of the codes are evaluated in dynamic conditions by first comparing the unsteady aerodynamic responses in the ordinary case of an airfoil undergoing harmonic pitch variations, while the flap is fixed to its neutral position. The responses from the ATEFlap model consider three sets of input data, which are generated from the steady responses computed by, respectively, EllipSys, NTUA 1W, and NTUA 2W. As the drag based on momentum theory is not available in dynamic conditions, the NTUA 1W drag data refer to the pressure integration results, and will reflect the biases already observed in the steady responses.

The codes show an excellent agreement when simulating the dynamics of the unsteady lift force in attached flow conditions, figure 4. All the methods characterize the unsteady lift with counter-clockwise loops (the loop direction is marked in the plots by the sequence of a larger and a smaller mark), with an effective slope slightly below the steady curve one; the differences in lift coefficients observed in the steady simulations, fig. 2(a), is reflected in the offset between the loops. The ATEFlap engineering model performs very well, and returns unsteady lift responses that overlie the corresponding curves. Both EllipSys and NTUA 1W predicts similar dynamics on the drag force, figure 4, while the responses from ATEFlap display loops with similar slopes, but slightly wider openings, and thus larger drag variations. The moment coefficient loops have small differences in slopes, as also observed in the steady data; as in the drag case, the ATEFlap code overestimates the dynamic effects and returns wider loops. The curve from NTUA 1W is corrupted by some wiggles, which originate from numerical instabilities in the boundary layer solution close to the transition point, and from the transition point traveling along the airfoil surface and switching to a different panel along the suction side.

By further increasing the reduced frequency to $k = 0.5$, figure 5, the unsteady lift responses trace loops with lower slopes, wider opening, and direction changed to clockwise; all the methods return similar changes in the dynamics, and the agreement with the ATEFlap is only slightly worse than in the previous case. The unsteady drag response displays a 'knot' in the loops, captured both by EllipSys and NTUA 1W; ATEFlap fails to predict this feature, and returns loops with wider openings in the drag and moment coefficients.

For harmonic oscillations of reduced frequency $k = 0.1$ around 12° aoa, figure 6, the influence of dynamic stall effects on the aerodynamic responses is evident, as the unsteady lift coefficients reach higher values than their steady counterparts; the effect is well captured by all models. ATEFlap returns loops with similar slope and openings for both steady input sets, and it is in fairly good agreement with EllipSys; NTUA 1W predicts larger lift variations. Apart from the offset observed in the steady data, the dynamics on the drag coefficient predicted by EllipSys and NTUA 1W are in good agreement, whereas ATEFlap overestimates the opening and slopes of the loops and, as for lower angles of attack, returns larger drag variations, figure 6. The wiggles in the drag and moment responses from NTUA 1W are again related to numerical instabilities from the transition point travelling and the boundary layer solution in its proximities.

As the angle of attack is increased, flow separation along the airfoil becomes more marked, and the thin-wake assumption is no longer valid; the NTUA 2W double-wake implementation is thus necessary to avoid significant biases in the response predicted by the viscous-inviscid interaction method. Figure 7 displays the responses simulated in the challenging case of well developed stalled conditions, harmonic pitch motion occurring around 18° aoa, with a reduced

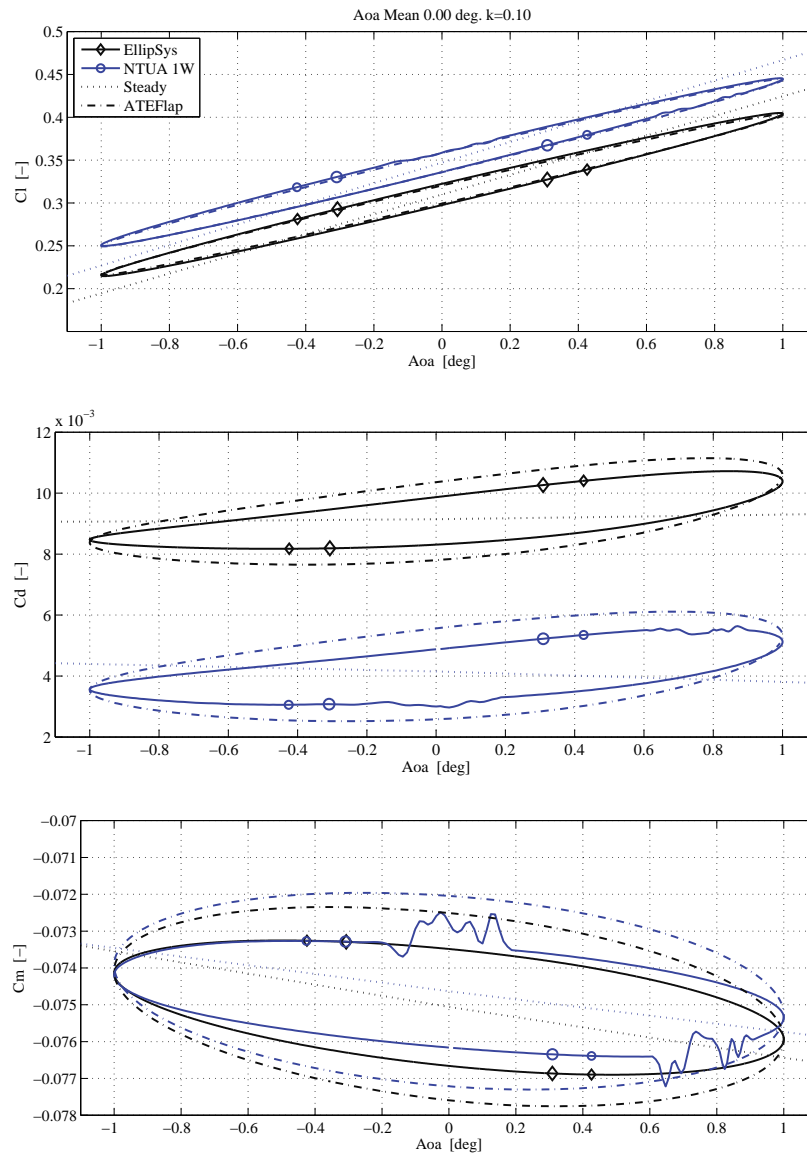


Figure 4. Attached flow conditions. Unsteady aerodynamic response for harmonic pitching motion around 0° aoa, reduced frequency $k = 0.1$. The markers show the direction of the dynamic loops, unfolding from larger to smaller markers. Unless otherwise specified, the ATEFlap loops have the same direction as the corresponding loops from EllipSys or NTUA codes.

frequency $k = 0.1$, and an amplitude of $\pm 2.5^\circ$. Besides the offset already observed in the steady data, the numerical methods EllipSys and NTUA 2W return similar dynamic responses: the unsteady lift loops have steeper slopes than the corresponding steady curves, and displays a total lift variation much higher than the corresponding steady one, due to stall hysteresis effects; on the contrary, the drag coefficient loops have less steep slopes and smaller drag variations than given by the steady curves, figure 7.

EllipSys and NTUA 2W display similar high frequencies oscillations in the down stroke response, which are caused by unsteady vortex shedding in the wake of the airfoil, resembling the classic von Karman vortex street behind a cylinder. The agreement with ATEFlap is deteriorated in such highly separated flow conditions. The engineering model predicts correctly the direction of the loops, but has a tendency to under-predict the variations in the lift force, and to over-predict the drag dynamics in comparison to the results of the more complex models. The moment variations predicted by ATEFlap

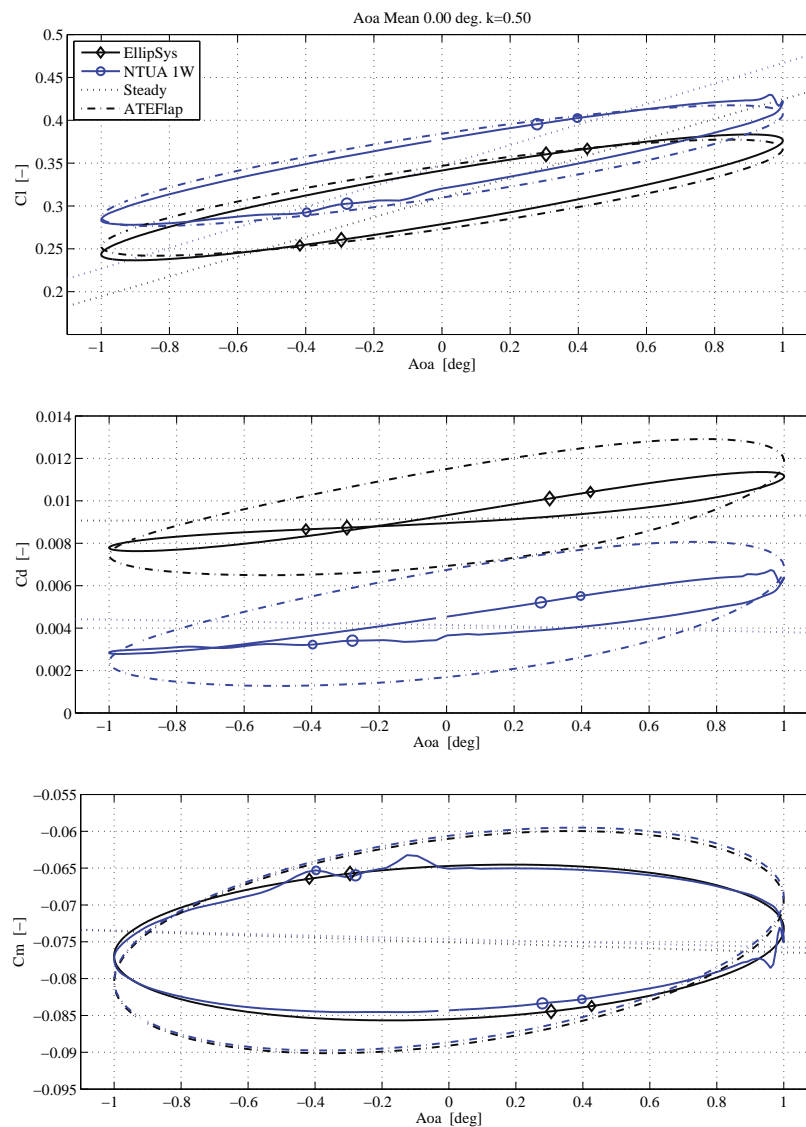


Figure 5. Attached flow, highly unsteady conditions. Unsteady aerodynamic response for harmonic pitching motion around 0° aoa (attached flow), reduced frequency $k = 0.5$. The ATEFlap results trace clockwise loops for the lift and drag, and counterclockwise loops for the moment coefficients.

have a similar range as in EllipSys and NTUA 2W, but a different phase, thus yielding to different slopes in the dynamic loops.

5.2. Harmonic flap deflections

The ability of the codes to describe the dynamic effects of the flap motion is determined by comparing the unsteady responses for the airfoil undergoing harmonic flap deflections, while the angle of attack is maintained unchanged; a few representative cases are discussed in the following paragraphs.

The flap deflection generates unsteady aerodynamic forces with dynamics similar to the ones caused by variations in angle of attack. In attached flow, figure 8, the lift force delineates dynamic loops with an effective slope slightly below the steady one; as the deflection frequency increases, the effective slope is further reduced. The ATEFlap engineering model shows excellent agreement with the unsteady lift simulated by the numerical models, figure 8, while the dynamics on the

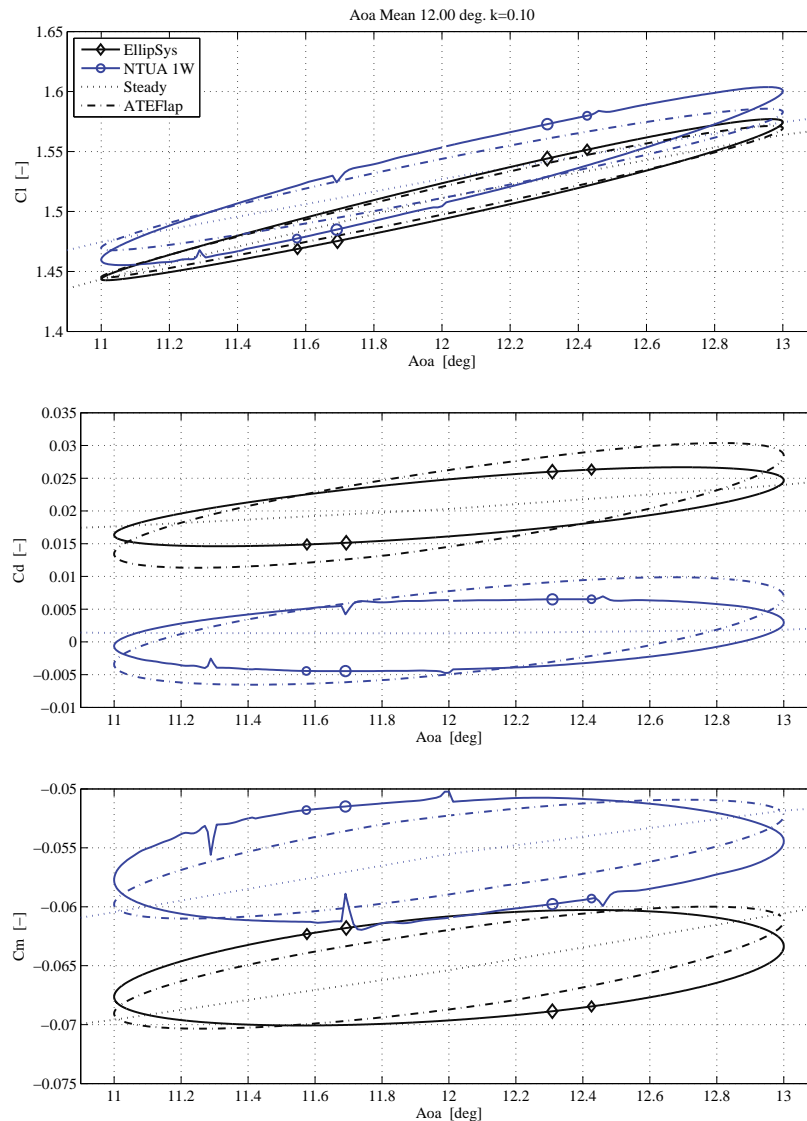


Figure 6. Separation onset. Unsteady aerodynamic response for harmonic pitching motion around 12° aoa, reduced frequency $k = 0.1$. The ATEFlap loops have the same direction of revolution as the corresponding loops from EllipSys or NTUA 1W.

drag force are slightly over-estimated; a good agreement on the lift force prediction is also maintained at higher reduced frequencies, not shown here. All models agree in predicting moment coefficient responses where the steady variation caused by the flap deflection is by far dominant over the dynamic effects; the loops outlined by the dynamic responses remain very close to their steady curve values, as also predicted by thin-airfoil theory. The offsets between the mean values of the dynamic response loops reflect the difference in the airfoil steady coefficients (see fig. 2), whereas the differences in the slopes are related to the steady coefficient variations given by the flap deflection (see fig. 3).

At higher angles of attack, figure 9, the reduction of the flap effects on the lift force returns both steady curves and dynamic lift loops with less steep slopes than reported in the attached flow case; the reduction is particularly evident on the NTUA 1W simulations. All the models, including ATEFlap, display good agreement on the drag response simulations, which maintain similar dynamics to the ones observed at lower angles of attack.

The ATEFlap model, while correctly reproducing the lift dynamics predicted by EllipSys, shows an interesting mismatch in the lift response based on the NTUA 1W steady data: the loop simulated by ATEFlap is much closer to

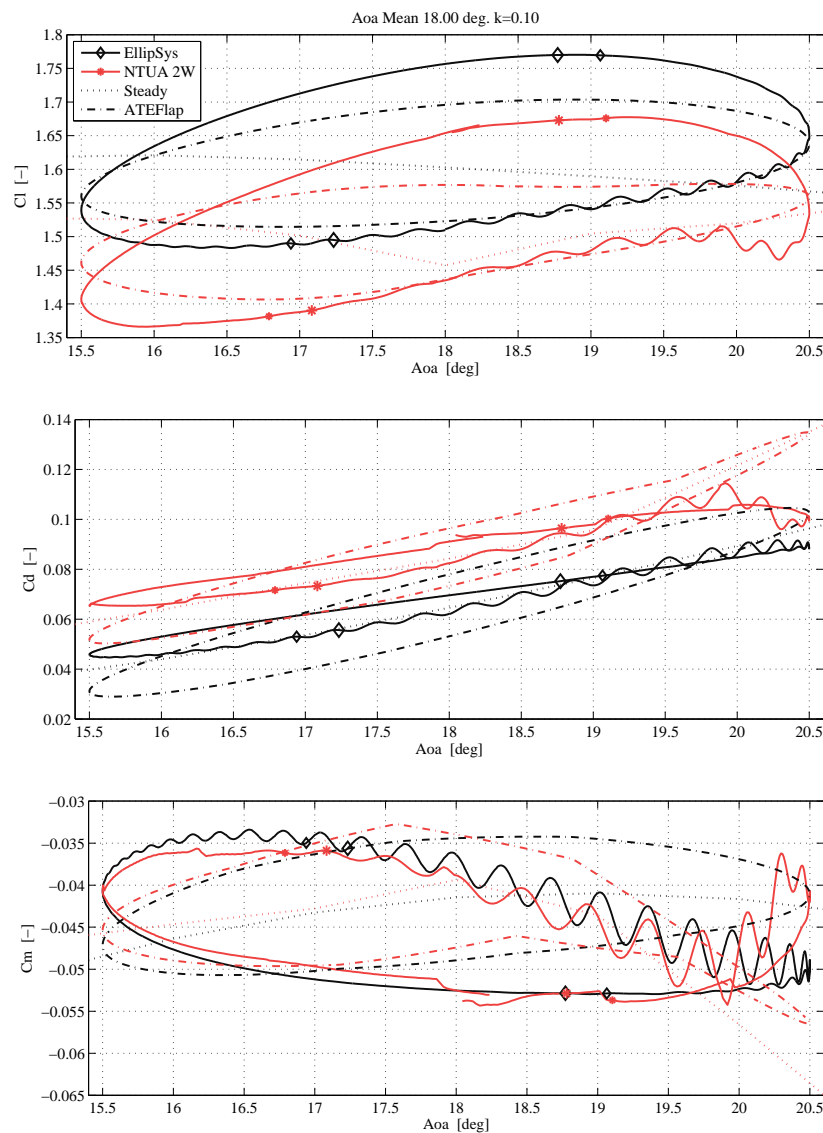


Figure 7. Airfoil in stalled conditions. Unsteady aerodynamic response for harmonic pitching motion around 18° aoa, reduced frequency $k = 0.1$. The ATEFlap loops have the same direction of revolution as the corresponding loops from EllipSys or NTUA 2W.

the steady curve and rotates clockwise, figure 9. The cause of the mismatch roots in the steady input data, where, for higher angles of attack, NTUA 1W predicts a more marked reduction of the steady lift variation achieved by the flap than EllipSys does, see fig. 3(a); the reduction in the flap lift effectiveness is reckoned by the ATEFlap model as caused by flow separation, consequently, the model assumes the degree of flow separation to vary considerably as the flap deflection changes. The lift response predicted by ATEFlap based on the NTUA 1W data at 12° aoa is thus largely affected by flow separation dynamics, which are not present to such an extent in the corresponding unsteady simulations by NTUA 1W. As the flow separation dynamics are much slower than the attached flow ones, the lift response from ATEFlap and the corresponding NTUA 1W loop display a considerable mismatch. A comparison with experimental data reproducing this particular condition would be of greatest interest.

At an angle of attack of 16° , which is above the maximum lift one, the lift response loops get closer to the steady curves, figure 10; the behavior is captured by all models, although ATEFlap returns loops with slightly lower slopes, and

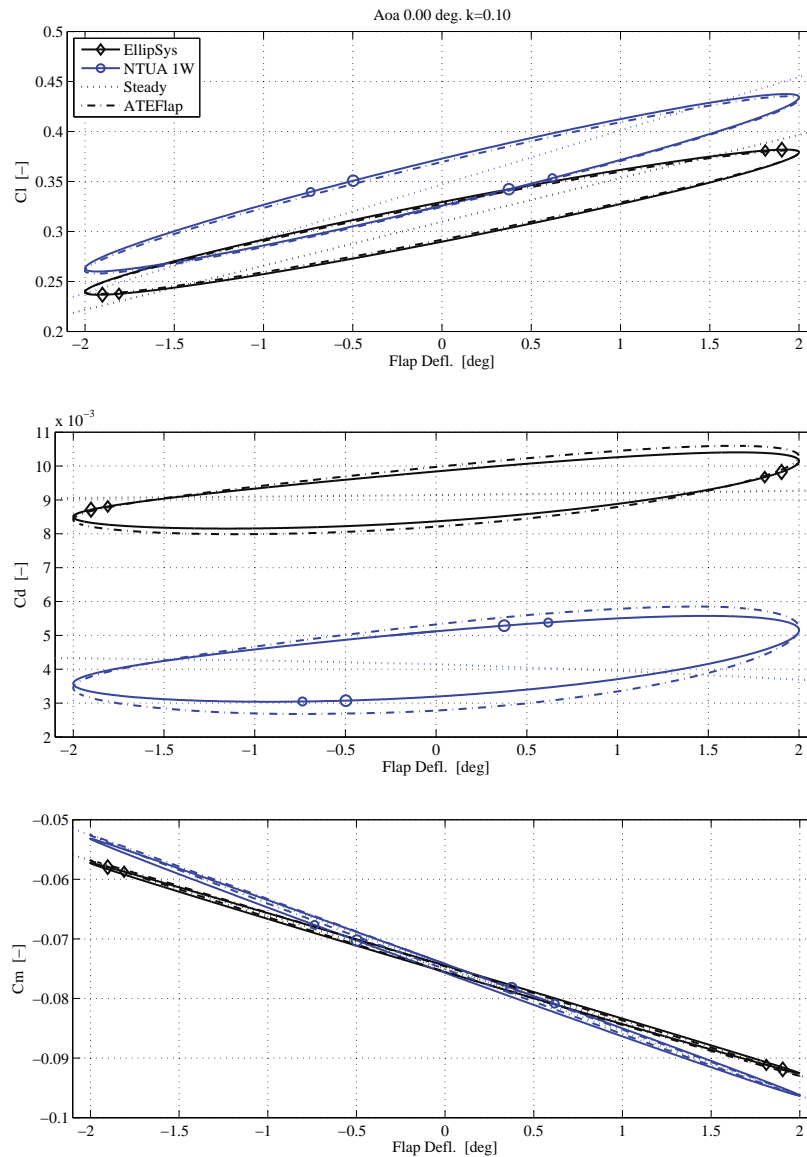


Figure 8. Attached flow conditions. Unsteady aerodynamic response for harmonic flap deflections, angle of attack fixed at 0° aoa, reduced frequency $k = 0.1$. The markers show the direction of the dynamic loops, unfolding from larger to smaller markers. The ATEFlap loops have the same direction of revolution as the corresponding loops from EllipSys or NTUA 1W.

thus smaller lift variations. EllipSys and NTUA 2W return unsteady drag loops with similar shapes, and larger openings than at lower angles of attack; the loops are fairly well predicted by the ATEFlap model, which returns similar drag variations, although with less open loops. The moment coefficients still maintain very close to their steady values.

Due to highly stalled conditions, the simulation of the response at 18° angle of attack and for flap deflections of $\pm 5^\circ$ poses the greatest challenges, figure 11. Both EllipSys and NTUA 2W display high frequency oscillations, again related to the unsteady vortex street shed in the wake of the airfoil. The unsteady response from EllipSys develops around a mean value different from the steady one; offset aside, ATEFlap is able to capture the characteristics of the EllipSys response, and returns loops with similar opening, and the same direction: counter-clockwise for the lift coefficient, and clockwise for the drag. The lift response simulated with NTUA 2W outlines instead a clockwise loop, with a similar opening for negative flap deflection, but a marked decrease in lift and an increase in drag as the flap starts to move upwards; the behavior is

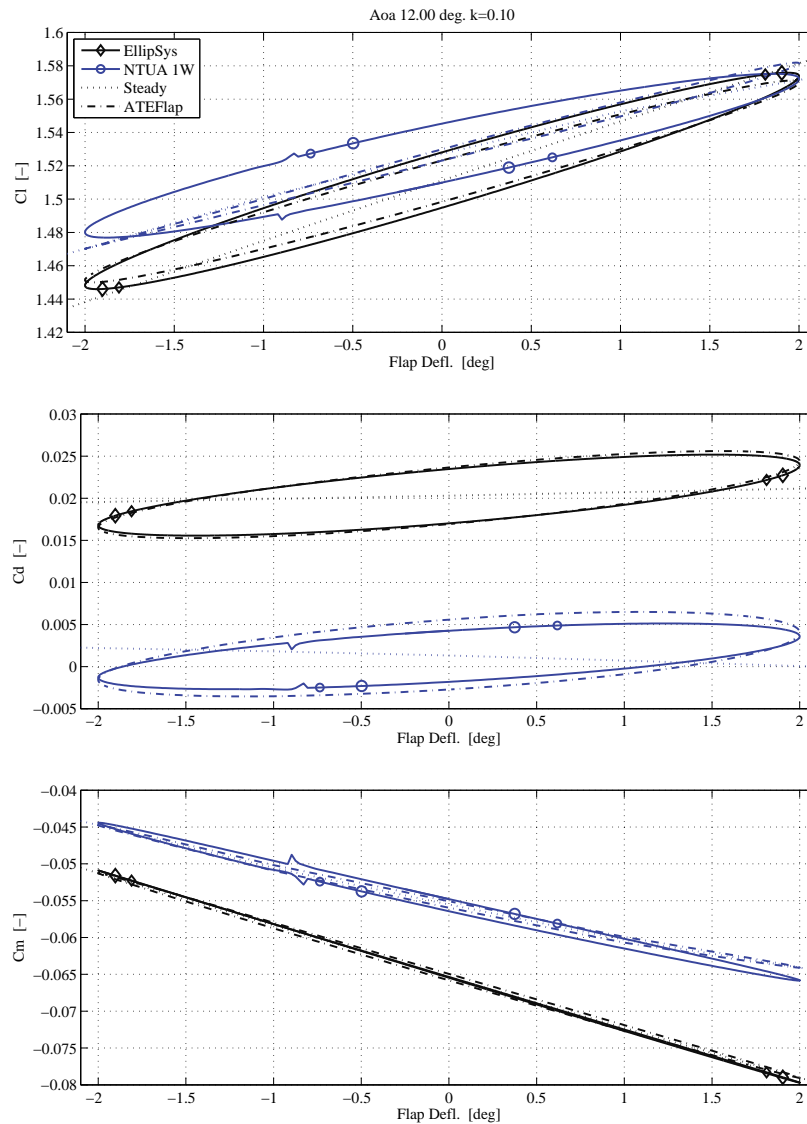


Figure 9. Separation onset. Unsteady aerodynamic response for harmonic flap deflections, angle of attack fixed at 12° aoa, reduced frequency $k = 0.1$. The ATEFlap loops have the same direction of revolution as the corresponding loops from EllipSys; the ATEFlap loop based on NTUA 1W data are clockwise both for drag, and lift coefficients.

driven by the local deep in the steady C_l curve around 18° aoa noted in NTUA 2W results, which suggests local stall conditions and gives rise to higher dynamic stall hysteresis effects. ATEFlap returns loops with the same direction, but fails to capture the lift drop, and instead returns a figure-eight loop. The moment coefficients are also affected by high frequency oscillations, but the response is still largely dominated by the steady moment variations.

6. CONCLUSION

The aerodynamic response of an airfoil section with a trailing edge flap has been characterized in steady and unsteady conditions, simulating the effects of changes in angle of attack, and flap deflection. Simulations were carried out with three

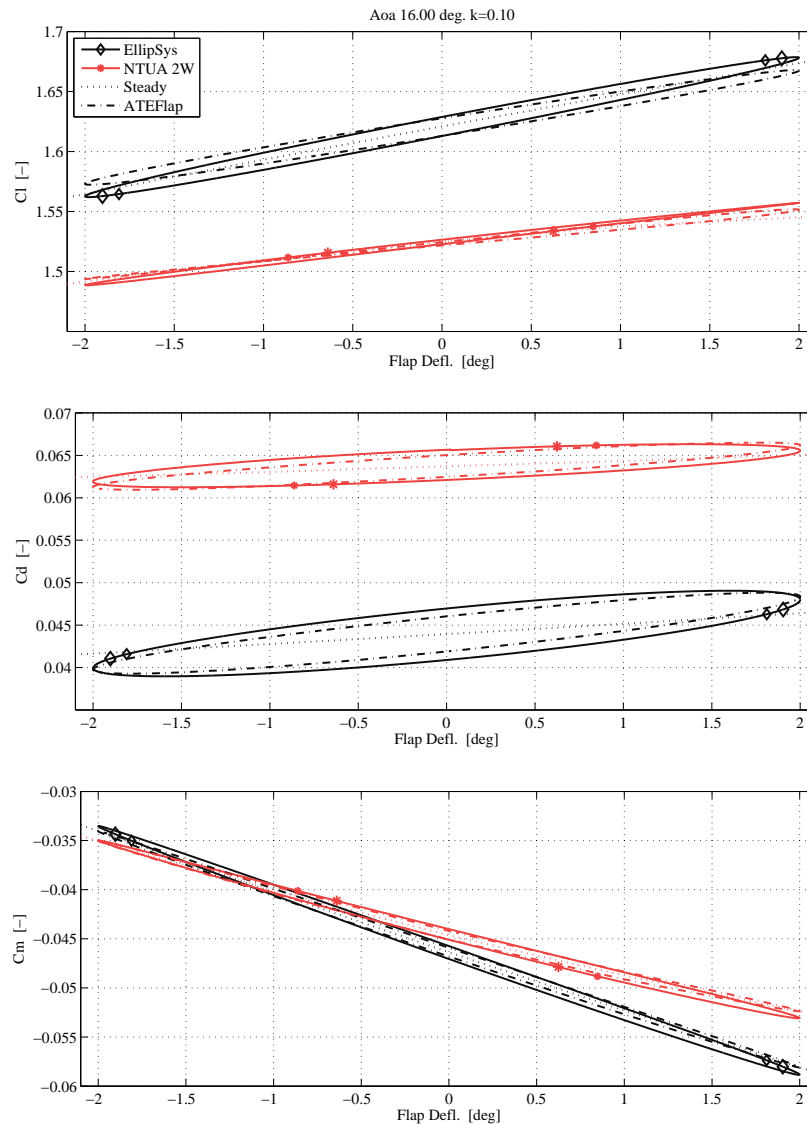


Figure 10. Stalled flow conditions. Harmonic flap deflections, angle of attack fixed at 16° aoa, reduced frequency $k = 0.1$. The ATEFlap loops have the same direction of revolution as the corresponding loops from EllipSys or NTUA 2W.

different codes: EllipSys Navier-Stokes solver, NTUA viscous-inviscid interaction method, and the ATEFlap engineering model.

In steady conditions, simulations of the flap effects with EllipSys and the NTUA viscous-inviscid codes outline the same trends: a downward deflection yields an increase in lift, and a downward pitching moment; as the angle of attack is increased, the lift and moment variations brought by the flap deflection decrease, whereas the drag increment increases. Although they describe similar trends, the codes return steady coefficients with different values, a discrepancy which is then reflected throughout the dynamic response simulations.

The unsteady response is characterized by significant differences of the integral aerodynamic forces and moment coefficients from their steady counterparts. In attached flow conditions, harmonic pitching motion returns smaller lift variations, and larger drag and moment variations than returned by a simple look-up of the steady values. The response to harmonic flap deflections is characterized by similar dynamics on the unsteady lift and drag forces, whereas the variations in moment are dominated by the steady component. As flow separation develops along the airfoil, stall dynamics modify

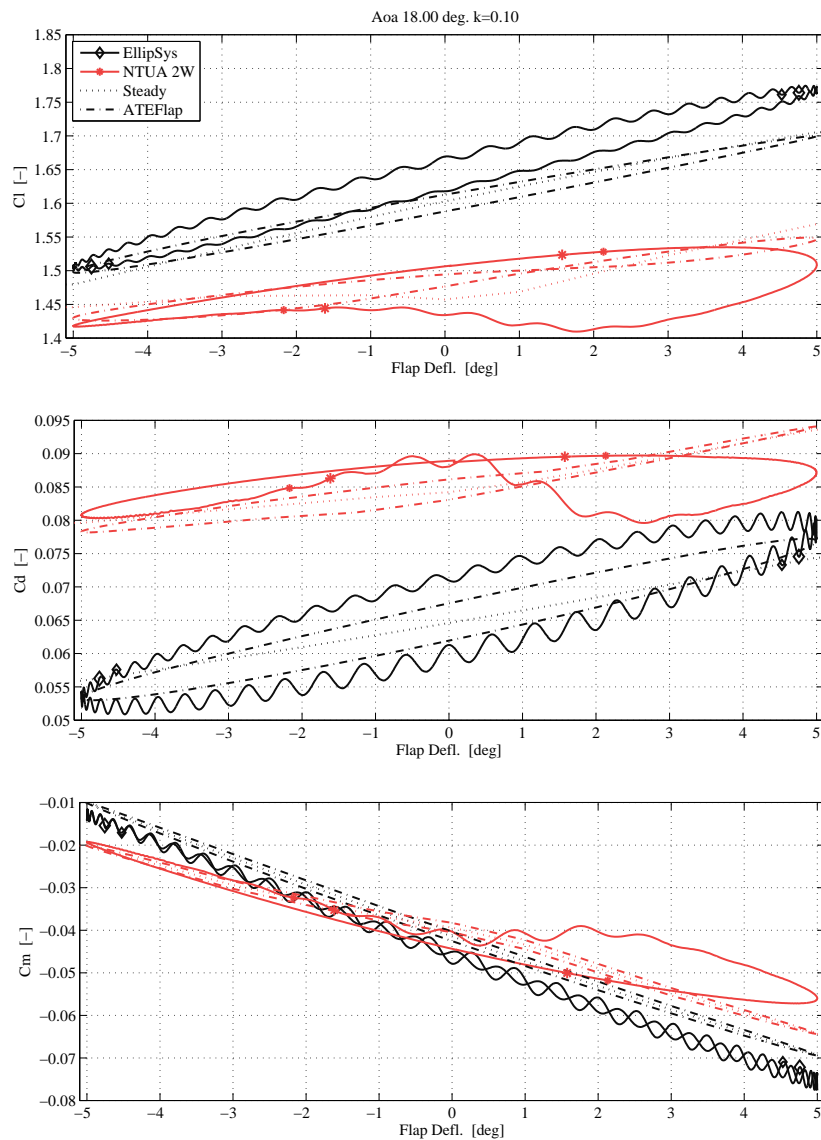


Figure 11. Highly stalled conditions. Harmonic flap deflections, angle of attack fixed at 18° aoa, flap variations $\pm 5^\circ$, reduced frequency $k = 0.1$. The ATEFlap loops have the same direction of revolution as the corresponding loops from EllipSys (counter-clockwise Cl, clockwise Cd) or NTUA 2W (clockwise loops).

the response, and harmonic pitch motions result in unsteady lift variations larger than the steady ones. The effect is not observed in the unsteady lift response from flap deflections, which instead get closer to the steady curves.

A comparison of the characteristics of the unsteady responses simulated by EllipSys and the NTUA 1W code highlights an excellent agreement of the dynamics of integral forces and moments predicted by the two methods in attached flow conditions, both for harmonic pitching motion, and flap deflection. The agreement deteriorates at higher angles of attack, as more complex stalled flow dynamics affect the unsteady response. Nonetheless, the unsteady responses from the two methods still display similar characteristics, and the differences in the dynamic responses produce anyway smaller variations than the ones observed in the steady data.

Similar considerations hold for the ATEFlap engineering model. In attached flow conditions, the model reproduces very well the dynamics of the unsteady lift force, both for pitch and flap deflection variations; at higher angles of attack, the responses simulated by ATEFlap start to diverge from the ones returned by more computationally expensive methods. No

effort is made in this study to reduce the differences by re-tuning the parameters τ_P and τ_B , which regulate the dynamics of the Beddoes-Leishmann type dynamic-stall model. Concerning the drag force and the aerodynamic moment, ATEFlap seems to slightly over-predict the dynamic effects from changes in the angle of attack, while a closer match is achieved on the unsteady drag and moment responses from flap deflection.

The ATEFlap engineering model has much lower computational requirements than the investigated numerical methods, a quality highly appreciated in aeroelastic simulation tools: the requirements are indicatively 500-800 times lower than EllipSys and 10-15 times lower than the viscous-inviscid interaction methods. Yet, in spite few differences from the response returned by the more complex methods, the ATEFlap model proved able to describe with sufficient accuracy the relevant dynamics of the unsteady forces and moments, originated both from airfoil motion and flap deflection. Considering also that the outer part of the blades on a pitch regulated turbine operates most of the time in attached flow conditions, the ATEFlap model is judged suitable for implementation in a BEM-based aeroelastic simulation tool. The aerodynamic response for an airfoil in highly stalled conditions computed by the ATEFlap model -as probably by any other engineering dynamic stall model- should be instead considered with greater circumspection.

The ATEFlap model, as many of the models used in aeroelastic simulations, relies on steady input data, which are generated by other methods. The simulations have shown that discrepancies in the steady input data might affect the aerodynamic response to a much higher degree than differences in the unsteady force modeling. In this sense, future work should consider a comparison between the steady aerodynamic responses predicted by the numerical methods and experimental data, including the effects of trailing edge flap deflections. Experimental data for the unsteady aerodynamic responses originated by flap deflection would certainly also be of great interest.

ACKNOWLEDGMENT

This work was partly funded by the European Commission under contract SES6 019945 (UpWind Integrated Project).

REFERENCES

1. Barlas TK, van Kuik G. State of the art and prospectives of smart rotor control for wind turbines. *Journal of Physics: Conference Series* 2007; **75**(1):012 080 (20 pp.).
2. Johnson SJ, Baker JP, van Dam CP, Berg D. An overview of active load control techniques for wind turbines with an emphasis on microtabs. *Wind Energy* Mar 2010; **13**(2-3):239–253, doi:10.1002/we.356.
3. Buhl T, Gaunaa M, Bak C. Potential load reduction using airfoils with variable trailing edge geometry. *Transactions of the ASME. Journal of Solar Energy Engineering* 2005; **127**(4):503–516.
4. Barlas TK, van der Veen GJ, van Kuik GA. Model predictive control for wind turbines with distributed active flaps: incorporating inflow signals and actuator constraints. *Wind Energy* 2011; doi:10.1002/we.503.
5. Castaignet D, Poulsen NK, Buhl T, Wedel-Heinen JJ. Model predictive control of trailing edge flaps on a wind turbine blade. *Proceedings of the American Control Conference 2011*, San Francisco, CA, USA, 2011.
6. Wilson DG, Berg DE, Barone MF, Berg JC, Resor BR, Lobitz DW. Active aerodynamic blade control design for load reduction on large wind turbines. *European Wind Energy Conference, Marseille, France*, 2009; 26(19).
7. Troldborg N. Computational study of the Risø-B1-18 airfoil with a hinged flap providing variable trailing edge geometry. *Wind Engineering* 2005; **29**(2):89–113.
8. van Dam CP, Chow R, Zayas JR, Berg DE. Computational investigations of small deploying tabs and flaps for aerodynamic load control. *Journal of Physics: Conference Series* 2007; **75**(1):012 027–1–10.
9. Heinz J, Sørensen NN, Zahle F. Investigation of the load reduction potential of two trailing edge flap controls using CFD. *Wind Energy* 2011; **14**(3):449–462, doi:10.1002/we.435.

10. Ng BF, Palacios R, Graham JMR, Kerrigan EC. Robust control synthesis for gust load alleviation from large aeroelastic models with relaxation of spatial discretization. *Conference proceedings, European Wind Energy Conference 2012*, Copenhagen, Denmark, 2012.
11. Ramos Garcia N. Quasi-3d aerodynamic code for analyzing dynamic flap response. Ph.D. thesis, Technical University of Denmark, Department of Mechanical Engineering, Lyngby, Denmark Apr 2011.
12. Riziotis VA, Voutsinas SG. Aero-elastic modelling of the active flap concept for load control. *Conference proceedings, European Wind Energy Conference 2008, Marseille, France, 2008*.
13. Lackner MA, van Kuik G. A comparison of smart rotor control approaches using trailing edge flaps and individual pitch control. *Wind Energy* Mar 2010; **13**(2-3):117–134, doi:10.1002/we.353.
14. Barlas TK, Van Kuik GAM. Aeroelastic modelling and comparison of advanced active flap control concepts for load reduction on the upwind 5MW wind turbine. *European Wind Energy Conference, Marseille, France, 2009*; 16(19).
15. Andersen PB, Gaunaa M, Bak C, Hansen MH. A dynamic stall model for airfoils with deformable trailing edges. *Wind Energy* 2009; **12**(8):734–751, doi:10.1002/we.326.
16. Riziotis VA, Voutsinas SG. Dynamic stall modelling on airfoils based on strong viscous-inviscid interaction coupling. *International Journal for Numerical Methods in Fluids* 2008; **56**(2):185–208, doi:10.1002/flid.1525.
17. Bergami L, Gaunaa M. ATEFlap aerodynamic model, a dynamic stall model including the effects of trailing edge flap deflection. *Technical Report R-1792(EN)*, Risoe National Laboratory. Technical University of Denmark, Roskilde, Denmark Feb 2012.
18. Gaunaa M, Riziotis VA, Timmer N, Snel H, Andersen PB, Heinz J. Comparison of code performance for computation of unsteady 2D aerodynamics of airfoils with deformable trailing edges. *Technical Report D2.5, UpWind - Integrated Wind Turbine Design* Feb 2011.
19. Michelsen JA. Basis3D - a platform for development of multiblock PDE solvers. *Technical Report AFM 92-05*, Technical University of Denmark 1992.
20. Michelsen JA. Block structured Multigrid solution of 2D and 3D elliptic PDEs. *Technical Report AFM 94-06*, Technical University of Denmark 1994.
21. Sørensen N. General purpose flow solver applied to flow over hills. *Technical Report Risoe-R-827(EN)*, Risoe National Laboratory, Roskilde (DK) 1995.
22. Menter FR. Two-equation eddy-viscosity turbulence models for engineering applications. *AIAA journal* 1994; **32**(8):1598–1605.
23. Voutsinas SG, Riziotis VA. A viscous-inviscid interaction model for dynamic stall simulations on airfoils. *Proceedings of 37th Aerospace Sciences Meeting and Exhibit*, vol. 99-0038, AIAA: Reno, Nevada, 1999.
24. Riziotis VA, Voutsinas SG, Politis E, Chaviaropoulos P. Stability analysis of parked wind turbine blades using a vortex model. *Proceedings of the Science of Making Torque from the Wind*, Heraklion, Greece, 2010.
25. Gaunaa M. Unsteady two-dimensional potential-flow model for thin variable geometry airfoils. *Wind Energy* 2010; **13**(2-3):167–192, doi:10.1002/we.377.
26. Bergami L, Gaunaa M, Heinz J. Indicial lift response function: an empirical relation for finite-thickness airfoils, and effects on aeroelastic simulations. *Wind Energy* 2012; **Early View**(published on-line), doi:10.1002/we.1516.
27. Hansen MH, Gaunaa M, Madsen HA. A Beddoes-Leishman type dynamic stall model in state-space and indicial formulations. *Technical Report R-1354(EN)*, Risoe National Laboratory, Roskilde (DK) 2004.

Article IV

Cyclic Control Optimization for a Smart Rotor

The article was presented and included in the proceedings of the 8th PhD seminar on Wind Energy in Europe, held in Zurich (Switzerland) in September 2012.

The content of the article is recalled in the synopsis section related to:

- *Preliminary investigations with feed-forward cyclic control*, section 6.1: cyclic control for blade load alleviation

CYCLIC CONTROL OPTIMIZATION FOR A SMART ROTOR

Leonardo Bergami^{*}, Lars C. Henriksen
DTU Wind Energy
Riso Campus, Roskilde, Denmark
^{*}e-mail: leob@dtu.dk

ABSTRACT

The paper presents a method to determine cyclic control trajectories for a smart rotor undergoing periodic-deterministic load variations. The control trajectories result from a constrained optimization problem, where the cost function to minimize is given by the variation of the blade root flapwise bending moment within a rotor revolution. The method is applied to a rotor equipped with trailing edge flaps, and capable of individual blade pitching. Results show that the optimized cyclic control significantly alleviates the load variations from periodic disturbances; the combination of both cyclic flap and pitch allows to reduce the action (and hence the wear) on the pitch actuators, and still to achieve considerable load alleviation.

NOMENCLATURE

GF	generalized aerodynamic forces
J	optimization cost function
M_x	blade root flapwise bending moment
u	control action
β	flap deflection angle
ψ	blade azimuthal position

Abbreviations

Ref.	reference control
Col.P.	collective pitch
Col.F.	collective flap

CPC	cyclic pitch control
CFC	cyclic flap control
CPCF	cyclic pitch and flap control

INTRODUCTION

Several research works have recently focused on *smart-rotor* concepts [1]: wind turbine rotors that, through a combination of sensors, processing units, and actuators, are able to actively alleviate the variation of the loads they are subject to, thus reducing the load requirements the structure has to withstand. Most of the load variations experienced by the wind turbine rotor originate from fluctuations in the flow field encountered by the rotating blades; the variations have a stochastic nature, mainly related to wind turbulence, but also an important deterministic periodic component [2], which originates, for instance, from terrain shear effects, tower passage, rotor misalignment. The periodic load variation, as such, is easily predictable, and its knowledge can enhance the load alleviation performances of the smart rotor. In their smart rotor controller, Van Wingerden et al. [3] include predictions on periodic load variations in the form of a feed-forward term; Houtzager et al. [4], starting from a lifted system representation, propose a repetitive control where cyclic pitch variation address exclusively periodic load variations.

The present work proposes a simple cyclic control formulation, where the control signal only depends on the blade azimuthal position, and follows a periodic trajectory, repeated at each rotor revolution. The control trajectory results from a constrained optimization problem, where the cost function is given by the variations of the flap root flap-wise bending moment. The optimization is simply based on measurements of the bending moment, and does not require any further knowledge on the controlled system.

The literature reports widespread figures on the load alleviation performances of smart rotors, see for instance the summary compiled in Barlas et al. [5]. Load alleviation depends, in fact, on a multitude of factors (simulation conditions, sensors choices, actuator setup, and control algorithm, among others), and is often difficult to distinguish the impact on load alleviation from each single factor. The control setup proposed in the study does not depend on additional sensors measurements, nor on a particular control algorithm, therefore, due to its simplicity, it could provide a standard ground to evaluate the performances of different smart rotor concepts, and would facilitate the comparison between actuator types and setups. The results from the cyclic optimization will also provide a useful term of comparison for future implementations of more complex feedback control algorithms.

The smart rotor configurations investigated in this study include collective flap deflection (*Col.Fl.*), cyclic pitch (*CPC*), cyclic flap (*CFC*), and a combination of both cyclic pitch and cyclic flap acting together (*CPCF*). To better evaluate the different control strategies, an attempt is made to estimate the energy requirements for each of the investigated control strategies.

The proposed method has some important limitations, which are inherent in the chosen optimization procedure. The method can not be used to assess the performances of smart rotors in alleviating the effects of stochastic load variations, caused, for instance by wind turbulence, as the proposed control algorithm can only address periodic disturbances. Furthermore, the method can not be directly applied to more realistic conditions. In fact, as the optimization procedure receives no other information on the state of the plant, any variation in the cost function is reckoned as a consequence of a variation in the control optimization variables. Therefore, the optimization procedure can be carried out only with no other disturbances affecting the state of the plant, so that atmospheric turbulence, and time variations

of the wind speeds have to be excluded from the simulation. More complex cyclic control methods could eventually overcome such limitations, for instance using iterative learning or repetitive control algorithms, as in Houtzager et al. [4].

In spite of its limitations, the proposed method allows for simple preliminary studies of smart rotor set-ups, and allows to compare different actuators configurations on the same basis, and set a term of reference for future controller development.

METHOD

The cyclic control trajectories are determined by solving a constrained optimization problem where the cost variable is evaluated from aeroelastic simulations of the NREL 5 MW reference turbine [6]. The turbine standard controller is applied, and the pitch control signals returned by the optimization are simply super-imposed to the reference signal from the standard controller. The turbine blades are equipped with trailing edge flaps, which cover 20% of the blade span, from 77.6% to 97.6% of the blade radius. The flaps extend for 10% of the chord length, and their deflection is limited to ± 10 degrees, returning variations of the steady lift coefficient from -0.45 to $+0.41$. The wind field in the simulations is purely deterministic; it accounts for tower shadow effects, and for the terrain shear as prescribed in the IEC standard [7].

The response of the turbine is simulated with the aeroelastic code HAWC2 [8], which couples multi-body structural dynamics with a BEM-based aerodynamic formulation; in order to capture the aerodynamic effects of the flap deflection, the unsteady aerodynamic model *ATEFlap* [9] is adopted. To reduce the simulation time, in this study aeroelastic simulations are run with a simplified model, where the structural degrees of freedom have been excluded, thus describing an ideally stiff turbine. The results are then compared, for selected wind speeds, against the ones returned by the full model, which includes all the structural degrees of freedom and multi-body dynamics; similarity and differences from the stiff turbine results are commented in the text.

The solution to the constrained optimization problem returns the cyclic control trajectory $u(\psi)$, which prescribes, as function of the blade azimuthal position ψ , the control actions to be repeated at each rotor revolution, and on each

of the three blades. The optimization cost function J is evaluated within a complete rotor revolution, yielding to the constrained optimization problem:

$$\min_{u(\psi)} J_{\psi: [-\pi, +\pi]}, \quad (1)$$

subject to the control signal constraints:

$$u(\psi) \in \mathbb{R} \mid -10^\circ \leq u \leq +10^\circ, \text{ for the flap actuators, and}$$

$$u(\psi) \in \mathbb{R} \mid -90^\circ \leq u \leq +90^\circ, \text{ for the blade pitch.}$$

The problem is solved iteratively using the gradient-based constrained optimization algorithm described in Waltz et al. [10].

The cyclic control trajectory $u(\psi)$ is a continuous signal, which would render the optimization problem infinite-dimensional. To limit the problem dimension, the continuous trajectory $u(\psi)$ is described by a finite set of values x_i , which prescribe the control value at fixed azimuthal locations ψ_i ; the control signal among the fixed points is determined using Piecewise Cubic Hermite Interpolating Polynomials (PCHIP) [11]. The optimization variables are given by the values of the the fixed points x_i , plus an additional variable returning the phase shift of the predetermined azimuthal locations of the points. In this work, six points are used to describe the cyclic control trajectories, giving thus six plus one optimization variables.

The cost function minimizes the amplitude of the variations on the blade root flapwise bending moment M_x ; in addition, to avoid the trivial solution of down rating the turbine operation to reduce the loads, a strong penalization is added for power output P_{avg} descending below rated power P_0 :

$$J_{ar} = (\max M_x(\psi) - \min M_x(\psi))^2 + \rho_{\text{pow}} (\max [P_0 - P_{\text{avg}}, 0])^2. \quad (2)$$

The case of both cyclic pitch and cyclic flap acting together (CPCF) also includes a small penalty on the amplitude of the pitch angle variation, so to favor the less energy consuming flap action.

The operating wind speed considered in the optimization are 12, 16, 20, 24 m/s, and the following control strategies are considered:

- Reference (*Ref.*), the NREL standard controller keeps the rotor near rated rotational speed, and power limitation is achieved by collective pitching to feather.
- Collective flap (*Col.F.*), all the flaps sections are deflected to negative values, so to decrease the load on the outer part of the blades, while decreasing the collective pitch value allow to maintain the same power output. The solution is conceptually similar to a collective partial pitch on the outer span of the blades.
- Cyclic pitch (*CPC*), the blade pitch follows the cyclic control trajectory returned by the optimization; the pitch angle of each blade is a function of the azimuthal position, while the mean pitch level is regulated by the standard controller.
- Cyclic flap (*CFC*), the flap deflection follows the optimized control trajectory; the collective blade pitch angle is determined by the standard controller.
- Cyclic pitch and flap (*CPCF*), the optimization returns a control trajectory for the blade pitch angles, and another for the flap deflection values.

ESTIMATION OF ACTUATION ENERGY

An attempt is made to quantify the energy required to modify the blades pitch angle, and the deflection of the flap sections. The problem is rather complex, and highly dependent on the actuator devices used to perform the control action. Only a very simplified estimation is given here, assuming steady conditions, linearity, and neglecting the energy requirements of the physical actuator devices; the results are thus to be intended more as general guidelines, and indications of the actuator wear, rather than as rigorous figures.

The energy required to modify the blade pitch angle of one degree $E_{d\theta}$ is evaluated simply as the mean pitch moment at the blade root M_z over a complete rotor revolution:

$$E_{d\theta} = \frac{1}{2\pi} \int_{-\pi}^{\pi} M_z(\psi) \frac{\pi}{180} d\psi \quad [J/deg] \quad (3)$$

The estimation of the energy requirement for one degree flap deflection $E_{d\beta}$ is derived from the expression of the aerodynamic general forces on an airfoil with flap, as expressed in [12], and [13]. The generalized force on the airfoil is computed as the sum of four contributions, depending on: angle of attack at three-quarter chord $GF_{\alpha 3/4}$,

airfoil camber-line GF_{cmb} , flap deflection GF_{β} , and flap deflection rate $GF_{\dot{\beta}}$:

$$\begin{aligned}
 GF &= GF_{\alpha_{3/4}} + GF_{cmb} + GF_{\beta} + GF_{\dot{\beta}}, \\
 GF_{\alpha_{3/4}} &= -2\rho b_{hc} U_0^2 PI_5^{\beta} \cdot \alpha_{3/4}, \\
 GF_{cmb} &= \rho b_{hc} \frac{U_0^2}{\pi} \left(PI_8^{\beta, cmb} + PI_5^{\beta} H_{dydx}^{cmb} - H_{dydx}^{cmb} PI_7^{\beta} \right), \\
 GF_{\beta} &= \rho b_{hc} \frac{U_0}{\pi} \left(PI_5^{\beta} H_y^{\beta} + b_{hc} PI_3^{\beta} - H_y^{\beta} PI_7^{\beta} + PI_9^{\beta} \right) \cdot \dot{\beta}, \\
 GF_{\dot{\beta}} &= \rho b_{hc} \frac{U_0^2}{\pi} \left(PI_8^{\beta, \dot{\beta}} + PI_5^{\beta} H_{dydx}^{\beta} - PI_7^{\beta} H_{dydx}^{\beta} \right) \cdot \dot{\beta},
 \end{aligned} \tag{4}$$

where, b_{hc} is the chord half length, and U_0 is the relative flow speed on the airfoil. $PI_{\#}^x$, and $H_{\#}^x$ are deflection shape integrals, as specified in Gaunaa [12]; the suffix β refers to shape integrals of the flap circular arc deflection shape, while cmb refers to integrals of the camber-line shape (a NACA 6417 camber is assumed).

The energy required to deflect the flap from zero to $\Delta\beta$ on a unit span airfoil section $E_{d\beta}^{dZ}$ is then evaluated as the integral of the generalized forces times the flap deflection. Assuming the terms on the angle of attack, and camber are constant in β , and that the flap deflection rate $\dot{\beta}$ is also constant, the integral simplifies to:

$$\begin{aligned}
 E_{d\beta}^{dZ} &= \frac{1}{\Delta\beta} \int_0^{\Delta\beta} GF d\beta \\
 &= GF_{\alpha_{3/4}} + GF_{cmb} + GF_{\beta} + \frac{1}{\Delta\beta} \int_0^{\Delta\beta} GF_{\dot{\beta}} d\beta. \tag{5}
 \end{aligned}$$

The term depending on the flap deflection rate is scarcely significant when compared to the other terms, and is therefore omitted. The energy estimation is then depending on the considered flap range $\Delta\beta$, which is here chosen to 10 degrees, corresponding to half the total flap range. The total energy required to deflect all the flaps on a blade is then computed as the summation of the energy at each airfoil section times its spanwise extension.

The energy requirements for flap deflection and pitch variation are estimated at different operating mean wind speed, assuming steady conditions. The requirements are referred to a single degree actuation (fig. 1), and assume

that the same energy is required for actions in both directions. Although largely approximative, the estimations indicate that the energy required to pitch the whole blade of one degree is from 20 to 90 times larger than the energy required to deflect the flaps covering the outer 20 % span of the same blade.

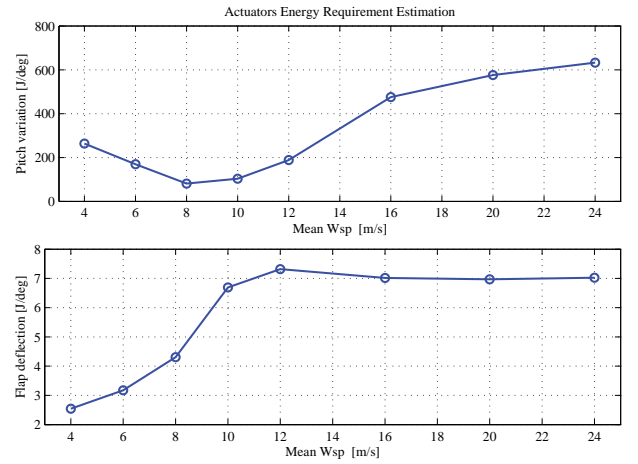


FIGURE 1. Indicative estimation of the energy requirements for actuators actions, comparison between pitch variation (top) and flap deflection (bottom); values referred to one degree actuation for a single blade with flaps covering 20% span.

OPTIMIZED CONTROL FOR LOAD ALLEVIATION

First, a very simple control strategy is investigated by deflecting completely the flaps upwards. The aerodynamic loads on the outer part of the blade are reduced, while rated power is maintained by decreasing the blades pitch angle. The setup is similar to a partial blade pitch, and the mean blade root bending moment is lowered, but its azimuthal variation, and the fatigue loads, are nearly the same as in the reference case (fig. 2).

The optimized cyclic trajectories for the pitch (CPC) and flap (CFC) control returns slightly higher mean loading on the blade, but a significant reduction of the blade root load variation (fig. 2, top). The corresponding equivalent fatigue loads (fig. 3, top) are nearly one-quarter of the fatigue loads reported in the reference case; Houtzager et al. [4] report similar reductions with an individual pitch repetitive controller.

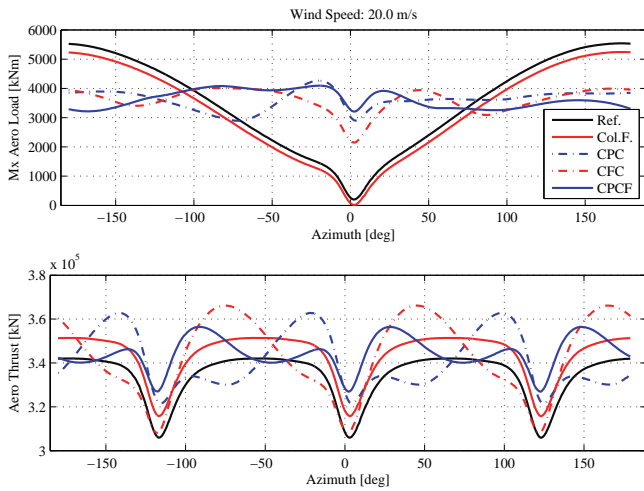


FIGURE 2. Load alleviation, example at 20 m/s of load variation on the blade root flapwise bending moment (top), and thrust on rotor (bottom) with the reference controller and the optimized control trajectories.

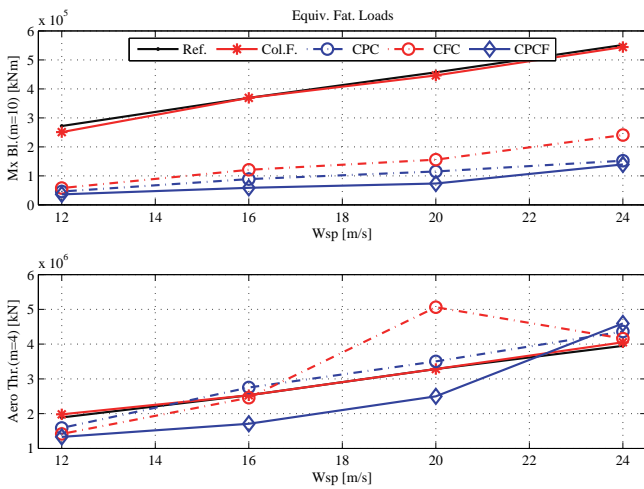


FIGURE 3. Load alleviation, equivalent fatigue loads for the reference controller, and the optimized control trajectories. The equivalent loads correspond to a full rotor revolution referred to 600 cycles, and are based on the blade root flapwise bending moment (top), and on the rotor thrust force (bottom).

The optimized control trajectories (fig. 4) try to compensate for the variations in the wind field encountered by the rotating blade: when the blade is pointing downwards (0° azimuth) the aerodynamic forces are increased by reducing the pitch angle, or increasing the flap deflection, so to compensate for the decrease in wind speed. The trajec-

tories reach their maximum (or minimum) *before* the blade passes in front of the tower; the optimization procedure is thus able to correctly identify, and anticipate, the delay in the response of the system.

Cyclic pitch control achieves higher load alleviation than cyclic flap, especially at wind speed of 20 and 24 m/s, where the flap has reached the limits of the deflection range (fig. 4). The required flap deflection is much higher (approximately five times) than the variation in pitch angle; on the other hand, the energy required by the cyclic pitch control is from 10 to 20 times higher than required by the cyclic flap (fig. 5).

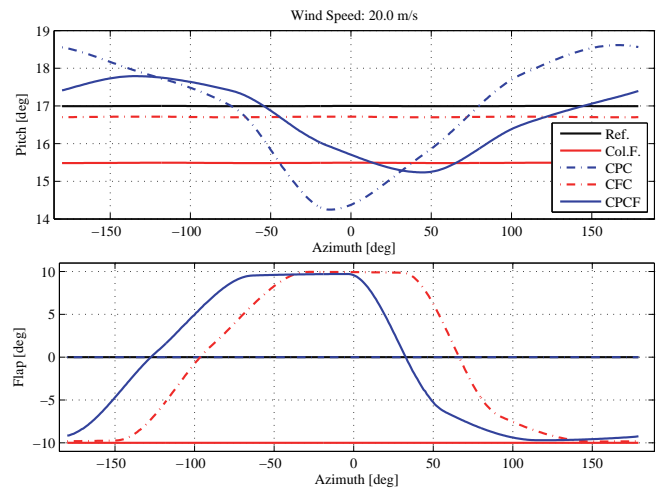


FIGURE 4. Load alleviation, example at 20 m/s of the cyclic control trajectories optimized for blade root load alleviation. Pitch (top) and flap (bottom) control signals.

By combining cyclic pitch and cyclic flap control, and adding a small penalty to the pitch action, the advantages of the two strategies are combined (CPCF series in fig.4–5). The cyclic flap control compensates for most of the load variation at lower wind speeds, while the cyclic pitch contribution takes over once the flap has reached the deflection limits. The energy consumption, and hence the actuators wear, is lowered to nearly half the case of the cyclic pitch control alone, and the equivalent fatigue loads are reduced to 15% of the reference ones.

The variation in the thrust force (fig. 2), and the corresponding equivalent fatigue loads (fig. 3), which were not part of the optimization, are increased by the cyclic con-

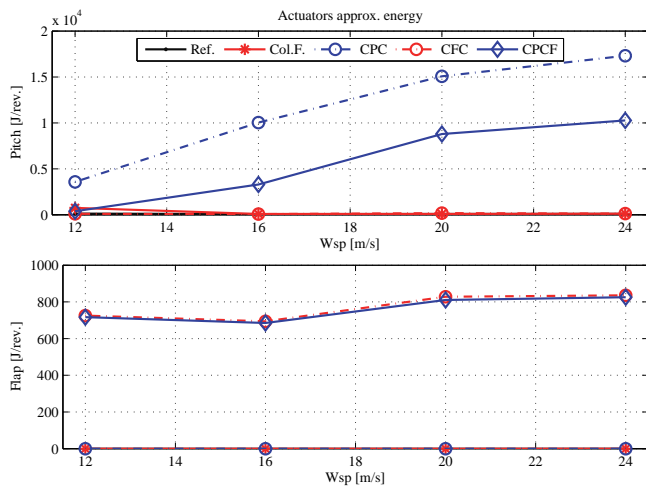


FIGURE 5. Load alleviation, estimation of the energy requirements for the flap and the pitch control actions performed at each rotor revolution following the optimized control trajectories.

control actions. Simulations including all the structural degrees of freedom return similar figures in terms of blade root load alleviation, although the displacement required to both pitch and flap actuators is higher, as the flexibility of the blade reduces the effects of the control actions. Simulations with the flexible turbine model also show a significant increase in the variation of the tower bottom fore-aft bending moment, especially for the cases involving flap cyclic action. If confirmed, future work should consider including a penalty for the tower load variation in the optimization cost function.

CONCLUSION

The optimized control trajectories show that cyclic control can significantly reduce the fatigue loads on the blade root flapwise bending moment caused by deterministic variations of the aerodynamic loads. Reductions of nearly 75% are reported for cyclic pitch control, whereas cyclic flap control returns a lower reduction, approximately 70%, since, especially at high wind speeds, the flap reaches its deflection limits. Particularly good results are obtained by combining the cyclic pitch and flap actions; the equivalent fatigue loads from deterministic variations of the aerodynamic forces are reduced to 15% of the loads in the reference case, and the presence of the flaps lowers to nearly half the requirements on the pitch actuators action.

Few simulations with a fully flexible model have confirmed the load alleviation potentiality, but have also highlighted an important increase in the tower bottom fatigue load, which should be addressed in future investigations.

To conclude, within its limitation, the proposed optimization method proved adequate to quantify in a simple manner the potentiality of different smart-rotor control configurations to compensate for periodic variations in the wind field. The method can be also applied to other objectives, as, for instance, to evaluate the potential of increasing the energy output below rated conditions by exploiting smart rotors control possibilities.

REFERENCES

- [1] Barlas, T. K., and van Kuik, G., 2007. "State of the art and perspectives of smart rotor control for wind turbines". *Journal of Physics: Conference Series*, **75**(1), p. 012080 (20 pp.).
- [2] Bergami, L., and Gaunaa, M., 2012. "Analysis of aeroelastic loads and their contributions to fatigue damage". In Paper submitted for proceedings of the conference 'The science of making Torque from the Wind' Oldenburg, October 2012.
- [3] van Wingerden, J. W., Hulskamp, A., Barlas, T., Houtzager, I., Bersee, H., van Kuik, G., and Verhaegen, M., 2011. "Two-degree-of-freedom active vibration control of a prototyped "Smart" rotor". *IEEE Transactions on Control Systems Technology*, **19**(2), Mar., pp. 284–296.
- [4] Houtzager, I., van Wingerden, J. W., and Verhaegen, M., 2012. "Wind turbine load reduction by rejecting the periodic load disturbances". *Wind Energy*.
- [5] Barlas, T. K., van der Veen, G. J., and van Kuik, G. A., 2011. "Model predictive control for wind turbines with distributed active flaps: incorporating inflow signals and actuator constraints". *Wind Energy*.
- [6] Jonkman, J., Butterfield, S., Musial, W., and Scott, G., 2009. Definition of a 5-MW reference wind turbine for offshore system development. Tech. Rep. NREL/TP-500-38060, National Renewable Energy Laboratory (NREL).
- [7] Commission, I. E., 2005. IEC 61400-1: Wind turbines part 1: Design requirements. Tech. rep., International Electrotechnical Commission.
- [8] Larsen, T. J., 2009. How 2 HAWC2 the user's man-

- ual. Tech. Rep. R-1597(EN), Risø National Laboratory. Technical University of Denmark, Roskilde, Denmark.
- [9] Bergami, L., and Gaunaa, M., 2012. ATEFlap aerodynamic model, a dynamic stall model including the effects of trailing edge flap deflection. Tech. Rep. Risoe-R-1792(EN), Risoe, National Laboratory. Technical University of Denmark, Roskilde, Denmark.
- [10] Waltz, R. A., Morales, J. L., Nocedal, J., and Orban, D., 2006. “An interior algorithm for nonlinear optimization that combines line search and trust region steps”. *Mathematical Programming*, **107**(3), p. 391–408.
- [11] Fritsch, F. N., and Carlson, R. E., 1980. “Monotone piecewise cubic interpolation”. *SIAM Journal on Numerical Analysis*, p. 238–246.
- [12] Gaunaa, M., 2010. “Unsteady two-dimensional potential-flow model for thin variable geometry airfoils”. *Wind Energy*, **13**(2-3), pp. 167–192.
- [13] Bergami, L., and Gaunaa, M., 2010. “Stability investigation of an airfoil section with active flap control”. *Wind Energy*, **13**(2-3), pp. 151–166.

Article V

A Smart Rotor configuration with Linear Quadratic control of Adaptive Trailing Edge Flaps for active load alleviation

The article was submitted for publication as research article to the *Wind Energy* journal in February 2013.

The content of the article is recalled in the synopsis section related to:

- *Model Based control algorithms for a rotor with ATEF*, section 7.1 and 7.2: short description of the SISO-LQ control algorithm, and discussion on the load alleviation results.

RESEARCH ARTICLE

A Smart Rotor configuration with Linear Quadratic control of Adaptive Trailing Edge Flaps for active load alleviation

Leonardo Bergami*, Niels K. Poulsen[‡]

* DTU Wind - Department of Wind Energy, Technical University of Denmark, Denmark.

[‡] DTU Informatics - Department of Informatics and Mathematical Modeling, Technical University of Denmark, Denmark.

ABSTRACT

The paper proposes a smart rotor configuration where Adaptive Trailing Edge Flaps (ATEF) are employed for active alleviations of the aerodynamic loads on the blades of the NREL 5 MW reference turbine. The flaps extend for 20 % of the blade length, and are controlled by a Linear Quadratic (LQ) algorithm based on measurements of the blade root flapwise bending moment. The control algorithm includes frequency weighting to discourage flap activity at frequencies higher than 0.5 Hz. The linear model required by the LQ algorithm is obtained from subspace system identification; periodic disturbance signals described by simple functions of the blade azimuthal position are included in the identification to avoid biases from the periodic load variations observed on a rotating blade. The LQ controller uses the same periodic disturbance signals to handle anticipation of the loads periodic component.

The effects of active flap control are assessed with aeroelastic simulations of the turbine in normal operation conditions, as prescribed by the IEC standard. The turbine lifetime fatigue damage equivalent loads provide a convenient summary of the results achieved with ATEF control: a 10 % reduction of the blade root flapwise bending moment is reported in the simplest control configuration, whereas reductions of approximately 14 % are achieved by including periodic loads anticipation. The simulations also highlight impacts on the fatigue damage loads in other parts of the structure, in particular, an increase of the blade torsion moment, and a reduction of the tower fore-aft loads.

Copyright © 2012 John Wiley & Sons, Ltd.

KEYWORDS

Adaptive Trailing Edge Flaps; LQ controller for smart rotors; active fatigue damage load alleviation

Correspondence

Leonardo Bergami, DTU Wind, Risø Campus, Frederiksborgvej 399, 4000 Roskilde, Denmark. Email: leob@dtu.dk

Received . . .

1. INTRODUCTION

The continuously increasing size of modern utility-scaled wind turbines calls for technical solutions able to reduce the loads the turbine has to withstand, thus allowing for lower structural requirements, and savings in rotor weight and material usage. Several investigations have highlighted the potential of *smart rotor* concepts [1]: wind turbine rotors that, through a combination of sensors, control units, and actuators, actively alleviate the aerodynamic loads the rotor is subject to.

Smart-rotors can employ traditional blade pitch actuators [2, 3], or active aerodynamic devices, which can modify the aerodynamic forces locally along the blade span. Active devices as Adaptive Trailing Edge Flaps (ATEF) with a continuous deflection shape have favorable aerodynamic characteristics [4]; their potential was first assessed on 2D airfoil sections, with simulations [5, 6], and wind tunnel experiments on non-rotating rigs [7, 8]. The application of Adaptive Trailing Edge Flaps to alleviate loads on wind turbine rotors was then investigated by means of aeroelastic simulations, and also by two rotating experiments: the DUWIND group at Delft university tested a two bladed smart-rotor in an open jet wind tunnel [9, 10], and Castaignet et al. [11] carried out a full scale experiment on a 225 kW turbine with flaps on one of the three blades.

All the investigations confirmed that smart rotors with trailing edge flaps have a potential for reducing the fatigue loads experienced by the turbine; nevertheless, they reported rather widespread results, with load reductions figures ranging from

5 to 47 percent, see the summary compiled by Barlas et al. [12]. Differences in the alleviation performances can originate from several sources: the models used in the aeroelastic simulations, the conditions of the wind field and its turbulence levels, the maximum deflection and extension of the flap actuators, and also the choices made in designing the flap control system, as the assumptions on the available sensors and measurements, and the type of control algorithm implemented.

Most of the studies opted for control algorithms based on classic PID methods, applied either to each blade independently [13, 14, 15, 16, 17], or to the whole rotor through multi-blade coordinate transformation [18, 19]; other investigations have instead applied model based control algorithms, as Linear Quadratic Regulators (LQR) [20], Model Predictive Control (MPC) [12, 21], or H_∞ control [9]. The flap control actions respond to the deformation state of the rotor blades; in some cases, rotor sensors are assumed to provide direct measurements of the blade deflection and deflection rate [15, 20, 22, 17], whereas other controllers use measurements of the blade flapwise bending moment, either at selected locations along the span [14, 16], or, more simply, at the blade root [19, 12, 21, 10]. Some studies have also investigated flap control algorithms where additional information on the in-flow condition along the blade are provided, for instance, by measurements performed with Pitot's tubes mounted on the blade leading edge [14, 12, 21].

The present work considers a setup where the flaps on each of the blades are controlled based on measurements of the flapwise bending moment at the root of the same blade. The setup has the advantage of relying on a simple sensor arrangement, relatively easy to implement and maintain. Furthermore, the controller aim is to alleviate fatigue loads at the blade root, taking measurements at the same location guarantees that the control unit processes measurement signals describing the same loads it has to alleviate. Measuring the flapwise bending moment at the blade root though poses some challenges to the control algorithm, as the effects of the flap deflection on the root moment are observed with a delay, and display non-minimum phase behavior: the variation in the measured signals has an initial transient of sign opposite to the load variation reached at the end of the transient. A model based Linear Quadratic (LQ) regulator is chosen to better cope with the large delay and the non-minimum phase response.

The LQ control algorithm, described in section 3.2, adopts a state-space formulation, where the states are estimated from the blade root flapwise bending moment measurements with a Kalman observer [23]. Each blade is treated as an independent Single Input Single Output (SISO) system, and the control and the Kalman observer models are obtained by subspace system identification [24]. Frequency weighting of the control action is introduced to reduce the flap activity at high frequency, and thus limit actuator wear. The classic LQ formulation is modified to handle periodic disturbance rejection [25]. An important contribution to the load variation on a wind turbine blade has in fact a deterministic periodic nature [26, 27]: constant or slow varying sources of disturbances (as gravity, tower shadow, tilt, wind shear, yaw misalignment) produce on the rotating blade load variations with marked periodic components, which depend on the blade azimuthal position and occur at every rotor revolution. Knowledge of the periodic, and hence predictable, disturbances is exploited in the control algorithm, which anticipates, and try to compensate for, the load variations caused by the periodic components. The periodic disturbances are described by simple functions of the blade azimuthal position, and disturbance anticipation does not require additional measurements other than the blade azimuthal position, which again can be obtained with relatively simple and low-maintenance sensors.

The investigation on the flap potential is carried out by means of aeroelastic simulations performed with the code HAWC2 [28], which couples a multi-body structural model with a Blade Element Momentum (BEM) aerodynamic model including steady and dynamic effects of the flap deflection [29]. The load alleviation potential is evaluated for wind conditions prescribed by the IEC standard [30], with turbulence intensity for a class B turbine and a 3D turbulent field generated according to Mann's model [31]; the flap performances are evaluated at mean wind speed above rated, ranging from 12 to 24 m/s. The following section describes the simulation environment, the flap actuator setup, and briefly introduces the models used by the aeroelastic code HAWC2. The LQ control algorithm is presented in section 3, and section 4 reports the results of the aeroservoelastic simulations and quantifies the load alleviation potential achieved by the active flap control.

2. SIMULATION ENVIRONMENT

2.1. Aeroelastic code HAWC2

All the simulations in the study are carried out using the aeroelastic code HAWC2 [28], which features a structural model based on a multi-body finite element formulation. The wind turbine structure is represented by a number of bodies, each of them modeled as a sequence of Timoshenko beam elements, which include beam shear and torsion properties. The torsion degree of freedom, of particular importance given the significant aerodynamic torsional moment generated by the flaps, is thus innately included in the structural model. The turbine blades are then represented by a series of bodies, thus accounting for the non-linear and coupling effects introduced by large blade deflections.

The aerodynamic part of the code follows a Blade Element Momentum (BEM) formulation: a 2D model is used to compute the integral aerodynamic forces and pitching moments on each blade section, and is coupled with a rotor induction

<i>Reference Wind Turbine</i>		<i>Flap Setup</i>	
Rat. Power	5 MW	Chordwise ext.	10%
Num.Blades	3	Deflect.limits	$\pm 10^\circ$
Rotor Diam.	126 m	Max. ΔCl	$-0.45 \sim +0.41$
Blade length	61.5 m	Spanwise length	12.3 m (20% blade length)
Rat. Rot.Sp.	1.267 rad/s	Spanwise loc.	from 47.7 m to 60.0 m span
Hub height	90 m	Max. ΔM_x .Bl.Rt	approx. ± 1100 kNm

Table I. Main characteristics of the NREL reference wind turbine [36], and the adaptive trailing edge flaps setup considered in the investigation.

model that includes Glauert and Prandtl corrections, as well as a dynamic inflow model [32]. The ATEFlap model [29] is used to describe the dynamics of lift, drag, and moment on 2D blade sections with flaps, and consists essentially of a potential flow solution [33] coupled with a Beddoes-Leishmann type of dynamic stall model [34]; the potential flow solution is based on a superposition of Wagner-type indicial response functions, here the classic flat plate response function is slightly modified to account for the thickness of the airfoil [35].

2.2. Reference wind turbine and flap setup

The study considers a smart rotor setup where adaptive trailing edge flaps are applied to the NREL 5-MW reference wind turbine [36], which has a rotor of 126 m diameter and a 3 bladed up-wind configuration typical of modern multi-MW turbines, table I. The turbine baseline controller operates the rotor at variable speed below rated conditions, and limits the power above rated by collectively pitching the blades to feather based on low-pass filtered measurements of the shaft speed [36]. The baseline controller is left unchanged, and the active flap load control is simply superimposed; in the investigated cases, the mutual interference between the flap load control and the pitch power limitation was found to be very small.

The load alleviation achieved with active flap control greatly depends on the extension and type of flap actuators. The adaptive trailing edge flaps in this investigation, table I, extend for 10% of the airfoil chord, and introduce a smooth deflection shape in the airfoil camber-line that outlines a circular arc [29]. The flaps are applied to the NACA 64 airfoil of 17% thickness found in the outboard part of the turbine blades; the flap deflection is limited to $\pm 10^\circ$, and the corresponding variations of the steady aerodynamic coefficients for the airfoil section are computed with Computational Fluid Dynamics [29], figure 1. The maximum steady lift coefficient variation ranges from -0.45 to $+0.41$, which indicatively corresponds to the lift coefficient variation obtained with angle of attack changes from -3.9° to $+3.6^\circ$; due to the smooth deformation shape only a minor drag penalty is reported at small angles of attack, figure 1(b).

The flaps cover 20% of the blade spanwise length, from 47.7 m to 60.0 m of the blade span; when deflected to their $+10^\circ$ limit they cause a variation in the blade root flapwise bending moment (ΔM_x .Bl.Rt) of approximately 1100 kNm (fig.3), which is roughly equivalent to the variation achieved by 1° change of the whole blade pitch angle. In this study, flap sections located on the same blade are all deflected according to the same control signal, which is based on measurements of the blade azimuthal position, and the flapwise bending moment at the root of the same blade.

2.3. Wind conditions

The aim of the aeroelastic simulations is to evaluate the load alleviation potential achieved with the adaptive flaps in realistic operation conditions. The simulations are thus carried out in wind conditions prescribed by the IEC standard design load case 1.1 [30], which corresponds to normal wind turbine operation. The wind field is characterized by a normal terrain shear, described by the power law relation with exponent 0.2; the effects of tower shadow are accounted for, and Mann's turbulence model [31] is applied to generate a 3D turbulent field for a class B turbine, with turbulence intensity ranging from 17 % at 12 m/s to 14 % at 24 m/s.

Bergami and Gaunaa [27] report that wind turbine operations below rated wind speed are responsible for only minor contribution to the blade flapwise lifetime fatigue damage; furthermore, active alleviation of the rotor loads below rated power would reduce the turbine energy capture. Therefore, in this case, the flap load alleviation control is only applied to operation above rated wind speed, and aeroelastic simulations are performed for mean wind speeds from 12 to 24 m/s. A total of 1 hr turbulent wind field is simulated at each mean wind speed (6 seeds of 10 minutes), and identical turbulent fields are used to compare the different control configurations. The mean wind speed distribution, used to evaluate lifetime equivalent loads on the turbine structure, follows a Rayleigh probability density function, with average wind speed of 8.5 m/s (class II turbine in the IEC standard [30]).

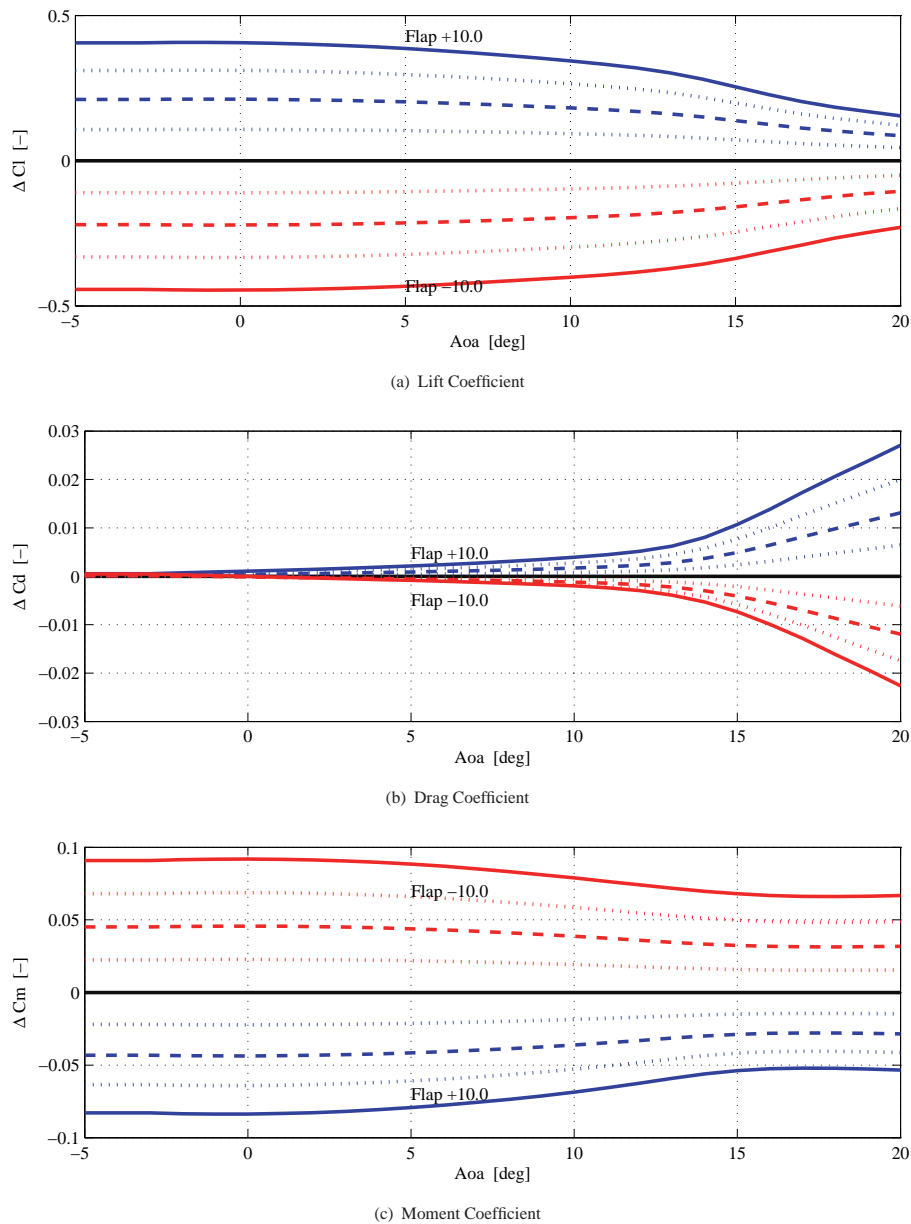


Figure 1. Airfoil section steady aerodynamic coefficient variations achieved by the investigated Adaptive Trailing Edge Flaps. Blue lines indicate positive (downward) flap deflections, red lines negative (upwards) deflections; full lines corresponds to the maximum deflections of $\pm 10^\circ$, dashed lines to $\pm 5^\circ$, and the dotted lines to $\pm 2.5^\circ$ and $\pm 7.5^\circ$.

3. CONTROL DESIGN

The active flap control presented here relies on a model based control algorithm that requires a linear time invariant model of the system to be controlled. The control model should be as simple as possible, and, at the same time, sufficiently complex to capture the relevant dynamics of the system, and to outline, with an accuracy adequate to the control scope, the relation between the measured output y , the control input u , and the disturbances acting on the system. In this case, the measured output y consists of the blade root flapwise bending moment ($M_{x.BI.Rt}$), the control signal u determines the flap deflection angle, and the disturbances are split into a stochastic component e , and a periodic (measurable) component d . The control model is described by a state-space system in discrete time, where the system states at time step i are collected

by the vector x_i . The discrete time state-space system is cast in innovation form [23], thus reading:

$$\begin{cases} x_{i+1} = \mathbf{A}x_i + \mathbf{B}u_i + \mathbf{G}d_i + \mathbf{K}e_i, \\ y_i = \mathbf{C}x_i + e_i. \end{cases} \quad (1)$$

Each of the three rotor blades, with its flap actuators and bending moment sensor, is described by a separate Single Input Single Output (SISO) system, eq. (1), which is assumed independent from the others; although based on a rather crude assumption, the approximation is a convenient practice to simplify the blade load control problem.

3.1. System Identification

A model for the system to control could be retrieved from the same first principle models that are used in the aeroelastic simulation code. Such models though would return a rather complex description, characterized by non-linearities and a large number of states, and would require further processing in order to obtain a model suitable for our control purposes. Instead, a model of the system dynamics of interest is obtained by applying system identification techniques to ‘measurements’ of the system response, which are collected from simulations performed with the aeroelastic code HAWC2.

System identification on a rotating blade is complicated by the strong influence of periodic disturbances, which violate the assumption of measurements noise of stochastic nature. The periodic component would produce a bias in the identified system, as the identification process would try to explain the periodic variations observed in the measurements by altering the system dynamics. Van der Veen et al. [37] propose an elegant solution by including in the identification process additional input signals, which are generated by periodic signals with the same period as the blade rotation.

The additional periodic input signals are formulated as an external periodic disturbance term, d in eq. (1); the periodic disturbance signals are simple functions that only depend on the blade azimuthal position, and are hence easy to measure, and predict. Two types of periodic disturbance signals are considered in the study:

- $d \text{ Sin-Cos}$: following the classic approach [37, 9, 10], a two components signal is built by taking the sine and the cosine of the blade azimuthal position, blue lines in the top plot of figure 4.
- $d \text{ Wsp}$: a single component periodic signal is retrieved from a simple model of the free wind speed variations observed in the blade rotating frame. The wind speed variation only account for terrain shear and tower shadow effects, the latter causing the marked indentation of the signal around 0° azimuth, red line in the top plot of figure 4.

The identification is performed on set of ‘measurements’ of the blade root flapwise bending moment that are retrieved from aeroelastic simulations of the turbine in normal operation while the flap actuators excite the blade following a Pseudo Random Binary Signal (PRBS) that spans the maximum available deflection range of $\pm 10^\circ$. The identification is carried out with the subspace method described by Ljung [24], which supports the narrow-banded additional input signals given by the periodic disturbance terms, and returns a system description in state-space innovation form, eq. (1), hence providing a direct estimation of the Kalman gain matrix \mathbf{K} , eq. (13).

A linear system description with four states was found adequate for the control purposes of this study. The frequency response from flap deflection to blade root flapwise bending moment of the identified four state linear model (blue line in the Bode plots of fig. 2) is compared to the response outlined with spectral estimation (black full line), and to the frequency response obtained from a series of aeroelastic simulations where the flap deflection follows a single-frequency sinusoidal signal and all the sources of periodic disturbances have been ideally removed from the simulation (gray circles in fig. 2). The identified model describes fairly well the response for frequencies up to the second blade flapwise mode (at approximately 1.7 Hz), with a small discrepancy in the low frequency range. Both the simulated response and the spectral estimation show a small indentation slightly above 0.3 Hz, not captured by the identified model; the indentation corresponds to the first natural frequency of the tower, which absorbs part of the energy from the flap actuation. The presence of tower dynamics in the blade response to the flap deflection indicates that the assumption of each blade being independent from the rest of the structure is not entirely correct; nevertheless, its effects are only of secondary importance for the control aim of the study. The Bode plots also report the frequency response obtained with a spectral estimate where the additional periodic disturbance inputs are not taken into account (dashed line *Spa npt* in fig. 2); the estimate in this case would display a clear bias close to the 1P rotational frequency of 0.2 Hz. The effects of neglecting the blade torsional degree of freedom are assessed by simulating the frequency response from flap action with a turbine model where the blades are stiff in torsion (gray line with diamonds in fig. 2); the results indicate an overestimation of the response magnitude ranging between 2 and 3.5 dB. A correct representation of the blade torsion degree of freedom is hence important in aeroelastic simulation evaluating the effects of active flap control, as neglecting it would yield to an overestimation of the flap effects, which, in this particular case, ranges between 20 and 45 %.

The identified models are verified in the time domain by comparing the response to a step flap deflection against the step response simulated with HAWC2, figure 3; again, ideal conditions are enforced in the HAWC2 simulations by removing

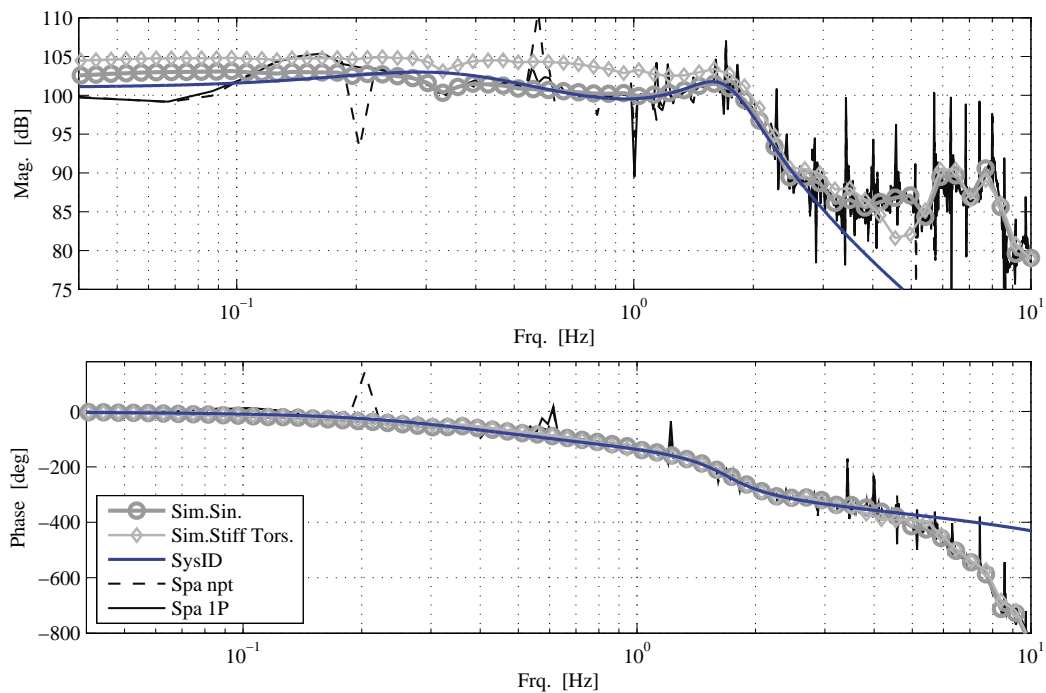


Figure 2. Bode plot, frequency response from flap action to blade root flapwise bending moment $M_{x,Bl,Rt}$. The response from the identified system (blue line) is compared to a spectral estimate (full black line), and to the response from a series of sinusoidal flap action simulations in ideal conditions (gray circles). The response for spectral estimate without periodic term correction (dashed black line), and for simulations with blades stiff in torsion (gray diamonds) are given for comparison.

the sources of periodic disturbances (gravity, wind shear, tower shadow, rotor misalignment). The identified linear model reproduces the main characteristics of the simulated step response: the non-minimum phase transient, the raising time, and the total variation achieved in the root flapwise bending moment. The simulated response presents a low frequency oscillation that is not captured by the identified model, and probably corresponds to the offset observed in the low frequency range of the Bode plots.

The identified systems also describe the influence that periodic disturbances have on the blade flapwise moment. The bending moment variations predicted by the identified linear systems in response to the periodic disturbance signals $d \text{ Sin-Cos}$ and $d \text{ Wsp}$ are compared against the bending moment variation observed in HAWC2 simulations of the turbine operating in a non-turbulent wind field, lower plot in figure 4. Both identified models capture the bending moment variation related to terrain shear effects, and correctly estimate the amplitude and phase of the load variation. The linear system with the $d \text{ Wsp}$ disturbance signal also captures the effects of the tower passage, and correctly reproduces the phase lag observed in the system dynamics, as the blade flapwise bending moment variation is felt with a phase delay of approximately 20° after the tower passage. Note that the flapwise bending moment variation from periodic components (approx. ± 2000 kNm) is already larger than the variation achieved by the flap actuators (approx. ± 1100 kNm). The flaps will thus often operate close to their deflection limits; future work might investigate whether a model predictive control algorithm, which takes into account the flap deflection constraints, would deliver better load alleviation performances than the chosen Linear Quadratic controller.

Finally, the identified linear model is tested by reproducing the response to gaussian random activity of the flap actuator on the rotating blades, and comparing the time series against the one simulated with the complete aeroelastic turbine model in HAWC2, figure 5. With low wind turbulence intensity (2%), the identified model is able to reproduce the simulated output with a good approximation. The agreement between the linear models predictions and the aeroelastic simulation results is quantified in terms of variance-accounted-for (VAF) [37, 10]. The linear model with the $d \text{ Sin-Cos}$ periodic disturbance signal accounts for 94.3% of the variance observed in the simulated output; whereas, the model with the $d \text{ Wsp}$ disturbance signal reaches higher VAF (95.4 %), and better captures the sharp bending moment variations caused by the blade tower passage.

The dynamics of the bending moment response from flap deflection maintain similar characteristics at different operating wind speed, as long as the rotor speed keeps close to its rated value. On the contrary, the system response to the periodic disturbance signals depends on the wind speed, as the amplitude of the periodic load variation increases

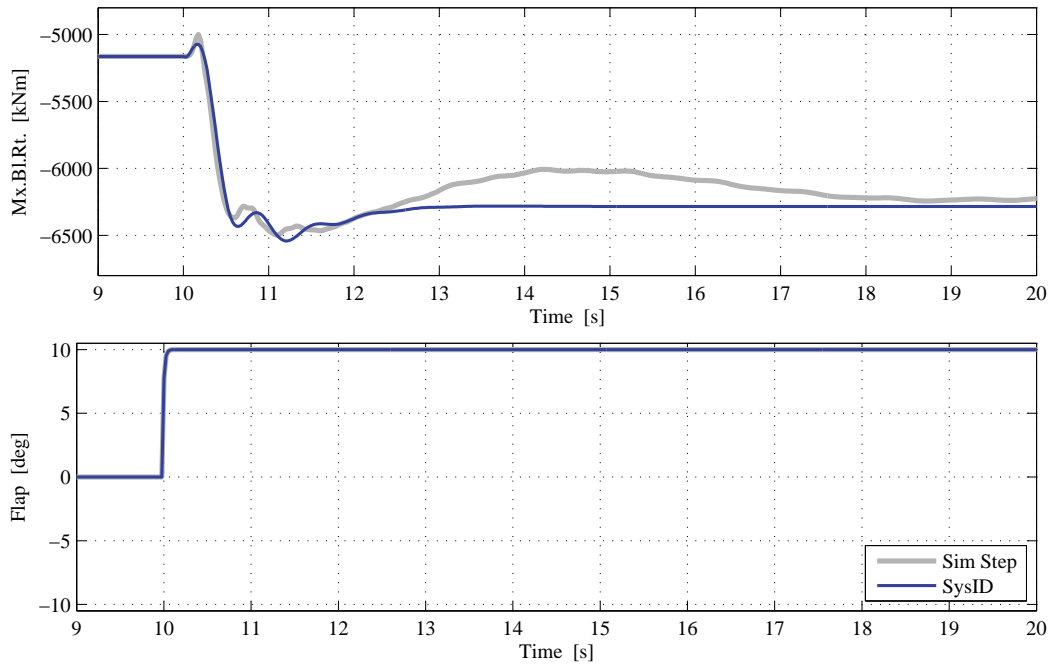


Figure 3. Step response to a positive flap deflection: the increase in lift further deflects the blade to leeward (negative flapwise bending moment). Comparison of the response predicted by the identified system (blue line), and the response from aeroelastic simulations with removed periodic effects (gray line).

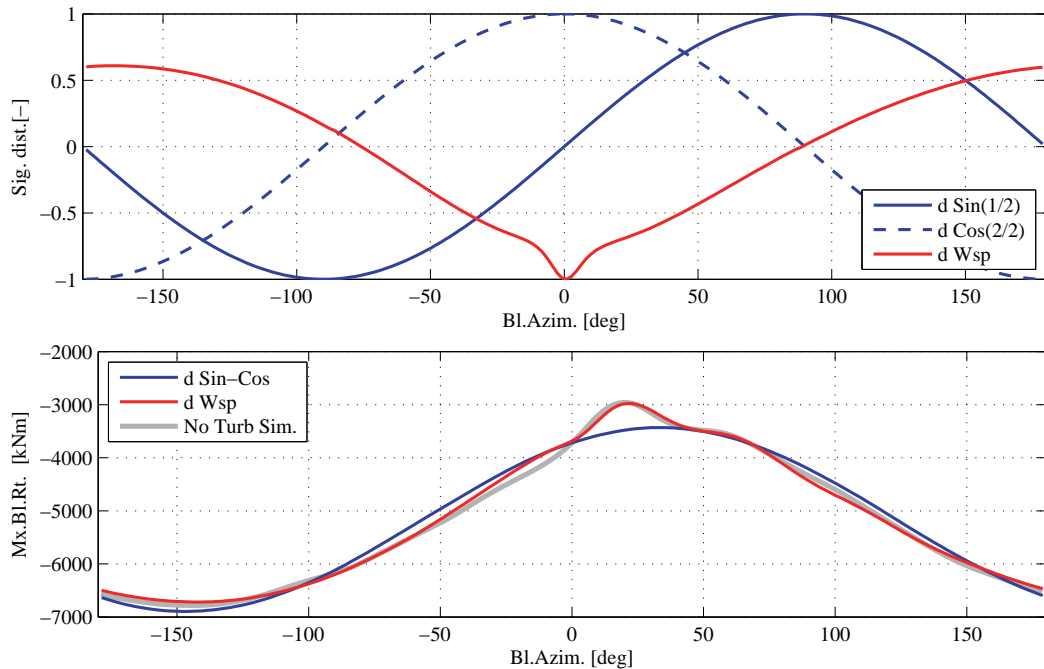


Figure 4. Periodic disturbance signals (top), and periodic component of the blade root flapwise bending moment variation versus blade azimuthal position at 16 m/s (bottom); the blade pointing downwards in front of the tower has 0 ° azimuth, positive direction for clockwise rotations when looking downwind.

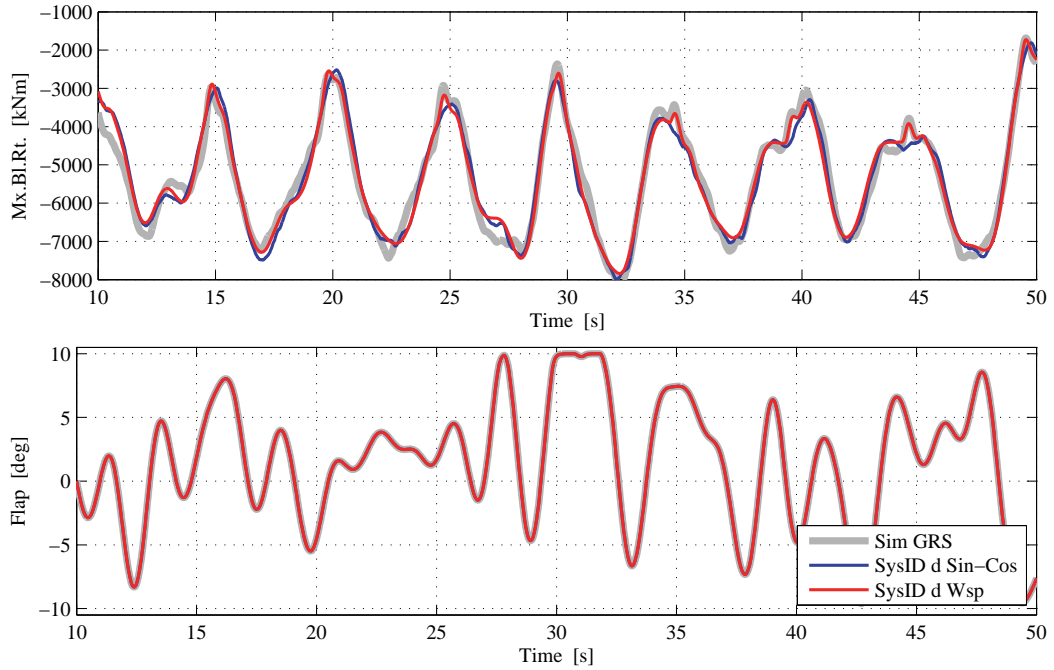


Figure 5. System identification validation time series, blade root flapwise bending moment response to deflection of flap following a GRS series. Comparison of the response predicted from the identified linear models with aeroelastic simulation.

with the mean wind speed. In this investigation, the problem is tackled by simply retrieving a linear model description for each of the operating mean wind speed that will be considered in the load alleviation simulations. Future works might consider solutions more suitable to ‘real-life’ applications, as control algorithms including linear parameter variation or on-line system identification.

3.2. Linear Quadratic regulator with disturbance rejection

Given the dynamic system described by the discrete time affine linear time invariant model in eq. (1), the objective of the Linear Quadratic regulator is to return a control signal u that minimizes the cost function

$$J = \sum_{i=0}^N z_i^T \mathbf{W} z_i, \quad (2)$$

where the augmented error vector z includes both the controlled output y and the control action u :

$$z_i = \begin{bmatrix} \hat{y}_i \\ u_i \end{bmatrix} = \begin{bmatrix} \mathbf{C} \\ \mathbf{0} \end{bmatrix} x_i + \begin{bmatrix} \mathbf{0} \\ \mathbf{I} \end{bmatrix} u_i = \mathbf{C}_z x_i + \mathbf{D}_z u_i. \quad (3)$$

The objective of the controller is thus to limit the variation of the output signal y , and, at the same time, limit the control action u . The weight on the control action is adjusted by the tuning parameter ρ_u , which is included in the cost function weight matrix \mathbf{W} :

$$\mathbf{W} = \begin{bmatrix} 1 & 0 \\ 0 & \rho_u^2 \end{bmatrix}. \quad (4)$$

The cost function can be rewritten as

$$J = \sum_{i=0}^N \begin{bmatrix} x_i^T & u_i^T \end{bmatrix} \begin{bmatrix} \mathbf{Q} & \mathbf{N} \\ \mathbf{N}^T & \mathbf{R} \end{bmatrix} \begin{bmatrix} x_i \\ u_i \end{bmatrix}, \quad \text{where} \quad (5)$$

$$\mathbf{Q} = \mathbf{C}_z^T \mathbf{W} \mathbf{C}_z, \quad \mathbf{R} = \mathbf{D}_z^T \mathbf{W} \mathbf{D}_z, \quad \mathbf{N} = \mathbf{C}_z^T \mathbf{W} \mathbf{D}_z;$$

which is the standard formulation of a Linear Quadratic (LQ) problem with cross coupling terms.

The LQ problem is solved taking into account the disturbance signal d , here given by simple functions of the blade azimuthal position (see fig. 4). The periodic disturbance signals d thus serve a double scope: first they avoid biases from periodic variations during the system identification step; then, the relation between the same signals and the output is exploited by the LQ controller, which is thus able to anticipate future load variations caused by the periodic disturbance components.

Lewis et al.[25] indicate a stationary solution (for $N \rightarrow \infty$) to the LQ problem, where the control signal u_i is given by a sum of a feedback on the system states x_i , on the current disturbance d_i , and on a signal v_{i+1} that includes future disturbances:

$$u_i = -(\mathbf{L}x_i + \mathbf{U}v_{i+1} + \mathbf{M}Gd_i), \quad \text{where:} \quad (6)$$

$$\mathbf{L} = (\mathbf{R} + \mathbf{B}^T \mathbf{S} \mathbf{B})^{-1} (\mathbf{B}^T \mathbf{S} \mathbf{A} + \mathbf{N}^T), \quad \mathbf{U} = (\mathbf{R} + \mathbf{B}^T \mathbf{S} \mathbf{B})^{-1} \mathbf{B}^T, \quad \mathbf{M} = (\mathbf{R} + \mathbf{B}^T \mathbf{S} \mathbf{B})^{-1} \mathbf{B}^T \mathbf{S}, \quad (7)$$

a closed-loop description of the system is thus available. The matrix \mathbf{S} in the control action terms is the solution to the algebraic Riccati equation:

$$\mathbf{S} = \mathbf{A}^T \mathbf{S} \mathbf{A} + \mathbf{Q} - (\mathbf{A}^T \mathbf{S} \mathbf{B} + \mathbf{N}) (\mathbf{R} + \mathbf{B}^T \mathbf{S} \mathbf{B})^{-1} (\mathbf{B}^T \mathbf{S} \mathbf{A} + \mathbf{N}^T). \quad (8)$$

The signal v_i is given by the adjoint of the closed loop system with a backwards recursion on the (predicted) future disturbance signals:

$$v_i = (\mathbf{A} - \mathbf{B}\mathbf{L})^T (v_{i+1} + \mathbf{S}Gd_i), \quad (9)$$

with terminal condition $v_N = 0$, where, in practice, N is a finite number sufficiently large as to avoid any transient effect.

3.2.1. Frequency weighting

Frequency weighting is introduced in the LQ cost function, eq. (2), in order to penalize output variations or flap actions in certain frequency ranges. The error signal z is given by filtered versions of the output y^f and the control action u^f , which are obtained through linear state-space descriptions chosen as to increase the response gain in the frequency range to penalize:

$$u : \begin{cases} x_{i+1}^u &= \mathbf{A}^u x_i^u + \mathbf{B}^u u_i \\ u_i^f &= \mathbf{C}^u x_i^u + \mathbf{D}^u u_i \end{cases} \quad \text{and} \quad \hat{y} : \begin{cases} x_{i+1}^y &= \mathbf{A}^y x_i^y + \mathbf{B}^y \hat{y} \\ y_i^f &= \mathbf{C}^y x_i^y + \mathbf{D}^y \hat{y} \end{cases} \quad (10)$$

The state vector of the system is extended x^{ext} to include the filter states x^u and x^y , the extended error signal z is computed as

$$z_i = \begin{bmatrix} y_i^f \\ u_i^f \end{bmatrix} = \begin{bmatrix} \mathbf{D}^y \mathbf{C} & \mathbf{C}^y & \mathbf{0} \\ \mathbf{0} & \mathbf{0} & \mathbf{C}^u \end{bmatrix} \begin{bmatrix} x_i \\ x_i^y \\ x_i^u \end{bmatrix} + \begin{bmatrix} \mathbf{0} \\ \mathbf{D}^u \end{bmatrix} u_i = \mathbf{C}_z^{\text{ext}} x_i^{\text{ext}} + \mathbf{D}_z^{\text{ext}} u_i, \quad (11)$$

and the state equation, eq. (1), is reformulated in terms of extended state vectors and extended matrices:

$$x_{i+1}^{\text{ext}} = \begin{bmatrix} x_{i+1} \\ x_{i+1}^y \\ x_{i+1}^u \end{bmatrix} = \begin{bmatrix} \mathbf{A} & \mathbf{0} & \mathbf{0} \\ \mathbf{B}^y \mathbf{C} & \mathbf{A}^y & \mathbf{0} \\ \mathbf{0} & \mathbf{0} & \mathbf{A}^u \end{bmatrix} \begin{bmatrix} x_i \\ x_i^y \\ x_i^u \end{bmatrix} + \begin{bmatrix} \mathbf{B} \\ \mathbf{0} \\ \mathbf{B}^u \end{bmatrix} u_i + \begin{bmatrix} \mathbf{G} \\ \mathbf{0} \\ \mathbf{0} \end{bmatrix} d_i = \mathbf{A}^{\text{ext}} x_i^{\text{ext}} + \mathbf{B}^{\text{ext}} u_i + \mathbf{G}^{\text{ext}} d_i. \quad (12)$$

The frequency weighting is included in the controller by using the extended matrices in the equations for the cost function matrices eq. (5), the algebraic Riccati equation (8), and the LQ gain matrices eq. (7).

In this investigation, frequency weighting is only applied to the control signal u , and penalizes control actions with frequencies above 0.5 Hz. The frequency weighting reduces flap activity and flap deflection speed, thus potentially increasing the life-time of the flap actuators; the effects on the fatigue load alleviation reduction are minor, as the largest contribution to the blade fatigue damage originates at lower frequencies [19, 27].

3.2.2. State estimation

The control action is based on a feedback from the system states x . The states though, are not measured directly, in their place the control uses estimated states \hat{x} , which are retrieved with a Kalman filter estimator [23] from measurements of the blade root flapwise bending moment y_i :

$$\hat{x}_{i+1} = \mathbf{A}\hat{x}_i + \mathbf{B}u_i + \mathbf{G}d_i + \mathbf{K}(y_i - \mathbf{C}\hat{x}_i). \quad (13)$$

The linear model descriptions used by the Kalman filter estimator, as well as the Kalman gain matrix \mathbf{K} , are also retrieved from the innovation state-space description returned by the subspace system identification, eq. (1), thus avoiding the need of further tuning the Kalman observer.

4. AEROELASTIC SIMULATION RESULTS

The LQ regulator is implemented in the simulation tool, and the blade load alleviation performances of the smart rotor set-up are assessed with a series of aeroelastic simulations during normal production, above rated wind speed, and with the turbulent wind field prescribed by the IEC standard [30] for a class B turbine.

Three flap control configurations are investigated, and the resulting loads are compared to the reference case of no active flap control. In the first control configuration (denoted as *d 00*), the LQ regulator has no information about the periodic disturbances: it does not anticipate the periodic load variation, and it only acts based on the measurement feedback. The *d Sin-Cos* configuration handles periodic disturbance anticipation based on the harmonic sine and cosine disturbance signals; the *d Wsp* configuration anticipates instead the periodic load variation based on the disturbance signal of the simplified free wind speed variation. All the control configurations are tuned by acting on the control weight, ρ_u in eq. (4), so to reach a compromise between blade flapwise fatigue damage alleviation, and flap activity.

An extract of the simulated time series of the blade root flapwise bending moment, and of the corresponding flap actions is displayed in figure 6; the load series with active flap control have the same mean value as the reference one, but the load variations are decreased and some peaks smoothed out, thus indicating correct operation of the active flap control in all the three configurations. The time series of the flap actions remark how the load variation achieved by the flap actuators is far less than the load variations caused by the disturbances, often pushing the flap actuators to their deflection limits of $\pm 10^\circ$. Future work should thus investigate the benefit of a control algorithm, e.g. model predictive control, that accounts for the flap deflection constraints, and it should determine whether higher load alleviations could be achieved with a more powerful actuator setup.

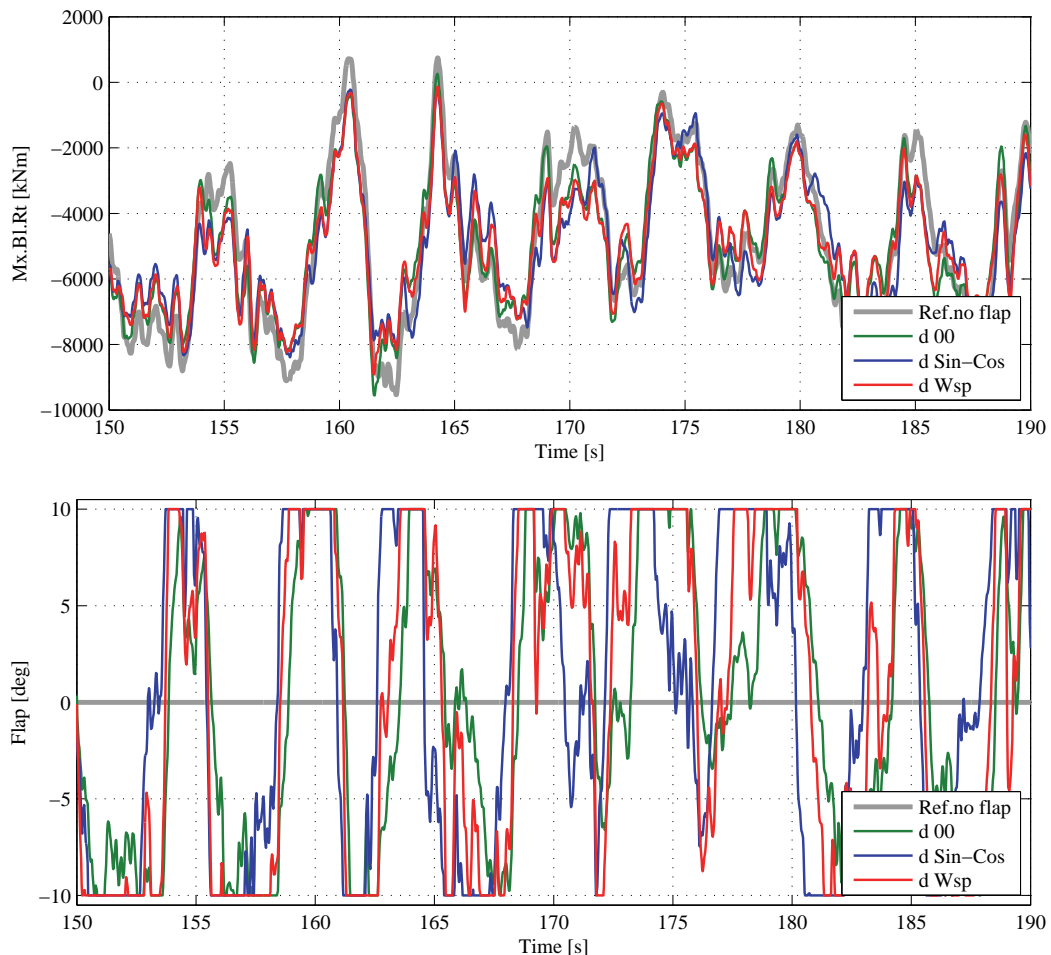


Figure 6. Extract of time series simulation at mean wind speed of 16 m/s. Blade root flapwise bending moment (top), and flap activity (bottom). The reference case of no active flap control is reported with the light gray line, the active flap configurations with green, blue, and red lines.

The loads on the rotating blade obtained from one hour simulation with mean wind speed 16 m/s are plotted versus the blade azimuthal position, figures 7 and 8. The mean load at each azimuthal position is indicative of the periodic component of the load variation (lines with markers); whereas, the dashed lines displaying the standard deviation range represent the influence of the stochastic load component, which is mainly generated by the atmospheric turbulence. The active flap control reduces both the periodic variations of the flapwise bending moment (fig. 7), and the stochastic component of the loads. The reduction of the stochastic component is similar for the three control configurations, as it mainly depends on the feedback mechanism of the LQ control. On the contrary, the alleviation of the periodic load variation is more marked in the *d Sin-Cos* and *d Wsp* configurations, which handle periodic disturbance anticipation; the loads from *d Wsp* simulations also displays a slightly smoother variation around the tower passage (notch at 20° azimuth), although the positive effects of the more accurate periodic disturbance description (cfr fig. 4) are partly limited by the flap actuators reaching their deflection limits.

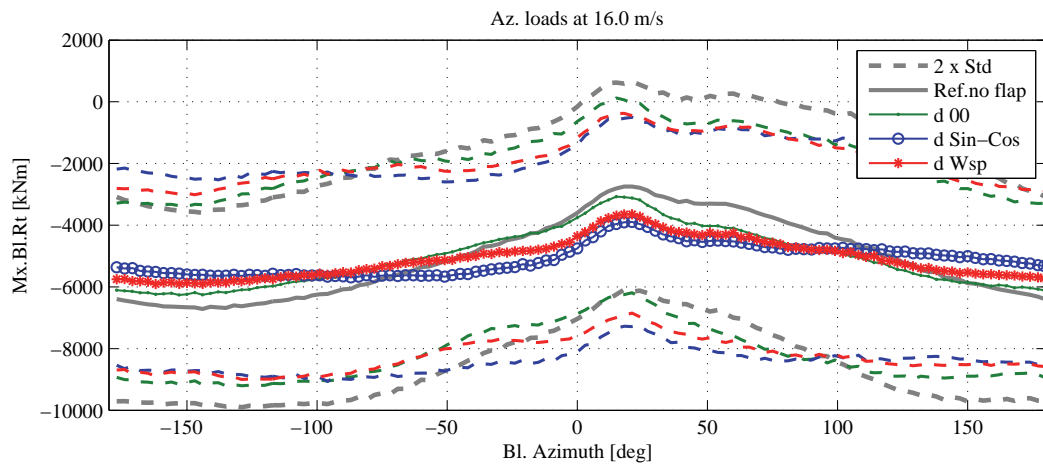


Figure 7. Blade root flapwise bending moment versus blade azimuthal position. Results for 1 hr simulation at mean wind speed of 16 m/s. For each azimuthal position the means of the simulated loads (lines with markers) indicate the periodic component of the load variation, the standard deviations (dashed lines) are instead proportional to the stochastic load variation. Active flap control reduces both component of the flapwise load variation.

The reduction of the blade flapwise bending moment comes at the price of increased variations of the blade torsion moment (fig. 8), which are caused by the aerodynamic pitching moment introduced by the flaps. Usually, the blade torsion loads are not a driving parameter in rotor design, nevertheless the substantial increase that might be generated by active aerodynamic devices should be taken into account in future smart rotor designs. Active flap control slightly increases the range of load variations also on the blade edgewise bending moment, but gravity loads are by far still dominating in this direction.

The effects of the active load control are verified for the whole range of mean wind speeds above rated conditions, from 12 to 24 m/s. For each mean wind speed and each control configuration simulations are carried out for a total of one hour turbulent wind (divided into six ten minutes turbulence seeds), as prescribed by the normal turbulence model in the IEC standard [30]. Statistics on the simulated loads confirm the observations of the azimuthal load analysis: the mean flapwise bending moment is unchanged (fig. 9), whereas the maximum load variations (distance between the upper and lower dashed lines) are reduced by approximately 13%. The standard deviation of the flapwise load displays significant variations among the turbulence seeds, but still shows a marked reduction in the cases with active flap control; on average, the standard deviation with the *d 00* active control configuration is 15.5% lower than in the not controlled case, and higher reduction are achieved with the *d Sin-Cos* configuration (22%) and the *d Wsp* one (24%). As already observed, active flap control has also an effect on other loads on the structure: the standard deviation of the blade torsion moment is increased, whereas a reduction of the load variation is observed at the tower bottom flange, where the standard deviation in the fore-aft bending moment is 7% lower than in the reference case. Minor reductions in standard deviation are also observed on the shaft yaw and tilting moments, and on the tower top yaw moment.

The total activity required by the active load control to the flap actuators is measured as the total angular distance traveled by the flap, either with upward or downward deflections; the angular distance is then normalized by the total operation time, thus returning an average deflection speed, figure 10. The *d Wsp* control configuration, which achieves higher reductions of the flapwise loads standard deviation, also demands higher flap activity; the *d 00* configuration, instead, in spite of lower alleviation performances, requires higher flap activity than the *d Sin-Cos* configuration. The reduction of flap activity as the mean wind speed increases, in spite of increased loads variations, is probably explained by the flap reaching more

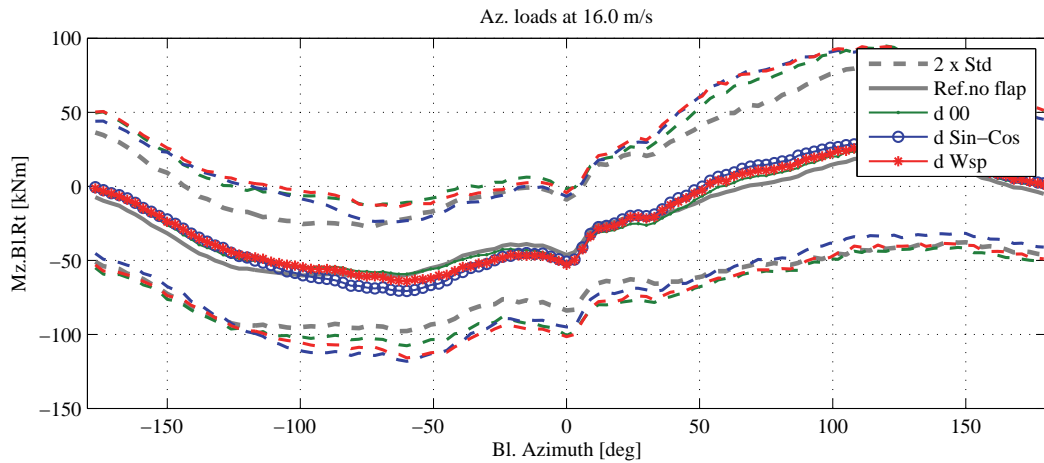


Figure 8. Blade root torsion moment versus blade azimuthal position. Results for 1 hr simulation at mean wind speed of 16 m/s. As before, the plot displays the periodic component of the loads (mean), and the stochastic one (standard deviation). Active flap control produces an increase in the torsion load variations.

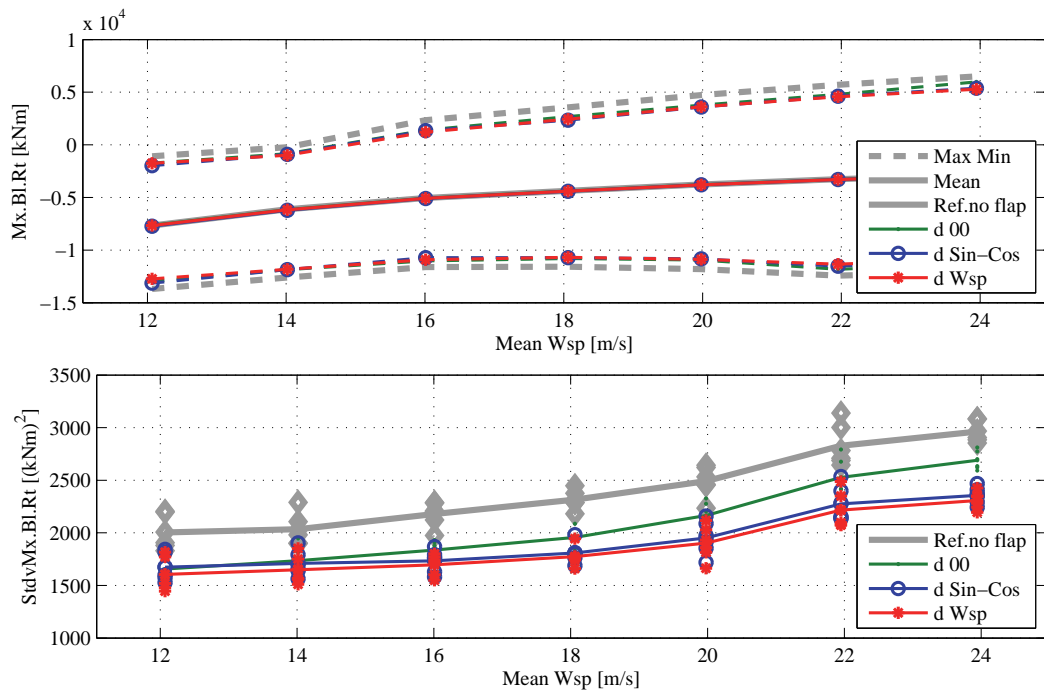


Figure 9. Load statistics: blade root flapwise bending moment mean and load ranges (top), and loads standard deviation (bottom). Each of the mark in the standard deviation plot corresponds to a single 10 minutes time simulation. Active flap control reduces the load range, and the standard deviation.

often the actuator deflection limits. The maximum deflection rate of the flap actuator is not constrained in the simulations. Nevertheless, with the frequency weighting penalizing high frequency flap activity, 99 % of the flap activity observed in the simulations requires deflection rates below 90 deg/s; the introduction of deflection rate constraints close or above this limit is thus expected to have no significant effects on the smart rotor load alleviation potential.

The power spectral density of the blade flapwise moment, figure 11, shows that most of the load alleviation occur for frequencies close to 1P, the rotor revolution frequency (0.2 Hz). A small increase in the spectral energy content is instead observed around 1 Hz. The increase is limited by the frequency weighting, but the introduced penalization appear not sufficient to keep the power spectrum below the baseline value in this frequency range; attempts to further increase the

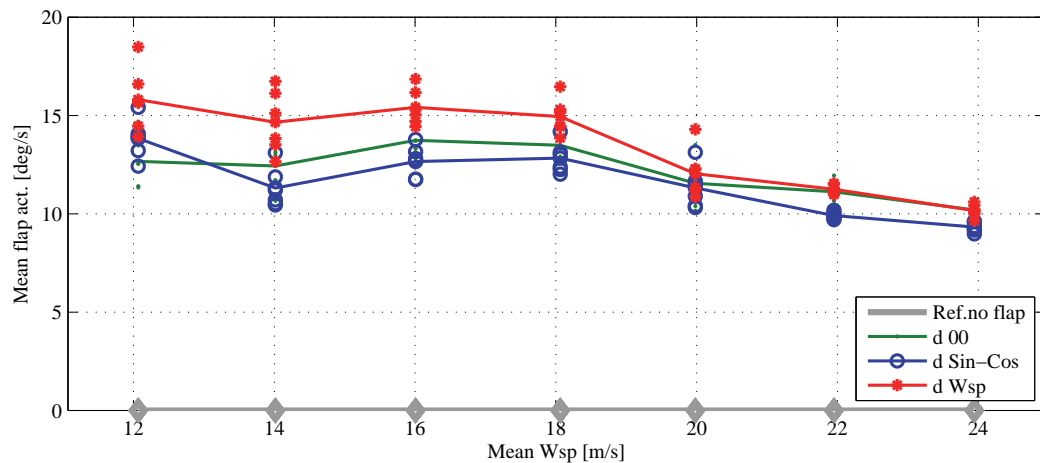


Figure 10. Flap activity for the three control configurations. Total flap traveled distance normalized by the simulation time, for each of the investigated mean wind speeds.

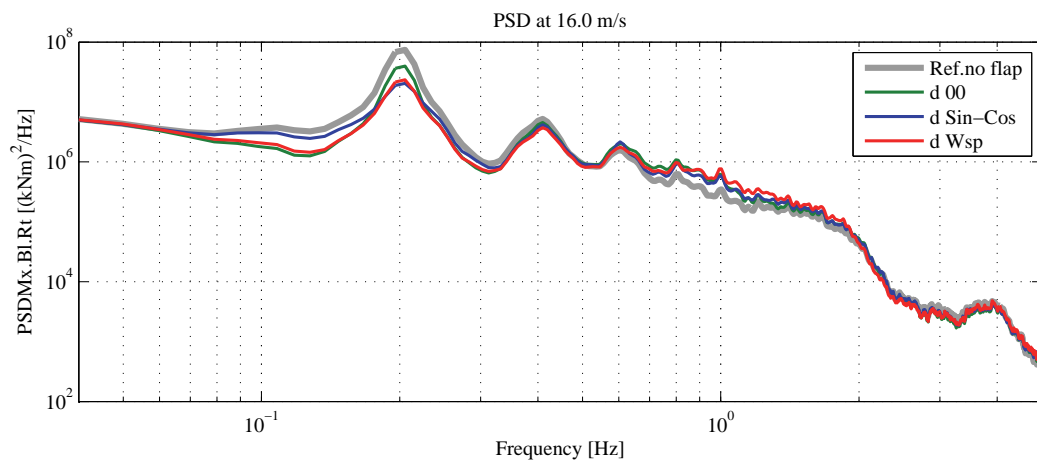


Figure 11. Power spectral density of the blade root flapwise bending moment; the plot refers to simulations with mean wind speed of 16 m/s, similar figures are obtained for the other investigated wind speed. The load reduction from the active flap control is mainly concentrated in the frequency range around 1P, the rotor revolution frequency of 0.2 Hz.

frequency penalization resulted in lower flap activity, but also lower blade load alleviation. The power spectrum of the flap activity (fig. 12) is dominated by the 1P rotational frequency and its harmonics; the frequency content of the flap activity decreases significantly above 1 Hz, both as an effect of the frequency weighting, and also for the lower energy content in the loads addressed by the flap control.

The performance of the smart rotor is finally quantified in terms of reduction of fatigue damage equivalent loads (DEL). The equivalent loads are computed under Palmgren-Miner linear damage assumption [38], and a Wöhler curve exponent of 10 is used for the loads on the blades, and 4 for the rest of the structure. The damage equivalent loads are here referred to 25 years of operation, and 10 millions equivalent cycles; the mean wind speed occurrence is weighted according to a Rayleigh distribution with 8.5 m/s average wind speed, as prescribed by the IEC standard [30] for a class II turbine.

The active flap control succeeds in all the investigated configurations in reducing the fatigue damage of the blade root flapwise bending moment, figure 13. The *d 00* configuration, acting exclusively on the feedback from bending moment measurements, has the poorest performance, with alleviations ranging from 7.5 to 12.6 % at low wind speed, and a total lifetime fatigue equivalent damage load by 10.2 % lower than the reference case without active flap control. The control configurations with periodic disturbances anticipation achieve higher reductions: the *d Sin-Cos* control alleviates the lifetime fatigue damage by 13.8 %, and the *d Wsp* configuration reaches a lifetime reduction of 14.5%, albeit with higher flap activity. Looking at each of the 10 minutes turbulence series individually, markers in figure 13, a large spread in the load alleviation potential is reported among the different simulation series, ranging from 9 % to 19 %. Experiment or

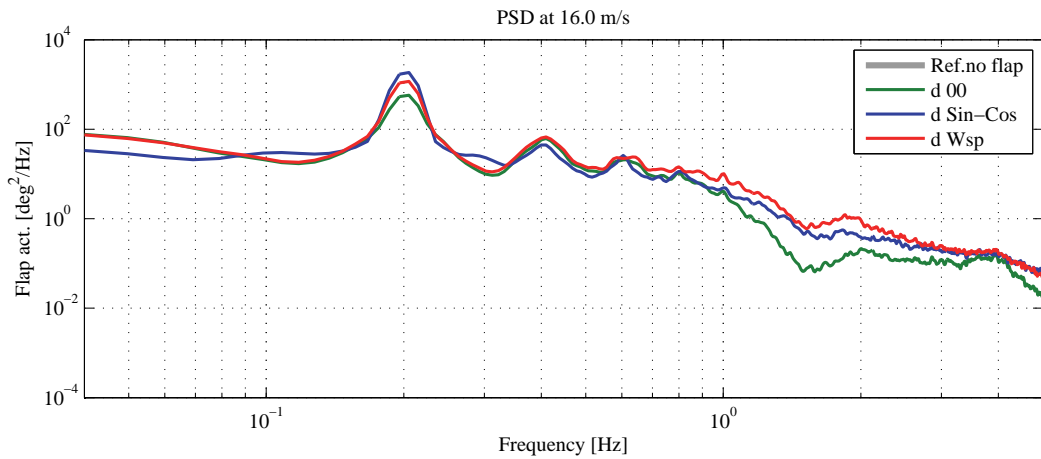


Figure 12. Power spectral density of the flap activity. For the three control configurations most of the flap activity is concentrated around the rotational frequency 1P (0.2 Hz) and its harmonics.

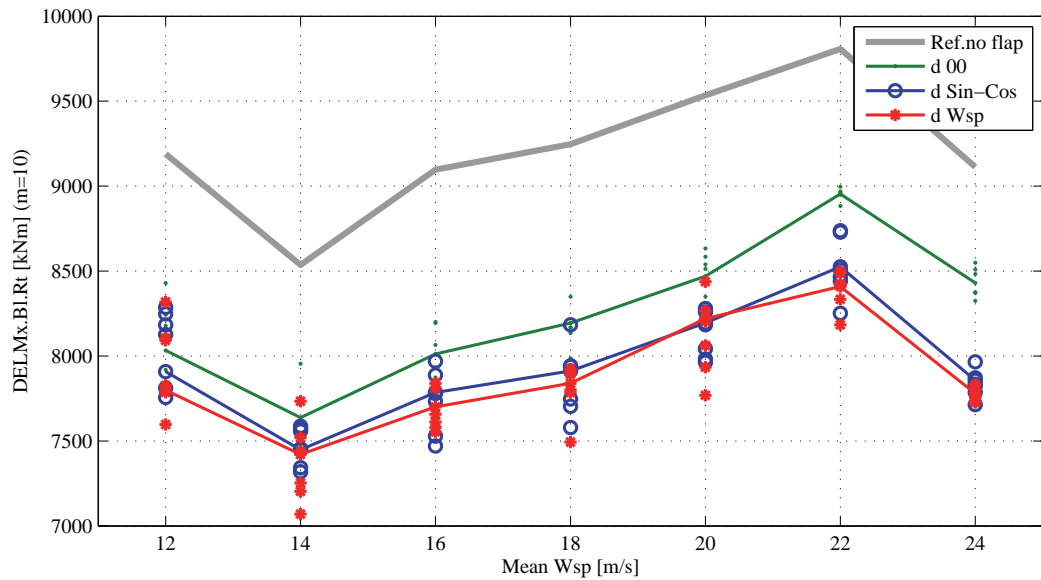


Figure 13. Fatigue Damage Equivalent Loads (DEL) at the blade root flapwise bending moment. The DEL refer to a 25 yr lifetime and 10 millions equivalent cycles, the figures at each mean wind speed are weighted by the occurrence of the mean wind speed according to a Rayleigh distribution for a class II turbine. The dots report the spreading of fatigue damage reduction recorded in each of the 10 minutes simulation series.

simulation in turbulent wind conditions should thus consider time series of sufficient length to ensure statistically relevant conclusions on the load alleviation potential; in the investigated case, at least 40 minutes of simulation are required to reach alleviation estimations within one point percent of the result obtained by turbulent wind simulation of 60 minutes, which is the minimum requirement specified by the IEC standard [30].

The active flap control also affects the fatigue damage of components not included in the control objectives. The lifetime damage equivalent load on the blade root torsion moment is increased by about 10 %; the blade edgewise bending moment and the shaft torsion DEL are also increased by about 6%. On the other hand, a reduction in the fatigue damage is observed at the tower bottom flange, in the fore-aft direction, figure 14: the *d 00* configuration reduces the tower lifetime damage by 6.5 %, and smaller figures are obtained with *d Wsp* (5.6 %), and *d Sin-Cos* (3 %). In spite of a reduction in the standard deviation, the tower side-to-side loads and the bending moment on the shaft do not report relevant changes in the lifetime fatigue damages.

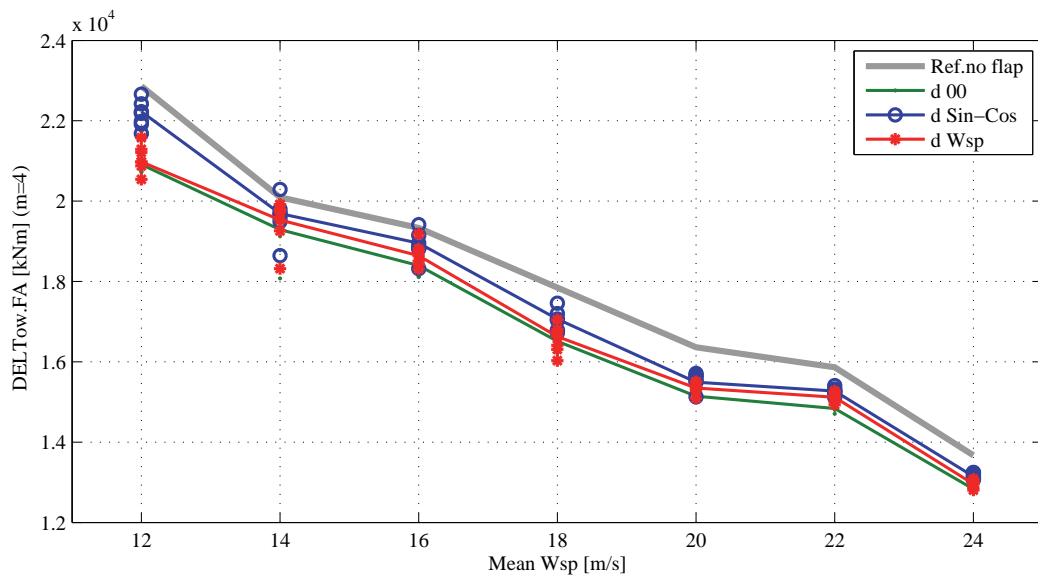


Figure 14. Fatigue Damage Equivalent Loads (DEL) at the tower bottom flange in fore-aft direction. The DEL at each mean wind speed account for the time each mean speed is expected to occur (higher wind speeds are less likely, hence they yield lower fatigue damage).

To verify the performance of the active flap control in operation conditions slightly different from the control design ones, a series of simulation is performed with a yaw misalignment error. The blade flapwise damage equivalent loads are computed for one hour simulation with mean wind speed of 16 m/s and yaw misalignment of $\pm 8^\circ$, figure 15; the same flap control configurations as in the normal production cases are used, without any re-tuning nor modifications of the periodic disturbance signals. The fatigue damage equivalent load is higher than in the aligned case for positive yaw misalignment, i.e. the right hand side part of the rotor (looking downwind) is displaced to leeward; the fatigue reduction from the active flap control is also slightly higher than in the aligned rotor case: 12.2 % for *d 00*, 15.5 % for *d Sin-Cos*, and 15.7 % for *d Wsp*. On the contrary, for the negative yaw misalignment, the fatigue damage is slightly lower, and so is the reduction from the active flap control, with figures ranging from 11.2 % to 14.2 %, figure 15. As in the aligned case, the flap control reduces the loads at the tower bottom flange in the fore-aft direction, while it increases the blade torsion and edgewise bending fatigue damages. The tower and shaft yaw fatigue damage loads, in both cases higher than in the aligned case, are nearly left unchanged by the active flap control, but the maximum loads are instead reduced by approximately 14 % when the flap load control is active.

5. CONCLUSION

Simulations of a smart rotor with adaptive trailing edge flaps are carried out with the aeroelastic code HAWC2, which features an aerodynamic model describing both attached and stalled flow dynamics, and a multibody structural model that accounts also for the blade torsion degree of freedom. Blade torsion is particularly relevant for aeroelastic simulations of a rotor with flaps, as the flap deflection introduces a significant aerodynamic pitching moment; therefore, by omitting the blade torsion compliance, the flap ability to alleviate the loads on the blade would be overestimated. The adaptive trailing edge flaps are applied to the NREL 5 MW reference turbine rotor [36]; they cover 20 % of the blade span, and are controlled by a linear quadratic (LQ) algorithm based on a simple sensor arrangement: the flap on each of the blades is controlled based on the root flapwise bending moment and azimuthal position of the same blade. The effects of the active flap control are quantified in terms of load statistics, spectra, and fatigue damage equivalent loads, reproducing the simulation conditions prescribed by the IEC standard [30] for a class IIb turbine.

Active flap control allows to reduce the maximum load range on the blade root flapwise bending moment by approximately 13 %, and the standard deviation of the bending moment is 15-24 % lower than in the reference case without active control. The adaptive flap controllers alleviate loads mainly in the low frequency range of the spectrum (0.1-0.5 Hz), and especially around the 1P rotational frequency (0.2 Hz). As the loads in the low frequency range are responsible for the largest contribution to the blade root flapwise fatigue damage [19, 27], it is beneficial to discourage the activity of the flap actuators at higher frequencies by introducing a frequency-dependent weighting in the LQ control

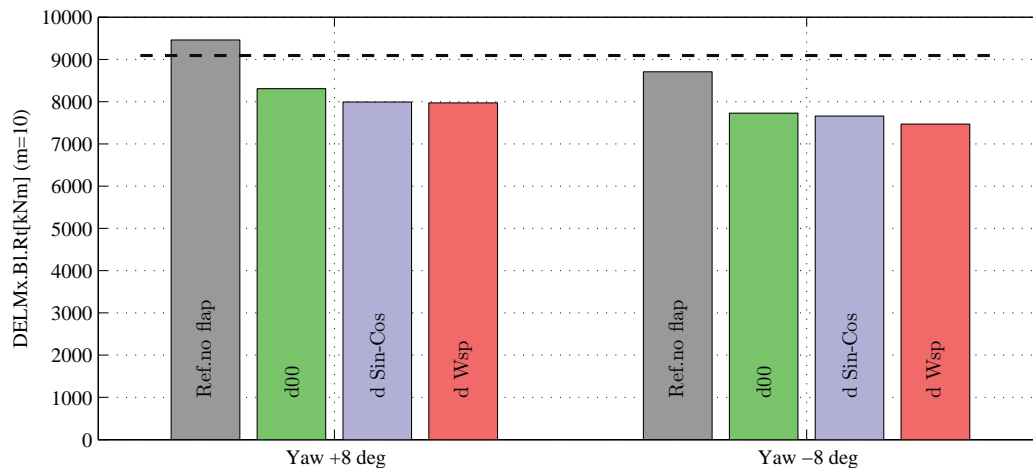


Figure 15. Fatigue Damage Equivalent Loads (DEL) at the blade root flapwise bending moment for the rotor in yawed conditions for operation at a single mean wind speed (16 m/s); positive yaw angles imply that the right hand side of the rotor (looking downwind) is displaced to leeward. The dashed black line correspond to the DEL reported for the aligned rotor in the reference case of no flap control.

algorithm. The frequency weighting penalizes control activity at frequencies above 0.5 Hz, thus limiting the total flap movement and the maximum deflection rate, hence effectively reducing the wear of hypothetical flap actuators.

Ultimately, the effects of the adaptive trailing edge flap control are quantified in terms of lifetime fatigue damage equivalent load reduction. The control configuration based on only measurements feedback (*d 00*) lowers the lifetime fatigue equivalent damage on the blade root flapwise bending moment by about 10 %, a result in line with previous investigations that considered similar setups [12, 17]. Periodic load anticipation, which is based on the blade azimuthal position and handled by the LQ algorithm as a prediction on periodic disturbance signals, allows to reach higher lifetime damage alleviation: 13.8 % with the *d Sin-Cos* configuration, and 14.5 % with *d Wsp*. The increase in load alleviation potential by nearly 4 % achieved by including periodic load anticipation is comparable to the increase previous investigations have attained using additional in-flow sensors [12, 14], with the advantage that the periodic load anticipation approach does not require a sensor setup as complicate and delicate as demanded for in-flow measurements. As an effect of active load alleviation with adaptive trailing edge flaps, a significant increase of the blade torsion fatigue damage equivalent load is reported (nearly 10 %); the increase of the torsional loads, and, to a lesser extent, of loads on other components, should be hence taken into account in the design of smart rotor structures. Positive reduction of damage equivalent loads are instead reported for the tower bottom flange fore-aft bending moment (by approx. 5%); the load alleviation on the blade flapwise moment and on the tower bottom flange are also confirmed in yawed inflow conditions.

To conclude with a consideration on possible future work, according to the results reported in this study and in the literature, the load alleviation potential achieved by the smart rotor appears to be mainly limited by the strength of the aerodynamic actuators employed on the rotor. In fact, the variation of blade root flapwise bending moment obtained by the current flap setup is simply too small to compensate to an higher degree for the load variations observed on the blade during normal operation. Future work should thus consider, first, whether a control algorithm that handles flap deflection constraints, as for instance model predictive control [21, 12], could improve the load alleviation performances. Secondly, future investigations might focus on whether fatigue loads could be further reduced by fitting the smart rotor with a more powerful actuator setup, either by augmenting the blades surface covered by adaptive flaps, or by complementing the flap efforts with individual blade pitch actions.

ACKNOWLEDGMENT

It is gratefully acknowledged that this work is partly funded by the Danish project *Development of Adaptive Trailing Edge Flap (ATEF) System for Wind Turbines* by the Advanced Technology Foundation, Advanced Technology Projects 2007.

REFERENCES

1. Barlas TK, van Kuik G. State of the art and prospectives of smart rotor control for wind turbines. *Journal of Physics: Conference Series* 2007; **75**(1):012 080 (20 pp.). Journal Article.
2. Bossanyi EA. Individual blade pitch control for load reduction. *Wind Energy* 2003; **6**(2):119–128. Journal Article.
3. Larsen TJ, Madsen HA, Thomsen K. Active load reduction using individual pitch, based on local blade flow measurements. *Wind Energy* 2005; **8**(1):67–80. Journal Article.
4. Troldborg N. Computational study of the Riso-B1-18 airfoil with a hinged flap providing variable trailing edge geometry. *Wind Engineering* 2005; **29**(2):89–113. Journal Article.
5. Buhl T, Gaunaa M, Bak C. Potential load reduction using airfoils with variable trailing edge geometry. *Transactions of the ASME. Journal of Solar Energy Engineering* 2005; **127**(4):503–516.
6. Johnson SJ, Baker JP, van Dam CP, Berg D. An overview of active load control techniques for wind turbines with an emphasis on microtabs. *Wind Energy* Mar 2010; **13**(2-3):239–253, doi:10.1002/we.356.
7. van Wingerden JW, Hulskamp AW, Barlas T, Marrant B, van Kuik GAM, Molenaar DP, Verhaegen M. On the proof of concept of a 'Smart' wind turbine rotor blade for load alleviation. *Wind Energy* 2008; **11**(3):265–280. Journal Article.
8. Bak C, Gaunaa M, Andersen PB, Buhl T, Hansen P, Clemmensen K. Wind tunnel test on airfoil risø-b1-18 with an active trailing edge flap. *Wind Energy* 2010; **13**(2-3):207–219, doi:10.1002/we.369. URL <http://onlinelibrary.wiley.com/globalproxy.cvt.dk/doi/10.1002/we.369/abstract>.
9. van Wingerden J, Hulskamp A, Barlas T, Houtzager I, Bersee H, van Kuik G, Verhaegen M. Smart dynamic rotor control: Part 3, advanced controller design. *Proc. of the 3rd conference, The Science of Making Torque from Wind*, Eraklion, Crete, Greece, 2010; 702–708.
10. Barlas T, van Wingerden W, Hulskamp A, van Kuik GM, Bersee HN. Smart dynamic rotor control using active flaps on a small-scale wind turbine: aeroelastic modeling and comparison with wind tunnel measurements. *Wind Energy* 2012; **Early View**(published on-line), doi:10.1002/we.1560.
11. Castaignet D, Wedel-Heinen JJ, Kim T, Buhl T, Poulsen N. Results from the first full scale wind turbine equipped with trailing edge flaps. *Proceedings of 28th AIAA Applied Aerodynamics Conference*, American Institute of Aeronautics and Astronautics: Chicago, IL (US), 2010, doi:10.2514/6.2010-4407.
12. Barlas TK, van der Veen GJ, van Kuik GA. Model predictive control for wind turbines with distributed active flaps: incorporating inflow signals and actuator constraints. *Wind Energy* 2011; doi:10.1002/we.503. URL [here-is-the-test-url](http://onlinelibrary.wiley.com/doi/10.1002/we.503).
13. Riziotis VA, Voutsinas SG. Aeroelastic modeling of the active flap concept for load control. *Scientific proceedings. 2008 European Wind Energy Conference and Exhibition, Brussels (BE)*, 2008; 22–26. Conference Proceedings.
14. Andersen PB, Henriksen LC, Gaunaa M, Bak C, Buhl T. Integrating deformable trailing edge geometry in modern mega-watt wind turbine controllers. *Scientific proceedings. 2008 European Wind Energy Conference and Exhibition, Brussels (BE)*, 2008; 15–21. Conference Proceedings.
15. Resor B, Wilson D, Berg D, Berg J, Barlas T, van Wingerden JW, van Kuik GAM. Impact of higher fidelity models on simulation of active aerodynamic load control for fatigue damage reduction. *Proceedings of the 48th AIAA/ASME*, Orlando, FL, 2010.
16. Andersen PB, Henriksen L, Gaunaa M, Bak C, Buhl T. Deformable trailing edge flaps for modern megawatt wind turbine controllers using strain gauge sensors. *Wind Energy* Mar 2010; **13**(2-3):193–206, doi:10.1002/we.371.
17. Baek P. Unsteady flow modeling and experimental verification of active flow control concepts for wind turbine blades. Ph.D. thesis, Risø DTU, Technical University of Denmark, Roskilde, Denmark Dec 2011.
18. Barlas TK, Van Kuik GAM. Aeroelastic modelling and comparison of advanced active flap control concepts for load reduction on the upwind 5MW wind turbine. *European Wind Energy Conference, Marseille, France*, 2009; 16–19.
19. Lackner MA, van Kuik G. A comparison of smart rotor control approaches using trailing edge flaps and individual pitch control. *Wind Energy* Mar 2010; **13**(2-3):117–134, doi:10.1002/we.353.
20. Wilson D, Resor B, Berg D, Barlas T, van Kuik G. Active aerodynamic blade distributed flap control design procedure for load reduction on the UpWind 5MW wind turbine. *Proceedings of the 48th AIAA Aerospace Sciences Meeting*, 2010; 4–7.
21. Castaignet D, Poulsen NK, Buhl T, Wedel-Heinen JJ. Model predictive control of trailing edge flaps on a wind turbine blade. *Proceedings of the American Control Conference 2011*, San Francisco, CA, USA, 2011.
22. Berg D, Wilson D, Resor B, Berg J, Barlas T, Crowther A, Halse C, House R. System ID modern control algorithms for active aerodynamic load control and impact on gearbox loading. *Proceedings of the Conference on the Science of Making Torque from Wind*, 2010.
23. Åstrom KJ. *Introduction to stochastic control theory, Mathematics in science and engineering*, vol. 70. Academic Press: London, 1970.
24. Ljung L. *System identification: theory for the user*. PTR Prentice-Hall: Upper Saddle River (NJ), 1999.

25. Lewis FL, Vrabie D, Syrmos VL. *Optimal control*. Wiley, 2012.
26. Houtzager I, van Wingerden JW, Verhaegen M. Wind turbine load reduction by rejecting the periodic load disturbances. *Wind Energy* May 2012; doi:10.1002/we.547.
27. Bergami L, Gaunaa M. Analysis of aeroelastic loads and their contributions to fatigue damage. *Submitted to Journal of Physics: Conference Series* Oct 2012; .
28. Larsen TJ. How 2 HAWC2 the user's manual. *Technical Report R-1597(EN)*, Risø National Laboratory. Technical University of Denmark 2009.
29. Bergami L, Riziotis VA, Gaunaa M. Aerodynamic response of an airfoil section undergoing pitch motion and trailing edge flap deflection: a comparison of simulation methods. *Submitted to Wind Energy* Jan 2013; .
30. Commission IE. IEC 61400-1: Wind turbines part 1: Design requirements. *Technical Report*, International Electrotechnical Commission 2005.
31. Mann J. Wind field simulation. *Probabilistic Engineering Mechanics* Oct 1998; **13**(4):269–282, doi:10.1016/S0266-8920(97)00036-2. URL <http://www.sciencedirect.com/science/article/pii/S0266892097000362>.
32. Madsen HA, Riziotis V, Zahle F, Hansen MO, Snel H, Grasso F, Larsen TJ, Politis E, Rasmussen F. Blade element momentum modeling of inflow with shear in comparison with advanced model results. *Wind Energy* May 2011; **Early View**(published on-line), doi:10.1002/we.493.
33. Gaunaa M. Unsteady two-dimensional potential-flow model for thin variable geometry airfoils. *Wind Energy* 2010; **13**(2-3):167–192, doi:10.1002/we.377.
34. Hansen MH, Gaunaa M, Madsen HA. A beddoes-leishman type dynamic stall model in state-space and indicial formulations. *Technical Report R-1354(EN)*, Risoe National Laboratory, Roskilde (DK) 2004.
35. Bergami L, Gaunaa M, Heinz J. Indicial lift response function: an empirical relation for finite-thickness airfoils, and effects on aeroelastic simulations. *Wind Energy* 2012; **Early View**(published on-line), doi:10.1002/we.1516.
36. Jonkman J, Butterfield S, Musial W, Scott G. Definition of a 5-MW reference wind turbine for offshore system development. *Technical Report NREL/TP-500-38060*, National Renewable Energy Laboratory (NREL) Feb 2009.
37. van der Veen G, van Wingerden J, Verhaegen M. Closed-loop system identification of wind turbines in the presence of periodic effects. *Proc. of the 3rd conference, The Science of Making Torque from Wind*, Eraklion, Crete, Greece, 2010.
38. Hansen M. *Aerodynamics of wind turbines : rotors, loads and structure*. James & James: London, 2000.

Article VI

A Model Based Control methodology combining Blade Pitch and Adaptive Trailing Edge Flaps in a common framework

The article was presented at the European Wind Energy Association Conference in Vienna (Austria), in February 2012, and is published in the conference proceedings. Lars, first author on the article, developed the MIMO-MPC control algorithm, to which I collaborated by including the flap effects in the aerodynamic part of the model. Concerning the article, I was responsible for processing the simulation results, and for writing the last three sections.

The content of the article is recalled in the synopsis sections related to:

- *Model Based control algorithms for a rotor with ATEF*, section 7.1 and 7.3: short description of the MIMO-MPC control algorithm, and discussion on the load alleviation results.

A Model Based Control methodology combining Blade Pitch and Adaptive Trailing Edge Flaps in a common framework

L. C. Henriksen
DTU Wind Energy
DK-4000 Roskilde, Denmark
larh@dtu.dk

L. Bergami
DTU Wind Energy
DK-4000 Roskilde, Denmark
leob@dtu.dk

P. B. Andersen
DTU Wind Energy
DK-2800 Kgs. Lyngby, Denmark
pbja@dtu.dk

Abstract:

This work investigates how adaptive trailing edge flaps and classical blade pitch can work in concert using a model-based state space control formulation. The trade-off between load reduction and actuator activity is decided by setting different weights in the objective function used by the model-based controller. The combined control approach allow to achieve higher load alleviations, furthermore, in the presence of e.g. deterioration of an actuator, it enables an online re-tuning of the workload distribution of blade pitch and trailing edge flaps, thus potentially increasing the smart rotor reliability.

Keywords: aeroelasticity, active load control, smart rotor

1 Introduction

Wind turbines are constantly exposed to unsteady loads due to turbulence and gusts in the incoming flow and this increases significantly the cost. Therefore, researchers and industry are aimed at finding technical solutions that can alleviate the loads on the turbines. Local control of the aerodynamic forces along the blade span, as well as active pitching of the whole blade, can be used to compensate for the variations in the incoming flow, and

thus reduce the loads arising on the turbine rotor, a concept often referred to as *smart-rotor* [1]. Local aerodynamic control with Adaptive Trailing Edge Flaps (ATEF) with a smooth and continuous deformation shape has been under development in several research institutions; the load alleviation potential is confirmed by several aeroelastic simulations [2, 3, 4, 5, 6], and experiments [7, 8].

Most of the investigations documented in the literature follow a control design approach where the turbine power control part is developed separately from the active load alleviation control, which is often designed in a second phase and exclusively manages the flap activity. Mutual interference between the two control algorithms is then avoided by frequency separation, with the power control targeting low frequency variations, and the active load control the rest of the range. This paper presents an innovative control design approach where both load alleviation and power control objectives are managed by the same model based control algorithm; the algorithm returns the reference control signals for the turbine generator torque, for the blade pitch angles, and for the deflection of the adaptive trailing edge flaps (ATEF) distributed along the blades. The control problem is solved in a model predictive formulation, where the control design model is retrieved from first princi-

ples considerations.

The proposed control algorithm is applied to the NREL 5 MW reference turbine [9] in a smart rotor configuration with ATEF; the turbine response is simulated with the aero-servo-elastic code HAWC2 [10]. The paper is structured as follows: the control design model is presented in Section 2, with particular focus on the modeling of the Adaptive Trailing Edge Flap (ATEF) contributions. A brief introduction to the controller is found in Section 3. Finally, results are presented and discussed in Section 5, and conclusions are drawn in Section 6.

2 Model for controller design

The control design model is derived from first principles considerations, and follows a similar formulation to the one presented in Henriksen et al. [11]. The structural model includes: 1 drive-shaft torsion degrees of freedom (DOF), 1 tower fore-aft DOF, 1 tower side-side DOF, 2 blade edgewise and 2 flapwise DOFs. Models for the blade-wide distribution of the turbulent wind speed and the wind speed normal to the rotor plane are also included in the control design model.

The aerodynamic part of the model is extended to include the effect deformable trailing edge flaps. In Henriksen et al. [11] the lift and drag coefficients, C_l and C_d , are only functions of the angle of attack α ; the model is now extended to describe the dependency on the ATEF angle β [12]. In the model used in this work, the flap effect is approximated by a linear formulation:

$$C_l(\alpha, \beta) \approx C_l(\alpha, 0) + \frac{\partial C_l(\alpha, 0)}{\partial \beta} \beta \quad (1)$$

$$C_d(\alpha, \beta) \approx C_d(\alpha, 0) + \frac{\partial C_d(\alpha, 0)}{\partial \beta} \beta \quad (2)$$

The change in lift and drag forces cause a change in induction factors, which are thus functions of the pitch angle θ , the tip-speed ratio λ , and the flap deflection β . The dependency on the flap deflection is also simplified by a linear approximation:

$$a_n(\theta, \lambda, \beta) \approx a_n(\theta, \lambda, 0) + \frac{\partial a_n(\theta, \lambda, 0)}{\partial \beta} \beta \quad (3)$$

$$a_t(\theta, \lambda, \beta) \approx a_t(\theta, \lambda, 0) + \frac{\partial a_t(\theta, \lambda, 0)}{\partial \beta} \beta \quad (4)$$

The control model is transformed from a time-varying system to a linear time-invariant description using the Coleman transform [13]. The correct implementation of the linearized model, and its ability to capture the relevant system dynamics are verified by comparing the frequency response predicted by the linear model against the response simulated with the multi-body time-marching aeroelastic code HAWC2. Figure 1 reports the corresponding Bode plots of the frequency response from harmonic pitch actions (on the left column), and from harmonic flap deflection (right column); the response is measured at the blade root flapwise bending moment (first row), and at the tower top acceleration in the fore-aft direction (second row). The linearized model used in the control formulation (indicated by the purple dashed lines) describes sufficiently well the dynamics of the system to be controlled, especially in the low frequency range.

3 Controller

The controller presented in this work is based on the one by Henriksen et al. [11], extended to account for the presence of the Adaptive Trailing Edge Flap devices. The controller setup is sketched in Figure 2, where an extended Kalman filter estimates the states of the control design using the following set of sensors:

- Pitch angle of each blade

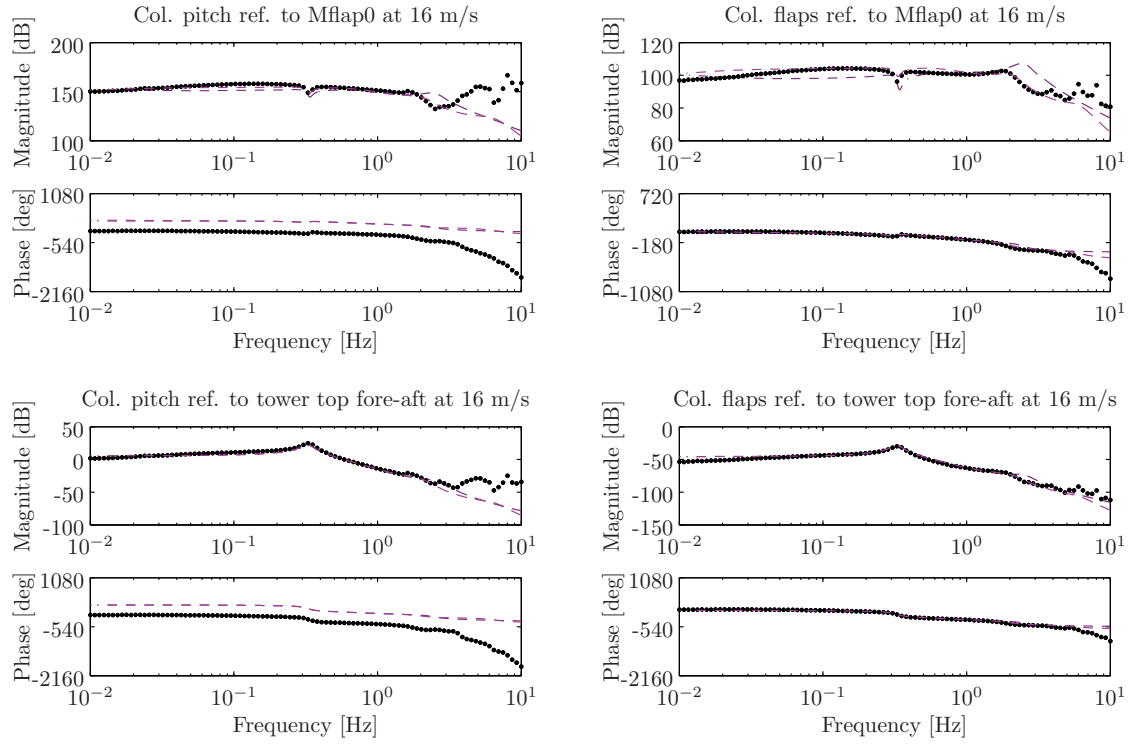


Figure 1: Bode plots of the frequency response at a mean wind speed of 16 m/s, comparison of the response given by the linearized model (dashed lines) with the response simulated by the aeroelastic code HAWC2 (black dots).

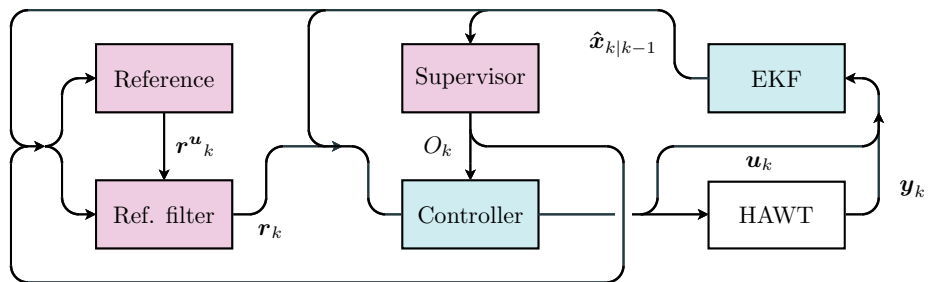


Figure 2: Setup of the hybrid controller. An extended Kalman filter (EKF) provides estimates of states used by other blocks in the diagram. Supervisor block provides partial or full load control objectives to controller depending on switching conditions. Reference and reference filter blocks provide references for the controller to track depending on whether partial or full load operation is active.

- Generator torque
- Generator power
- Generator speed
- Rotor Speed
- Tower top fore-aft acceleration
- Tower top side-side acceleration
- Flapwise blade root bending moment of each blade
- Edgewise blade root bending moment of each blade

The estimated states are used by a Model Predictive Control algorithm, which calculates the optimal control actions that minimizes the objective cost function. The cost function is given by the summation of several contributions, and includes:

- Weight on generator power
- Weight on generator speed
- Weight on tower top fore-aft velocity
- Weight on tower top side-side velocity
- Frequency dependent weight on collective pitch angle
- Frequency dependent weight on cyclic pitch angles
- Frequency dependent weight on generator torque
- Frequency dependent weight on collective ATEF
- Frequency dependent weight on cyclic ATEF: *Weight ATEF act.*
- Weight on cyclic flapwise blade root bending moments: *Weight ΔM_x Cycl.*

The weight on the last two elements of the cost function will be varied in the following investigations, so to explore different control configurations and combinations of pitch and flap activity.

4 Test Case

The NREL 5 MW baseline wind turbine in its on-shore configuration is taken as reference model for the aeroelastic simulations presented in this work. The wind turbine, thoroughly described by Jonkman et al. [9], is representative of modern multi-megawatt models, it has a three bladed rotor of 126 m diameter with up-wind orientation, variable speed and pitch-to-feather control. Jonkman et al. [9] also define a baseline PI control algorithm, where power regulation above rated is obtained by collective blade pitch actions based on low pass filtered measurements of the drive train speed. The load results obtained with the baseline PI control will be used as a term of reference in the following analysis.

The turbine rotor is equipped with adaptive trailing edge flaps, which extend for 10 % of the airfoil chord and cover 20 % of the blade length, from 47.7 m to 60.0 m span. The maximum flap deflection is limited to $\pm 10^\circ$, resulting in maximum steady lift coefficient variations of ± 0.42 . All the flaps on the same blade are controlled by the same signal, and no constraints are applied on the flap maximum deflection speed; nevertheless, the frequency weighting on the control cost function inhibits high frequency activity of the flap, thus giving flap deflection signals that very rarely require maximum deflection rates above 50 deg/s. The pitch and generator actuator dynamics are modeled as second and first order low pass filters, respectively.

Aeroelastic simulations are performed with the HAWC2 code [10], reproducing the wind

field conditions prescribed by the IEC standard [14] for a class A turbine. In this paper, only results referring to mean wind speed 18 m/s are considered, and a total of 40 minutes (4 x 10 minutes seeds) turbulent wind is simulated for each control configuration.

5 Results

The performances of the combined model based control are investigated by running aeroelastic simulations of the NREL 5 MW turbine under different control weight configurations. Several combinations of pitch and flap activity are obtained by acting on two of the weight parameters of the control cost function introduced in section 3:

- *Weight ATEF act.* determines the penalization imposed on the flap activity. Low values corresponds to a control setting that favor the flap activity, whereas high values favor the blade pitch action.
- *Weight $\Delta M_x Cycl.$* determines the penalization on cyclic variation of the blade root flapwise bending moment. Higher values indicate a control configuration that focuses more on blade root flapwise bending moment alleviation.

The blade pitch and ATEF activities are quantified as the total distance traveled by the actuators (in degrees), then normalized by the simulation time. The activity registered with the investigated control weight combinations is reported in figure 3 for the blade pitch, and figure 4 for the flap. As expected, the highest pitch activity (dark red color in fig. 3) occurs for weight settings that penalize flap action (high *ATEF act.* weights), and focus on cyclic load alleviation (high $\Delta M_x Cycl.$ weights); as a term of reference, the pitch activity with the NREL 5 MW baseline PI controller is around 0.3 deg/s, at the bottom of the color scale.

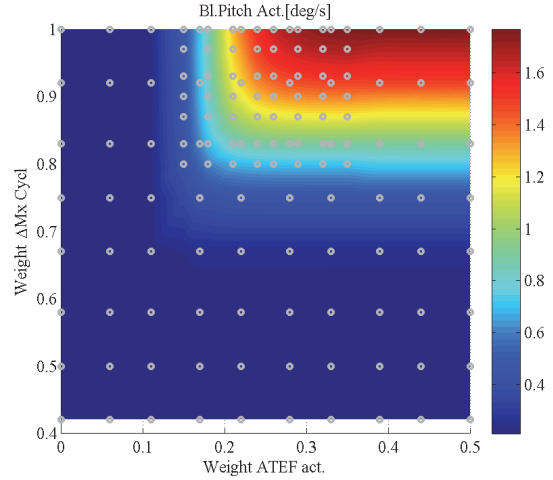


Figure 3: Blade pitch activity for different combinations of the control cost function weights. The actuator activity is measured as the total traveled distance (in degrees), normalized by the simulation time.

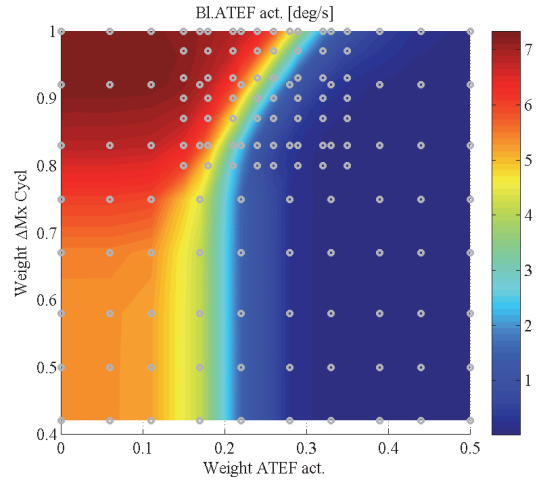


Figure 4: Adaptive Trailing Edge Flap activity for different combinations of the control cost function weights. The actuator activity is measured as the total traveled distance (in degrees), normalized by the simulation time.

High flap activity is obtained with high $\Delta M_x Cycl.$ weights, and low *ATEF act.* penalization; the gray circles in the plots mark the weight

combinations where simulations were actually performed.

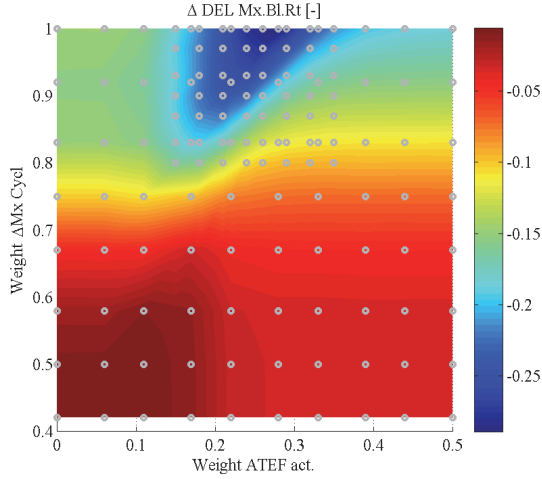


Figure 5: Performance of the active control in terms of alleviation of Fatigue Damage Equivalent Loads (DEL) at the blade root flapwise bending moment, Wöhler curve exponent of 10. Results given as percentage variation from the DEL measured on the baseline NREL 5 MW turbine with its standard PI controller [9]; simulations are performed in the points indicated by the gray circles.

Load alleviation performances of the combined control system are measured in terms of fatigue Damage Equivalent Loads (DEL), which are computed under Palmgren-Miner linear damage assumption by applying rain-flow counting to the simulated time series; a Wöhler curve fatigue exponent of 10 is used for the blade DEL, and an exponent of 4 for the tower loads. The load alleviation is expressed as the DEL difference between the active load control case, and the reference baseline one; negative values thus indicate a reduction of fatigue loads. The difference is then normalized by the DEL in the reference case. Among the investigated control weight combinations, higher fatigue load alleviation on the blade root flapwise bending moment are ob-

tained by increasing the weight on the bending moment cyclic variation, and the highest DEL alleviation is achieved by using a combination of both flap and pitch control actions, dark blue area in figure 5.

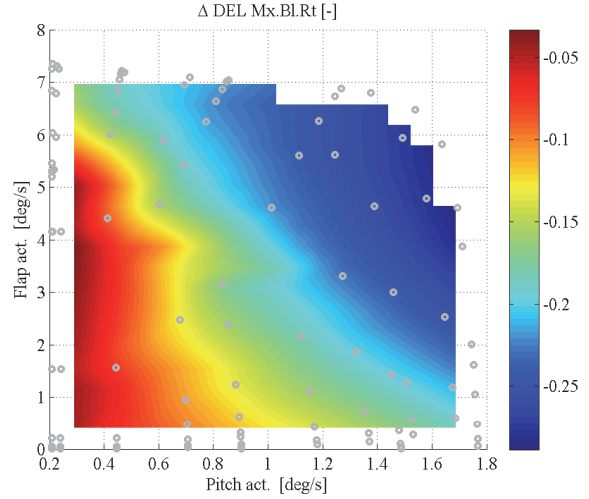


Figure 6: Fatigue Damage Equivalent Loads (DEL) alleviation at the blade root flapwise bending compared to the baseline NREL 5 MW turbine, Wöhler curve exponent of 10. The load alleviation is plotted as a function of both the blade pitch actuator traveled distance (horizontal axis), and the flap actuator traveled distance (vertical axis). Simulation data are only available for the points indicated by the gray circles.

A more informative display of the controller performances is obtained by remapping the load alleviation results as a function of both the blade pitch and the flap activity, figure 6. The plot immediately highlights that larger load alleviations require higher control activity, either with pitch or flap actuators. Active load alleviation with exclusively blade pitch actuators reaches to 18-20 % DEL reduction, whereas lower figures (approximately 15 %) are achieved when the flap actuators alone target the cyclic loads, a result in-line with previous

investigations featuring similar smart rotor setups [6]. The highest load alleviation performances are achieved when the controller employs a combination of both the blade pitch and the flap actuators: load alleviation is increased from 18 % for the pitch alone, to nearly 30 % for the combined control actions.

Another advantage of the combined control formulation lies in the possibility of one actuator to partly take over and reduce the work load of the other. For instance, actively reducing the DEL by 16 % with blade pitch alone would require an average activity of 1.5° pitch variation every second of operation; by including flap action in the task, the work load on the pitch actuator is lowered down to one third, without compromising on the DEL alleviation. The possibility of one actuator relieving the work load of the other could be exploited to decrease actuator wear, and eventually postpone maintenance operations.

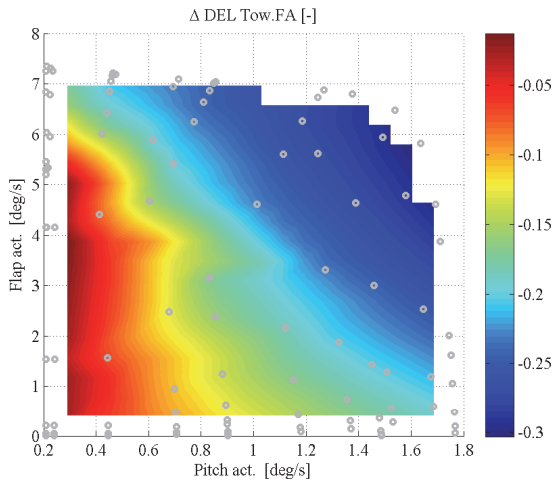


Figure 7: Fatigue Damage Equivalent Loads (DEL) alleviation at the tower bottom flange fore-aft bending moment compared to the baseline NREL 5 MW turbine, Wöhler curve exponent of 4. Simulation data are only available for the points indicated by the gray circles.

To avoid increasing the loads on the tower as a consequence of the alleviation on the rotor, estimations of the tower top velocities are included in the control cost function, section 3. The model based control algorithm is thus able to reduce at the same time the loads on the blades, and at the tower bottom flange: in the fore-aft direction fatigue DEL alleviation up to 30 % are achieved, with a distribution similar to the one observed for the blade root flapwise DEL, figure 7.

6 Conclusion

The paper presented an algorithm that combines generator torque, blade pitch, and adaptive trailing edge flaps in the same model predictive control framework. The control model is retrieved from first principle models of the turbine structural components and from a linearized BEM-based aerodynamic formulation; comparisons of the frequency response predictions with the results from aeroelastic simulations show that the control linear model is able to describe the dominant system dynamics.

The performances of the proposed control algorithm are evaluated in terms of fatigue damage equivalent loads alleviation on the NREL 5 MW reference turbine, with a smart rotor configuration featuring flaps on the outer 20 % span of the blades. Aeroelastic simulations have highlighted some advantages of a model based control strategy able to combine and supervise both flap and pitch activity:

- Higher fatigue load alleviation is achieved by combining flap and pitch control actions. Reduction of fatigue damage equivalent loads (DEL) in the blade root flapwise bending moment up to 30 % are reported when both pitch and flap are in use; in comparison, active alleviation with either flap or pitch actions alone bring

DEL reductions of 15 % and 18 %, respectively.

- The combined framework allows to shift the control activity required for load alleviation between the pitch and the flap actuators. By including flap actions, the blade pitch workload, and thus the actuator wear, is significantly reduced, while still achieving the same reduction of fatigue damage.

Fatigue damage at the tower bottom flange is also reduced by active load alleviation, the variation of the tower fore-aft DEL from the reference case shows a maximum reduction close to 30%, and an overall trend similar to the blade flapwise load alleviation.

The combined model based control methodology proved rather powerful and efficient in pursuing the blade and tower load alleviation objectives; future work should consider extending the methodology to other objectives, as, for instance, increase of power capture below rated conditions, or reduction of the drive train loads and generator speed variations. Independent flap actuators and sensors distributed along the blade span are other topics that might be worth consider in future investigations.

References

- [1] T. K. Barlas and G. van Kuik. State of the art and prospectives of smart rotor control for wind turbines. *Journal of Physics: Conference Series*, 75(1):012080 (20 pp.), 2007.
- [2] T. Buhl, M. Gaunaa, and C. Bak. Potential load reduction using airfoils with variable trailing edge geometry. *Transactions of the ASME. Journal of Solar Energy Engineering*, 127(4):503–516, 2005.
- [3] Peter Bjoern Andersen, Lars Henriksen, Mac Gaunaa, Christian Bak, and Thomas Buhl. Deformable trailing edge flaps for modern megawatt wind turbine controllers using strain gauge sensors. *Wind Energy*, 13(2-3):193–206, March 2010.
- [4] Matthew A. Lackner and Gijs van Kuik. A comparison of smart rotor control approaches using trailing edge flaps and individual pitch control. *Wind Energy*, 13(2-3):117–134, March 2010.
- [5] D.G. Wilson, B.R. Resor, D.E. Berg, T.K. Barlas, and G.A.M. van Kuik. Active aerodynamic blade distributed flap control design procedure for load reduction on the UpWind 5MW wind turbine. In *Proceedings of the 48th AIAA Aerospace Sciences Meeting*, page 47, 2010.
- [6] T. K Barlas, G. J van der Veen, and G. A.M van Kuik. Model predictive control for wind turbines with distributed active flaps: incorporating inflow signals and actuator constraints. *Wind Energy*, Early view(published on-line), 2011.
- [7] Damien Castaignet, Jens Jakob Wedel-Heinen, Taeseong Kim, Thomas Buhl, and Niels Poulsen. Results from the first full scale wind turbine equipped with trailing edge flaps. In *Proceedings of 28th AIAA Applied Aerodynamics Conference*, Chicago, IL (US), June 2010. American Institute of Aeronautics and Astronautics.
- [8] T.K. Barlas, W. van Wingerden, A.W. Hulskamp, G.A. M. van Kuik, and H.E. N. Bersee. Smart dynamic rotor control using active flaps on a small-scale wind turbine: aeroelastic modeling and comparison with wind tunnel measurements. *Wind Energy*, Early View(published on-line), 2012.

- [9] J. Jonkman, S. Butterfield, W. Musial, and G. Scott. Definition of a 5-MW reference wind turbine for offshore system development. Technical Report NREL/TP-500-38060, National Renewable Energy Laboratory, 1617 Cole Boulevard, Golden, Colorado 80401-3393, February 2009.
- [10] T. J. Larsen and A. M. Hansen. How 2 HAWC2, the user's manual. Technical Report Risø-R-1597(ver. 3-1)(EN), Risø National Laboratory, 2007.
- [11] Lars Christian Henriksen, Morten Hartvig Hansen, and Niels Kjølstad Poulsen. Beyond the cp-curve in model-based control of wind turbines. In *Scientific Proceedings of EWEA 2012 - European Wind Energy Conference & Exhibition*, pages 147–152, Copenhagen, Denmark, April 2012. EWEA - The European Wind Energy Association.
- [12] Leonardo Bergami and Mac Gaunaa. ATEFlap aerodynamic model, a dynamic stall model including the effects of trailing edge flap deflection. Technical Report R-1792(EN), Risoe National Laboratory. Technical University of Denmark, Roskilde, Denmark, February 2012.
- [13] G. Bir. Multi-blade coordinate transformation and its application to wind turbine analysis. In *46th AIAA aerospace sciences meeting and exhibit*, Reno, NV., 2008.
- [14] IEC/TC88. *IEC 61400-1 Ed.3: Wind turbines - Part 1: Design requirements*. International Electrotechnical Commission (IEC), 8 2005.

Report A

The ATEF project finalization report: Preliminary load analysis of the NREL 5 MW

The following section is an excerpt of my contribution to the *The ATEF project finalization report*, part II Aero-elastic analysis, section 3.2. The technical report, edited by Jens Jakob Wedel-Heinen, Tim Behrens, and Peter B. Andersen concludes the project *Development of Adaptive Trailing Edge Flaps (ATEF) System for Wind Turbines* by the Danish Advanced Technology Foundation (Højteknologifonden), under Advanced Technology Projects 2007. The report was compiled in October 2011, and made public in April 2013 as technical report DTU Wind Energy E-0024.

The content of the report is recalled in the synopsis sections related to:

- *Simulation Environment*, section 2.2: definition of the NREL 5 MW reference turbine.
- *Load Analysis*, section 3.1: reduced set of design load cases.

Preliminary load analysis of the NREL 5 MW turbine

1.1 Introduction

The chapter reports on the analysis of the aeroelastic loads on a reference multi-MW turbine, thus providing a convenient background for the future design of the Adaptive Trailing Edge Flap system, whose aim is to actively alleviate the loads experienced by the turbine. The NREL 5 MW wind turbine in its onshore configuration [5] is taken as reference model, and the aeroelastic response is simulated in the time domain using the HAWC2 aero-servo-elastic code [7]. A wide set of simulation conditions is outlined by following the Design Load Cases (DLC) described in the IEC standard [4]; deterministic and stochastic wind inputs, normal operation and extreme events are considered. The simulated time series describing the turbine aeroelastic response are summarized in terms of *fatigue damage equivalent loads* (DEL) and *ultimate loads*, at selected locations on the structure.

The Design Load Cases that return the highest fatigue and ultimate loads indicate which operation conditions are particularly critical for the turbine in its baseline configuration. Active load alleviation in these specific cases would yield a direct benefit to the whole wind turbine structure. The DLC returning critical fatigue or ultimate loads provide thus a (conveniently reduced) set

of representative simulation conditions, which can be used for designing, testing, and assessing the performances of the ATEF active load control system. Please note that different load figures and another set of critical design load cases might result from simulations considering a different wind turbine model.

In the last section, the possibility of simplifying the aerodynamic model used in the simulations is investigated through a sensitivity analysis on the fatigue and ultimate loads, which assesses the effects of such simplifications on the predicted design loads.

1.2 Model and Method

1.2.1 Wind Turbine Model

The NREL 5 MW baseline wind turbine is chosen as a reference model. The turbine presents a typical configuration: 3 blades, up-wind rotor, variable rotor speed, and collective-pitch-to-feather power limitation; the characteristics of the turbine are publicly available, and thoroughly described in Jonkman et al. [5].

The same reference provides the turbine baseline control system, which includes torque control for the variable speed generator, and collective blade pitch to feather for power limitation. The baseline control does not support operation in non-power production cases, therefore, the first analysis on the complete set of DLC, which include non-production cases, are run using the standard Risø-controller [6].

The correct implementation of the wind turbine structural model is verified by checking the natural frequencies of the isolated blade and tower, table 1.2, and by comparing the full turbine frequencies at standstill returned by HAWC2 to the ones reported by Jonkman et al. [5], table 1.2. Steady curves from aeroelastic simulations in uniform wind conditions are also compared to verify the correct implementation of the aerodynamic inputs.

	<i>Tower</i>		<i>Blade</i>	
	f_n [Hz]	δ	f_n [Hz]	δ
1	0.378	1.915	0.64	3.08
2	0.378	1.918	0.97	4.75
3	2.832	6.353	1.75	2.95
4	2.845	6.361	2.82	10.80
5	7.440	13.497	3.53	4.70
6	7.795	15.093	4.75	17.81
7	9.453	12.410	5.42	6.85
8	10.792	13.520	6.63	24.77

Table 1.1: *HAWC2* estimation of natural eigenfrequencies and logarithmic damping for isolated blade and tower.

	<i>NREL report</i>		<i>Timoshenko Beam</i>		<i>Stiff Shear</i>		<i>Modes:</i>
	<i>Fast</i>	<i>Adams</i>	f_n [Hz]	δ	f_n [Hz]	δ	
1	0.312	0.316	0.300	1.509	0.301	1.505	Tower Side to Side
2	0.324	0.320	0.302	1.516	0.303	1.512	Tower Fore Aft
3	0.621	0.609	0.589	3.926	0.608	4.104	Shaft Torsion, Collective Edge
4	0.666	0.630	0.610	2.759	0.635	2.668	1st asym. Flap Yaw
5	0.668	0.669	0.637	3.037	0.665	2.968	1st asym. Flap Tilt
6	0.699	0.702	0.667	3.337	0.697	3.296	1st Collective Flap
7	1.079	1.074	0.967	4.690	1.073	4.949	1st asym. Edge Heave
8	1.090	1.088	0.979	4.754	1.086	5.019	1st asym. Edge Sway
9	1.934	1.651	1.582	2.626	1.709	2.717	2nd asym. Flap Yaw
10	1.922	1.856	1.691	2.947	1.855	3.138	2nd asym. Flap Tilt
11	2.021	1.960	1.767	3.002	1.960	3.146	2nd Collective Flap
12	–	–	2.200	10.087	2.637	8.950	2nd Collective Edge
13	2.900	2.859	2.641	6.557	2.774	6.139	3rd asym.flap tilt+edge heave
14	2.936	2.941	2.696	7.745	2.911	11.543	3rd asym.flap yaw+edge sway
15			2.802	8.667	3.223	5.573	Tower SS + asym edge sway
16			2.846	10.071	3.944	14.146	2nd asym. Edge heave
17			3.027	6.156	4.015	13.643	3rd asym. Flap Yaw
18			3.533	4.755	4.442	6.539	3rd Flap Collective
19			3.573	4.932	4.493	5.977	3rd Flap Tilt, tower FA
20			4.124	6.717	5.060	7.591	Asym. Flap Yaw

Table 1.2: *HAWC2* estimation of natural eigenfrequencies and logarithmic damping for the wind turbine at standstill, comparison with FAST and ADAMS results.

1.2.2 Fatigue Damage Equivalent Loads

The fatigue analysis estimates the accumulated fatigue damage that the wind turbine is expected to experience in its lifetime due to the fluctuating loadings on the structure. The fatigue damage is expressed in terms of fatigue damage equivalent loads (DEL), which are computed from the simulated time series using a Rain Flow Counting (RFC) algorithm and Palmgren-Miner linear damage assumption.

The RFC algorithm counts the load cycles contained in the time series, and sorts them depending on their amplitude range s_i . Once the time series is described in terms of number of cycles n_i , and their corresponding stress ranges s_i , the fatigue damage contribution D_j from the series j is computed using Palmgren-Miner linear fatigue damage procedure [2]. The procedure assumes that the total fatigue damage is equivalent to the sum of the fatigue contributions from each single stress cycle (linear damage hypothesis), and that fatigue only depends on the cycle amplitude s_i (neglecting thus the effects of cycle mean value):

$$D_j = \sum_i^{N_{\text{ranges}}} \frac{n_i}{N_i}. \quad (1.1)$$

Where n_i is the number of cycles counted in the i th stress range s_i , and N_i is the corresponding maximum number of cycles with s_i amplitude that the material can tolerate prior to fatigue failure.

The Wöhler curve expression relates the critical number of cycles N_i to the cycle stress amplitude s_i :

$$N_i = \left(\frac{S_0}{s_i} \right)^m, \quad (1.2)$$

where S_0 is the critical stress level, and m is a fatigue strength exponent. The value of m depends on the mechanical characteristics of the material, indicatively, an higher value implies larger fatigue tolerance to small amplitude cycles; the following analysis all adopt $m = 4$ for steel components (tower and drive train), and $m = 10$ for the blades (Glassfiber Reinforced Plastic).

Substituting (1.2) in (1.1),

$$D_j = S_0^{-m} \sum_i^{N_{\text{ranges}}} n_i s_i^m, \quad (1.3)$$

where S_0^{-m} is constant, as it only depends on the material properties.

The total fatigue damage in the wind turbine life-time D_{tot} is estimated as a weighted sum of the single series fatigue damages D_j ,

$$D_{tot} = S_0^{-m} \sum_j^{N_{\text{series}}} \left(f_j \sum_i^{N_{\text{ranges}}} n_i s_i^m \right)_j. \quad (1.4)$$

The weight coefficients f_j account for the time-span during which the wind turbine is expected to operate in the conditions simulated by the time series j . For power production cases (DLC 1.1), the time corresponding to each mean-wind speed condition is assigned using a Weibull probability density function with mean wind speed 8.5 m/s , which corresponds to a turbine class II in the IEC standard [4], figure 1.1; the total number of hours corresponds to a turbine lifetime of 25 years.

The fatigue damage is expressed in terms of damage equivalent loads S_{eq} ; the equivalent load indicates the amplitude of cycles in a simplified stress history that by repeating n_{eq} load cycles, would return a fatigue damage equivalent to the simulated one:

$$D_{tot} = S_0^{-m} n_{eq} S_{eq}^m \rightarrow S_{eq} = \left(\frac{D_{tot} S_0^m}{n_{eq}} \right)^{\frac{1}{m}} = \left(\frac{\sum (f_j \sum n_i s_i^m)_j}{n_{eq}} \right)^{\frac{1}{m}}, \quad (1.5)$$

the equivalent number of cycles can be set to an arbitrary value, typically (and in the following) $n_{eq} = 10^6$.

The fatigue analysis is performed directly on bending moments time series (and *not* on stress histories); therefore, the fatigue damage equivalent loads presented in the following sections have the unit of bending moments. The loads are measured in the following points:

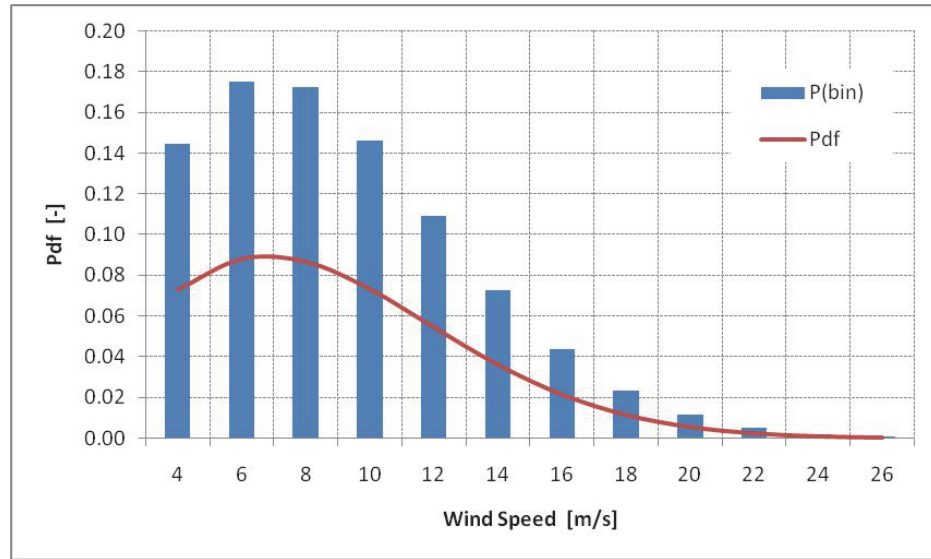


Figure 1.1: *Probability Density Function for the Rayleigh distribution and probability for the wind speed bins; turbine class II, mean wind speed 8.5 m/s.*

- Blade root: flapwise (M_x), edgewise (M_y), and torsion (M_z) bending moments.
- Tower bottom: fore-aft (M_{FA}), and side-to-side (M_{SS}) bending moments.
- Tower torsion at the top flange (M_{yaw}).
- Torque on the main shaft (M_{DT}).

Turbulence seeds averaging and relative contributions Most of the fatigue design load cases required by the IEC standard [4] involve a turbulent wind input, which in the HAWC2 simulations is based on Mann's turbulence model [7]. Due to the stochastic nature of turbulence, every simulation in turbulent wind is repeated with different seeds number, so to improve the statistical relevance of the results.

The equivalent fatigue load is computed from the average of the fatigue

damages obtained with the different turbulence seeds k :

$$S_{eq} = \left(\frac{E [D_{tot,k} \cdot S_0^m]_k}{n_{eq}} \right)^{\frac{1}{m}}. \quad (1.6)$$

In analogy, the relative contribution to the overall fatigue damage from a specific operation condition j is determined as the fatigue damage D_j caused by all the series simulating the specific condition j , normalized by the total life-time fatigue D_{tot} , both averaged for the turbulence seeds k :

$$k_j = \frac{E [D_{j,k}]_k}{E [D_{tot,k}]_k}. \quad (1.7)$$

1.2.3 Ultimate loads

The aim of the ultimate load analysis is to determine the magnitude of the maximum loads the wind turbine will experience during its life-time, and, thereof, obtain an indication of the ultimate strength required to its components.

For ultimate load analysis, the IEC standard [4] prescribes a set of simulations that include not only frequent operation condition, but also more rare events, describing plausible worst-case-scenarios.

The ultimate load for each simulated time series is simply given by the maximum load recorded in the series. In simulation conditions with deterministic wind fields, the ultimate load for the specific DLC is equal to the maximum load reported among all the time series relative to the same load case. For simulations involving a turbulent stochastic wind field, first, the maximum load among time series with the same set of turbulence seeds is computed; the ultimate load is then taken equal to the average of the maxima coming from the different seeds sets. The extrapolation procedure indicated by the IEC standards for loads from simulations in normal operation conditions is not followed.

The same ‘sensors’ as in the fatigue analysis are monitored. Bending moments are measured at the root of the blade for flap (M_x), edge (M_y), and

torsion (M_z). The tower bending moments are measured in fore-aft (M_{FA}) and side to side (M_{SS}) direction at the tower base, the tower torsion (M_{yaw}) at the tower top; the torque moment (M_{DT}) monitors torsion on the main shaft.

1.2.4 Fatigue and Ultimate load analysis

1.2.4.1 Fatigue loads results

Figure 1.2 reports the contribution to the fatigue damage from each wind speed bin at different operating conditions. The exact shape of the curves is sensitive to the material fatigue exponent (m , in eq. (1.2)); nevertheless, it is observed that in most of the cases, the highest fatigue contributions originate from wind speed bins close to rated speed. The blade flapwise bending moment shows instead larger contributions at higher wind speeds, and reports higher fatigue damage for operation with a positive yaw misalignment.

Due to the large amount of hours, power production conditions (DLC 1.1) dominate the fatigue damage on nearly all components, the only exception being the tower fore-aft bending moment where cut-out operations also have an important contribution. The fatigue loads from cut-out though might be overestimated in the simulations, since the procedure is simulated as a grid-loss case: the generator is disconnected before starting the pitching action, thus resulting in higher loads on the tower.

The relative contributions to the total life-time fatigue damage are grouped according to the operation condition that has generated the fatigue damage, figure 1.3. Normal power production operations (DLC 1.1) are responsible for most of the fatigue damage on the structure, and thus represent a critical case in the turbine fatigue design. An active load alleviation system, as the ATEF, that operates during normal power production has hence the potential to yield sensible reductions to the overall fatigue damage.

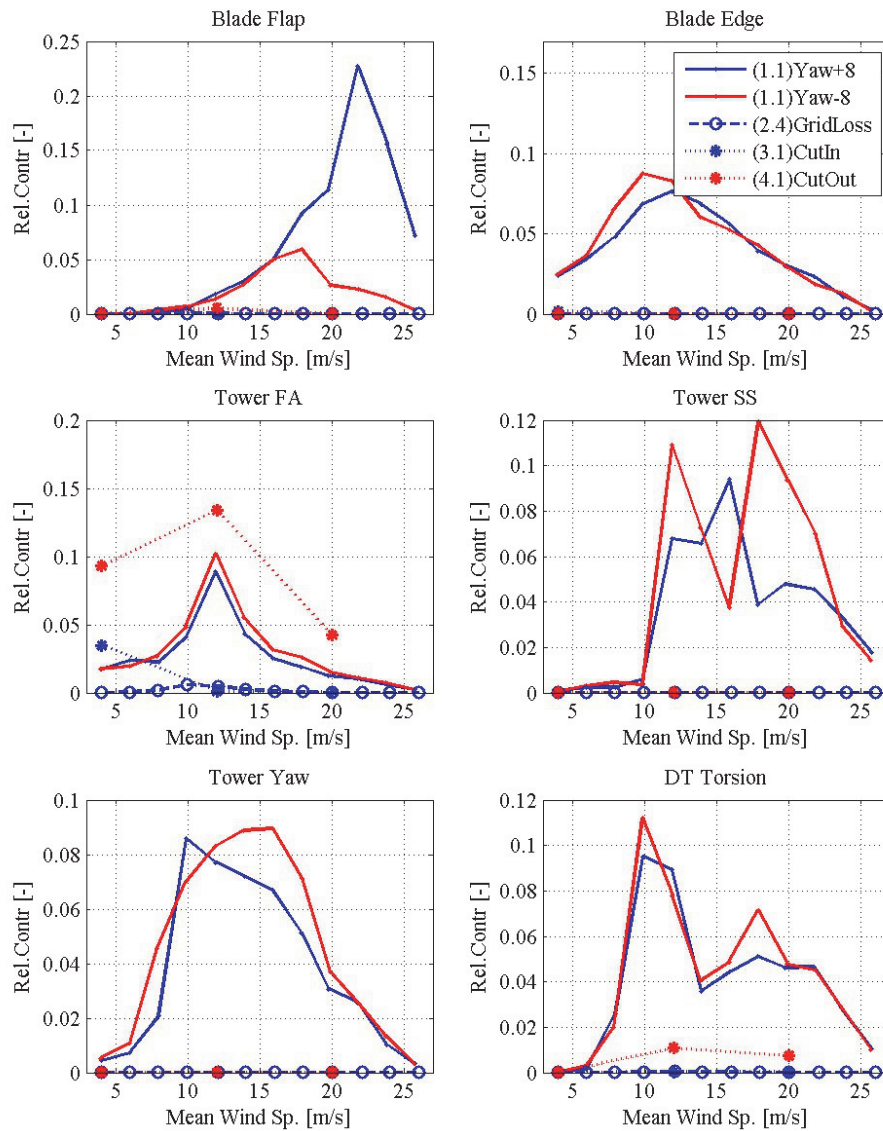


Figure 1.2: Relative contributions to the fatigue damage from each wind speed bin, at different operation conditions and Design Load Cases. A material fatigue exponent $m = 4$ is used for tower and drive train, $m = 10$ for the blade.

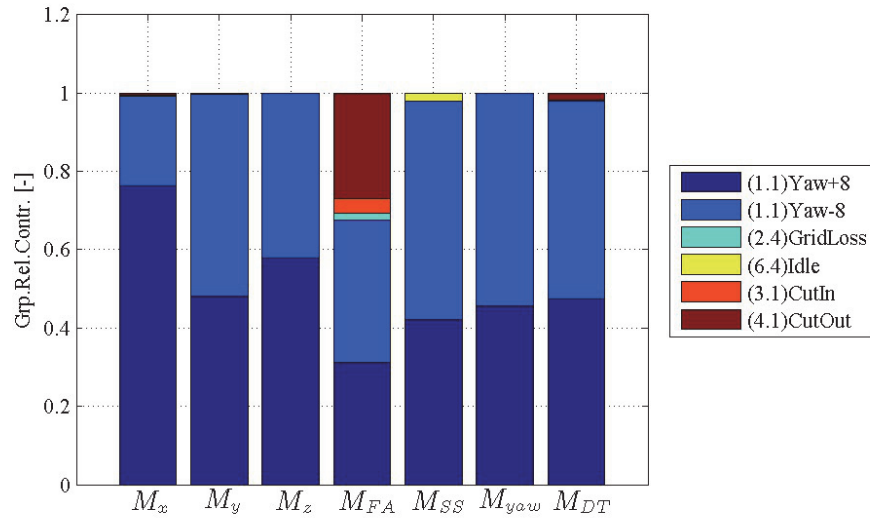


Figure 1.3: Relative contributions to the fatigue damage at each sensor location. The bar length reports the relative contribution from the different operation conditions and Design Load Cases. A material fatigue exponent $m = 4$ is used for tower and drive train, $m = 10$ for the blade.

1.2.4.2 Ultimate loads results

Figure 1.4 collects the ultimate loads resulting from the simulation conditions prescribed by each Design Load Case. The *gl* suffix in the bar label indicates load cases that require grid loss simulation, and, therefore, can not be handled by the NREL baseline controller; the suffix *ngl* for DLC 2.3 indicates that the case is simulated without disconnecting the generator during the gust occurrence.

The highest simulated loads are reported for operations under extreme coherent gust (DLC 2.3), extreme turbulence (DLC 1.3), or extreme coherent gust with direction change (DLC 1.4). Simulation of this reduced set of DLC is thus sufficient to determine the critical ultimate loads for the structure; the three DLC should be also considered in the design process of the ATEF control system, as a load alleviation in these specific DLC would yield a direct benefit to the overall ultimate load requirements.

The extreme coherent gust DLC 2.3 yields to higher tower loads when concurrent to a grid-loss event; in fact, keeping the turbine generator connected to the grid (*ngl* column) returns a lower tower fore-aft ultimate load. On the other hand, the maximum load reported during the grid-loss event is very much dependent on the particular turbine stop procedure; as a standard stop procedure is not defined for the NREL baseline turbine, and in order to use the standard baseline turbine controller [5], it is chosen in the following load analysis to skip the grid-loss event, and maintain the turbine in power production for all the simulated DLC. The high loads reported on the tower side-to-side bending moment for the parked wind turbine conditions (DLC 6.1–6.3) should be regarded with caution as they might be partly biased by poor performances of the aerodynamic model in highly separated flow conditions.

1.2.4.3 Sensitivity Analysis

A sensitivity analysis is carried out on the predicted fatigue and ultimate loads; the aim is to quantify the effects on the simulated loads from simplifications in the 2D aerodynamic model used in the aeroelastic simulation code.

The model describes the unsteady aerodynamic forces that are generated on a 2D airfoil section; it includes the flow dynamics in attached conditions, and the dynamics of stall flow separation [3]. The effects on the simulated loads from the two parts of the model are investigated separately.

The dynamics in attached flow conditions are modeled through a superposition of indicial step responses, where, in the default case, the step response is given by the flat plate indicial function. Finite-thickness airfoils have a slower indicial response than the flat plate one [1]; the effects on the predicted loads from changes in the indicial response are investigated by setting the model to the indicial response function of a 25% thick airfoil (DU 91-W2-250).

A common approximation in attached flow is to simplify the model by assuming a quasi-steady behavior. A step change in the quasi-steady angle of attack would thus correspond to a step change in the aerodynamic forces, and

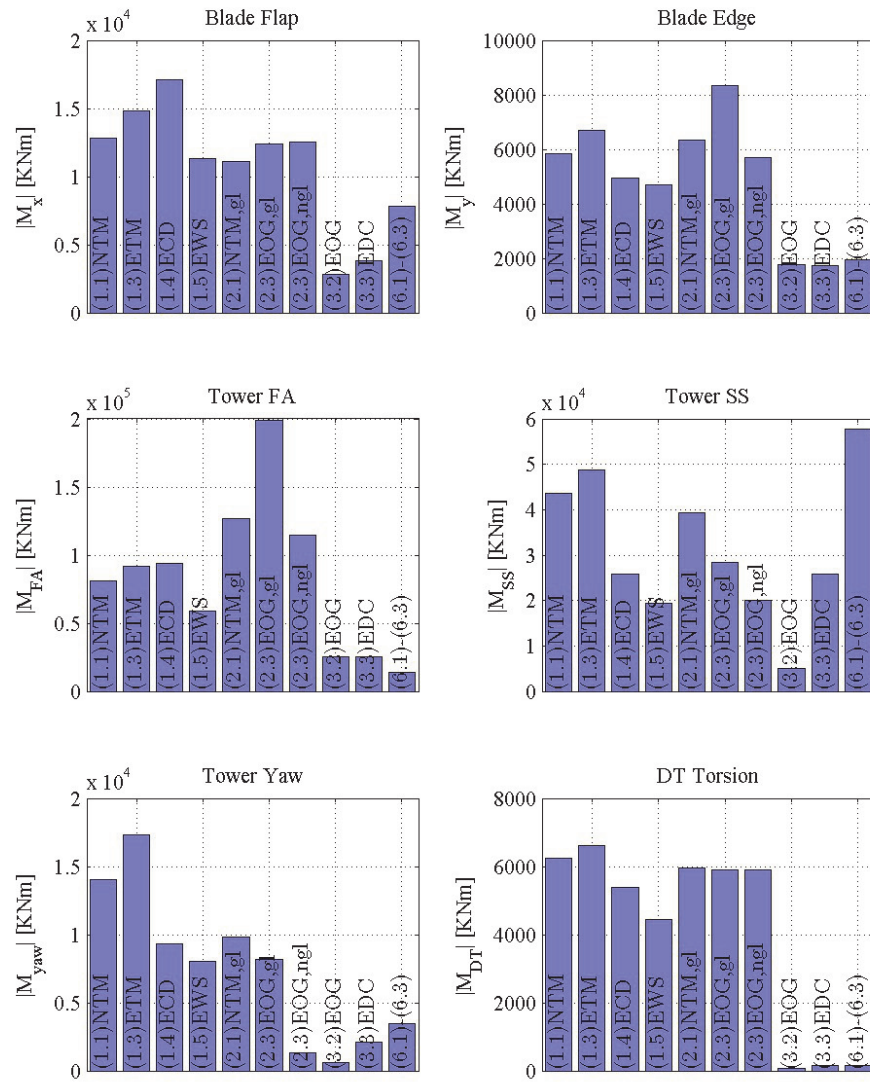


Figure 1.4: Ultimate load analysis. Ultimate loads reported in each DLC; the suffix gl indicates a design load case involving grid loss during the simulation, ngl indicates that the case has been simulated without grid loss events.

the corresponding indicial response function would be constant and equal to unit (weight parameters $A_{1,2}$ set to zero).

Concerning the dynamics of flow separations, the effects of simplifying the aerodynamic model by neglecting its dynamic stall part are assessed by setting the stall model time constants to a very small value. Table 1.3 summarize the different setups considered in the sensitivity analysis; all the simulations were run using the NREL baseline controller. Table 1.4 reports the effect measured on the equivalent fatigue loads, and table 1.5 the variations in ultimate loads.

<i>Setup:</i>	A_1	A_2	b_1	b_2	τ_p	τ_b
<i>Def. Flat Pl.</i>	0.165	0.335	0.046	0.3	1.5	6
<i>Quasi-St.</i>	0	0	–	–	1.5	6
<i>DU 250</i>	0.19	0.416	0.041	0.262	1.5	6
<i>Ds τ</i>	0.165	0.335	0.046	0.3	10^{-3}	10^{-3}

Table 1.3: *Different setups of the 2D aerodynamic model for the sensitivity analysis of fatigue and ultimate loads. The first row gives the parameters in the default case, which will be used as a reference; the standard baseline control system is used in the simulations.*

Changing the attached flow dynamics to fit the indicial response of an airfoil with finite-thickness (*DU 250* row) has a small effect on the simulated loads; both fatigue and ultimate loads are only slightly reduced. On the contrary, the attempt to simplify the model by using Quasi-Steady dynamics in attached flow leads to considerably overestimated fatigue, and ultimate loads (*Quasi-St.* row in the tables).

Neglecting the dynamic stall part of the model (*Ds τ* rows) has a rather small impact on the equivalent fatigue loads, table 1.4; in fact, in the normal power production case DLC 1.1, which determines the equivalent fatigue load, the rotor operates most of the time in attached flow conditions. On the contrary, in the design load cases considered by the ultimate load simulations, the rotor gets to operate under large angles of attack, especially in the case of an extreme coherent gust with direction change (DLC 1.4). The DLC 1.4 drives the blade ultimate loads, as a consequence, when the dynamic stall part of the model is neglected, a significant overestimation of ultimate loads is reported in the blade flapwise and torsion bending moments.

To conclude, aeroelastic simulations used for calculation of design loads should be based on an aerodynamic model that includes both attached flow, and stall separation dynamics. Simplifying the model to a quasi-steady one would, in fact, lead to considerable overestimations of both fatigue and ultimate loads.

S_{eq}	M_x	M_y	M_z	M_{FA}	M_{SS}	M_{yaw}	M_{DT}
<i>Ref.Flat Pl. [MNm]</i>	13.73	10.69	0.25	77.12	39.55	20.60	3.86
Δ <i>Quasi-St. [%]</i>	5.49	1.10	20.54	6.44	3.89	9.15	15.05
Δ <i>DU 250 [%]</i>	-1.06	-0.00	-2.48	-1.02	-0.39	-1.83	-2.21
Δ <i>Ds τ [%]</i>	-0.54	-0.06	-2.15	-0.53	-0.10	-1.17	-1.03

Table 1.4: Sensitivity of the fatigue damage equivalent loads (DEL) to changes in the 2D aerodynamic model. All the variations Δ are normalized with respect to the reference case (first line), corresponding to the equivalent loads obtained with the default setup and the baseline control system. Blade DEL are computed with $k = 10$, all the others with $k = 4$; the figures refer to a reference number of cycles $n_{eq} = 10^6$ and 25 years turbine lifetime.

$\max(\mathbf{M})$	M_x	M_y	M_z	M_{FA}	M_{SS}	M_{yaw}	M_{DT}
<i>Ref.Flat Pl. [MNm]</i>	14.94	6.92	0.22	112.46	45.08	17.44	6.62
Δ <i>Quasi-St. [%]</i>	6.93	2.29	25.26	-1.98	3.44	6.07	5.45
Δ <i>DU 250 [%]</i>	-0.73	-0.39	-2.21	0.41	-0.55	-1.14	-1.33
Δ <i>Ds τ [%]</i>	10.52	-1.89	11.73	-1.99	1.72	-2.19	-1.02

Table 1.5: Sensitivity of the ultimate loads to changes in the 2D aerodynamic model. Variations Δ are normalized with the corresponding values for the reference case (flat plate response, in the first line).

1.2.5 Conclusion

An analysis of the loads on a multi-MW turbine is carried out by simulating its aeroelastic response in different operation conditions. The load analysis of the turbine in its baseline configuration provided useful insights for the future development of the ATEF active load alleviation system.

From the full set of simulation conditions prescribed by the IEC standard, the analysis has identified a reduced set of design load cases that are critical

in terms of either fatigue or ultimate loads. The reduced set provides a convenient test field for design and performance assessment of the ATEF system, as load alleviation in these design cases yields a direct benefit to the overall turbine loading conditions.

The aerodynamic model used in the aeroelastic simulations should account for the forces dynamics both in attached flow, and in stall separation conditions. A sensitivity analysis has in fact shown that quasi-steady simplifications in the model lead to an overestimation of both fatigue and ultimate design loads.

Bibliography

- [1] Leonardo Bergami, Mac Gaunaa, and Joachim Heinz. Indicial lift response function: an empirical relation for finite-thickness airfoils, and effects on aeroelastic simulations. *Wind Energy*, Early View (published on-line), 2012.
- [2] Martin Hansen. *Aerodynamics of wind turbines : rotors, loads and structure*. James & James, London, 2000.
- [3] Morten Hartvig Hansen, Mac Gaunaa, and Helge Aagaard Madsen. A Beddoes-Leishman type dynamic stall model in state-space and indicial formulations. Technical Report R-1354(EN), Risoe National Laboratory, Roskilde (DK), 2004.
- [4] International Electrotechnical Commission (IEC). IEC 61400-1: Wind turbines part 1: Design requirements. Technical report, International Electrotechnical Commission, 2005.
- [5] J. Jonkman, S. Butterfield, W. Musial, and G. Scott. Definition of a 5-MW reference wind turbine for offshore system development. Technical Report NREL/TP-500-38060, National Renewable Energy Laboratory (NREL), February 2009.
- [6] T. J Larsen and T. D Hanson. A method to avoid negative damped low frequent tower vibrations for a floating, pitch controlled wind turbine. In *Journal of Physics: Conference Series*, volume 75, page 012073, 2007.

- [7] Torben Juul Larsen. How 2 HAWC2 the user's manual. Technical Report R-1597(EN), Risø National Laboratory. Technical University of Denmark, 2009.

Report B

ATEFlap Aerodynamic Model, a dynamic stall model including the effects of trailing edge flap deflection

The report was compiled to document the ATEFlap aerodynamic model implemented in the aeroelastic code HAWC2, and was published as technical report Risø-R-1792(EN) in February 2012. The version presented here is updated with few additional comments and footnotes suggested by the kind and patient feedback of colleagues and students that ventured through the report after its publication.

The content of the report is recalled in the synopsis chapter 4, *ATEFlap Aerodynamic Model*.

Contents

1	Introduction	217
2	Preprocessor for ATEFlap dynamic stall model	221
2.1	Background and motivation	221
2.2	Preprocessor Algorithm	225
2.2.1	Reconstructing steady data	225
2.2.2	Compute linear lift parameters	225
2.2.3	Compute separation function	227
2.2.4	Compute fully attached and fully separated lift	228
2.2.5	Manual corrections by the user	228
2.2.6	Preprocessor output - ATEFlap input	229
3	ATEFlap aerodynamic model	231
3.1	Lift: potential flow	232
3.1.1	Assumption of constant flow velocity over the chord	237
3.2	Lift: dynamics of flow separation	239
3.3	Drag	242
3.4	Moment	244
4	Model validation	247
4.1	Comparison with standard dynamic stall model	247
4.2	Comparison with CFD solutions	251
4.2.1	Harmonic pitching motion	252
4.2.2	Harmonic flap deflection	253

5 Conclusion	263
Bibliography	266
A Modifications with respect to previous versions of the model	267
A.1 Preprocessor for dynamic stall model	267
A.1.1 Gradient $\partial C_l / \partial \alpha$ and flap deflection	268
A.1.2 $\partial C_l / \partial \alpha$ algorithm	268
A.1.3 C_l^{fs} and C_l^{att} at $f = 1$ and $f = 0$	269
A.1.4 C_d flap steady contribution	269
A.2 Aerodynamic model for an airfoil section with flap	269
A.2.1 Quasi-Steady flap deflection	270
A.2.2 Intermediate separation function	270
A.2.3 Flap steady drag contribution	271
A.2.4 Induced drag contribution from separation function	272
A.2.5 Flap acceleration term in non-circulatory contributions	273
B Details of ATEFlap implementation in HAWC2 code	275
B.1 Airfoil section reference system	275
B.1.1 Angle of Attack	275
B.1.2 Flow speed	276
B.1.3 Direction of forces	276
B.1.4 Pitching moment at the quarter-chord point	277
B.2 Terms for non-circulatory contributions	279
B.2.1 Flap deflection rate	279
B.2.2 Section torsion rate	279
B.3 Operational aspects in HAWC2	280
B.3.1 Defining a rotor with flaps in the input file	280
B.3.2 Estimating linear parameters $\partial C_l / \partial \alpha$ and α_0	282
B.3.3 Linear interpolation algorithm	283
C User's guide to Preprocessor for ATEFlap	285
C.1 Quick-start guide	285
C.2 I/O files formats	286
C.2.1 Input: Clean Airfoil	287
C.2.2 Input: Flap Delta-steady	287
C.2.3 Output: <code>.ds ATEFlap</code> steady aerodynamic input file	288

Introduction

The report describes the *ATEFlap* aerodynamic model, which returns unsteady lift, drag, and moment coefficients for a 2D airfoil equipped with a trailing edge flap. The *ATEFlap* model has been integrated in the aeroelastic simulation tool HAWC2 [12], and reproduces steady and dynamic characteristics of the forces on an airfoil undergoing arbitrary motion and flap deflection, both in attached and separated flow conditions. The model can handle standard hinged flaps, as well as flaps introducing any other deformation shape of the airfoil camber-line.

The unsteady dynamics in attached flow are based on Gaunaa's [6] work for a thin airfoil in potential flow, while the dynamic stall part is derived from the Beddoes-Leishmann-type of model [3, 13] that is described in Hansen et al. [8].

The current *ATEFlap* implementation is developed from the model presented in Andersen et al. [1], and follows the same approach in coupling the potential flow solution with the Beddoes-Leishmann dynamic stall model. The model from Andersen showed satisfactory performances in most of the investigated cases; nevertheless, for airfoils undergoing partial flow separation,

the dynamics of the forces predicted by the model were, in few occurrences, corrupted by discontinuities and spikes in the simulated time series [7]. The current algorithm is modified to avoid such discontinuities, and to allow for a better integration with the latest versions of the HAWC2 code; appendix A lists the major changes to the algorithm compared to previous versions of the aerodynamic model.

A particularly relevant change is the introduction of an external application to pre-process the steady data required by the Beddoes-Leishmann dynamic stall model [3, 13]. In this type of dynamic stall model, the lift force is described as a weighted sum of a fully attached flow component, and a fully separated one. The two lift components, here referred to as *Beddoes-Leishmann lift components*, are derived from the steady lift characteristics of the airfoil. In case of an airfoil with trailing edge flap, the operation is not trivial, and the algorithm gives rise to singularity points, which lead to discontinuities in the lift components, and, ultimately, to the spikes observed in the aerodynamic forces computed by the previous model.

Such discontinuities have no physical meaning, and should be corrected before the data are further processed in the aerodynamic model. It was not possible to formulate a reliable algorithm to automate the verification and correction of the processed steady input data; therefore, the pre-processing phase is collected in an external application, allowing for manual corrections by the user. The external application pre-processes the steady lift data, and returns the required baseline steady data and lift components; the user has the possibility to check the data that will be used in the aerodynamic model, and correct eventual discontinuities.

The following chapter describes the algorithm used by the preprocessor application to derive the steady Beddoes-Leishmann lift components from the steady lift characteristics of the airfoil and trailing edge flap. The preprocessor algorithm has been implemented in an executable, *Preprocessor for ATEFlap Dynamic Stall Model, ver.2.04*; practical details on the use of the executable, as input and output file formats, and a short user-guide are given in appendix C.

The core of the *ATEFlap* aerodynamic model is presented in the next chapter; the algorithm to compute lift, drag, and moment coefficients is described,

and details of the actual implementation in the HAWC2 aeroelastic code are given. The document refers to the model implemented in HAWC2 version 10.6, release date October 2011.

The last chapter reports validation cases, where the aerodynamic forces computed by the *ATEFlap* model are compared with the output from the classic dynamic stall model from Hansen et al. [8] for an airfoil undergoing harmonic changes of angle of attack. The model is further validated by comparison with CFD results for a NACA 64-418 airfoil at Reynolds number of 6 millions; the unsteady forces are compared for harmonic flap deflections, as in the UpWind report [7], and for harmonic changes of angle of attack.

Preprocessor for ATEFlap dynamic stall model

2.1 Background and motivation

The *ATEFlap* model is based on a Beddoes-Leishmann dynamic stall formulation [3, 8, 13], where the steady lift coefficient C_l^{st} is decomposed as the weighted sum of two lift components:

$$C_l^{st} = C_l^{att} f^{st} + C_l^{fs}(1 - f^{st}). \quad (2.1)$$

The first lift component C_l^{att} corresponds to the lift coefficient that would be obtained in case fully attached flow conditions were maintained at any angle of attack; a second component C_l^{fs} corresponds to the lift force that would be generated with fully separated flow conditions; the weight factor is given by the steady separation function f^{st} .

Figure 2.1 reports the steady C_l^{st} function and the corresponding Beddoes-Leishmann lift components in the standard case of a cambered rigid airfoil;

the steady lift, and the Beddoes-Leishmann lift components are simply a function of the angle of attack.

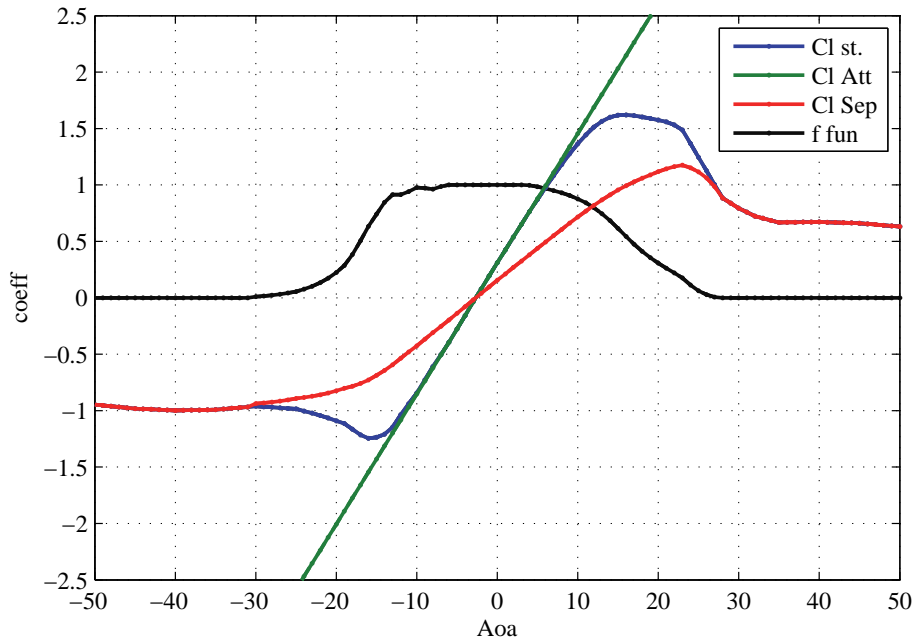


Figure 2.1: Steady lift coefficient curve, as a linear combination of the steady components required by the Beddoes-Leishmann model: fully attached and fully separated lift coefficients, weighted by the separation function f .

The separation function f^{st} is indicatively related to the flow separation conditions along the airfoil; its value identifies three steady regions:

- $f^{st} = 1$ fully attached flow, $C_l = C_l^{att}$.
- $f^{st} = 0$ fully separated flow, $C_l = C_l^{fs}$.
- $0 < f^{st} < 1$ transition region.

The fully-attached curve C_l^{att} corresponds to the lift on the airfoil in case the viscous effects of flow separation were neglected, under this assumption,

the fully attached lift coefficient for a rigid airfoil is described by the linear relation:

$$C_l^{att} \approx C_l^{lin}(\alpha) = \frac{\partial C_l}{\partial \alpha}(\alpha - \alpha_0), \quad (2.2)$$

where α_0 is a parameter corresponding to the angle of attack that returns a null steady lift.

It is then assumed that steady lift values below the corresponding linear ones are caused by partial flow separation along the airfoil. The degree of separation is expressed through the separation function f^{st} , which is derived from the expression of the flat plate lift in Kirchoff flow,

$$\left(\frac{1 + \sqrt{f^{st}}}{2} \right)^2 = \frac{C_l^{st}}{C_l^{lin}}, \quad (2.3)$$

and, thereof,

$$f^{st} = \left(2\sqrt{\frac{C_l^{st}}{C_l^{lin}}} - 1 \right)^2. \quad (2.4)$$

The steady lift force is expressed as a weighted sum of the fully attached (linear) component and a fully separated one C_l^{fs} , eq. (2.1); the remaining C_l^{fs} component is determined in the transition region $0 < f^{st} < 1$ from eq. (2.1):

$$C_l^{fs} = \frac{C_l^{st} - C_l^{lin} f^{st}}{1 - f^{st}}. \quad (2.5)$$

To account for the effect of a trailing edge flap [1], the steady lift coefficient C_l^{st} depends not only on the angle of attack α , but also on the flap deflection β ; the steady lift coefficient, as well as the Beddoes-Leishmann components C_l^{att} , C_l^{fs} , and f^{st} , are function of both angle of attack α , and flap deflection β , and can be represented by surfaces, figure 2.2.

When applied to an airfoil with trailing edge flap, the equation for the separation function (2.5) gives rise to singularity points, resulting in strong discontinuities in the steady components. Furthermore, steady lift coefficient

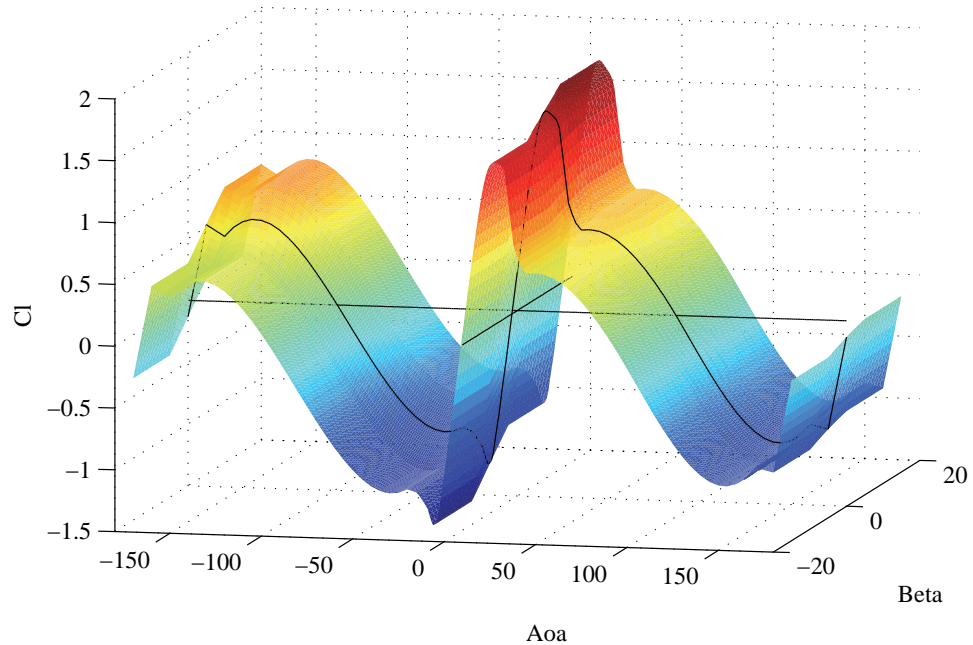


Figure 2.2: Lift coefficient C_l^{st} in the case of an airfoil with trailing edge flap. The lift is a function of both angle of attack α and flap deflection β , and can be represented by a surface.

retrieved from actual measurement or simulations rarely follows a perfectly linear trend even in the attached flow region, giving thus additional discontinuities in the steady Beddoes-Leishmann lift components used by the aerodynamic model.

The effects of the discontinuities in the steady input data might be amplified by the aerodynamic model, resulting in non-physical (and rather annoying) spikes in the aerodynamic forces time histories. A user intervention is required to ensure that the steady components passed to the aerodynamic model are free from discontinuities, as no sufficiently reliable algorithms were found to automatically remove such discontinuities; hence the need for an external preprocessor application.

The application has been implemented in an executable program, *Preprocessor for ATEFlap Dynamic Stall Model, ver.2.04*, which provides the user

with a graphical interface to check, and eventually correct, the steady aerodynamic component inputs that will be passed to the dynamic stall model. The preprocessor output is a file that contains all the baseline steady aerodynamic data required by the model, in the same format required by the aerodynamic model in HAWC2; appendix C gives practical details on files format, and use of the preprocessor program.

2.2 Preprocessor Algorithm

2.2.1 Reconstructing steady data

The input to the preprocessor consists of two sets of data: a *Clean Airfoil*, and a *Flap Delta-steady* input. The *Clean Airfoil* set contains the same input data required for a standard aerodynamic model without flap, and provides steady lift, drag, and moment coefficients as function of the angle of attack. The *Flap Delta-steady* input gives, for different angles of attack, the steady variations in lift, drag, and moment coefficients caused by flap deflections; please refer to appendix C.2 for details on the input files formats.

The steady data of lift C_l^{st} , drag C_d , and moment C_m coefficients are computed as function of both angle of attack and flap deflection; the coefficients in the *Clean Airfoil* input are summed to the respective variations in the *Flap Delta-steady* input. Linear interpolation is applied to cover a range of angle of attack from -180 to +180; the coefficients corresponding to angles of attack outside the range specified in the input file are taken equal to the closest available values.

2.2.2 Compute linear lift parameters

As mentioned, the input data for the dynamic stall model are obtained by splitting the steady lift coefficient C_l^{st} into a fully attached component C_l^{att} , and a fully separated C_l^{fs} one, weighted by the steady separation function

f^{st} :

$$C_l^{st} = C_l^{att} f^{st} + C_l^{fs}(1 - f^{st}). \quad (2.1)$$

The fully attached component C_l^{att} is computed assuming that the lift in fully attached flow is given by a linear function of angle of attack α and flap deflection β :

$$C_l^{lin} = \frac{\partial C_l}{\partial \alpha}(\alpha - \alpha_0) + \frac{\partial C_l}{\partial \beta}(\beta); \quad (2.6)$$

The function describes a flat plane in the $(\alpha, \beta, C_l^{st})$ space. For a set of steady data corresponding to a specific airfoil and flap, the fully attached lift plane is univocally characterized by three parameters: $\partial C_l / \partial \alpha$, $\partial C_l / \partial \beta$, and α_0 .

Linear parameter $\partial C_l / \partial \alpha$ The gradient $\partial C_l / \partial \alpha$ gives the steady lift variations caused by unit change in angle of attack, for a fixed flap deflection, which is specified by the user. In the case of a standard airfoil without flap, the gradient $\partial C_l / \partial \alpha$ corresponds to the slope of the lift curve in the linear region, figure 2.1; for a flat plate in potential flow $\partial C_l / \partial \alpha = 2\pi$.

The gradient $\partial C_l / \partial \alpha$ is determined using the same algorithm as implemented in the HAWC2 aerodynamic model for standard airfoils MHH [12]; the algorithm is described in appendix B.3.2.

Linear parameter α_0 The angle α_0 corresponds to the angle of attack that returns a null linear steady lift $C_{l,\alpha_0}^{lin} = 0$, for null flap deflection. In the case of a standard airfoil without flap, figure 2.1, α_0 sets the intercept of the linear lift line with the zero lift axis.

The value of α_0 is computed together with the $\partial C_l / \partial \alpha$ gradient; the algorithm is presented in appendix B.3.2.

Linear parameter $\partial C_l/\partial\beta$ The gradient $\partial C_l/\partial\beta$ gives the variation of fully attached lift corresponding to unit flap deflection, for a fixed angle of attack.

The angle of attack is fixed at the value α_0 . The gradient is then evaluated as the variation $\Delta C_l^{st}/\Delta\beta$ for flap deflection values of $\pm 1^\circ$ from the user specified value.

All the parameters required by equation (2.6) are thus determined, and the linear lift coefficient C_l^{lin} is computed in the whole range of angles of attack and flap deflections.

2.2.3 Compute separation function

The next step is to compute the values of the steady separation function f^{st} . The expression for the flat-plate lift in Kirchoff flow eq. (2.3) leads to:

$$f(\alpha, \beta) = \left(2\sqrt{\frac{C_l^{st}}{C_l^{lin}}} - 1 \right)^2. \quad (2.4)$$

The steady separation function f^{st} should be real and bounded $0 \leq f^{st} \leq 1$, thus singularities arise when:

- $C_l^{st}/C_l^{lin} < 0$, the singularity is solved, in case of negative C_l^{st} , by forcing the function to 0; in case of positive C_l^{st} , by forcing the function to 1.
- $C_l^{st}/C_l^{lin} > 1$, solved by forcing $f^{st} = 1$.

Further adjustments to avoid discontinuities in the f^{st} function are left to user's corrections, which are manually applied through the graphical interface. The user has also the possibility to specify the range of angles of attack corresponding to fully separated flow conditions; in the specified range, the separation function is forced to zero, $f^{st} = 0$.

2.2.4 Compute fully attached and fully separated lift coefficients

The value of the separation function f^{st} outlines three regions, corresponding, respectively, to fully attached, fully separated, and transition flow conditions. In each of the three regions the coefficients are computed as follows:

- Fully attached region, the separation function is $f^{st} = 1$. In order to keep the steady lift coefficient equal to the input one, the C_l^{att} is taken equal to C_l^{st} , rather than C_l^{lin} .

$$f^{st} = 1 \quad \rightarrow \quad \begin{cases} C_l^{att} = C_l^{st} \\ C_l^{fs} = C_l^{st}/2 \end{cases} ; \quad (2.7)$$

- Fully separated region, the separation function is $f^{st} = 0$.

$$f^{st} = 0 \quad \rightarrow \quad \begin{cases} C_l^{fs} = C_l^{st} \\ C_l^{att} = C_l^{lin} \end{cases} ; \quad (2.8)$$

- Transition region:

$$0 < f^{st} < 1 \quad \rightarrow \quad \begin{cases} C_l^{att} = C_l^{lin} \\ C_l^{fs} = \frac{C_l^{st} - C_l^{lin} f^{st}}{1 - f^{st}} \end{cases} . \quad (2.9)$$

2.2.5 Manual corrections by the user

The steady coefficients and the Beddoes-Leishmann lift components required by the dynamic stall model have now been computed as function of both angle of attack, and flap deflection. Due to numerical issues, the steady coefficient values might present discontinuities, which would negatively affect the dynamic output of the aerodynamic model. Through the graphical interface, the user has the possibility to manually smooth out discontinuities in the steady coefficient.

Whenever the user modifies the f^{st} separation function, the corresponding C_l^{fs} values are recomputed as specified in the previous paragraph, so that the total steady lift is kept equal to the input one C_l^{st} .

If the fully separated steady values C_l^{fs} are modified by the user, in order to keep the total steady lift equal to the input one, the separation function is recomputed as

$$f = \frac{C_l^{st} - C_l^{fs}}{C_l^{lin} - C_l^{fs}}. \quad (2.10)$$

The user has also the possibility to modify the values of the fully attached lift component C_l^{att} , although the action would result in a total steady lift, eq. (2.1), different from the C_l^{st} input one.

2.2.6 Preprocessor output - ATEFlap input

The steady coefficients and Beddoes-Leishmann lift components returned by the preprocessor and corrected by the user are saved in a file, which will be used as input by the aerodynamic model, please refer to Appendix C.2 for details on the file format.

In order to reach the discretization required by the result file, a *linear* interpolation is performed; the interpolation algorithm is the same as used inside the ATEFlap model, and is described in appendix B.3.3.

All the operations required in the preprocessing phase are collected in a stand-alone application, which allows the user to check, and eventually correct, all the baseline steady data that will be used in the *ATEFlap* aerodynamic model; the application user's guide is reported in appendix C. The file returned by the preprocessor application is ready for use by the *ATEFlap* model in the HAWC2 aeroelastic simulation tool.

ATEFlap aerodynamic model

The *ATEFlap* aerodynamic model returns the lift, drag, and moment acting on an airfoil undergoing arbitrary motion and trailing edge flap deflection (arbitrary in the limits of the plane wake assumption). The input to the aerodynamic model consists of steady lift, drag, and moment coefficients, and the Beddoes-Leishmann lift components as function of angle of attack, and flap deflection; the steady input data are contained in the file generated by the *Preprocessor for ATEFlap Dynamic Stall Model*.

The model is integrated in the HAWC2 aeroelastic simulation tool [12], details of the implementation in the aeroelastic code are given in appendix B; appendix A.2 reports the major changes from previous implementations of the algorithm.

The *ATEFlap* model captures both steady and dynamic characteristics of the aerodynamic forces. The dynamic effects reproduced by the model can be split into three categories:

- *Added mass* effects, or *non-circulatory* (potential flow) contributions, describe the forces that arise simply as a reaction of the fluid accelerated

by the airfoil (or the flap) motion. The term has no memory effects, and only depends on the instantaneous motion of the airfoil or flap.

- Effects from *wake dynamics*, or *circulatory* (potential flow) effects, describe the memory effects of the vorticity shed into the wake, following a change of the airfoil aerodynamic loading, as, for instance, due to a variation in angle of attack or flap deflection.
- *Dynamic stall* effects represent the dynamics of the forces on an airfoil undergoing flow separation (stall).

The dynamics in attached flow conditions are determined by the *added mass* and the *circulatory potential flow* effects; the algorithm used in the model is based on Gaunna's [6] model for a thin airfoil in potential flow.

The flow separation part of the model follows the Beddoes-Leishmann dynamic stall formulation given in Hansen et al. [8], where the circulatory lift is expressed as a weighted sum of a fully attached and fully separated contribution. The weight coefficient accounts for the dynamics of flow separation, and it is retrieved from the steady input data at an equivalent angle of attack, and flap deflection; the equivalent angle of attack and flap deflection values are determined from the lift coefficient returned by the potential flow part of the model.

3.1 Lift: potential flow

The fully attached contribution to the lift force corresponds to the lift that would be generated on the airfoil if it was to operate in fully attached flow conditions at every angle of attack; in other words, the viscous effects on the lift force are neglected (potential flow assumption), with the exception of the Kutta condition, enforcing flow velocity continuity at the trailing edge.

Following the formulation from Von Karman and Sears [11], the lift force in potential flow can be modeled as the sum of three components: a non-circulatory lift, a quasi-steady circulatory contribution, and a wake memory

effect. The *non-circulatory* lift, or *added mass* term, describes the lift force that arises in a non-circulatory flow, as a reaction from the fluid accelerated by the airfoil motion; the non-circulatory term only depends on the instantaneous motion of the airfoil and has no memory effect.

The *quasi-steady* circulatory lift corresponds to the lift force that would act on the airfoil if the current deformation (and motion) conditions were held constant for an infinite time. The contribution is derived as a simple look-up in the steady input data:

$$C_l^{qs} = C_l^{att}[\alpha_{qs}, \beta_{qs}]. \quad (3.1)$$

The ‘quasi-steady’ designation simply refers to the fact that changes in the flow conditions caused by the eigen-movement of the airfoil are accounted for. For instance, the quasi-steady angle of attack α_{qs} includes the terms due to the steady angle of attack α_{st} , the heave velocity \dot{y} , and the pitch ratio $\dot{\alpha}$; the quasi-steady angle of attack is evaluated at the three-quarter chord point, assuming the airfoil elastic axis to be located at ϵ_{ea} (-1 is LE, +1 is TE, and b_{hc} is the half-chord length):

$$\alpha_{qs} = \alpha_{3/4} = \alpha_{st} - \frac{1}{U_0} \dot{y} + \frac{(0.5 - \epsilon_{ea})b_{hc}}{U_0} \dot{\alpha}. \quad (3.2)$$

The quasi-steady equivalent for the flap deflection includes a deflection-rate term, whose contribution is derived from Gaunaa’s [6] work on thin-airfoil theory:

$$\beta_{qs} = \beta - \frac{1}{U_0} \frac{H_y}{\partial C_l / \partial \beta} \dot{\beta}, \quad (3.3)$$

where H_y corresponds to the flap deflection shape integral given in Gaunaa [6]. H_y , which has dimension of meters, is obtained in the code by multiplying the dimensionless input H_y^* with half the chord length: $H_y = H_y^* b_{hc}$, see appendix B.3.1.2.

Following a step-change in the airfoil circulation (as for instance a step change in angle of attack, or flap deflection), the actual circulatory lift does not follow the step described by the corresponding quasi-steady lift, figure 3.1; in fact, the effective lift lags behind the quasi-steady one. Such *lift deficiency* is

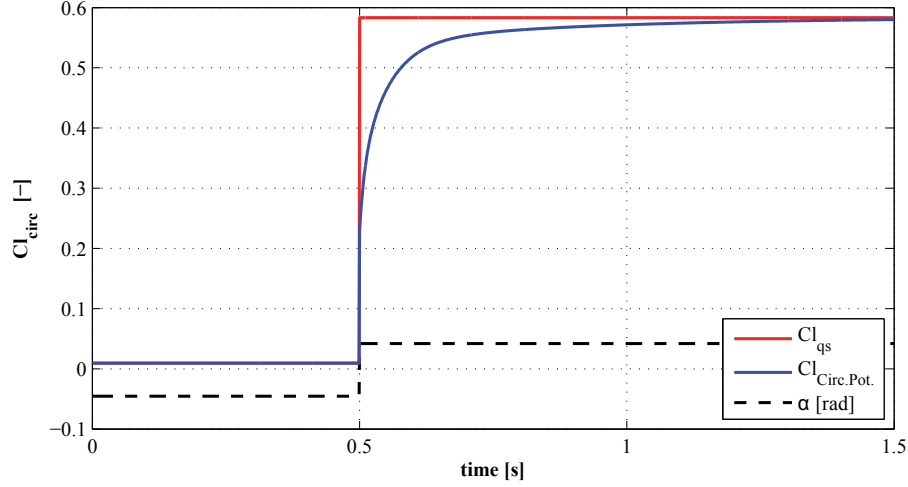


Figure 3.1: *Circulatory lift in attached flow, effect of the wake memory term: the lift based on effective angle of attack α_{eff} does not follow the step in the quasi-steady lift. Computation for NACA 64-418 indicial response and steady curve, wind speed 70 m/s, unit chord length.*

caused by the wake memory effect, originated by the vorticity shed into the wake following the change of circulation around the airfoil.

In Hansen et al. [8] the wake memory effects due to a change in the quasi-steady angle of attack are described by means of an equivalent effective downwash speed w_{eff} . For the case of a rigid airfoil, the effective downwash relates to an effective equivalent angle of attack as $\alpha_{eff} = w_{eff}/U_0$; the effective angle of attack corresponds to the angle that returns a steady-lift value equal to the effective circulatory lift (blue line in fig. 3.1), including the wake effects.

Following the approach of Von Karman and Sears [11], in Hansen et al. [8] the effective downwash from an arbitrary motion is computed as a superposition of step responses. The step response is described by an exponential indicial response function Φ :

$$\Phi = 1 - \sum_{i=1}^{N_{lag}} A_i \exp^{b_i \tau}, \quad \tau = \frac{U_0 t}{b_{hc}}; \quad (3.4)$$

the coefficients A_i , and b_i define the shape of the indicial function. Jones's [9]

values are usually adopted for the response of a flat plate; airfoils with finite thickness have a different and slower response [4].

The exponential form of the indicial function allows for a convenient numerical integration of the Duhamel's superposition integral; in fact, the integral value at every time step can be evaluated as a decay factor multiplying the previous time-step value, summed to an increment term, which only includes integration along the current time step (and not from t_0). The effective downwash is then computed as [8]:

$$w_{eff} = w_{qs} \left(1 - \sum_{i=1}^{N_{lag}} A_i \right) + \sum_{i=1}^{N_{lag}} z_i, \quad (3.5)$$

where w_{qs} is the quasi-steady equivalent downwash at the three quarter chord point. The terms z_i are state variables accounting for the wake memory effect following the step changes; they are described by first order differential equations:

$$\dot{z}_i = -\frac{1}{b_{hc}} U_0 b_i z_i + \frac{1}{b_{hc}} U_0 b_i A_i w_{qs}, \quad (3.6)$$

which, assuming piecewise constant values, is evaluated in a time stepping integration as:

$$z_{i,t} = z_{i,t-\Delta t} \exp\left(-\frac{U_0 b_i}{b_{hc}} \Delta t\right) + A_i w_{qs,t} \left(1 - \exp\left(-\frac{U_0 b_i}{b_{hc}} \Delta t\right)\right). \quad (3.7)$$

Gaunaa [6] presents an analytical model for the unsteady aerodynamic forces on an airfoil undergoing arbitrary motion and camber line deformation, under the assumptions of potential flow, thin-airfoil, and plane wake. He shows that modeling the effects of the vorticity shed into the wake through an equivalent effective downwash speed is a valid approach also for an airfoil undergoing camber line deformation. The wake memory effects following a variation in the airfoil quasi-steady loading can be modeled through an effective downwash, independently from the source of the quasi-steady loading variation; the same indicial response approach can be used for either a change in the angle of attack, or in the heave displacement velocity, or a camber line deformation.

The same model can be thus used to describe the wake memory effects caused by flap deflections.

In the current formulation, the equivalent effective downwash speed is split into a contribution α_{eff} from the angle of attack (including also heave velocity, and pitch rate), and a contribution β_{eff} from the flap deflection. Each of the two terms is computed from the respective quasi-steady values:

$$\text{Q.St.} \quad \begin{cases} \alpha_{qs} = \alpha_{st} - \frac{1}{U_0} \dot{y} + \frac{(0.5 - \epsilon_{ea}) b_{hc}}{U_0} \dot{\alpha} \\ \beta_{qs} = \beta - \frac{1}{U_0} \frac{H_y}{\partial C_l / \partial \beta} \dot{\beta} \end{cases}; \quad (3.8)$$

and the corresponding effective variables:

$$\text{Eff.} \quad \begin{cases} \alpha_{\text{eff}} = \alpha_{qs} \Phi(0) + \sum_{i=1}^{N_{\text{lag}}} z_i^\alpha \\ \beta_{\text{eff}} = \beta_{qs} \Phi(0) + \sum_{i=1}^{N_{\text{lag}}} z_i^\beta \end{cases}, \quad (3.9)$$

where $\Phi(0)$ gives the indicial response value at the initial instant:

$$\Phi(0) = 1 - \sum_{i=1}^{N_{\text{lag}}} A_i. \quad (3.10)$$

The wake memory variables z_i are computed assuming piecewise constant time integration as

$$z_i \quad \begin{cases} z_{i,t}^\alpha = z_{i,t-\Delta t}^\alpha \exp\left(-\frac{U_0 b_i}{b_{hc}} \Delta t\right) + A_i \alpha_{qs,t} \left(1 - \exp\left(-\frac{U_0 b_i}{b_{hc}} \Delta t\right)\right) \\ z_{i,t}^\beta = z_{i,t-\Delta t}^\beta \exp\left(-\frac{U_0 b_i}{b_{hc}} \Delta t\right) + A_i \beta_{qs,t} \left(1 - \exp\left(-\frac{U_0 b_i}{b_{hc}} \Delta t\right)\right) \end{cases}. \quad (3.11)$$

The total circulatory lift in attached flow, accounting for both quasi-steady and wake memory effects, is determined by selecting from the steady input data the fully attached lift coefficient C_l^{att} that corresponds to the effective angle of attack and flap deflection:

$$C_l^{\text{Circ.Pot.}} = C_l^{\text{att}}[\alpha_{\text{eff}}; \beta_{\text{eff}}]. \quad (3.12)$$

The non-circulatory contribution accounts for both torsion rate $\dot{\alpha}^{\text{str}}$ and flap deflection rate; the contribution from higher order terms was found negligible:

$$C_l^{\text{nc}} = \pi \frac{b_{hc}}{U_0} \dot{\alpha}^{\text{str}} + \frac{F_{\text{dydxLE}}}{\pi} \frac{b_{hc}}{U_0} \dot{\beta}; \quad (3.13)$$

the non-circulatory contribution from the flap deflection rate is again derived from Gaunaa's work [6], and expressed through the deflection shape integral F_{dydxLE} .

The total lift in fully attached condition (potential flow), is then given by the sum of the non-circulatory and the circulatory contribution:

$$C_l^{\text{Pot}} = C_l^{\text{Circ.Pot.}} + C_l^{mc} \quad (3.14)$$

Fully Attached lift without flap contribution To determine the flow separation dynamics, presented in the following sections, the fully attached (potential flow) lift is also computed considering the case of the standard airfoil without flap, and therefore considering only the contribution from angle of attack and torsion rate (i.e., null flap deflection):

$$C_{l,\beta=0}^{\text{Pot}} = C_l^{\text{att}}[\alpha_{\text{eff}}; 0] + \pi \frac{b_{hc}}{U_0} \dot{\alpha}^{\text{str}}. \quad (3.15)$$

3.1.1 Assumption of constant flow velocity over the chord

In the *ATEFlap* model, as in most aerodynamic models for wind turbine aeroelastic simulations, all variations in the oncoming flow are approximated as equivalent changes of angle of attack, and thus resolved in the time domain through a superposition of Wagner-like indicial response functions, equations (3.9) - (3.11).

It is thus implied that flow variations normal to the airfoil occur simultaneously and uniformly along the airfoil length. Flow variations with a perturbation front traveling progressively along the airfoil chord are indeed common, as the airfoil goes through a non-uniform wind field, affected, for instance, by atmospheric turbulence, wind shear, induced velocities variation, or tower shadow effects. The aerodynamic response to perturbations traveling along the airfoil should be described by Küssner-type response functions [11]; the perturbation is instead approximated to an uniform variation, and the response is also described by Wagner-like functions. The simplification results

in an error in the phase, and an overestimation of the magnitude of the aerodynamic response to flow variations.

Nevertheless, the error introduced by the simplification is small for perturbations with long wavelength compared to the airfoil chord; that is to say, for perturbations that develop slowly compared to the airfoil relative velocity. Buhl et al. [5] present an analysis in the frequency domain of the lift response to a sinusoidal vertical gust; the correct response, returned by Sears function, is compared to the approximated response returned by Theodorsen function, which instead assumes uniform flow variation along the airfoil chord. They show that the response error introduced by the simplification is small, both in magnitude and phase, for perturbations with reduced frequencies k ¹ below 0.3. The authors quantify the simplification error for an airfoil rotating in a wind field with standard atmospheric turbulence; since for high frequencies the energy content of the turbulence spectrum is low, the total simplification error in the response magnitude is below 0.2%, and the phase shift is close to 0.01 degrees.

Induced velocity variations and terrain wind shear are also expected to result in only marginal biases to the computed 2D airfoil aerodynamic response, as the perturbations they introduce in the flow field have a slow development. A low pass filter is usually applied to the induced velocity to model dynamic in-flow effects, thus cutting out all the fast variations. Likewise, for a rotating blade, the terrain wind shear corresponds to flow perturbations with frequencies close to the rotational one, which, for most of the blade span (with the exception of the innermost sections), correspond to reduced frequencies k ² below 0.2.

The tower shadow is also expected to result in only a minor bias in the response estimation. In fact, for a multi-MW wind turbine with upwind configuration, the perturbation induced by the tower shadow corresponds, in the outer sections of the blade, to reduced frequencies in the range $0.2 \sim 0.3$.

¹Reduced frequency $k = \frac{\omega b_{ch}}{U_0}$

²For a frequency f equal to P times the rotational frequency, the reduced frequency along the blade sections can be roughly evaluated as $k \approx P \frac{b_{hc}}{r}$; where b_{hc} is the chord length and r is the radial position from the rotor center.

To conclude, the assumption of uniform oncoming flow variations over the airfoil chord, which is adopted in the *ATEFLap* model, returns a biased response for flow perturbations traveling along the airfoil chord. Nonetheless, the error introduced by the simplification is small in the investigated cases; the assumption seems thus to hold for common wind turbine aeroelastic applications, where the changes in the wind field are not too abrupt.

3.2 Lift: dynamics of flow separation

The part of the model that accounts for the dynamics of flow separation and dynamic stall follows the Beddoes-Leishmann formulation given in Hansen et al. [8]. The circulatory lift is expressed as a weighted sum of a fully attached and a fully separated contribution:

$$C_l^{\text{Circ.Dyn}} = C_{l, [\alpha_{\text{eff}}; \beta_{\text{eff}}]}^{\text{att}} f^{\text{dyn}} + C_{l, [\alpha_{\text{eff}}; \beta_{\text{eff}}]}^{\text{fs}} (1 - f^{\text{dyn}}). \quad (3.16)$$

The dynamics of flow separation are described through the separation function f^{dyn} , which assigns the weight between the fully attached and the fully separated components. The fully attached C_l^{att} and fully separated C_l^{fs} lift terms are given by a lookup of the steady input data, corresponding to effective angle of attack, and flap deflection.

The model mimics the dynamics of the boundary layer by accounting for the fact that flow separation requires some time to converge to steady conditions. The typical lag in the airfoil stall is a direct consequence of the flow separation delay: for an airfoil in the stall region, an increase in angle of attack, which in steady conditions would correspond to a decrease in lift, is actually causing an initial increase in lift, figure 3.2.

As in Hansen et al. [8], the dynamics of flow separation and stall are modeled by the separation function f^{dyn} ; the separation function value that accounts for trailing edge separation dynamics is computed in three steps.

1. Lagging potential flow lift The total lift computed under potential flow assumption, including circulatory and non-circulatory contributions,

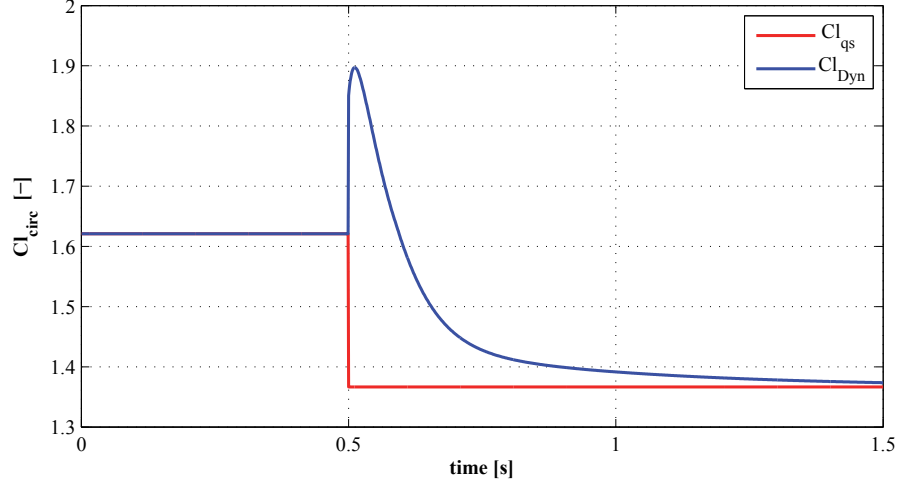


Figure 3.2: *Dynamic Stall model: circulatory lift for an airfoil in the stall region. The angle of attack is increased from 16 deg (point of max Cl) to 22 deg. The quasi-steady lift decreases as the airfoil is in stall region; the circulatory dynamic lift, accounting for the stall delay phenomenon, first increases, and then, as the flow separation develops along the airfoil chord, it converges down to the steady value. Note the presence of two ‘dynamic effects’: the potential flow one, as the lift is increased after the step, and the dynamic stall one; the two phenomenon have different time scales, the potential flow effect being much faster than the dynamic stall one. Computation for NACA 64-418, wind speed 70 m/s, unit chord length.*

eq. (3.14), is lagged through a first-order low-pass filter. The filter non-dimensional time parameter τ_P corresponds to the parameter referred to as ‘pressure time constant’ in Hansen et al. [8]:

$$\dot{C}_l^{\text{lag}} = -\frac{U_0}{b_{hc}} \frac{1}{\tau_P} C_l^{\text{lag}} + \frac{U_0}{b_{hc}} \frac{1}{\tau_P} C_l^{\text{Pot}}. \quad (3.17)$$

The ordinary differential equation is solved by numerical integration in time, assuming piecewise constant values; the potential flow lift computed with null flap contribution, eq. (3.15), undergoes the same first order filter:

$$\begin{cases} C_{l,t}^{\text{lag}} = C_{l,t-\Delta t}^{\text{lag}} \exp\left(-\frac{U_0}{b_{hc}} \frac{1}{\tau_P} \Delta t\right) + C_{l,t}^{\text{Pot}} \left(1 - \exp\left(-\frac{U_0}{b_{hc}} \frac{1}{\tau_P} \Delta t\right)\right) \\ C_{l,\beta=0,t}^{\text{lag}} = C_{l,\beta=0,t-\Delta t}^{\text{lag}} \exp\left(-\frac{U_0}{b_{hc}} \frac{1}{\tau_P} \Delta t\right) + C_{l,\beta=0,t}^{\text{Pot}} \left(1 - \exp\left(-\frac{U_0}{b_{hc}} \frac{1}{\tau_P} \Delta t\right)\right) \end{cases}. \quad (3.18)$$

2. Intermediate separation function An intermediate separation function $f^{C_{l,\text{lag}}}$ is determined from a look-up of the steady input data f^{st} , in correspondence to an equivalent angle of attack α^* and flap deflection β^* , which are computed from the lagged lift coefficients C_l^{lag} .

It is assumed that the contributions from angle of attack and flap deflection maintain the same relative weight as in the potential flow lift; therefore, the equivalent angle of attack α^* is determined as the angle of attack that would return a *potential flow* lift equal to the lagged lift with null flap contribution $C_{l,\beta=0}^{\text{lag}}$.

Similarly, the equivalent flap deflection β^* is computed as the deflection that would give a *linear* lift increment equal to the difference between the lagged lift terms with, and without the flap contribution:

$$f^{C_{l,\text{lag}}} = f_{[\alpha^*;\beta^*]}^{st} \begin{cases} \alpha^* = \frac{C_{l,\beta=0}^{\text{lag}}}{\partial C_l / \partial \alpha} + \alpha_0 \\ \beta^* = \frac{C_l^{\text{lag}} - C_{l,\beta=0}^{\text{lag}}}{\partial C_l / \partial \beta} \end{cases} . \quad (3.19)$$

Please note that the potential lift linear parameters ($\alpha_0, \partial C_l / \partial \alpha, \partial C_l / \partial \beta$) used in the computation should match exactly the parameters used in the input data preprocessing phase, eq. (2.6); otherwise, an offset from the steady lift value arises in the cases of partially separated flow.

3. Dynamic separation function The intermediate separation function $f^{C_{L,\text{lag}}}$ is passed through another first-order low-pass filter; the filter non-dimensional time parameter τ_B is referred to as ‘boundary layer time constant’ in [8]:³

$$\dot{f}^{dyn} = -\frac{U_0}{b_{hc}} \frac{1}{\tau_B} f^{dyn} + \frac{U_0}{b_{hc}} \frac{1}{\tau_B} f^{C_{l,\text{lag}}}; \quad (3.20)$$

by applying integration under piecewise constant values assumption, the equation reads

$$f_t^{dyn} = f_{t-\Delta t}^{dyn} \exp\left(-\frac{U_0}{b_{hc}} \frac{1}{\tau_B} \Delta t\right) + f_t^{C_{l,\text{lag}}} \left(1 - \exp\left(-\frac{U_0}{b_{hc}} \frac{1}{\tau_B} \Delta t\right)\right) \quad (3.21)$$

³Indicative values for the filters non-dimensional time constants are: $\tau_P = 1.5$, and $\tau_B = 6.0$. The values correspond to the default choices in HAWC2 [12].

The resulting separation function f^{dyn} accounts for the dynamics of flow separation and stall.

Total lift coefficient The final total circulatory contribution to the lift coefficient, which accounts for both potential flow and flow separation dynamics, is given by the weighted sum

$$C_l^{Circ.Dyn} = C_{l, [\alpha_{eff}; \beta_{eff}]}^{att} f^{dyn} + C_{l, [\alpha_{eff}; \beta_{eff}]}^{fs} (1 - f^{dyn}). \quad (3.16)$$

The non-circulatory contribution is given by the first-time-derivative added mass terms, eq. (3.13),

$$C_l^{nc} = \pi \frac{b_{hc}}{U_0} \dot{\alpha}^{str} + \frac{F_{dydxLE}}{\pi} \frac{b_{hc}}{U_0} \dot{\beta}. \quad (3.13)$$

Finally, the total lift coefficient is obtained as the sum of the circulatory and non-circulatory contributions:

$$C_l^{dyn} = C_l^{Circ.Dyn} + C_l^{nc}. \quad (3.22)$$

3.3 Drag

The drag on the airfoil is computed as the sum of a contribution from the steady input data at the effective angle of attack and flap deflection, plus three induced drag contributions:

$$C_d = C_d^{eff} + C_{d,ind}^{\alpha} + C_{d,ind}^{\beta} + C_{d,ind}^f. \quad (3.23)$$

The value C_d^{eff} is obtained from a look-up of the steady input data, for angle of attack and flap deflection corresponding to the effective ones:

$$C_d^{eff} = C_d[\alpha_{eff}; \beta_{eff}]. \quad (3.24)$$

The induced drag contributions represent the additional drag component caused by a shift in the effective dynamic conditions of the aerodynamic forces due to the vorticity shed into the wake. The direction shift can be shown to be related to the difference between the quasi-steady and the effective downwash velocity.

The contribution from the angle of attack is computed from a simplification of the induced drag in potential flow (see appendix B.1.3):

$$C_{d,ind}^{\alpha} = C_l^{\text{Circ.Dyn}} \cdot (\alpha_{qs} - \alpha_{eff}). \quad (3.25)$$

The flap induced drag corresponds to the shift in downwash caused by the flap contribution to the potential flow lift; it is thus evaluated as an equivalent shift in the effective angle of attack that would return the same linear lift variation as produced by the difference of the effective and steady flap deflection:

$$C_{d,ind}^{\beta} = C_l^{\text{Circ.Dyn}} \cdot \frac{\partial C_l / \partial \beta}{\partial C_l / \partial \alpha} (\beta_{qs} - \beta_{eff}) f^{dyn}. \quad (3.26)$$

The flap contribution to the induced drag is scaled by the separation function f^{dyn} . This choice is only supported by intuitive interpretation of the two extreme cases $f = 1$ and $f = 0$; in fully attached conditions $f = 1$, the induced drag from flap deflection should match the value computed under potential flow assumption, while, once the flow is fully separated $f = 0$, the flap induced drag has a negligible effect on the total drag. Furthermore, the agreement with CFD results is improved by applying the f^{dyn} scaling factor.

The induced drag contribution from the separation function f accounts for the change in drag due to the separation delay. As in Hansen et al. [8], it is computed by scaling an estimation of the actual non-friction drag (term in the first parenthesis) with a function of the dynamic and intermediate separation function values:

$$\begin{aligned} C_{d,ind}^f &= (C_d^{\text{eff}} - C_{d, [\alpha_0; 0]}) \cdot \left[\left(\frac{1 - \sqrt{f^{dyn}}}{2} \right)^2 - \left(\frac{1 - \sqrt{f C_{l, \text{lag}}}}{2} \right)^2 \right] \\ &= (C_{d, dyn}^{lu} - C_{d, [\alpha_0; 0]}) \cdot \frac{1}{4} \left[f^{dyn} - f^{C_{L, \text{lag}}} + 2 \left(\sqrt{f C_{l, \text{lag}}} - \sqrt{f^{dyn}} \right) \right]. \end{aligned} \quad (3.27)$$

3.4 Moment

The moment coefficient is evaluated with respect to the quarter-chord point $\epsilon_{ea} = -0.5$, positive nose-up. It is computed as the sum of a quasi-steady table lookup value, plus non-circulatory contributions from torsion rate and flap deflection rate:

$$C_m = C_m^{qs} + C_m^{mc,\dot{\alpha}} + C_m^{mc,\dot{\beta}}. \quad (3.28)$$

The quasi-steady term is given by a look-up of the steady input data. The steady flap deflection β_{st} is used, as potential flow theory indicates that no memory terms affect the moment evaluated at the quarter-chord point, see appendix B.1.4; furthermore, also for non-attached flow condition, the resulting dynamics are in better agreement with the results from CFD simulations, than the results obtained by using the β_{eff} term. For the angle of attack, the α_{eff} value is used in the look-up, to keep consistency with the MHH HAWC2 aerodynamic model for sections without flap:

$$C_m^{qs} = C_m[\alpha_{eff}; \beta_{st}]. \quad (3.29)$$

The non-circulatory contribution from the torsion rate is computed as

$$C_m^{mc,\dot{\alpha}} = -0.5\pi \frac{b_{hc}}{U_0} \dot{\alpha}^{str}. \quad (3.30)$$

The non-circulatory contribution from the flap deflection is derived from Gaunaa [6], and here only includes terms related to the deflection rate; the term is simplified by considering the moment with respect to the quarter-chord point, appendix B.1.4:

$$C_m^{mc,\dot{\beta}} = \dot{\beta} \left[-0.5 \frac{b}{U_0} \frac{1}{\pi} (G_{dydxLE} + 0.5 F_{dydxLE}) + 0.5 \frac{1}{U_0} \left(\frac{F_{y,LE}}{\pi} + \frac{H_y}{2} \right) \right]. \quad (3.31)$$

The terms G_{dydxLE} , F_{dydxLE} , $F_{y,LE}$, H_y are parameters derived from the deflection shape integrals described in Gaunaa [6]; $F_{y,LE}$ and H_y have dimensions of meters, and are obtained by multiplying the dimensionless inputs

H_y^* and $F_{y,LE}^*$ with the airfoil half chord length (refer to appendix B.3.1.2 for specifying customized integral values in the input file):

$$H_y = H_y^* \cdot b_{hc}, \quad (3.32)$$

$$F_{y,LE} = F_{y,LE}^* \cdot b_{hc}. \quad (3.33)$$

The dynamic contribution to the moment that derives from the shifting of the pressure center position during the dynamics of the trailing edge separation, $\Delta C_m^{f''}$, which is mentioned in Hansen et al. [8], is omitted in the *ATEFlap* implementation; the term is also omitted in the current HAWC2 implementation of the MHH model for standard airfoils without flap. Please note that the equation for the non-circulatory contribution to the moment specified in eq. A8 of Andersen et al. [1] is erroneous.

Model validation

The *ATEFlap* model and its correct implementation in the aeroelastic code HAWC2 have been verified by comparison against other models results. First, the flap is locked to a zero deflection position while the angle of attack is changed harmonically; the resulting aerodynamic forces are compared with the forces predicted by the standard dynamic stall model for an airfoil without flap, which is described in Hansen et al. [8]. The forces computed by *ATEFlap* model are also compared to CFD solutions for the case of harmonic pitching motion, and harmonic flap deflections.

4.1 Comparison with standard dynamic stall model

The results from the *ATEFlap* aerodynamic model are compared with the ones from the dynamic stall model for an airfoil without flap; the model is given by the `dynstall_mhh` option in the HAWC2 code [12], and corresponds

to the one described by Hansen et al. [8] (without the pressure center term $\Delta C_m^{f''}$).

The steady input data refer to a DU 21-A17 airfoil section, which is used at 60 % blade span on the NREL 5-MW baseline turbine [10]; the indicial response coefficients are taken equal to Jones's flat plate response. The Adaptive Trailing Edge Flap is locked to a zero deflection, $\text{Beta} = 0.0$, and the angle of attack is changed harmonically with different reduced frequencies $k = \omega b/U$; different mean angles are considered, so to verify the model both in attached flow and stalled conditions.

In attached flow conditions, figure 4.1, the results of the two models are exactly overlapping. Also in stalled conditions, figure 4.2, the results are practically identical, as the observed difference is very small, and most likely related to differences in pre-processing phase. The agreement between the two model has proved excelent for all the investigated angles of attack and reduced frequencies.

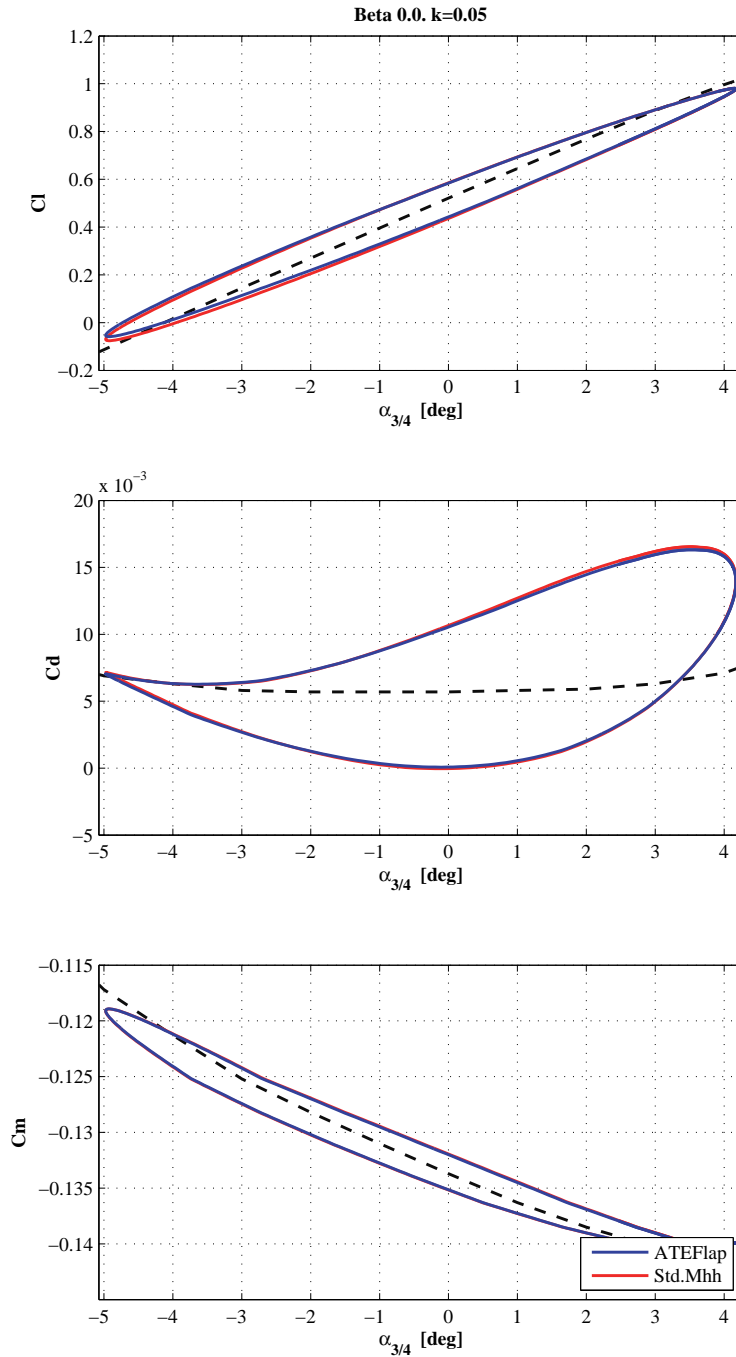


Figure 4.1: Model validation, comparison of the aerodynamic forces computed with the ATEFlap aerodynamic model and the MHH model for a section with flap deflection equal to 0.0; the results are overlapping. Attached flow region, mean angle of attack 0° ; steady data for DU 21-A17 airfoil, flat plate indicial response. For both aerodynamic models, the C_l loop has counter-clockwise direction, C_d and C_m clockwise.

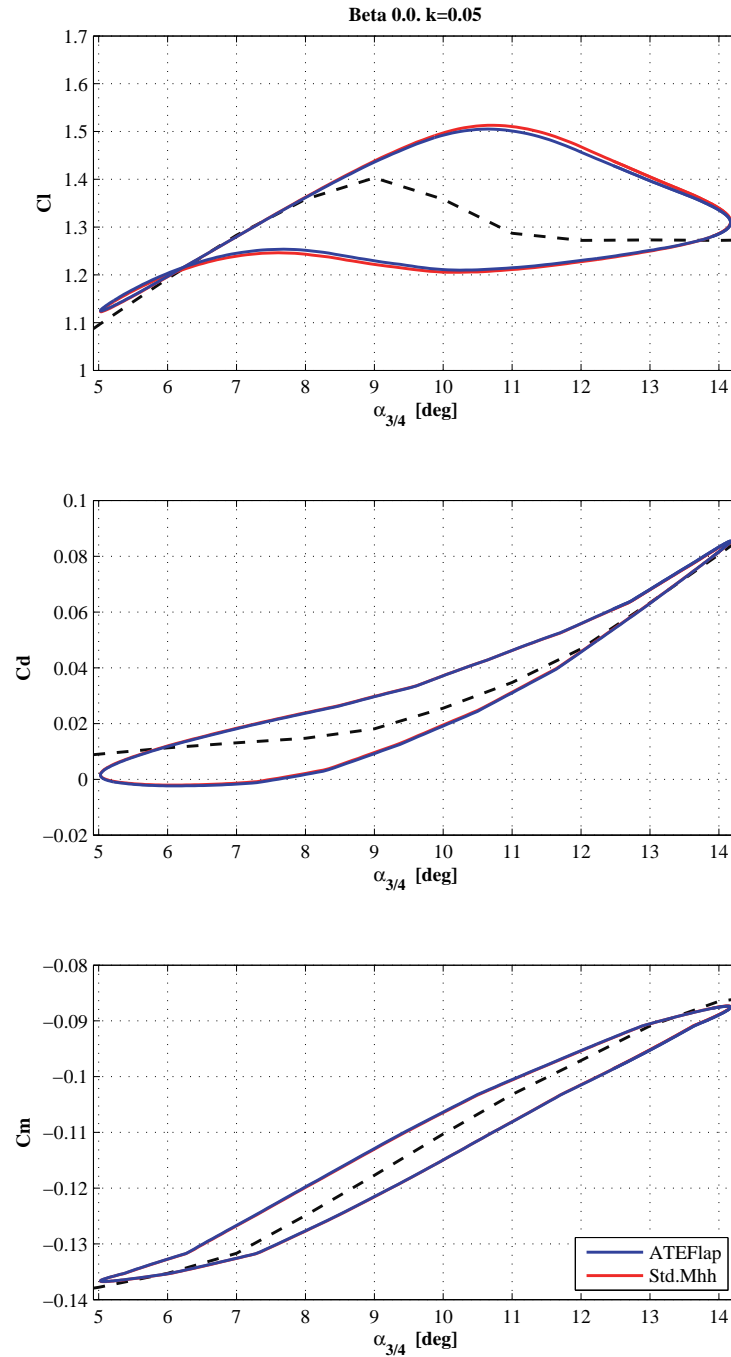


Figure 4.2: Model validation, comparison of the aerodynamic forces computed with the ATEFlap aerodynamic model and the MHH model for a section with flap deflection equal to 0.0; minor differences in the lift coefficient due to flow separation. Mean angle of attack 10° ; steady data for DU 21-A17 airfoil, flat plate indicial response. For both aerodynamic models, the C_l and C_d loops have clockwise direction, C_m counter-clockwise.

4.2 Comparison with CFD solutions

The aerodynamic forces simulated by the *ATEFlap* model are compared with CFD results; CFD simulations have been carried out with a Reynolds number of six millions, and for harmonic flap deflection corresponds to the cases published in the UpWind ‘Code performance comparison’ report [7].

A NACA 64-418 airfoil is fitted with a trailing edge flap covering the last 10% of the chord. The camberline deformation Δy_{camb} due to the flap deflection β is given as $\Delta y_{\text{camb}} = \beta \cdot y_{fl}$. The function y_{fl} describes the deflection shape of the flap, i.e. the camber-line variation for a unitary flap deflection.

The deflection shape for a unit chord length airfoil is defined as a circular arch starting at 90 % of the chord length $x_h = 0.9$; the radius of the circle is set so that the line connecting the point on the arch at the trailing edge $x_{TE} = 1.0$ with the point at $x_h = 0.9$ forms an angle of 1 degree with the x-axis, figure 4.3 :

$$y_{fl}/c \begin{cases} y_{fl}/c = 0.0 & \text{for } x/c < 0.9 \\ y_{fl}/c = \sqrt{R_c^2 - (x/c - 0.9)^2} - R_c & \text{for } x/c \geq 0.9 \end{cases} \quad (4.1)$$

where the radius of the circular arch is given by

$$R_c = \frac{0.1^2 + \delta_y^2}{2\delta_y}, \quad (4.2)$$

$$\delta_y = 0.1 \tan(1 \cdot \pi/180). \quad (4.3)$$

The aerodynamic forces are computed for the airfoil undergoing harmonic pitching motion around the quarter-chord point, and for the case of harmonic flap deflection. Three reduced frequencies are tested: $k = 0.02$, $k = 0.1$, $k = 0.5$; the mean angle of attack is varied from the fully attached region, to the stall region.

The steady input data for the model are retrieved from CFD computations on the same airfoil, and the indicial lift response function is tuned to fit the step response of a NACA 64-418 [4]; the corresponding coefficients are given in table 4.1.

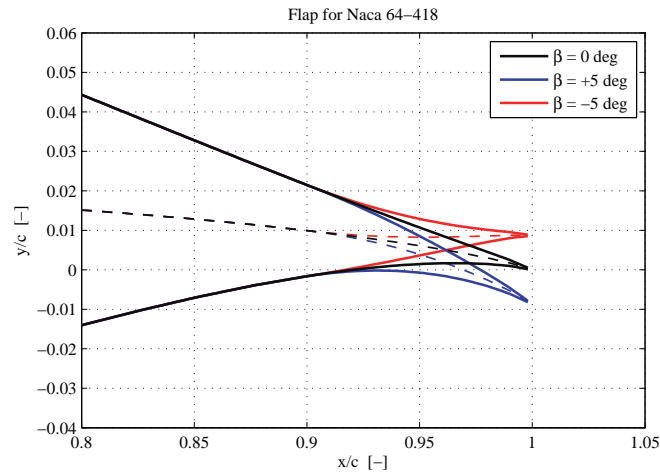


Figure 4.3: *Camber-line deformation corresponding to flap deflections of $\pm 5^\circ$ on the investigated NACA 64-418 airfoil profile [7].*

A_i	0.1784	0.07549	0.3933
b_i	0.8000	0.01815	0.1390

Table 4.1: *Indicial lift response function coefficient for the NACA 64-418 airfoil, from curve fitting to panel code simulation of the airfoil step response [4].*

4.2.1 Harmonic pitching motion

Several cases are run for the airfoil undergoing harmonic pitching motion with respect to a hinge point located at the quarter-chord point; the flap is locked to a null deflection. Only results concerning a reduced frequency of $k = 0.1$ and a pitch variation of $\pm 1^\circ$ are here reported.

The performance of the model in the attached flow region are checked by setting the mean angle of attack at 0° , figure 4.4. The stall onset is investigated at mean angle of attack 12° , figure 4.5, and at mean angle 16° , for the behavior deeper in the stall region, figure 4.6.

In the attached flow case, fig. 4.4, the lift coefficient curve is practically overlapping the CFD one, and a good agreement is also reported for the drag curve, although the ATEFlap model slightly over predicts the dynamic

effects. The pitching moment dynamics are also captured by the model, although it seems to slightly over predict the dynamic effects, compared to the CFD results.

At stall on-set, fig. 4.5, there is still a very good agreement concerning the lift force; drag and moment dynamics are also captured, although the differences from CFD results are now larger.

In deeper stall, fig. 4.6, the quality of the agreement is deteriorated also for the lift force. Nevertheless, the model still captures the overall dynamics, the lift and drag loops have similar openings, and all the simulated loops display the same direction of rotation.

4.2.2 Harmonic flap deflection

The airfoil is fixed to a constant angle of attack, and the flap is deflected with harmonic variations around the undeflected position. Flap oscillation with an amplitude up to 5 degrees are considered, allowing thus to verify also non linear flap effects; the airfoil angle of attack is changed from 0 to 16 degrees, considering thus attached and separated flow conditions. Here, only cases corresponding to angle of attack of 0, 12, and 16 degrees, flap deflection of $\pm 5^\circ$, and reduced frequency $k = 0.1$ are presented.

In attached flow, figure 4.7, there is a very good agreement between the forces predicted by the model and the CFD ones, also for the drag and the moment coefficients. The flap deflection has nearly no dynamic effect on the moment coefficient; in fact, both the model and the CFD curves are very close to the steady one.

At stall onset, the lift, drag forces, and moment predicted by the model are still in good agreement with the results from the CFD simulations. The agreement is maintained also deeper in the stall region, fig. 4.9, although the lift loop predicted by the model depicts a major axis with a slope lower than the steady curve one, while a higher slope is given by the CFD loop. At an higher reduced frequency, $k = 0.5$, and same angle of attack, the agreement is improved and both the results from CFD and the model depict loops with

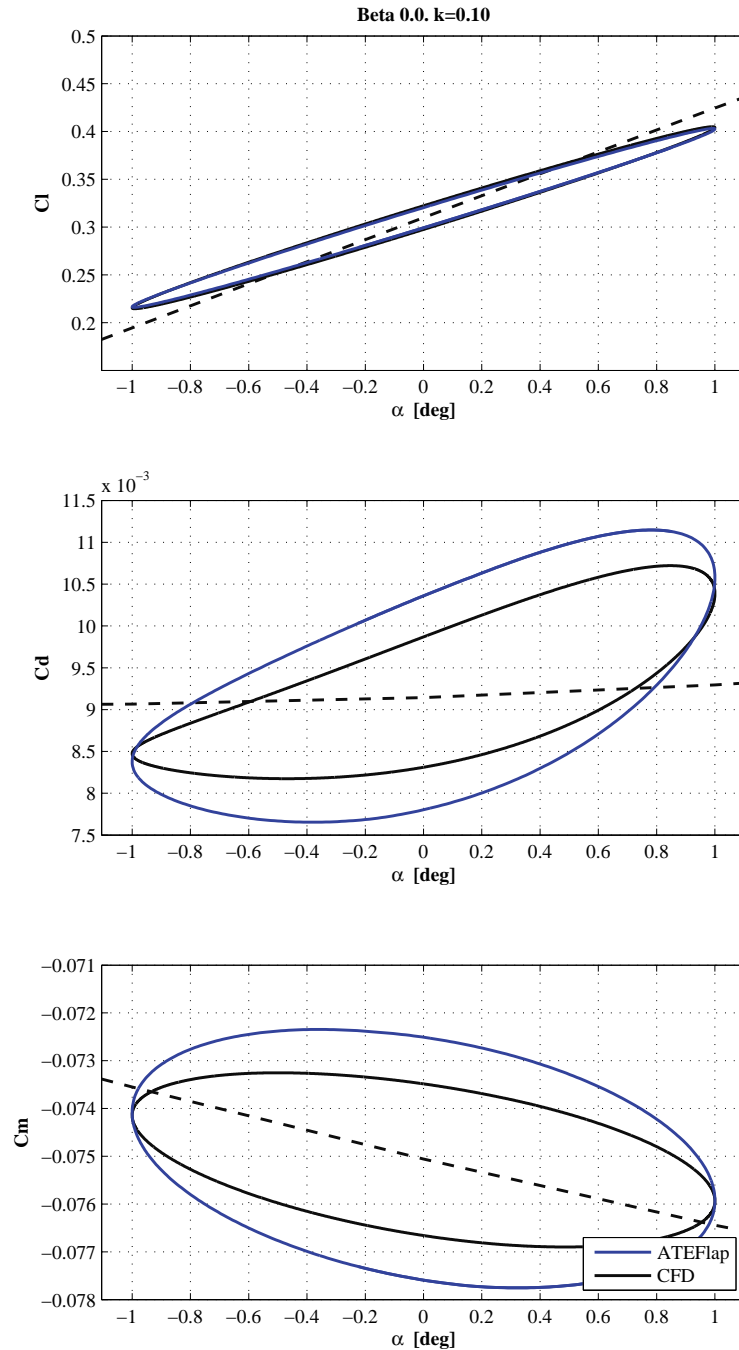


Figure 4.4: Model validation, comparison of aerodynamic forces with CFD results for a NACA 64-418 airfoil undergoing harmonic pitching motion. Attached flow region, mean angle of attack 0° . For both ATEFlap and CFD results, the C_l and C_m loops have counter-clockwise direction, C_d clockwise.

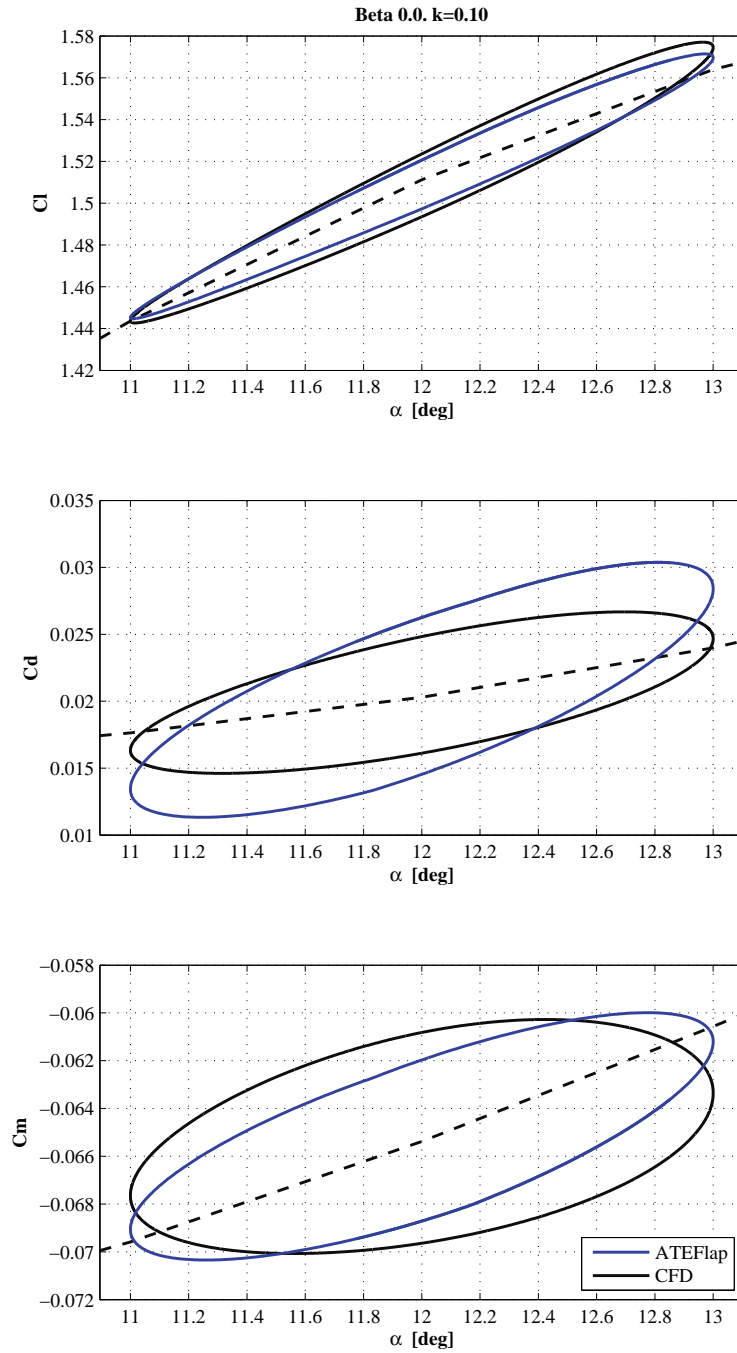


Figure 4.5: Model validation, comparison of aerodynamic forces with CFD results for a NACA 64-418 airfoil undergoing harmonic pitching motion. Stall on-set, mean angle of attack 12° . For both ATEFlap and CFD results, the C_l and C_d loops have clockwise direction, C_m counter-clockwise.

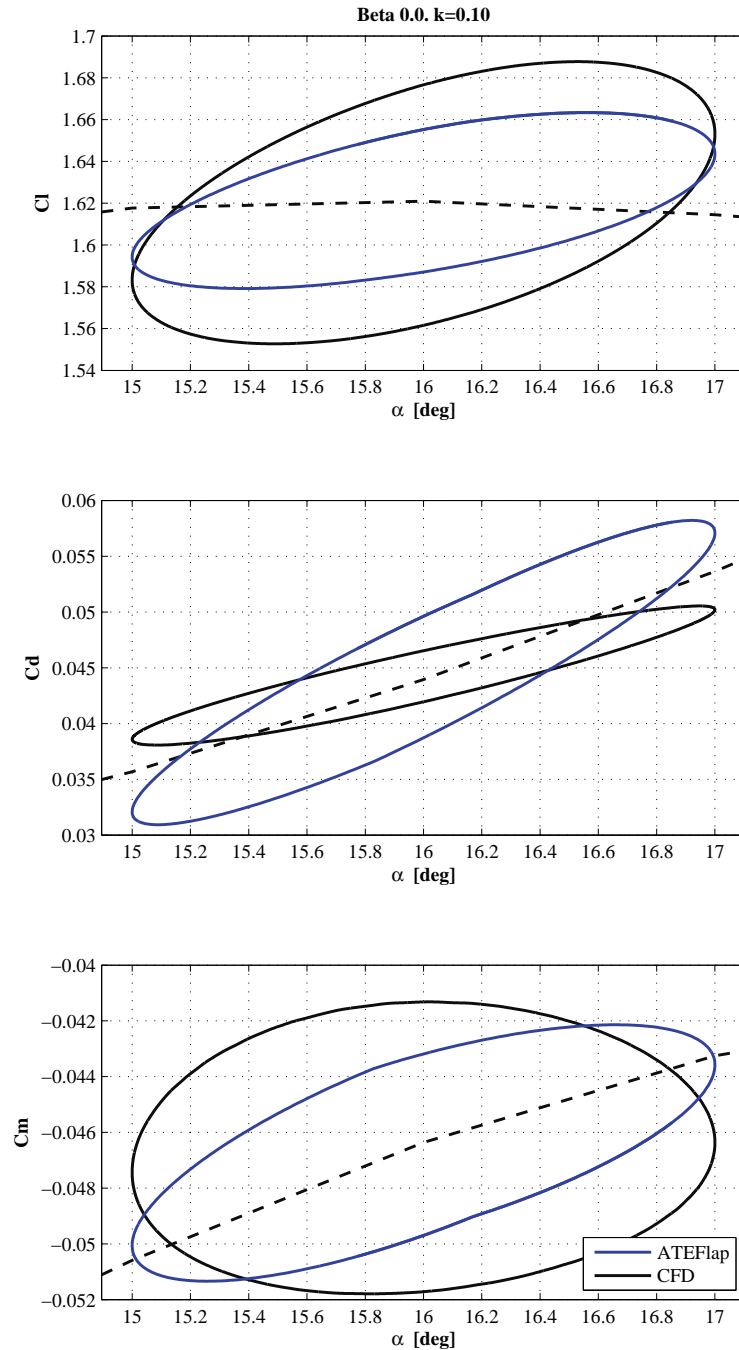


Figure 4.6: Model validation, comparison of aerodynamic forces with CFD results for a NACA 64-418 airfoil undergoing harmonic pitching motion. Stall region, mean angle of attack 16° . For both ATEFlap and CFD results, the C_l and C_d loops have clockwise direction, C_m counter-clockwise.

a major axis less inclined than the steady curve, figure 4.10.

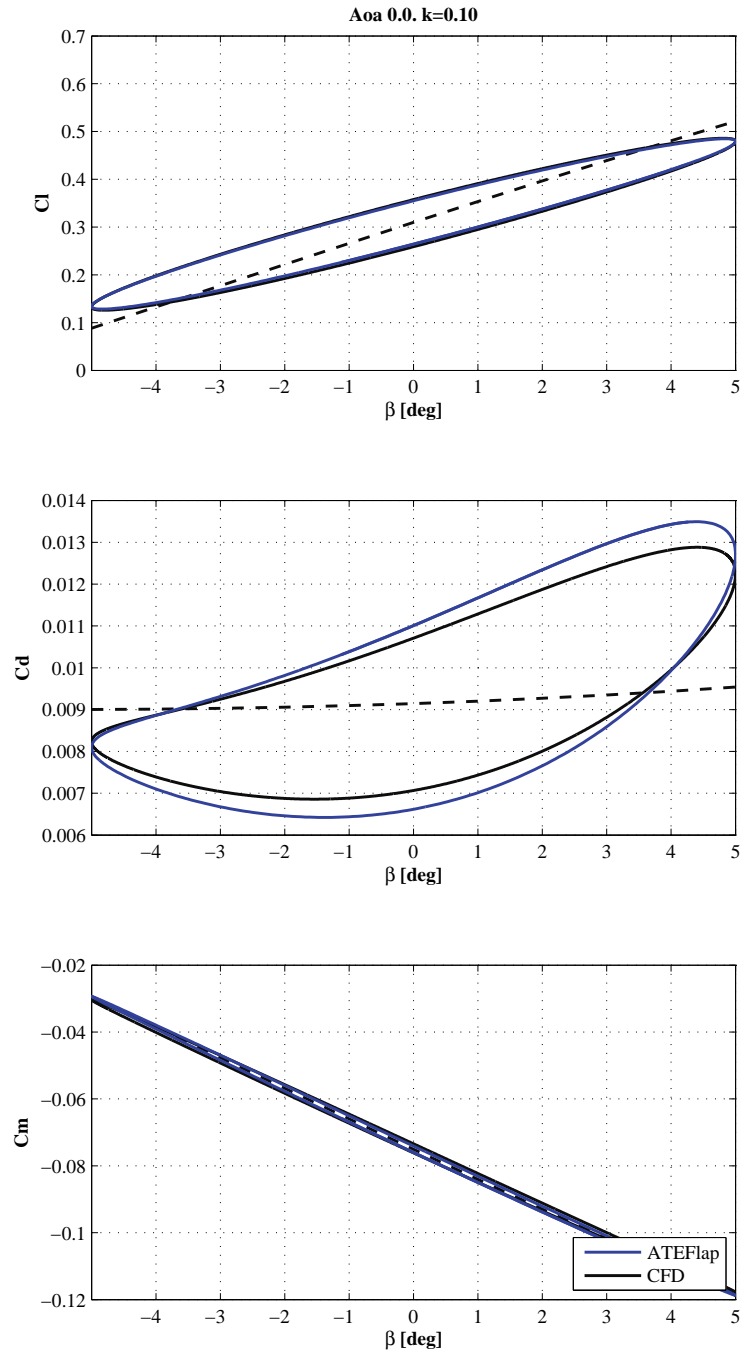


Figure 4.7: Model validation, comparison of aerodynamic forces with CFD results for a NACA 64-418 airfoil undergoing harmonic flap deflection; CFD results presented in the UpWind report [7]. Attached flow region, angle of attack 0° . For both ATEFlap and CFD results, the C_l loop has counter-clockwise direction, and C_d clockwise; for the C_m loop the ATEFlap model reports a counter-clockwise direction, while CFD clockwise; however, the loop opening is very small, and the values nearly lie on the steady curve.

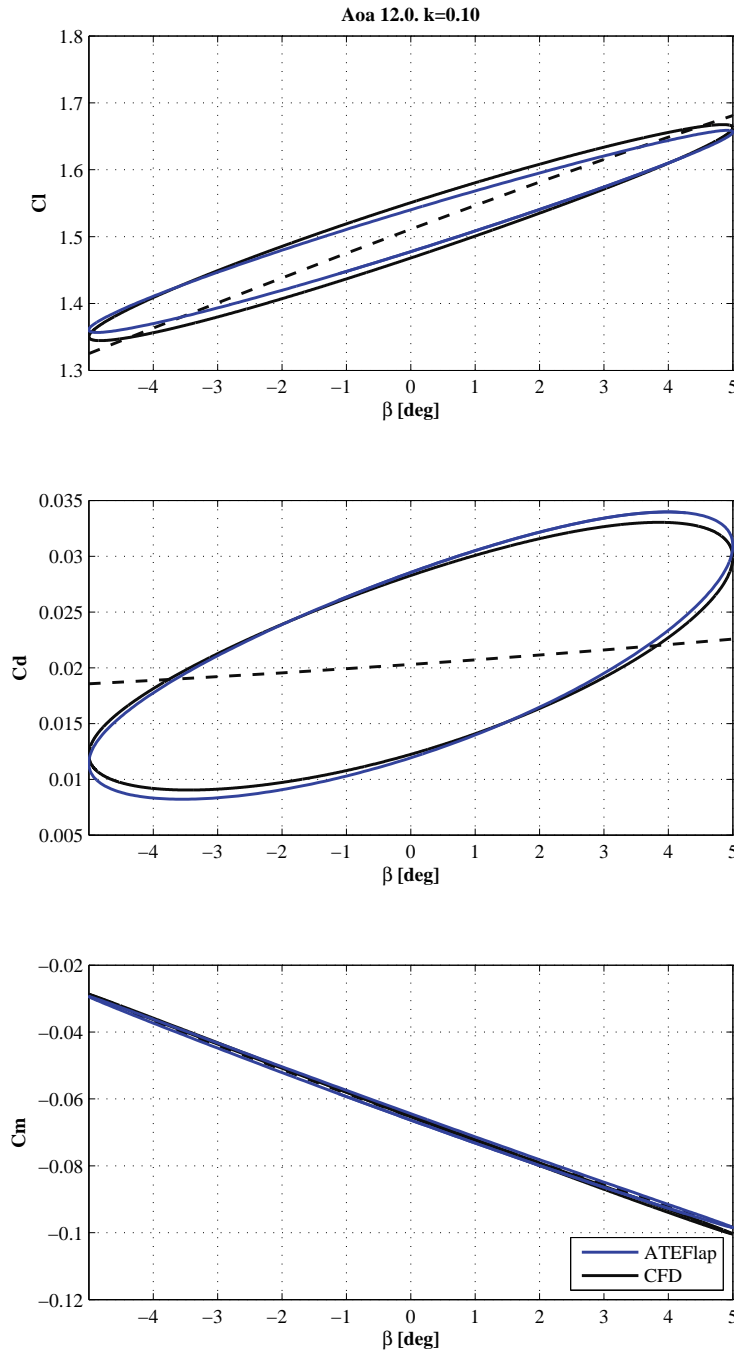


Figure 4.8: Model validation, comparison of aerodynamic forces with UpWind [7] CFD results for a NACA 64-418 airfoil undergoing harmonic flap deflection. Stall onset, angle of attack 12° . For both ATEFlap and CFD results, the C_l and C_m loops have counter-clockwise direction, C_d clockwise.

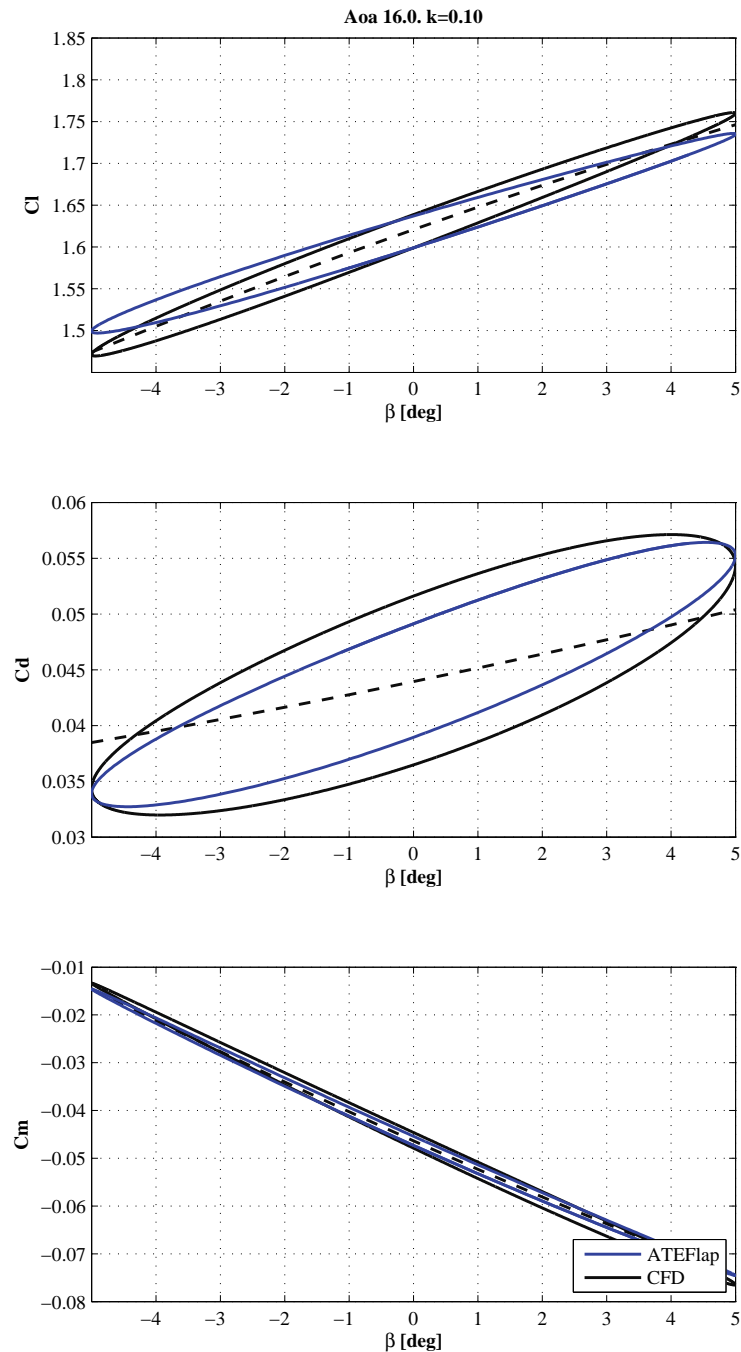


Figure 4.9: Model validation, comparison of aerodynamic forces with UpWind [7] CFD results for a NACA 64-418 airfoil undergoing harmonic flap deflection. Stall region, angle of attack 16° . For both ATEFlap and CFD results, the C_l and C_m loops have counter-clockwise direction, C_d clockwise.

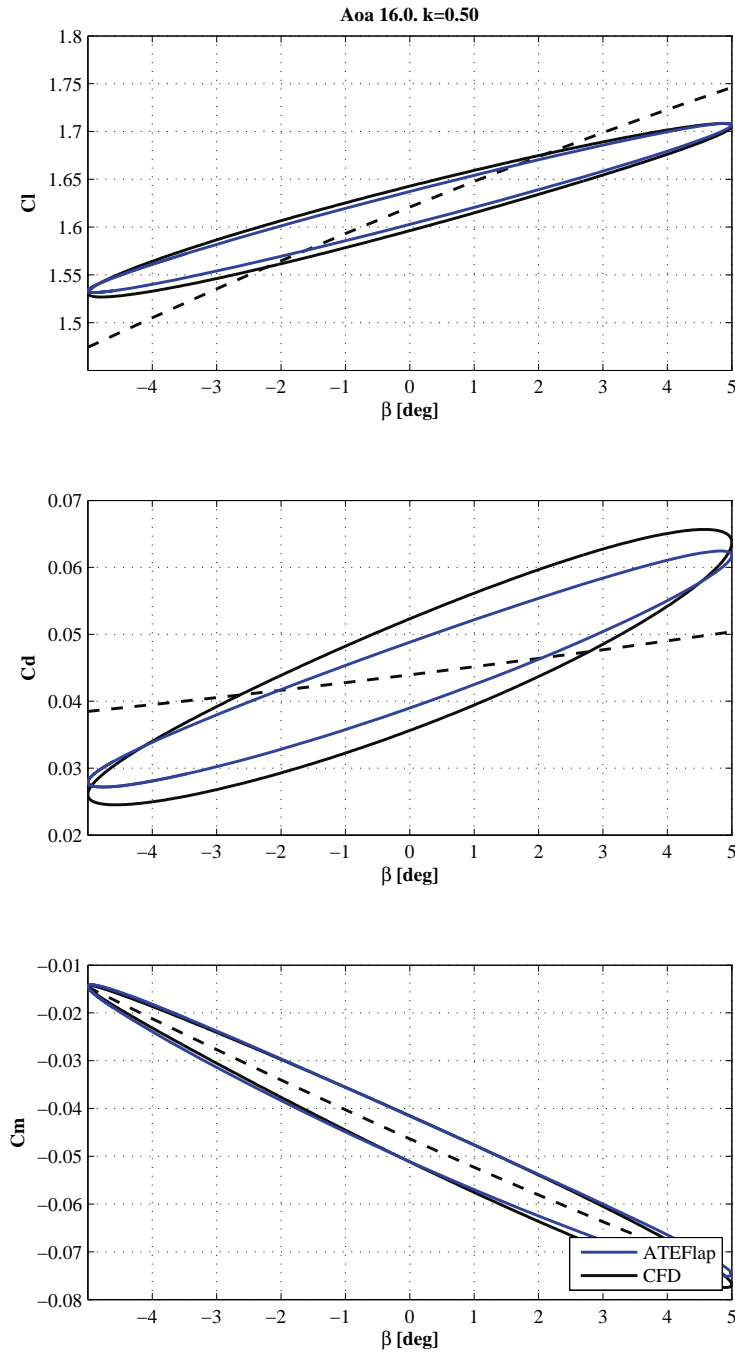


Figure 4.10: Model validation, comparison of aerodynamic forces with UpWind [7] CFD results for a NACA 64-418 airfoil undergoing harmonic flap deflection. Stall region, angle of attack 16° , higher reduced frequency $k = 0.5$. For both ATEFlap and CFD results, the C_l and C_m loops have counter-clockwise direction, C_d clockwise.

Conclusion

The *ATEFlap* aerodynamic model has been presented, and the algorithms underlying its implementation have been described. The model returns lift, drag, and moment coefficients for a 2D airfoil section equipped with an Adaptive Trailing Edge flap.

The *ATEFlap* model is a refinement of the model presented by Andersen et al. [1], and is obtained by merging Gaunaa's [6] model for a thin airfoil undergoing camberline deformation in potential flow, and the dynamic stall model for a rigid airfoil presented in Hansen et al. [8]. Under the assumption of plane wake approximation, trailing edge stall separation, and uniform upwash velocity along the chord, the model is able to describe the dynamics of the forces related both to the vorticity shed into the wake, and to flow separation.

The *ATEFlap* model has been integrated in the aeroelastic simulation tool HAWC2, while the preprocessing of the steady input data required by the Beddoes-Leishmann type of dynamic stall model is performed in an external application, which gives the user the possibility to verify, and eventually correct, the steady data.

A first validation is carried out by comparing the output of the *ATEFlap* model with the results from the model described by Hansen et al. [8]. An airfoil section with fixed undeflected flap and undergoing harmonic changes of angle of attack is considered; the resulting forces and moment loops are practically overlapping.

Further validations are obtained by comparison with CFD simulations of an airfoil undergoing harmonic pitching motion, or harmonic flap deflections. In case of harmonic pitching, minor discrepancies are reported between the aerodynamic coefficients resulting from the *ATEFlap* model and from CFD, in particular for drag and moment in separated flow conditions. In case of fixed angle of attack and harmonic flap deflections, the *ATEFlap* model shows a very good agreement with CFD results, both in attached and separated flow conditions.

The *ATEFlap* aerodynamic model is thus validated, and it is considered suitable to perform aeroelastic simulations of a wind turbine equipped with trailing edge flaps.

Bibliography

- [1] P. B. Andersen, M. Gaunaa, C. Bak, and M. H. Hansen. A dynamic stall model for airfoils with deformable trailing edges. *Wind Energy*, 12(8):734–751, 2009.
- [2] Peter Baek, Mac Gaunaa, Joachim Heinz, Leonardo Bergami, and John Korsgaard. A modified dynamic stall model for airfoils with active aerodynamic devices. *Submitted to Wind Energy*, December 2011.
- [3] T. S. Beddoes. Practical computations of unsteady lift. *Vertica*, 8(1):55–71, 1984.
- [4] Leonardo Bergami, Mac Gaunaa, and Joachim Heinz. Indicial lift response function: an empirical relation for finite-thickness airfoils, and effects on aeroelastic simulations. *Submitted for publication to Wind Energy*, August 2011.
- [5] T. Buhl, M. Gaunaa, and C. Bak. Potential load reduction using airfoils with variable trailing edge geometry. *Transactions of the ASME. Journal of Solar Energy Engineering*, 127(4):503–516, 2005.
- [6] M. Gaunaa. Unsteady two-dimensional potential-flow model for thin variable geometry airfoils. *Wind Energy*, 13(2-3):167–192, 2010.
- [7] Mac Gaunaa, Vasilis A. Riziotis, Nando Timmer, Herman Snel, Peter B. Andersen, and Joachim Heinz. Comparison of code performance for

- computation of unsteady 2D aerodynamics of airfoils with deformable trailing edges. Technical Report D2.5, UpWind - Integrated Wind Turbine Design, February 2011.
- [8] Morten Hartvig Hansen, Mac Gaunaa, and Helge Aagaard Madsen. A Beddoes-Leishman type dynamic stall model in state-space and indicial formulations. Technical Report R-1354(EN), Risoe National Laboratory, Roskilde (DK), 2004.
 - [9] R. T. Jones. The unsteady lift of a wing of finite aspect ratio. Technical Report 681, National Advisory Committee for Aeronautics (United States Advisory Committee for Aeronautics), 1940.
 - [10] J. Jonkman, S. Butterfield, W. Musial, and G. Scott. Definition of a 5-MW reference wind turbine for offshore system development. Technical Report NREL/TP-500-38060, National Renewable Energy Laboratory (NREL), February 2009.
 - [11] T. Karman and W. R. Sears. Airfoil theory for non-uniform motion. *Journal of the Aeronautical Sciences*, 5(10):379–390, 1938.
 - [12] Torben Juul Larsen. How 2 HAWC2 the user's manual. Technical Report R-1597(EN), Risoe National Laboratory. Technical University of Denmark, 2009.
 - [13] J. G. Leishman and K. Q. Nguyen. State-space representation of unsteady airfoil behavior. *AIAA journal*, 28(5):836–844, 1990.

APPENDIX A

Modifications with respect to previous versions of the model

This chapter lists the major changes that the algorithms used in the current versions of the preprocessor and *ATEFlap* model present in comparison with previous implementations of the aerodynamic model.¹

A.1 Preprocessor for dynamic stall model

In the first versions of the aerodynamic model for an airfoil with flap, the computation of the lift components required by the Beddoes-Leishmann dynamic stall model was performed directly by the aerodynamic model during aeroelastic simulations. The user had no possibility to check the steady input data, nor to correct discontinuities in the Beddoes-Leishmann components.

¹The report refers to the *Preprocessor for ATEFlap dynamic stall model* version 2.04, and to the *ATEFlap* aerodynamic model implemented in HAWC2 version 10.6, released in October 2011. Please refer to the HAWC2 version log to verify whether changes to the *ATEFlap* model have occurred in following versions.

By implementing the preprocessor algorithms in an external application, the user is given the possibility to verify and correct the steady data before their use in the aerodynamic model.

Previous versions of the steady data preprocessor were based on algorithms that differ from the current one, mainly in the following aspects:

A.1.1 Gradient $\partial C_l / \partial \alpha$ and flap deflection

In earlier versions of the algorithm, the gradient $\partial C_l / \partial \alpha$ used to determine the linear lift C_l^{lin} was computed separately for each flap deflection. The gradient was thus a function of the flap angle β ; as a result, the C_l^{lin} for $f^{st} < 1$ becomes non-linear in β . In fact, the β contributions appears not only in the term $\partial C_l / \partial \beta$ (linear contribution), but also through the term $\partial C_l / \partial \alpha|_{\beta}$, making it non-linear.

This non-linear mapping from the flap deflection β to the C_l^{att} coefficient yields, in the aerodynamic model, to a non-linear transformation from the flap deflection input to the lift force output. The non-linearity is responsible for some of the discontinuities in the lift coefficient loops observed at partially separated flow $f^{st} < 1$, as it appears in some of the loops in the UpWind report [7].

A.1.2 $\partial C_l / \partial \alpha$ algorithm

In previous versions of the preprocessor, the gradient $\partial C_l / \partial \alpha$ was computed as the average of any gradient above 50% of the maximum gradient. In the current version, the same algorithm as implemented in the HAWC2 MHH model is used, leading to a better consistency of the aerodynamic forces predicted by *ATEFlap* model and the MHH model for airfoils without flap. The algorithm is presented in section B.3.2.

A.1.3 C_l^{fs} and C_l^{att} at $f = 1$ and $f = 0$

In steady conditions, in fully attached flow $f = 1$, the term C_l^{fs} yields no contribution and could thus have any arbitrary value. Nevertheless, this does not apply in dynamic conditions where different lagging constants between separation function and angle of attack might lead to use a C_l^{fs} that would instead correspond to $f^{st} = 1$ in steady conditions.

In previous versions, in steady fully attached conditions $f^{st} = 1$, the value of C_l^{fs} was simply set equal to C_l^{st} , giving thus a strong discontinuity in the C_l^{fs} values. The discontinuity could also result in spikes in the aerodynamic force loops obtained with the previous versions, as observed in [7].

In the current version, to avoid discontinuities in the steady input data, C_l^{fs} is set to $0.5C_l^{st}$, as prescribed by classic Beddoes-Leishmann models. Similar considerations hold for C_l^{att} in fully separated condition $f^{st} = 0$, here C_l^{att} is set equal to C_l^{lin} also for $f^{st} = 0$.

A.1.4 C_d flap steady contribution

The steady data produced by the preprocessor account for the steady effects of flap deflections on the drag coefficient. In former implementations the steady drag coefficient was held constant for any flap deflection angle, and the drag contribution from the flap was formulated in terms of an equivalent change of angle of attack, see following section.

A.2 Aerodynamic model for an airfoil section with flap

The algorithms of the *ATEFlap* model called inside the aeroelastic simulation tool presents some differences from previous implementations of the aerodynamic model. The modifications were aimed to a better consistency

with the standard model for airfoils without flap, and to an improved agreement with steady results and dynamic CFD simulations. The modifications mainly concerned the following aspects:

A.2.1 Quasi-Steady flap deflection

In previous versions of the model, the term $\dot{\beta}$ was considered separately, as an equivalent angle of attack $\alpha_{\dot{\beta}}$,

$$\begin{cases} \alpha_{qs} &= \alpha_{st} - \frac{1}{U}\dot{y} + (0.5 - \epsilon)b\dot{\alpha} \\ \alpha_{\dot{\beta}} &= \dot{\beta}\frac{1}{2\pi}\frac{1}{U}H_y \\ \beta_{st} & \end{cases} ; \quad (\text{A.1})$$

the equivalent angle of attack $\alpha_{\dot{\beta}}$ was then summed to the α_{qs} contribution.

In the ideal case of fully potential flow and linear behavior of the lift coefficient, this approach should return equivalent results to the algorithm described earlier. On the other hand, the results might differ in the case of more realistic input steady data. It is thus decided to move the $\dot{\beta}$ contribution directly to the β_{qs} term, which also maintain similarity with the approach used for the quasi-steady angle of attack contribution, eq. (3.8).

A.2.2 Intermediate separation function $f^{C_{L,lag}}$

In previous version of the code, the intermediate separation function $f^{C_{L,lag}}$ was computed as

$$f^{C_{L,lag}} = f^{st} + \left(f^{C_{L,lag}} - f^{C_{L,tot}^{inv}} \right), \quad (\text{A.2})$$

where the separation function terms were obtained from a look-up of the steady input data, in correspondence of the angle of attack and flap deflection reported in table A.1.

The formulation ensured that the separation function would converge to its steady value in steady state conditions, as the terms $f^{C_{L,lag}}$ and $f^{C_{L,tot}^{inv}}$ cancel out in steady conditions, independently from the values of the gradient

<i>Out:</i>	α :	β :
f^{st}	α_{qs}	β_{st}
$f^{C_{L,lag}}$	$\frac{C_L^{lag}}{\partial C_L / \partial \alpha}$	0
$f^{C_{L,tot}^{inv}}$	$\frac{C_L^{tot}}{\partial C_L / \partial \alpha}$	0

Table A.1: Previous versions. Inputs for steady look-up of the separation function values.

$\partial C_L / \partial \alpha$. In the current formulation, eq. (3.19), the steady state value is reached only if the gradients $\partial C_L / \partial \alpha$ and $\partial C_L / \partial \beta$ have the same values that were used in preprocessing the steady input data.

In case of rather small variations of the flap deflection angle β and constant angle of attack α , the two formulations return similar results. On the other hand, whenever variations of the angle of attack around the stall point are considered (and thus larger variations in the separation function), the current formulation give results in better agreement with CFD computations, figure A.1. Furthermore, the current formulation also accounts for the effects of the flap deflection β in the separation mechanism.

A.2.3 Flap steady drag contribution

In the current version, the steady effects of flap deflection on the drag force are accounted for in the steady input data, where the drag coefficient is a function of both angle of attack and flap deflection. In former implementations of the model, the drag coefficient was only function of the angle of attack; the steady effects of the flap on the drag were then described through an equivalent change in angle of attack:

$$\Delta \alpha_{C_d \text{flap}} = \frac{\partial C_L / \partial \beta}{\partial C_L / \partial \alpha} \beta. \quad (\text{A.3})$$

The current implementation allows a more accurate tracking of the steady drag force, especially in the non-linear region of the steady coefficients.

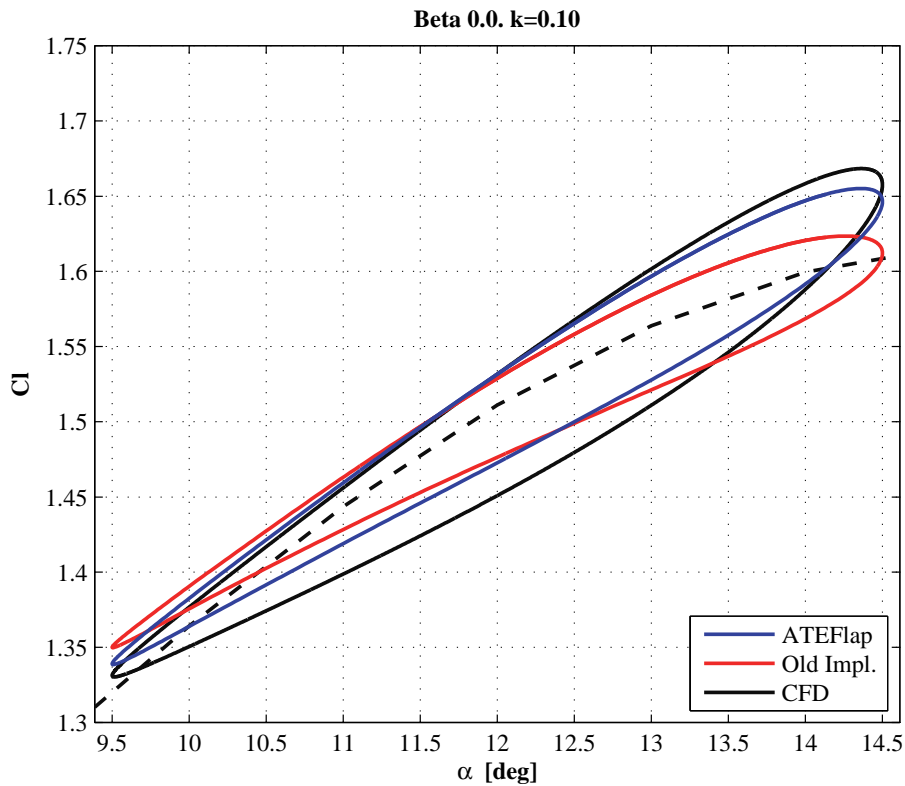


Figure A.1: Loop of C_l for harmonic variations of Angle of attack (Aoa); comparison of previous and current algorithm to compute the separation function f .

A.2.4 Induced drag contribution from separation function

In the current formulation the contribution of the separation function f to the induced drag is computed with respect to the f^{dyn} and $f^{C_{L,lag}}$. In the Beddoes-Leishmann model described in Hansen et al. [8], the $f^{C_{L,lag}}$ term is substituted by an f^{eff} one, based on a look-up of the steady curves with the effective angle of attack α_{eff} .

Several dynamic simulations have returned no appreciable difference in the two cases; while in steady conditions, as f^{eff} can be slightly different from

f^{C_l} , the f^{eff} formulation can result in a small non-zero contribution to the induced drag, and thus a small offset from steady data. Although no theoretical justification is given, it is chosen to keep the $f^{C_{L,lag}}$ formulation, thus saving also an extra term and the f^{eff} look-up operation.

A.2.5 Flap acceleration term in non-circulatory contributions

In previous versions, the non-circulatory moment contribution included a flap deflection acceleration term $\ddot{\beta}$; the term is neglected in the actual formulation. It has been verified that the flap acceleration term $\ddot{\beta}$ has an effect that is indicatively below the 5% of the total contribution for reduced frequencies up to $k = 1.5$; similar considerations hold for the contribution of the acceleration term $\ddot{\alpha}$.

APPENDIX B

Details of ATEFlap implementation in HAWC2 code

The ATEFlap aerodynamic model for an airfoil section with trailing edge flap is integrated in the aeroelastic simulation tool HAWC2. The following sections report some modifications and ‘interpretations’ to the aerodynamic model, which emerged during the implementation of the model in the multi-body aeroelastic code HAWC2.

B.1 Airfoil section reference system

B.1.1 Angle of Attack

In the working frame of the multibody code HAWC2 is rather hard to determine the steady geometric angle of attack of the profile section α_{st} . The

aerodynamic model is thus using the `alpha section` angle, which accounts for the structural deformation and corresponds to the quasi-steady angle evaluated at the three quarter chord point $\alpha_{qs} = \alpha_{3/4}$.

B.1.2 Flow speed

The flow speed value U_0 for the aerodynamic model is taken equal to the section `vrel`, which accounts for the free wind speed, the induced velocities, and the eigen motion of the blade, evaluated at the three-quarter chord point.

B.1.3 Direction of forces

In the aeroelastic code HAWC2, the direction of the aerodynamic forces returned by the model is referred to the direction of the relative velocity on the section, evaluated at the three-quarter-chord point. The lift acts with a direction perpendicular to the relative velocity, and the drag parallel to it. The direction of the drag returned by the model has thus an angle of α_{qs} from the airfoil chord, which varies depending on the torsion velocity $\dot{\alpha}$ of the section.

While the dependency on the reference direction has a negligible impact on the magnitude of the lift force, the relative influence on the drag magnitude can be significant. A thorough analysis is given in the appendix of Baek et al. [2], developing from the potential flow theory presented in Gaunaa [6]. The key points are repeated in the following paragraph, in relation to the HAWC2 implementation of the ATEFlap model.

The magnitude of the drag force depends on which location ϵ along the airfoil chord is the reference direction taken,

$$C_{d,ind}^\epsilon = C_l^{\text{Circ.Dyn}} \left(\frac{C_{l,qs}}{\partial C_l / \partial \alpha} - \frac{C_l^{\text{Circ.Pot}}}{\partial C_l / \partial \alpha} \right) + C_l^{\text{Circ.Pot}} (0.5 + \epsilon) - \frac{\pi}{2} \left(\frac{b_{hc} \dot{\alpha}}{U_0} \right)^2, \quad (\text{B.1})$$

where the location along the chord is given by the dimensionless coordinate ϵ , which is $\epsilon = -1$ at the leading edge and $\epsilon = +1$ at the trailing edge.

The second order term, depending on $\dot{\alpha}^2$, is usually neglected, as its contribution is found insignificant for reduced frequencies up to $k = 0.5$. Furthermore, by referring the drag to the flow direction evaluated at the quarter-chord point $\epsilon = -0.5$, the expression simplifies to:

$$C_{d,ind}^{1/4} = C_l^{\text{Circ.Dyn}} \left(\frac{C_{l,qs}}{\partial C_l / \partial \alpha} - \frac{C_l^{\text{Circ.Pot}}}{\partial C_l / \partial \alpha} \right). \quad (\text{B.2})$$

The equation for $C_{d,ind}^{1/4}$ corresponds to the expression that is actually used in the HAWC2 implementation of the ATEFlap model, eq. (3.25), in spite the drag is referred to the relative flow vector at the three-quarter-chord point. The approximation, which is also adopted in the MHH model, is anyway expected to have negligible effects on full wind-turbine aeroelastic simulations.

B.1.4 Pitching moment at the quarter-chord point

The aerodynamic moment, eq. (3.28), is evaluated at the quarter-chord point. It can be shown from thin-airfoil potential flow theory [6] that the dynamics of the thin-airfoil quarter-chord moment are exclusively given by non-circulatory forces, which have no memory term, as the circulatory forces effectively act in the quarter-chord point [11]. In potential flow theory the moment coefficient is only function of the flap deflection (giving a camber-line deformation), and the non-circulatory terms:

$$C_m^{\text{Pot.}} = f \left(\beta, \dot{\alpha}, \dot{\beta}, \ddot{\alpha}, \ddot{\beta} \right). \quad (\text{B.3})$$

In the current formulation, eq. (3.28), the acceleration terms $\ddot{\alpha}$ and $\ddot{\beta}$ are omitted, as their contribution is found negligible for the reduced frequencies of interest in wind turbine applications. Furthermore, a look-up term, eq. (3.29), is included to account for viscous effects accounted by the steady input data:

$$C_m = C_m^{qs} + C_m^{nc,\dot{\alpha}} + C_m^{nc,\dot{\beta}}. \quad (3.28)$$

The steady look-up term C_m^{qs} in α and β returns the largest contribution to the moment, while any term giving memory effects from the vorticity shed into the wake cancels out. In fact, the moment at the quarter chord point $\epsilon = -0.5$ reads,

$$M_{1/4} = M_{\epsilon_{ea}} - Lb_{hc}(\epsilon_{ea} + 0.5), \quad (\text{B.4})$$

where $M_{\epsilon_{ea}}$ is the aerodynamic moment evaluated around the elastic axis (the rotation axis for the section pitching motions), as given in Gaunaa [6].

The moment and lift components containing the memory effects are given in terms of the equivalent three-quarter effective downwash w_{eff} ; they read [6]:

$$M_{\epsilon_{ea}}^{w_{\text{eff}}} = 2\pi\rho b_{hc}^2 U_0 (0.5 + \epsilon_{ea}) \cdot w_{\text{eff}}, \quad (\text{B.5})$$

$$L^{w_{\text{eff}}} = 2\pi\rho b_{hc} U_0 \cdot w_{\text{eff}}. \quad (\text{B.6})$$

By substituting eq. (B.5) and (B.6) in eq. (B.4), the effective downwash terms cancel out, and return

$$M_{1/4}^{w_{\text{eff}}} = 0. \quad (\text{B.7})$$

The moment has no dependency on the memory effects of the vorticity shed into the wake, and it is thus appropriate to use quasi-steady values in the steady curve look-up. In eq. (3.29), the steady flap deflection β_{st} is used, while, to maintain consistency with the MHH model for airfoils without flap, the effective value of angle of attack α_{eff} is used.

Furthermore, by referring the pitching moment to the quarter-chord point, also the non-circulatory part simplifies, and has no dependency on the location of the section elastic axis ϵ_{ea} . In fact, by expanding the non-circulatory terms in $\dot{\alpha}$ and $\dot{\beta}$ from eq. (B.4) yields to

$$\begin{aligned} M_{1/4}^{\dot{\alpha}} &= -\pi b_{hc}^3 \rho U_0 (0.5 - \epsilon_{ea}) \dot{\alpha} - \pi b_{hc}^3 \rho U_0 (\epsilon_{ea} + 0.5) \dot{\alpha} \\ M_{1/4}^{\dot{\alpha}} &= -\pi b_{hc}^3 \rho U_0 \dot{\alpha} \quad \rightarrow \\ C_{m,1/4}^{\dot{\alpha}} &= \frac{M_{1/4}^{\dot{\alpha}}}{2\rho U_0^2 b_{hc}^2} = -0.5\pi \frac{b_{hc}}{U_0} \dot{\alpha}; \end{aligned} \quad (\text{B.8})$$

$$\begin{aligned}
M_{1/4}^{\dot{\beta}} &= b_{hc}^3 \rho \frac{U_0}{\pi} \epsilon_{ea} F_{\text{dydxLE}} \dot{\beta} - b_{hc}^3 \rho \frac{U_0}{\pi} F_{\text{dydxLE}} (\epsilon_{ea} + 0.5) \dot{\beta} \\
M_{1/4}^{\dot{\beta}} &= -0.5 b_{hc}^3 \rho \frac{U_0}{\pi} F_{\text{dydxLE}} \dot{\beta} \quad \rightarrow \\
C_{m,1/4}^{\dot{\beta}} &= \frac{M_{1/4}^{\dot{\beta}}}{2\rho U_0^2 b_{hc}^2} = -0.25\pi \frac{b_{hc}}{U_0} F_{\text{dydxLE}} \dot{\beta}; \tag{B.9}
\end{aligned}$$

and thus also the dependency on the elastic axis location ϵ_{ea} cancels out.

B.2 Terms for non-circulatory contributions

B.2.1 Flap deflection rate $\dot{\beta}$

The term $\dot{\beta}$ is computed internally in the *ATEFlap* model, and is evaluated simply as the difference between the actual and the previous time step flap deflection value, divided by the time step.

B.2.2 Section torsion rate $\dot{\alpha}$

The torsion rate $\dot{\alpha}^{\text{str}}$ only includes structural contributions, and no effects from changes in the angle of attack due to wind speed changes. The torsion rate is computed as the projection of the global rotation of the section `s1.omega` on the local aerodynamic plane; only the rotation component around the local span-wise axis z is considered. The term accounts for structural deformations of the blade or other parts of the structure, but also, in case of a coned rotor, it includes a constant contribution from the rigid-body rotation Ω of the whole rotor, which is projected in local coordinates as $\dot{\alpha}_{\Omega}^{\text{str}} = \Omega \sin \gamma_{\text{cone}}$. In the ‘stand-alone’ implementation of the model, for an isolated 2D airfoil section, the $\dot{\alpha}^{\text{str}}$ is simply computed as $\dot{\alpha}^{\text{str}} = d\alpha_{3/4}/dt$.

B.3 Operational aspects in HAWC2

B.3.1 Defining a rotor with flaps in the input file

The ATEFlap model is run in HAWC2 by selecting the `dynstall_method` number 3, in the `aero` command block, in the HAWC2 `.htc` input file; please refer to an updated manual release [12] for details on the commands syntax.

B.3.1.1 Required input data

The location of the flaps on the rotor is defined in the same `.htc` input file, in the `dynstall_ateflap` sub-command block. For each flap section the command `flap` is issued, followed by the spanwise positions of the flap section starting and ending points, and the file name for the corresponding `.ds` steady input file (which is returned by the pre-processor).

The locations along the blade are referred to the ‘stretched’ blade, i.e. along the curved line defined by the `c2_def` half-chord coordinates. The criteria for an aerodynamic computation point located at r_{pt} to be included in a flap section is $r_{start} \leq r_{pt} < r_{end}$; consequently, a computation point falling on the edge of two consecutive flap sections will be assigned to the outermost flap.

Overlapping flap sections are resolved by assigning the overlapped portion of the blade span to the flap sections involved in the overlap that was defined last in the `.htc` input.

A maximum number of 99 flap per blades can be defined, and a maximum of 500 computation points can address the same flap section, the limits are hard-coded.

The *ATEFlap* method applies the algorithm described in the previous chapter to compute the aerodynamic forces on the aerodynamic computation points that fall within a flap section. The computational points inside the same flap section all refer to the same steady input data; it is thus advised to split

a long flap-section in shorter sections if the steady input data are changed considerably along the flap section (e.g. because of thickness changes).

For blade locations where no-flap is defined, the model uses the same computation subroutines as the standard MHH model. In this case the steady input data are retrieved from the standard HAWC2 `.ae` and `.pc` input files. For sections without flap, the lift components for the dynamic stall model are computed internally, as well as the linear lifts parameters $\partial C_l / \partial \alpha$ and α_0 , which are estimated following the algorithm described in section B.3.2.

B.3.1.2 Optional input data

In the same `dynstall_ateflap` sub-command block in the `.htc` input file, the user can specify additional input commands, a complete list is reported in the HAWC2 manual [12].

The additional input allow to customize the *indicial response function*, see section 3.1, by specifying a set of three pairs of exponential series parameters A_i and b_i (`ais` and `bis` commands). If the commands are omitted, the default values are used, which describe the indicial response of a Risø B1-18 profile, with thickness ratio of 18. An empirical method to estimate indicial function parameters for finite-thickness airfoils is described in Bergami et al. [4].

In the same sub-command block the user can also specify the values of the *deflection shape integrals*, sec. 3.1, which depend on the camber-line deformation shape induced by unitary flap deflection, refer to Gaunaa [6] for details.

The deflection shape integrals used in the *ATEFlap* model implementation are (the corresponding command for the `.htc` file is given in parenthesis):

- F_{dydxLE} (`fdydxle`), and G_{dydxLE} (`gdydxle`)
- H_y^* (`hystar`), and $F_{y,LE}^*$ (`fylestar`), which correspond to the integrals H_y and $F_{y,LE}$ in Gaunaa [6], made dimensionless by normalization by the half-chord length: $H_y^* = H_y / b_{hc}$, $F_{y,LE}^* = F_{y,LE} / b_{hc}$.

The default values correspond to a 10% chord-length trailing edge flap with circular arc deformation shape, as used in the UpWind comparison report [7], and described in section 4.2. Please refer to Gaunaa [6] for the equations to compute deflection shape integrals with different flap deflection shapes.

B.3.2 Estimating linear parameters $\partial C_l/\partial\alpha$ and α_0

The linear parameters $\partial C_l/\partial\alpha$ and α_0 are estimated from the steady input data giving the lift coefficient C_l^{st} as function of the angle of attack α . The same algorithm is applied both in the preprocessor application (for sections with flap), and in HAWC2 in the initialization phase (for sections without flap). The algorithm has the following steps:

1. A first guess on the angle of attack returning zero lift α_0^* is made, simply by interpolating the C_l^{st} curve given as input.
2. An iterative procedure is carried out to find the angle of attack α_+ , giving the upper limit to the ‘linear-lift’ region. The iterations are carried out for all the points on the steady lift curve with positive lift $C_l^{st} > 0$; for each point k on the curve are stored:
 - The angle of attack α_k corresponding to the point.
 - The gradient $\Delta C_l/\Delta\alpha|_k$ of the line connecting the zero lift point α_0^* to the α_k point.
 - The relative error err_k resulting from approximating the C_l^{st} curve to a straight line C_l^{Appx} between α_0^* and α_k . The error is evaluated for $N_{pt} = 50$ points equally spaced between α_0^* and α_k as:

$$\text{err}_k = \left(\sum_{j=1}^{N_{pt}} \frac{C_{l,\alpha_j}^{st} - C_{l,\alpha_j}^{\text{Appx}}}{C_{l,\alpha_j}^{\text{Appx}}} \right) \cdot \frac{1}{N_{pt}},$$

where the approximated linear lift value is

$$C_{l,\alpha_j}^{\text{Appx}} = \frac{\Delta C_l}{\Delta\alpha} \Big|_k (\alpha_j - \alpha_0^*).$$

At the end of the iterations, the angle α_+ is given by the highest value between the α_{k^*} point that returns the maximum $\Delta C_l / \Delta \alpha|_k$, and all the α_{k^*} points for which the approximation error $\text{err}_k < 0.01$:

$$\alpha_+ = \max(\alpha_{(\max \Delta C_l / \Delta \alpha)}, \forall \alpha_{k^*} : \text{err}_{k^*} < 0.01).$$

3. A similar iterative procedure is carried out to find the angle of attack α_- , which gives the *lower* limit to the ‘linear-lift’ region. The iterations are now carried out for the points on the steady lift curve with negative lift $C_l^{st} < 0$.
4. The angles of attack α_+ and α_- are set, giving thus the bounds of the linear lift region. The linear parameters $\partial C_l / \partial \alpha$ and α_0 are then given by the slope and the intercept of the straight line connecting the α_+ and α_- points:

$$\frac{\partial C_l}{\partial \alpha} = \frac{C_{l,\alpha_-}^{st} - C_{l,\alpha_+}^{st}}{\alpha_- - \alpha_+},$$

and

$$\alpha_0 = \frac{C_{l,\alpha_-}^{st} \cdot \alpha_+ - C_{l,\alpha_+}^{st} \cdot \alpha_-}{C_{l,\alpha_-}^{st} - C_{l,\alpha_+}^{st}}.$$

B.3.3 Linear interpolation algorithm

A linear interpolation algorithm is used inside the HAWC2 routines to obtain the steady values corresponding to specific angle of attack or flap deflection values. The same linear interpolation algorithm is used in the pre-processor to export the steady data to the `.ds` input file.

Given y_0 and y_1 , corresponding respectively to x_0 , and x_1 , the interpolation returns the y_{aim} corresponding to x_{aim} , where:

$$x_0 \leq x_{\text{aim}} \leq x_1, \text{ and } y_0 \leq y_{\text{aim}} \leq y_1. \quad (\text{B.10})$$

An interpolation factor is defined as

$$k_{\text{int}} = \frac{x_{\text{aim}} - x_0}{x_1 - x_0}, \quad (\text{B.11})$$

and the sought value is given by the weighted sum

$$y_{\text{aim}} = k_{\text{int}} y_1 + (1 - k_{\text{int}}) y_0. \quad (\text{B.12})$$

The algorithm corresponds to the classic linear interpolation

$$y_{\text{aim}} = y_0 + \frac{y_1 - y_0}{x_1 - x_0} (x_{\text{aim}} - x_0), \quad (\text{B.13})$$

with the advantage that the interpolation factor k_{int} is not depending on the interpolated quantities y ; a more efficient computation is thus obtained, as the same factor k_{int} is used in the interpolation of different quantities (e.g. C_l , C_d , and C_m).

APPENDIX C

User's guide to Preprocessor for ATEFlap

C.1 Quick-start guide

This section lists the essential steps for using the application *Preprocessor for ATEFlap dynamic stall model, v. 2.04*.

1. Load the *Clean Airfoil* input file. `File -> Import Airfoil Cl, Cd, Cm`
2. Load the *Flap Delta-Steady* input file. `File -> Import Flap dCl| dCd| dCm`. If succeeded, the input fields will become active, a line is added in the status tab. The chart area is now active, zoom by holding the left mouse button, pan with the right button.
3. Insert a guess on the angles of attack where the fully separated region (deep stall) ends, and starts again. They should be inserted in the `Fully separated region limits` field, the lower value in the left

field. Please note that the computation of the gradient $\partial C_l / \partial \alpha$ will be performed only *inside* the range between the two specified values.

4. Specify the flap deflection angle to be used for the $\partial C_l / \partial \alpha$ gradient computation, in the `dCl/dAoa at beta` field; if present in the input file, 0 is the default and (*recommended*) value.
5. Once the input parameter have been specified, click on the **Compute!** button. Different curves will appear in the chart area, the flap deflection angles specified in the input file can be selected from the upper right field. In the **Status** tab, log lines are written as the computations proceed.
6. Scan through the different flap deflection angles to check steady input data, and Beddoes-Leishmann components. Eventually correct severe discontinuities in the curves (for instance in the f separation function curve), by clicking on the points and dragging them. Click on **Save Changes** button *before* changing the flap deflection value in order to store the modified curves. Repeat for all the given flap deflections.
7. When ready, export the result to the `.ds` flap steady aerodynamic input file, **File -> Export to dynamic stall model**. Verify that the option **Save Slopes in .ds output** is ticked. The generated file is ready to be used in the *ATEFlap* aerodynamic model in HAWC2.

C.2 I/O files formats

The input to the model consists of two ASCII files. The *Clean Airfoil* input gives lift, drag, and moment coefficients for an airfoil without any flap, as function of the angle of attack. The second input file is the *Flap Delta-steady* input, giving *variations* in steady lift, drag and moment caused by the flap deflection at different angle of attack.

The output of the pre-processor is saved in a `.ds` file, which is the flap steady aerodynamic input file required by the *ATEFlap* model in the aeroelastic tool HAWC2.

C.2.1 Input: Clean Airfoil

The file contains the steady lift, drag, and moment coefficients for a standard airfoil, without flap. The steady lift, drag, and moment coefficients are given as a function of the angle of attack.

Format requirements:

- The input file has 4 columns: 1.Angle of attack [deg]; 2.Cl; 3.Cd; 4.Cm. It has no header, nor comments, columns separated by space or *tab*.
- The angle of attack is sorted in *increasing* order, from negative to positive. Values from -180 to + 180 are recommended, otherwise first and last value will be repeated.
- A resolution of one degree is *recommended*. Arbitrary resolution is possible, although resolution higher than 1 degree is pointless as values are then exported with 1 degree resolution.

C.2.2 Input: Flap Delta-steady

It gives the steady *variation* (Delta) induced in the lift, drag, moment coefficients by the flap deflections, at different angles of attack.

Format requirements:

- The input file has 5 columns, organized as in table C.1. The file has no header, nor comments in the text; columns separated by space or tab.
- The *angle of attack* (Aoa) are given in degrees. The Aoa columns represents the *inner-loop*, values change from one row to the next. Values in *increasing* order (*mandatory*).

The angles of attack can start and end at arbitrary values, although is recommended to have first and last values equal to -180, +180, otherwise, first and last values will be assumed to keep constant up to -180, +180.

- The *flap deflection* β column give the *outer-loop*, the flap deflection value changes only after all the Aoa values are given. Values organized in *decreasing* order (*mandatory*).

The flap deflection value can start and end at arbitrary values, and the flap effects (Delta Cl, Cd, Cm) of minimum and maximum given flap deflections are assumed constant up to, respectively, -49, and +50.

- It is *strongly recommended* the presence in the input file of a block with flap deflection equal to 0.0, which corresponds, typically, to lift, drag, and moment variations also equal to 0.0. The 0.0 flap deflection value, will then be available as computation point for the linear slopes, see following sections.
- It is recommended that, in the range of interest of flap deflection and angle of attack, a resolution of 1.0 (degree) is kept.

1.	2.	3.	4.	5.
Aoa [deg]	Flap β	ΔC_l^{st}	ΔC_d	ΔC_m
Incr. -, +	Decr. +, -			

Table C.1: *Flap Delta-steady input. Coefficient variations for flap deflection (outer loop) at different angles of attack (inner loop).*

Note that the unit of the flap deflection specified in the input file can be arbitrary, as long as coherence is kept throughout the modeling and simulation (especially with the control algorithm). For instance, in case of a microtab actuator, requiring a +90,-90 degrees range, each unit of the flap deflection input can represent 2-degrees microtab rotation; similarly, to catch highly non linear behavior a single input unit can be set to represent 0.5 degrees flap deflection.

C.2.3 Output: .ds *ATEFlap* steady aerodynamic input file

The output file generated by the application contains the preprocessed data (steady data and Beddoes-Leishmann components) that will be used as input by the *ATEFlap* aerodynamic model in HAWC2.

Each different combination of airfoil (e.g. different thickness) or flap requires a different file. The data are saved in an ASCII file organized as follows:

- Row 1. Free for comments.
- Row 2. Free for comments.
- Row 3. Angle of attack (in radians) corresponding to a null steady lift when the flap deflection is zero: α_0 .
- Row 4. Free for comments.
- Row 5. Gradient of the steady lift function with respect to angle of attack variations: $\partial C_l / \partial \alpha$. The gradient is evaluated at the flap deflection value specified by the user in the `dCl/dAoa at beta` field. The gradient is measured in 1/rad.
- Row 6. Free for comments.
- Row 7. Gradient of the steady lift function with respect to flap deflection variations: $\partial C_l / \partial \beta$. The gradient is evaluated at angle of attack α_0 , for variations of ± 1 unit of flap deflection from the value specified by the user in the `dCl/dAoa at beta` field.
- Row 8. Free for comments.
- Row 9. N Total number of the following row-data entries.
- Row 10...9 + N . Data entries. Steady input data and Beddoes-Leishmann components as function of both angle of attack and flap deflection. The column order is given in table C.2. The format is as follow: Aoa is in degrees, varies from -180 to +180 with steps of 1 degree. The flap deflection goes from -49 to +50, with 1 unit steps. The flap deflection gives the 'inner-loop' (the value change at each row), the Aoa gives the 'outer-loop' (it changes value after going through all the flap deflections, i.e. every 100 rows). Values of angle of attack or flap that are outside the range that was given in the input are a repetition of the minimum or maximum value in the input.

If the option `Save slopes` in `.ds` output is un-ticked, then row 1-7 are skipped; for the input file to be read directly by the ATEFlap model in HAWC2, rows 1-7 are a *requirement* and therefore the option `Save slopes` in `.ds` output should be ticked.

1.	2.	3.	4.	5.	6.	7.	8.
Aoa [deg]	Flap β	C_l^{st}	C_l^{att}	C_l^{fs}	C_d	C_m	f sep.fun.

Table C.2: Columns order in the pre-processor output: `.ds` flap steady aerodynamic input file for the ATEFlap model in HAWC2. Steady data and Beddoes-Leishmann components are given as function of both angles of attack (outer loop), and flap deflection (inner loop).

The dissertation is submitted to the Technical University of Denmark, in partial fulfillment of the requirements for the obtainment of the PhD degree from the PhD School DTU Wind Energy.

The PhD project was carried out in the years 2010-2012 at the Aeroelastic Design Section of DTU Wind Energy, Department of Wind Energy (formerly Risø DTU, Wind Energy Department). The dissertation was submitted in March 2013, and successfully defended on the 4th July 2013.

Main Supervisor: Senior Scientist, Mac Gaunaa, DTU Wind Energy.

Co-supervisor: Associate Professor, Niels Kjølstad Poulsen, DTU Compute.

Co-Supervisor: Head of Section, Thomas Buhl, DTU Wind Energy.

DTU Wind Energy
Technical University of Denmark

Risø Campus, 118
Frederiksborgvej 399
4000
<http://www.vindenergi.dtu.dk/>

ISBN 978-87-92896-52-0